DISS. ETH NO. 30096

Optimization of the High-Intensity Muon Beamlines for MEG II, Mu3e and HIMB

A thesis submitted to attain the degree of

DOCTOR OF SCIENCES
(Dr. sc. ETH Zurich)

presented by

Giovanni Dal Maso
M. sc. Università degli Studi di Pisa

born on 16.10.1996

accepted on the recommendation of

Prof. Dr. K. S. Kirch
Prof. Dr. A. Papa
Prof. Dr. W. Ootani
Dr. J. Bernhard

2024

Abstract

High-intensity muon beams are excellent tools for searches Beyond Standard Model (BSM) physics that look for muon decays strongly suppressed in the Standard Model. In this context, the High Intensity Proton Accelerator (HIPA) facility at the Paul Scherrer Institut (PSI) in Switzerland plays a key role, delivering the most intense continuous muon beams in the world of up to a few $10^8\,\mu^+/\mathrm{s}$.
Two of the experiments measuring the so-called golden channels of charged Lepton Flavor Violation are hosted at HIPA: $\mu^+ \to e^+\gamma$ as searched for by the MEG II experiment, and $\mu^+ \to e^+e^+e^-$ as searched for by the upcoming Mu3e experiment. Part of the work presented here is dedicated to the commissioning of the Compact Muon Beam Line (CMBL), designed to deliver $\mathcal{O}(10^8\,\mu^+/\mathrm{s})$ to the Mu3e experiment for its first phase of data taking, expecting to reach a sensitivity of 10^{-15} on the branching ratio.
For its second phase, Mu3e will require larger statistics for its final sensitivity goal of 10^{-16} and therefore a higher muon rate. The High Intensity Muon Beams project at PSI aims to increase the delivered muon rates by two orders of magnitude to $\mathcal{O}(10^{10}\,\mu^+/\mathrm{s})$, with a huge impact for low-energy, high-precision muon experiments and muon spin rotation (μSR) techniques. The HIPA facility will be upgraded with two new beamlines, MUH2, dedicated to particle physics experiments, and MUH3, aimed at μSR measurements. In this thesis, the design of MUH2 and MUH3 and the optimization of their beam optics using genetic algorithm searches are presented, showing that the required muon rates can be achieved.
In the context of rare physics processes, the MEG II detector allows to test additional channels aiding the search for BSM physics. Thanks to a Cockroft-Walton accelerator decoupled from the main accelerator complex HIPA, a proton beam of up to 1.08 MeV in energy can be delivered to the center of the detector for an independent measurement of the anomaly observed by the ATOMKI collaboration in the angular distribution of the internal pair creation pairs in the reaction $^7\mathrm{Li}(\mathrm{p},\gamma)^8\mathrm{Be}$. The analysis framework of MEG II was extended and adapted for such a channel as part of this work. Particular emphasis is given to the treatment of systematics due to the limited available Monte Carlo statistics to model the background events.

Sommario

I fasci di muoni ad alta intensità sono strumenti eccellenti per la ricerca di fisica oltre il Modello Standard, attraverso decadimenti di muoni fortemente soppressi nel Modello Standard. In questo contesto, le infrastrutture del *High Intensity Proton Accelerator* (HIPA) all'Istituto Paul Scherrer (PSI) in Svizzera giocano un ruolo chiave, fornendo i fasci continui di muoni più intensi del mondo fino ad alcuni $10^8\,\mu^+/s$.
Due degli esperimenti alla ricerca dei cosiddetti *golden channels* della violazione di sapore dei leptoni carichi sono ospitati al HIPA: $\mu^+ \to e^+\gamma$, misurato dall'esperimento MEG II, e $\mu^+ \to e^+e^+e^-$, misurato dall'imminente esperimento Mu3e. Parte del lavoro presentato in questa tesi è dedicato al collaudo e messa in servizio della *Compact Muon Beam Line* (CMBL), progettata per fornire $\mathcal{O}(10^8\,\mu^+/s)$ all'esperimento Mu3e nella sua prima fase di presa dati, con una sensitività attesa di 10^{-15} sul *branching ratio*.
Per la sua seconda fase di presa dati, Mu3e necessiterà di una maggiore statistica per raggiungere una sensitività di 10^{-16}, e quindi di un incremento dell'intensità del fascio di muoni. Il progetto *High Intensity Muon Beams* al PSI mira ad incrementare l'intensità dei fasci di muoni di due ordini di grandezza, fino a $\mathcal{O}(10^{10}\,\mu^+/s)$, con un impatto significativo per esperimenti di precisione a bassa energia e per le tecniche di *muon Spin Rotation* (μSR). L'infrastruttura del HIPA sarà aggiornata con due nuove linee di fascio: MUH2, dedicata agli esperimenti di fisica delle particelle, e MUH3, dedicata alle misure di μSR. In questa tesi sono presentati il design di MUH2 e MUH3 e l'ottimizzazione della loro ottica tramite algoritmi genetici, mostrando che le intensità di muoni richieste possono essere raggiunte.
Nel contesto della ricerca di processi fisici rari, il rivelatore di MEG II permette di testare ulteriori canali che aiutano la ricerca di fisica oltre il Modello Standard. Grazie ad un acceleratore Cockroft-Walton disaccoppiato dal complesso principale HIPA dell'acceleratore, un fascio di protoni fino a 1.08 MeV di energia può essere trasmesso al centro del rivelatore per una misura indipendente dell'anomalia osservata dalla collaborazione ATOMKI nella distribuzione dell'angolo relativo nella produzione di coppia interna nel processo $^7\mathrm{Li}(p,\gamma)^8\mathrm{Be}$. Come parte di questo lavoro, il framework di analisi di MEG II è stato esteso e adattato per tale processo. Particolare attenzione è stata dedicata allo studio degli effetti sistematici dovuti alla limitata statistica di eventi Monte Carlo disponibile per modellare gli eventi di fondo.

Contents

Introduction

Rare physics processes have proven to be powerful tools to test the Standard Model (SM) of particle physics and to search for physics Beyond the Standard Model (BSM). In particular, the search for charged Lepton Flavor Violation (cLFV) processes, as yet unobserved, would be a clear sign of BSM physics.
Two channels are explored at the High Intensity Proton Accelerator (HIPA) facility at the Paul Scherrer Institut (PSI) in Switzerland: the $\mu^+ \to e^+\gamma$ decay, investigated by the MEG II experiment, and the $\mu^+ \to e^+e^+e^-$ decay, investigated by the Mu3e experiment. While possible in the SM, these processes are strongly suppressed, with branching ratios smaller than 10^{-54} [1], meaning that any observation would be a clear sign of BSM physics.
The sensitivity goals on the branching ratio of the MEG II experiment [2, 3] and of the first phase of Mu3e [4] data taking of 6×10^{-14} and 10^{-15} set stringent requirements on the intensity and properties of the muon beam. Today, these can only be met by the πE5 beamline at PSI delivering $\mathcal{O}(10^8\,\mu^+/s)$. The Compact Muon Beam Line (CMBL) was designed to deliver muons to the first phase Mu3e experiment without the necessity to remove the detector of the MEG II experiment from the πE5 area. The CMBL commissioning started in 2014 and continued until 2018 [5, 6] without the Mu3e spectrometer magnet, which was delivered to PSI only in 2020 [7]. In this thesis, the work carried out between 2021 and 2023 to finalize the commissioning of the complete CMBL is presented.

The second phase of the Mu3e experiment instead aims to reach a sensitivity of 10^{-16}, the requirements for which can currently not be met by any facility worldwide. The High Intensity Muon Beams (HIMB) project at PSI aims to increase the delivered muon rates by two orders of magnitudes to $\mathcal{O}(10^{10}\,\mu^+/s)$ by means of an upgraded target station [6] and two new beamlines based on solenoidal elements. The MUH2 beamline is dedicated to particle physics experiments, such as a second phase Mu3e detector, while the MUH3 beamline is aimed at muon spin rotation (μSR) measure-

ments. As part of this work, the simulation and optimization of the HIMB beamlines are presented.

In the context of rare physics processes, the MEG II detector allows to test additional channels aiding the search for BSM physics. In 2016 the ATOMKI collaboration measured an excess in the distribution of the angular correlation of the internal pair creation electrons and positrons [8, 9] in the $^7\mathrm{Li}(\mathrm{p},\gamma)^8\mathrm{Be}$ process and the MEG II detector is used to independently measure this anomaly. This is possible thanks to a Cockroft-Walton accelerator independent from the main accelerator complex, which is normally used for the calibration of the liquid xenon calorimeter of MEG II with the same process. In this thesis, the framework for the likelihood analysis of the MEG II experiment is extended and adapted for this channel.

The content of this thesis is organized as follows:

- Chapter 1 provides an overview of the theoretical motivations and a description of the experimental setups of the MEG II and Mu3e experiments. The production of muons in the HIPA facility is also outlined.
- Chapter 2 provides a brief introduction on elements of beam dynamics, setting the basis for the following chapters.
- Chapter 3 describes the πE5 beamline and the activities carried out between 2021 and 2023 to commission the CMBL. Special attention is given to the results obtained during the 2022 commissioning and to the characterization of the muon beam phase space used as an input to finalize the commissioning in 2023. The requirements stated in [4] are met and surpassed, with a muon rate of $7.5 \times 10^7\,\mu^+/\mathrm{s}$ delivered to the center of the Mu3e spectrometer.
- Chapter 4 introduces the context of the anomaly measured by the ATOMKI collaboration and gives a comprehensive outline of the activities carried out to repeat the measurement with the MEG II detector. Then, the analysis framework is presented, with particular emphasis on the treatment of the systematics due to the limited available Monte Carlo statistics to model the background events.
- Chapter 5 is dedicated to the HIMB project. First, the motivations and the requirements are introduced. Then the upgrade is presented, with particular emphasis on the design of the new beamlines, MUH2 and MUH3, and on the optimization of their optics using genetic algorithms showing that the goal of $\mathcal{O}(10^{10}\,\mu^+/\mathrm{s})$ can be achieved with the current layout.
- The Appendix is a collection of measurements and information complementary to the main text.

Chapter 1

The Mu3e and MEG II experiments

The MEG II experiment and the Mu3e experiment aim to measure the rare decays $\mu^+ \to e^+\gamma$ and $\mu^+ \to e^+e^+e^-$, respectively. Together with $\mu^-N \to e^-N$ these processes are referred to as golden channels because they are strongly suppressed in the Standard Model of particle physics (SM), allowing for background free searches of Beyond Standard Model (BSM) physics. In the following, an introduction to the SM is given and an outline of the theoretical framework of charged Lepton Flavor Violation (cLFV) is presented. The experimental set-up of the MEG II and Mu3e experiments are described in detail in the following sections. [1]

The theoretical justification of cLFV searches is given in the first two sections. Then, the MEG II and Mu3e phenomenology and experiments are outlined. The final section describes particle production at PSI. The chapter is an introduction to the science case motivating the work exposed in this thesis.

1.1 The Standard Model

The Standard Model of particle physics (SM) is the most accurate and predictive theory to date, in the frame of particle interactions. It is a gauge theory based on the group $SU(3)_C \times SU(2)_L \times U(1)_Y$ [11]: the group $SU(2)_L \times U(1)_Y$ describes the electroweak interaction; the group $SU(3)_C$ describes the strong interactions.

The theory is composed of 25 elementary fields:

[1] The content of this chapter follows closely the first chapter of the master thesis [10] of the author.

- 12 fermions: these are the components of matter and they are divided in leptons and quarks. The leptons interact only through electroweak interaction, and they are divided in charged leptons (e, μ, τ) and neutral leptons (ν_e, ν_μ, ν_τ). The quarks interact through electroweak and strong interactions and they are divided in up quarks (u, c, t), and down quarks (d, s, b). All of them are assumed to be massless.
- 12 bosons: these are the mediators of the interactions. They are: γ, Z, $W^\pm$, the mediators of the electroweak interaction; the 8 gluons (g) mediators of the strong interactions. All of them are assumed to be massless as well.
- Higgs: it is a scalar weak isospin doublet field responsible for the non-zero masses of the electroweak bosons and of the charged fermions.

Figure 1.1 shows a list of the SM particles.

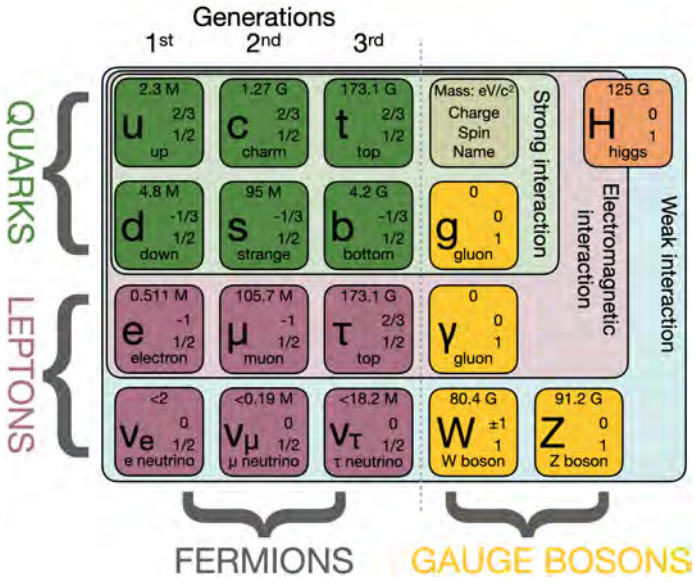

Figure 1.1: *Standard Model particles. Adapted from [12].*

The Lagrangian of the theory can be written as the sum of three contributions:

$$\begin{aligned}
\mathcal{L}_{SM} &= \mathcal{L}_{gauge} + \mathcal{L}_{Higgs} + \mathcal{L}_{Yukawa} \\
\mathcal{L}_{gauge} &= F^a_{\mu\nu} F^{a\mu\nu} + i\bar{\psi}\gamma^\mu D_\mu \psi + |D_\mu H|^2 \\
\mathcal{L}_{Higgs} &= \mu^2 H^\dagger H - \lambda (H^\dagger H)^2 \\
\mathcal{L}_{Yukawa} &= g^\ell_{i,j} \bar{\ell}_{i,R} H^\dagger \ell_{j,L} + g^U_{i,j} \overline{U}_{i,R} \tilde{H}^\dagger U_{j,L} + g^D_{i,j} \overline{D}_{i,R} H^\dagger D_{j,L} + h.c.
\end{aligned} \tag{1.1}$$

The gauge term describes the free fermion and boson fields, their interactions and the coupling with the Higgs field. $F^a_{\mu\nu}$ is the gauge-field strength

tensor, defined as:

$$F^a_{\mu\nu} = D_\mu G^a_\nu - D_\nu G^a_\mu - c f_{acb} G^b_\mu G^c_\nu \tag{1.2}$$

where G^a_μ are the gauge vector fields, and f_{abc} are the structure constants of the group.
D_μ is the covariant derivative:

$$D_\mu = \partial_\mu + i g_s \frac{\lambda^a}{2} G^a_\mu + i g \frac{\tau^a}{2} A^a_\mu + i g' Q_Y B_\mu \tag{1.3}$$

where λ^a are the generators of SU(3) (a = 1, 8, Gell-Mann matrices), τ^a are the generators of SU(2) (a = 1, 3, Pauli matrices), g_s, g, g' are the coupling of strong, weak and electromagnetic interactions. Q_Y is the weak hypercharge, defined similarly to the Gell-Mann-Nishijima formula:

$$Q_Y = 2(Q - T_3) \tag{1.4}$$

with Q the electric charge and T_3 the third component of weak isospin.

The Higgs term describes the Higgs potential with $\mu^2 > 0$. It has infinite degenerate minima corresponding to a non-zero vacuum expectation value equal to $\sqrt{\mu^2/2\lambda}$. This term introduces the spontaneous symmetry breaking that causes the mix between B^μ and $W^{0,\mu}$ into A^μ and Z^0, and the mass terms of the gauge bosons [13].

The Yukawa term connects the left-handed (weak isospin doublet) and right-handed component (weak isospin scalar) of the fermions through the Higgs doublet, giving them mass.

1.1.1 Muon decay

The Lagrangian that describes the dynamics of a muon is [1]:

$$\begin{aligned}
\mathcal{L}_\mu = \quad & e\bar{\mu}\gamma^\nu \mu A_\nu + \\
& -\tfrac{g}{\sqrt{2}}(\bar{\nu}_\mu \gamma^\nu \mu_L W^+_\nu + \bar{\mu}_L \gamma^\nu \nu_\mu W^-_\nu) + \\
& -\sqrt{g^2 + g'^2}\Big(\bar{\mu}_L \gamma^\nu \Big(-\tfrac{1}{2} + sin^2\theta_W \Big)\mu_L + \bar{\mu}_R \gamma^\nu sin^2\theta_W \mu_R\Big) Z^0_\nu + \\
& -\tfrac{m_\mu}{\nu}\bar{\mu}\mu H
\end{aligned} \tag{1.5}$$

From top to bottom, each line represents the: electromagnetic interaction, the charged current interaction, the neutral current interaction and the Yukawa interaction. Figure 1.2 shows the tree level Feynman diagram of the muon decay.

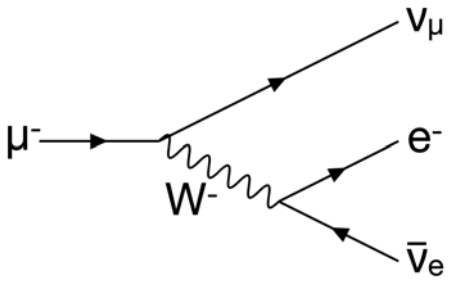

Figure 1.2: *Tree level diagram of muon decay process.*

The muon decay time is [14]:

$$\tau_\mu = 2.196\,981\,1(22)\,\mu s \tag{1.6}$$

Tab. 1.1 shows the decay channels and the respective branching ratios.

Decay channel	Branching Ratio	CL
$\mu^- \to e^- \bar{\nu}_e \nu_\mu$	$\approx 100\%$	
$\mu^- \to e^- \bar{\nu}_e \nu_\mu \gamma$	$(6.0 \pm 0.5) \times 10^{-8}$ (for $E_\gamma > 40\,\text{MeV}$)	
$\mu^- \to e^- \bar{\nu}_e \nu_\mu e^- e^+$	$(3.4 \pm 0.4) \times 10^{-5}$	
$\mu^- \to e^- \nu_e \bar{\nu}_\mu$	$< 1.2\,\%$	90 %
$\mu^+ \to e^+ \gamma$	$< 4.2 \times 10^{-13}$	90 %
$\mu^- \to e^- e^+ e^-$	$< 1.0 \times 10^{-12}$	90 %
$\mu^- \to e^- 2\gamma$	$< 7.2 \times 10^{-11}$	90 %

Table 1.1: Muon decay channels and their branching ratios [14].

1.2 Charged Lepton Flavour Violation

1.2.1 Neutrino oscillations

Charged Lepton Flavour Violation is strictly forbidden in the SM with massless neutrinos. But a decay such as $\mu \to e\gamma$ could be possible through neutrino oscillations.
The introduction of massive neutrinos leads to the following branching ratio [15]:

$$\mathcal{B}(\mu \to e\gamma) = \frac{3\alpha}{32\pi} \left| \sum_{i,j=1,2,3} U^*_{\mu i} U_{ej} \frac{\Delta m^2_{ij}}{m^2_W} \right|^2 \simeq 10^{-55} - 10^{-54} \tag{1.7}$$

where U_{ij} is the Pontecorvo-Maki-Nakagawa-Sakata (PMNS) matrix [16, 17] and Δm^2_{ij} is the difference between the squared masses of the i-th and j-th generation neutrinos.

Within this extended SM, such a process is forty orders of magnitude below the current experimental sensitivity and, practically, inaccessible. On the other hand, any observation of such a process would be a clear evidence of new physics. Thanks to this unique feature, the $\mu^+ \to e^+\gamma$ and $\mu^+ \to e^+e^+e^-$ processes are referred to as golden channels. Figure 1.3 shows the history of limits on the cLFV golden channels branching ratios, together with the expected sensitivity of MEG II, Mu3e and Mu2e.

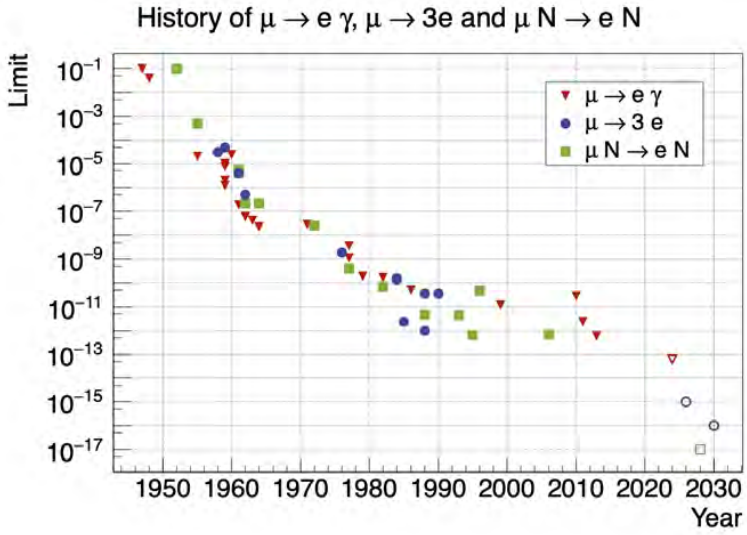

Figure 1.3: *The history of limits on the cLFV golden channels branching ratios. The open markers indicate projected sensitivities. Plot modified from [18].*

1.2.2 Beyond Standard Model Physics

Although very successful, the SM presents a number of criticalities which cannot be explained within the theory itself [11]:

- naturalness and hierarchy problem: the Higgs mechanism gives an elegant solution to the problem of the gauge bosons masses, but it needs an "unnatural" fine tuning $\sim \mathcal{O}^{-34}$ of the Higgs mass, if considering a cutoff constant $\Lambda \sim M_{Planck}$;
- dark matter and dark energy: from cosmological measurements it is known that only the 4.9 % of the universe is composed of ordinary matter, which is described by the SM. The 26.4 % is composed of Dark Matter and the remaining 68.7 % is composed of Dark Energy, whose components and nature are unknown;
- matter-antimatter asymmetry: CP violation in weak interactions cannot explain the absence of anti-matter in the observable universe;

- origin of neutrino masses.

A number of extensions to the SM aim to explain completely or in part the aforementioned issues and many of them predict cLFV in the reach of present-day experiments. Even though the picture is crowded with a large number of models, the measurement of cLFV processes can set strong constraints on the parameter space and set a guide to new physics.

A common model-independent approach is to consider an effective Lagrangian by setting a cut-off scale Λ and by adding high dimensional operators through the Wilson coefficients formalism. In the context of muon decays, the golden channels can be used to set constraints on some of these operators: as an example, Figure 1.4 shows the allowed region for coefficients C_{ee}^{VRR}, C_{ee}^{SLL} and C_{L}^{D} for the current and foreseen limits on the three golden channels at a W mass scale [19].

1.3 MEG II experiment

1.3.1 Process phenomenology

Being the $\mu \to e^+\gamma$ a two-body decay, the kinematics is fully constrained and model-independent. In the center of mass frame a positron and a photon are produced back to back (the μ^+ is at rest), with energy equal to half of the muon mass ($m_\mu/2 = 52.8\,\mathrm{MeV/c^2}$).

The decay is fully characterized by four kinematic variables: the photon energy E_γ, the positron momentum p_{e^+}, their relative angle $\Theta_{e^+\gamma}$ and timing $t_{e^+\gamma}$. The number of expected signals for a given ratio $\mathcal{B}$ depends on the stopping muon rate R_{μ^+}, the measurement time T, the solid angle Ω subtended by the photon and positron detectors, the efficiencies of these detectors (ε_γ, ε_{e^+}) and the efficiency of the selection criteria ε_s:

$$N_{sig} = R_{\mu^+} \times T \times \Omega \times \mathcal{B} \times \varepsilon_\gamma \times \varepsilon_{e^+} \times \varepsilon_s \tag{1.8}$$

The background can be distinguished in physical, due to the Radiative Muon Decay (RMD) $\mu \to e^+\nu_e\bar{\nu}_\mu\gamma$, and accidental, due to the coincidence between a Michel decay and a high energy photon coming from RMD, annihilation in-flight (AIF) or bremsstrahlung from Michel positrons. In the next paragraph the main characteristics of the backgrounds will be discussed.

1.3.1.1 Physical background

The background induced by RMD is caused by events with high energy photons and low energy neutrinos, where the positron and the photon are emitted back to back. The RMD branching ratio for $E_\gamma > 40$ MeV is $(6.0 \pm 0.5) \times 10^{-8}$, which is non negligible if compared to the sensitivity goal of

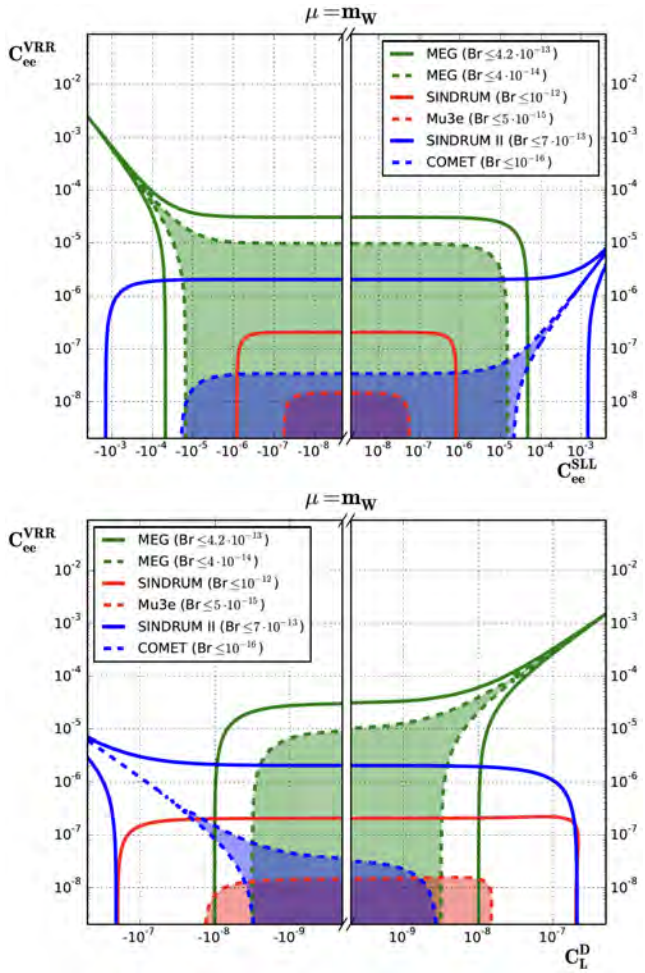

Figure 1.4: *Allowed regions in the $C_{ee}^{SLL} - C_{ee}^{VRR}$ (left) and in the $C_L^D - C_{ee}^{VRR}$ (right) planes from [19]. Existing (solid lines) and projected (dashed lines) limits are shown for $\mu^+ \to e^+\gamma$ (green), $\mu^+ \to e^+e^+e^-$ (red) and $\mu^-N \to e^-N$ (blue).*

MEG II. A tight cut around the signal region can suppress such events and depends only on the resolutions of the apparatus.
Figure 1.5 shows the dependence of the differential RMD branching ratio on the photon energy and on the energy resolution of the photon and positron reconstruction. The variables x, y and z are defined as follows:

$$x = \frac{2E_{e^+}}{m_\mu}, \quad y = \frac{2E_\gamma}{m_\mu}, \quad z = \pi - \Theta_{e^+\gamma}. \tag{1.9}$$

with E_{e^+} being the energy of the emitted positron. The branching ratios are computed with respect to the FWHM of x and y, δx and δy, imposing that the resolution on z satisfies $\delta z < 2\sqrt{\delta x \delta y}$.

The contribution in MEG II is expected to be smaller than 10^{-14}.

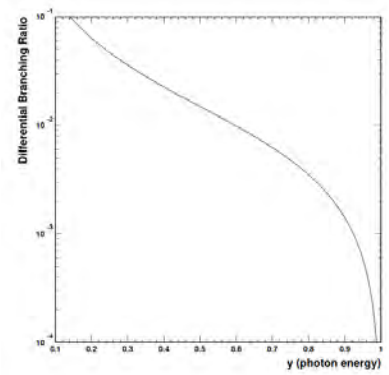

(a) Normalized energy spectrum for an RMD photon

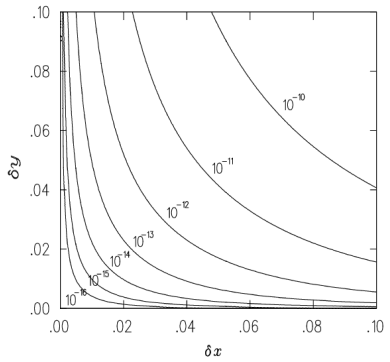

(b) Expected RMD branching ratio as a function of δx and δy. $\delta z < 2\sqrt{\delta x \delta y}$

Figure 1.5: *RMD branching ratio dependence [1].*

1.3.1.2 Accidental background

The major contribution to the background consists of accidental coincidences. The number of accidental events depends on the resolutions and on the stopping rate:

$$N_{acc} \propto R^2_{\mu^+} \times \Delta E^2_\gamma \times \Delta P_{e^+} \times \Delta \Theta^2_{e^+\gamma} \times \Delta t_{e^+\gamma} \times T \tag{1.10}$$

where Δ indicates the resolution on each measured quantity. Here, the dependence on the stopping rate is quadratic, while for the physical background it is linear. Analogously to Mu3e, such a feature favours continuous muon beams against pulsed muon beams, making the Paul Scherrer Institut (PSI) a suitable host for the experiment.

1.3.2 Experimental apparatus

The MEG apparatus was installed in the πE5 experimental area at PSI, in Switzerland, and the data-taking has been completed in 2013. In the last years many upgrades were performed in order to push the sensitivity by an additional order of magnitude. In the following, the major changes and the resolutions will be exposed. After commissioning, the data taking started in 2021 and is currently ongoing.

Figure 1.6 shows the MEG II detector. The apparatus consists of: the Liquid Xenon calorimeter (XEC), which measures the energy, the direction and the time of flight of the photon; the positron spectrometer, composed of the Cylindrical Drift CHamber (CDCH) and the superconducting solenoid named COBRA (COnstant Bending RAdius), which tracks the positron and measures its momentum; the pixelated Timing Counter (pTC), which measures the positron time of flight and improves the track reconstruction; the

Radiative Decay Counter (RDC), which was not present in MEG and vetoes events with low-energy positrons to further suppress the accidental background. The resolutions in the following are reported, if not specifically cited, in [2].

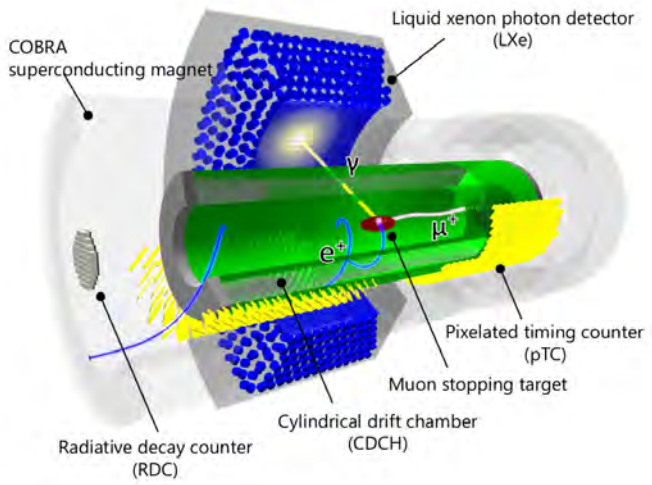

Figure 1.6: *3D schematic view of the MEG II detector from [2].*

1.3.2.1 The target

The muons are stopped in a thin target to reduce energy losses and improve energy resolution on the outcoming positrons. The upgraded target is a 174 µm thick scintillating disc tilted by 15° with respect to the beam direction. The slanting angle allows to stop the muons in a smaller volume, reducing both multiple scattering and AIF of the positrons, and to reduce the density of the decay vertices, and therefore minimize accidental background. The target foil is supported by two hollow carbon fiber frames (see Figure 1.7). The foil and the frame are printed with a pattern of white dots superimposed on black background to monitor the position and deformation of the target through the data taking. The dots are elliptical with a height of 0.51 mm and a width of 1.52 mm to appear circular when captured with the camera. Six holes are bored in the target to extract its position through the positron vertex distribution, allowing for redundancy.

1.3.2.2 The Liquid Xenon calorimeter

The XEC has been upgraded to improve the resolution and fix some of the major issues of the old version [3, 20]. It is a 900 L C-shaped tank 38.5 cm deep, corresponding to ~ 14 radiation lengths ($X_0 = 2.7$ cm), in order to completely contain the showers originating from the photon passage through

Figure 1.7: *The MEG II target from [2]. A pattern of white dots on black background is printed on the scintillating foil and on the frame to monitor the position and possible deformation of the target through data taking.*

Liquid Xenon. The scintillation process is possible thanks to the recombination and formation of the excited Xe_2^*, which is followed by ionisation. This dimer does not exist at the ground state, letting the calorimeter be transparent to the scintillation light.

The light is collected by 4092 Multi-Pixel Photon Counters (MPPC, see Figure 1.8) on the inner face and 668 2-inch PMTs on the other sides. In MEG, the PMTs were positioned on the inner face as well. The circular shape of the PMTs caused reduced coverage leading to disuniformities in the response of the detector. Each MPPC consists of four 6 mm $\times$ 6 mm sensors connected in series to reduce the effective capacitance of the total element and increase the timing accuracy. Figure 1.9 shows a view of the old and new versions of the calorimeter. To reach the aimed sensitivity a thorough understanding

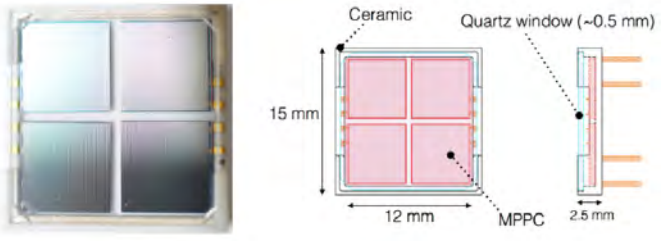

Figure 1.8: *Custom MPPCs used in the MEG II LXe calorimeter from [3]. On the left the picture of a MPPC. On the right the schematic view of a MPPC.*

of the detector response is required and the energy scale of the XEC is of particular relevance due to the performance drop of the MPPCs and to the gain drop of the PMTs with time. A number of calibration sources are used to cover the full calibration scale from UV light with LED mounted inside the detector up to 129 MeV during dedicated runs. Details can be found in

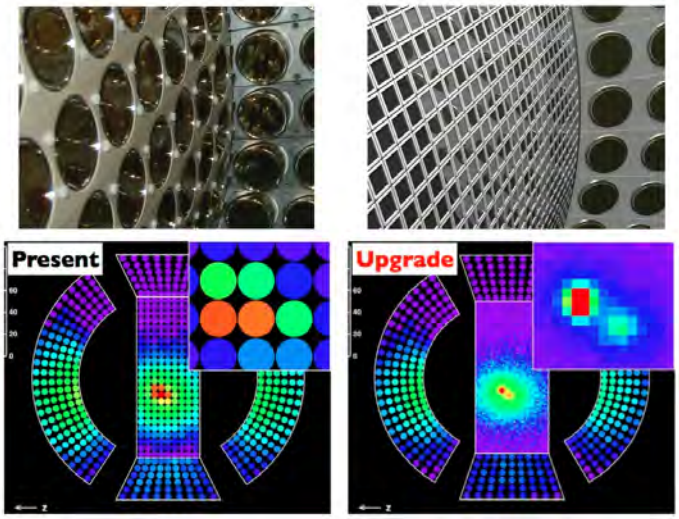

Figure 1.9: *In the top panels the inner face view of the old (left) and new (right) version of the calorimeter from [3]. In the bottom panels an example of scintillation light collection as detected by the old (left) or new (right) version of the calorimeter.*

[2]. Two of these calibrations are of relevance for this work:

- the $^7\mathrm{Li}(\mathrm{p},\gamma)^8\mathrm{Be}$ process, producing 14.8 MeV and 17.64 MeV;
- the $\pi^-\mathrm{p} \to \pi^0\mathrm{n}$ process or Charge EXchange (CEX) reaction.

The $^7\mathrm{Li}(\mathrm{p},\gamma)^8\mathrm{Be}$ is repeated three times per week, and the protons are produced and accelerated with a Cockroft-Walton (CW) accelerator completely independent from the proton accelerator facility of PSI and of MEG exclusive use. Details will follow in Chapter 4, where the measurement of the Beryllium anomaly [21] with the MEG II detector is presented.

The CEX reaction is crucial for the calibration of the detector: the π^0 is produced with a boost in the laboratory frame, leading to the emission of two γ with energy in the 55 MeV – 83 MeV range. The energy is selected by applying a selection in the relative angle between the photon detected by the XEC and that detected with a movable auxiliary detector based on Bismuth Germanate (BGO) crystals. The lower end-point of the CEX spectrum allows to reliably calibrate the energy scale close to the signal region. A concurrent process is the radiative capture $\mathrm{p}(\pi^-,\gamma)\mathrm{n}$ where the photon has a 129 MeV energy.
The CEX reaction is produced with a 70 MeV/c π^- beam. In Chapter 5, a tune for such a calibration is found for the MUH2 beamline of the High Intensity Muon Beams project.

1.3.2.3 The Cylindrical Drift Chamber and the COBRA magnet

MEG II uses a cylindrical shaped single volume drift chamber [3, 22]. The wires are positioned in a stereo configuration for longitudinal hit localization, inside a volume filled with a 90 %/10 % He-Isobutane gas mixture. The total radiation length is $1.5 \times 10^{-3} X_0$, allowing for a single hit resolution below 120 µm, a momentum resolution of 130 keV/c and angular resolutions of $\simeq$ 5.5 mrad in the azimuthal angle and $\simeq$ 4 mrad in the polar angle.

The solenoidal magnetic field produced by the COBRA superconducting magnet, varies from 1.27 T at the center to 0.49 T at either ends. The gradient is designed to guarantee a bending radius of positrons weakly depending on the polar angle and to sweep quickly spiraling positrons outside the spectrometer. Figure 1.10 shows the profile of the axial magnetic field of COBRA.

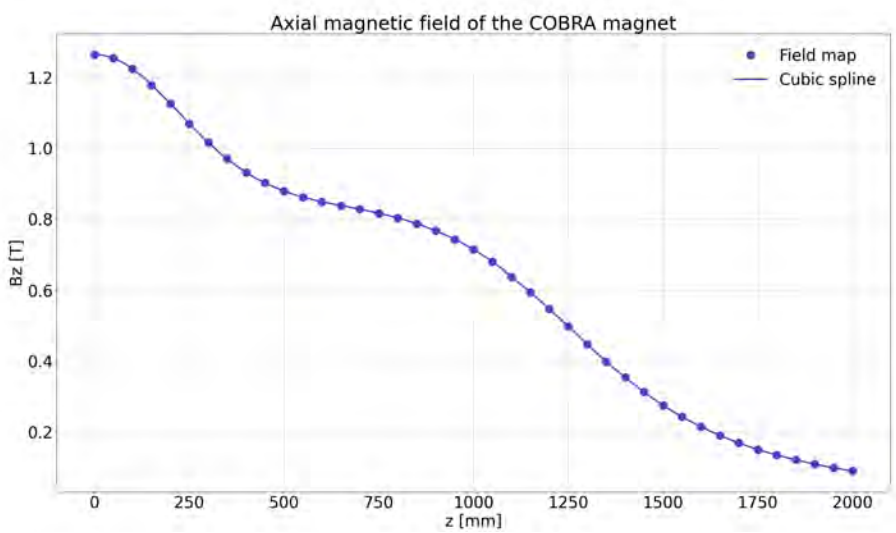

Figure 1.10: *Measured axial magnetic field of the COBRA magnet. The horizontal axis starts at COBRA center.*

The CDCH can be easily calibrated with Michel data, allowing for a continuous monitoring. Additionally, a 53 MeV/c positron beam can be delivered in πE5 to perform a calibration based on Mott scattering. Details can be found in [2]. In Chapter 5, a tune for such a calibration is found for the MUH2 beamline of the High Intensity Muone Beams project.

1.3.2.4 The Pixelated Timing Counter

The pixelated Timing Counter [23] consists of 512 elements composed of a plastic scintillating tile (100 mm × 40 mm × 5 mm or 100 mm × 50 mm × 5 mm sized, depending on the longitudinal position in the pTC) coupled

with multiple SiPMs. Each tile has a time resolution of ~ 75 ps. The overall timing resolution depends on the number of hits (tiles) in the pTC and it scales with a factor $1/\sqrt{N_{hit}}$. Figure 1.11 shows a single tile and the complete detector.

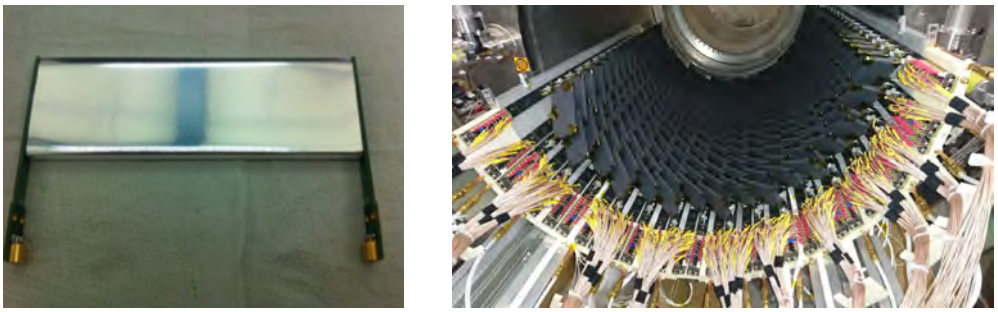

(a) Single pTC tile **(b)** Downstream side of pTC inside COBRA

Figure 1.11: *pTC view from [3].*

1.3.2.5 The Radiative Decay Counter

The Radiative Decay Counter is dedicated to the detection of low energy RMD positrons to tag high energy gammas in the XEC as potential accidental background events. Low energy particles spiral without hitting the CDCH and those drifting in the downstream direction are detected by the RDC as shown in Figure 1.12.
The RDC is expected to detect $\simeq 42\,\%$ of the RMD γ background and to improve the sensitivity on the $\mu^+ \to e^+\gamma$ search of a 15 % factor.

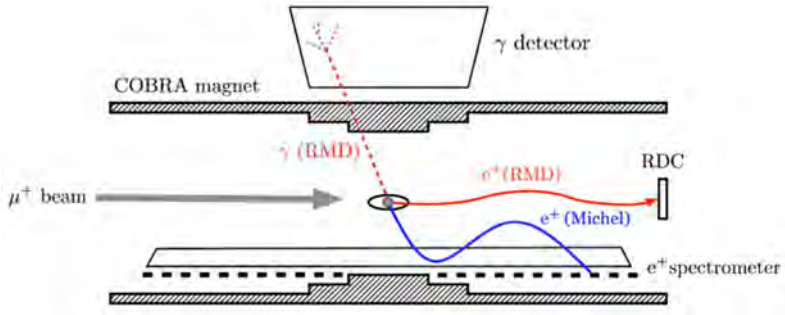

Figure 1.12: *Schematic view of the detection of RMD with the RDC from [3].*

The RDC consists of 12 plastic scintillators coupled to MPPCs, dedicated to timing measurements, and 76 LYSO crystals [24] coupled to one MPPC, used for calorimetry measurements. Figure 1.13 shows a schematic view of

the elements.

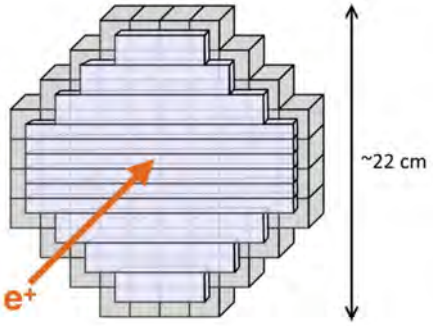

Figure 1.13: *Schematic view of the RDC. The horizontal long plates in front are the plastic scintillator bars, and the cubes behind are the LYSO crystals from [3].*

1.3.2.6 The Trigger and DAQ systems

The MEG II upgrade leads to an increase in the total read out channel of a factor three. The TDAQ system has been redesigned to cope with the new requirements and to possibly allow for increased muon stopping rates: different stopping rates have been tested and the current data taking is performed at $4 \times 10^7\ \mu^+/\mathrm{s}$, to be compared with the $3 \times 10^7\ \mu^+/\mathrm{s}$ of MEG.
Additionally, the requirement for an efficient offline pile-up reconstruction and rejection is the availability of full waveform information. The DAQ system has to provide state-of-the-art time and charge resolution and a sampling speed in the GSPS range [3].

In the following paragraphs, the TDAQ system of the MEG II experiment is introduced.

DAQ The system integrates the basic trigger and DAQ (TDAQ) functionalities onto the same electronics board, the WaveDREAM Board (WDB). Figure 1.14 shows a schematics and a picture of the WDB. It reads 16 channels with variable gain amplification (0.5 to 100) and flexible shaping through a programmable pole-zero cancellation. Two DRS4 chips [25] are connected to two 8-channel ADCs, which are read out by a Field-Programmable Gate Array (FPGA) that performs complex trigger algorithms (sum of the input channels, threshold cuts, etc.). When a trigger occurs, the DRS4 chip is stopped and the internal analogue memory is digitized through the same ADCs previously used for the trigger.
The WDBs can supply up to 240 V per channel thanks to an ultra-low noise bias voltage generator based on a Greinacher multiplier.

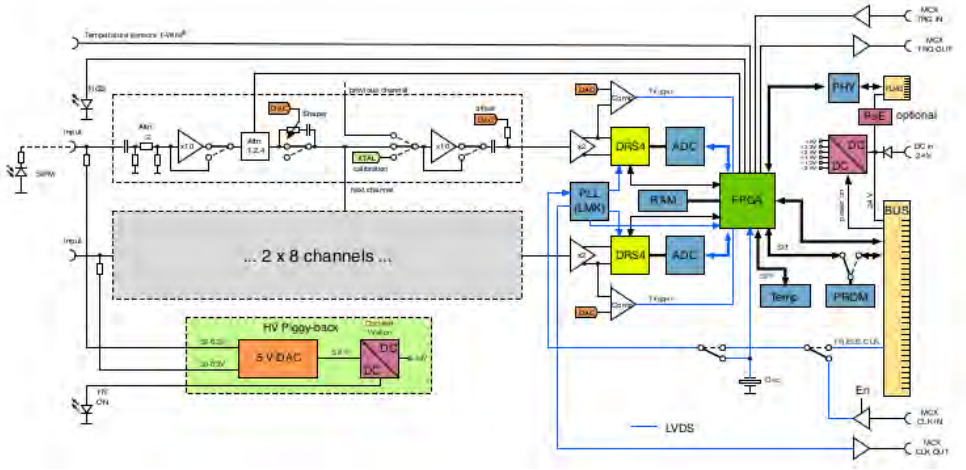

(a) WDB simplified schematics

(b) WDB picture

Figure 1.14: *WDB view from [3].*

Trigger The trigger is based on a real time reconstruction algorithm that relies on the fast response detectors: LXe for γ observables and pTC for e^+ observables. The FPGA in the WDB performs the reconstruction of decay products observables, such as momenta, relative timing and direction, through logic equations.

1.3.2.7 Expected sensitivity

Tab. 1.2 collects the resolutions and efficiencies of the MEG II detector as measured in 2022 compared to the performances of the MEG detector [2].The expected sensitivity is shown in Figure 1.15. Assuming 20 weeks of DAQ time per year, it is possible to achieve a 6×10^{-14} sensitivity in 2026.

	MEG	MEG II
Resolutions		
δE_{e^+} [keV]	380	89
$\delta\theta_{e^+}$ [mrad]	9.4	7.09
$\delta\varphi_{e^+}$ [mrad]	8.7	6.83
$\delta z_{e^+}/\delta y_{e^+}$ [mm]	2.4/1.2	1.85/0.75
δE_γ ($w > 2$ cm/$w < 2$ cm) [%]	2.4/1.7	2.0/1.7
$\delta u_\gamma/\delta v_\gamma/\delta w_\gamma$ [mm]	5/5/6	2.5/2.5/5.0
$\delta t_{e^+\gamma}$ [ps]	122	78
Efficiencies [%]		
Trigger	$\simeq 99$	$\simeq 82$
Photon	63	63
e^+ (tracking $\times$ matching)	30	64

Table 1.2: Comparison between the resolutions of MEG II and MEG [2].

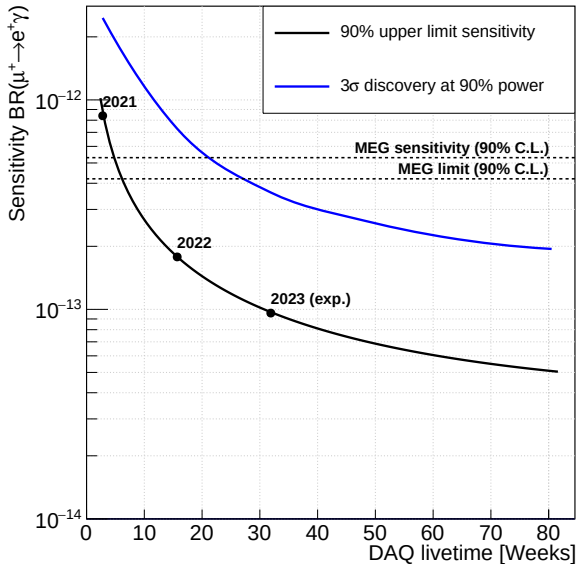

Figure 1.15: *Expected sensitivity of MEG II as a function of the DAQ time compared with the bounds set by MEG [26].*

1.4 Mu3e experiment

1.4.1 Process phenomenology

The signal of the Mu3e experiment is characterized by two positrons and one electron coming from a common vertex. The kinematics of a possible signal depends on the underlying physics and the sensitivity is model dependent [1, 4]. In the center of mass frame, the total momentum is zero and the total energy is the mass of the muon. Comparing different effective operators

scenarios, the highest energy particle in the decay is likely to have momenta higher than 35 MeV/c and the lowest energy is peaked close to zero and quickly decreasing to the kinematic edge ($m_\mu/2$) [15]. A low material budget is needed to measure such a process to measure the low energy particles. Additionally, the three particles lie in the same plane in the center of mass frame. The decay is then completely described by two variables and three rotation angles to individuate the decay plane.

Analogously to MEG II, both physical, radiative muon decays with internal conversion $\mu^+ \to e^+e^-e^+\nu_e\bar{\nu}_\mu$, and accidental (combinatorial) background are present. The latter can be induced by the combination of any among Michel Decays, RMDs, and Bhabha scattering, where a positron from the beam or any other source scatters on an electron in the target leading to an electron-positron pair with the same vertex. In the next paragraphs the main characteristics of the backgrounds will be discussed.

1.4.1.1 Physical Background

RMD with internal pair creation is the main source of background for the experiment. It is due to events with low energy neutrinos, setting stringent requirements on momentum resolution. To meet the sensitivity goal of the first phase of the Mu3e experiment, 2×10^{-15}, with a 2σ cut in the invariant mass, average resolutions better than $1\,\mathrm{MeV/c^2}$ are required [4].
Radiative pion decay with internal and external conversion can lead to events similar to signal events, but it is strongly suppressed due to the low pion contamination in the beam ($\lessapprox 10^{-7}$).

1.4.1.2 Accidental background

Positrons from Michel decays and RMDs can combine with electrons from RMDs with photon conversion into a fake signal event. Additionally positron tracks could be reconstructed as electrons. Bhabha scattering of positrons from the beam or other positron sources produce electron-positron pairs with a common vertex.
High resolution vertexing and timing are required to suppress the combination of these processes, together with a robust determination of the direction of motion of the particles.
Low positron contaminations in the muon beam are necessary and as for MEG II, continuous muon beams are preferred to minimize the background. Chapter 3 focuses on the commissioning of the Compact Muon BeamLine (CMBL) to serve the Mu3e experiment.

1.4.2 Experimental apparatus

The Mu3e experiment is planned in two distinct phases: phase I, at the currently available most intense continuous muon source to reach a sensitivity of 2×10^{-15}; phase II, to ultimately reach a sensitivity of 10^{-16}. The latter is a strong driver for the High Intensity Muon Beams project described in Chapter 5. Whereas the concept of phase II detector is the same, here the focus is set on the phase I apparatus.

A schematic view of the Mu3e detector is shown in Figure 1.16. The apparatus consists of: the spectrometer, composed of the Pixel Tracker and the Mu3e solenoid, to measure the momentum of positrons and electrons and resolve their vertices; the Scintillating Fibre detector (SciFi), to measure the timing and determine the direction of motion of the tracked particles; the Scintillating Tile detector (SciTile), to provide additional timing for particle recurling away from the target area. The resolutions in the following are reported, if not specifically cited, in [4].

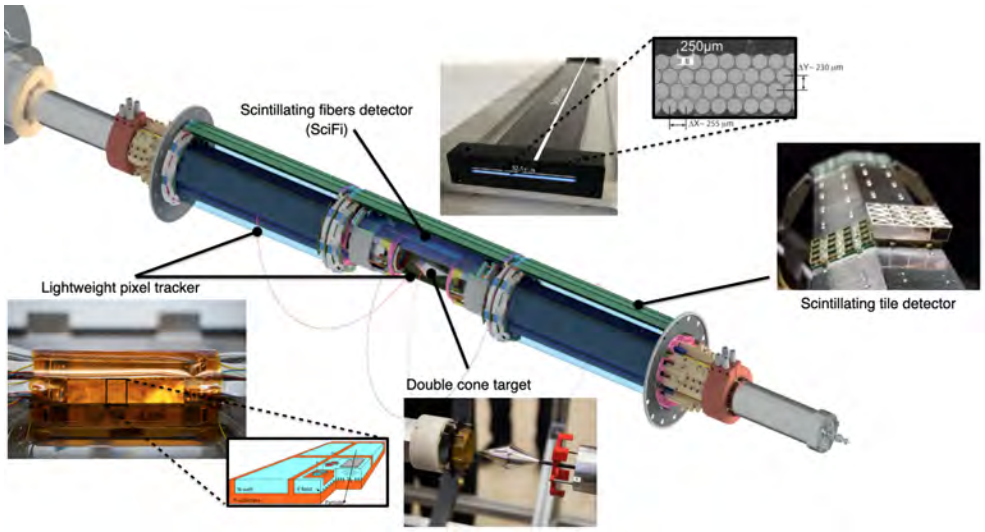

Figure 1.16: *3D schematic view of the Mu3e detector. Adapted from [4].*

1.4.2.1 The Target

The muons are stopped in a thin hollow double cone target to maximize the stopping power and minimize the material budget for the outcoming positrons and electrons. The target is long 100 mm with a radius of 19 mm and is made from 70 µm of aluminised Mylar® (biaxially-oriented polyethylene terephthalate) in the front part and 80 µm Mylar® in the back part. Figure 1.17 shows a scheme and a picture of the target. The conic shape allows to set a slanting angle between the muon beam and the surface of the

target leading to effects analogous to those described for the MEG II target: lower density of decay vertices and reduced multiple scattering and AIF of the positrons. The target is glued on a carbon tube fixed in a dedicated support structure with an alignment mechanism.

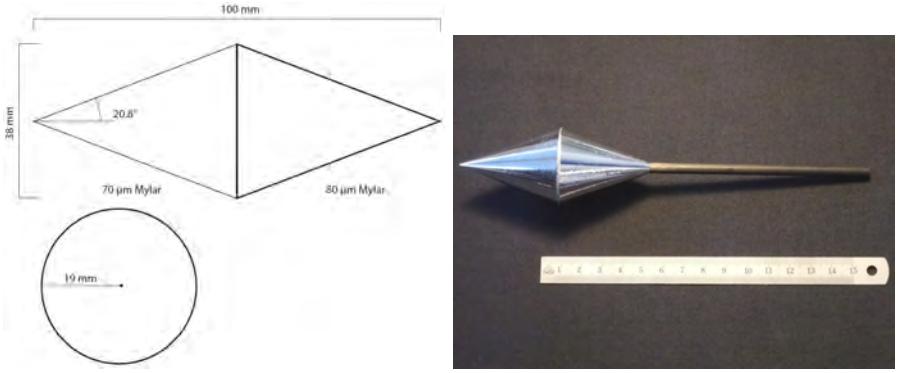

Figure 1.17: *The Mu3e target from [4]. Left: a sketch of the Mu3e target. Right: a picture of the Mu3e the target.*

1.4.2.2 Magnetic Spectrometer

As opposed to MEG, where the narrow acceptance of the detector is optimized to resolve the edge of the Michel spectrum, the Mu3e experiment needs to have a large acceptance, due to the kinematics of the three body decay, and a uniform magnetic field is preferred. To achieve the sensitivity goal, a homogeneous magnetic field of 1 T is preferred. The inhomogeneities along the axial direction are required to stay below 10^{-3} within ± 60 cm from the center. An iron shielding encloses the magnet to reduce the fringe fields to lower than 5 mT at a distance of 1 m.
Figure 1.18 shows the axial field profile of the magnet. Additionally the Mu3e solenoid provides focusing to transport the beam to the target. The coupling from the quadrupole section into the spectrometer is deepened in Chapter 3 as part of the commissioning of the Compact Muon Beam Line (CMBL) delivering the beam to the experiment.

1.4.2.3 Pixel Tracker

The pixel tracker, to measure the momentum of outcoming positrons and electrons, consists of a central part and two stations on the sides as shown in Figure 1.19. The central part provides the main hits for the vertexing and track reconstruction, while the side stations (*recurl stations*) allow for higher resolution on tracks which do not recurl in the central part.

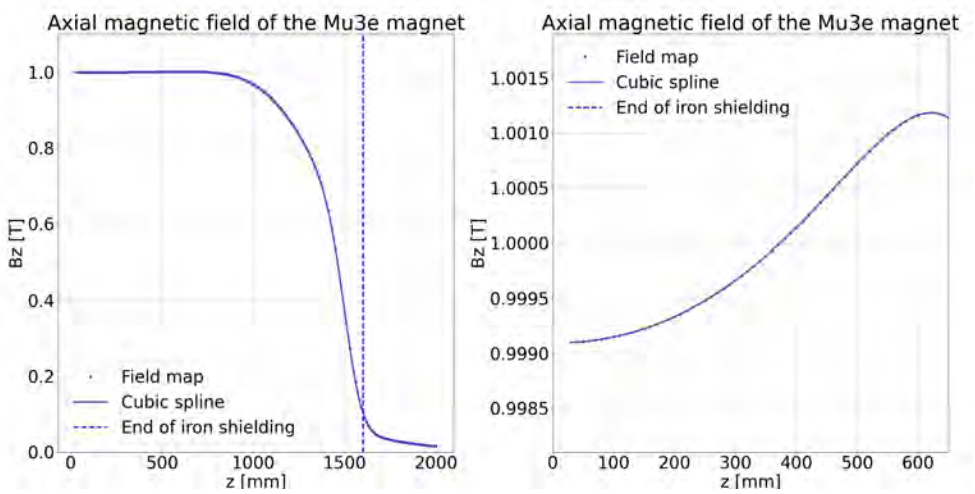

Figure 1.18: *Axial magnetic field of the Mu3e magnet. The horizontal axis starts at Mu3e center. The field is computed with the RADIA software [27].*

Each station consists of multiple layers of silicon sensors and each layer is composed of two half-shell modules. The modules integrate multiple ladders, the smallest mechanical unit in the tracker. The inner tracker consists of two layers 120 mm long with minimum radii 23.3 mm and 29.8 mm. The outer tracker consists of two layers 340 mm and 360 mm long with minimum radii 73.9 mm and 86.3 mm respectively. Figure 1.20 shows the details of the mechanical assembly of the central tracker.
To ensure low material budget, each ladder is a strip of 50 µm thick High-Voltage Monolithic Active Pixel Sensors (HV-MAPS), the MuPix sensors, mounted on a low mass flexible printed circuit. The MuPix sensors are all size 20 mm $\times$ 20 mm. Digital and analogue circuitry is on the side of each sensor, elongating them on one side to 23 mm. High Density Interconnect (HDI) circuits provide power to the sensors, transmit control signals and read out the data. The material budget for a single ladder is approximately $X/X_0 = 0.115\,\%$.

Due to the high power dissipation ($\sim 250\,\mathrm{mW/cm^2}$), the sensors are cooled with a continuous gaseous helium flow. Helium is chosen as a coolant to minimize the material budget on the tracked particles.

Figure 1.21 shows the momentum resolution from [4] in the accepted momentum bite for short (4 hits) and long (6-8 hits) tracks.

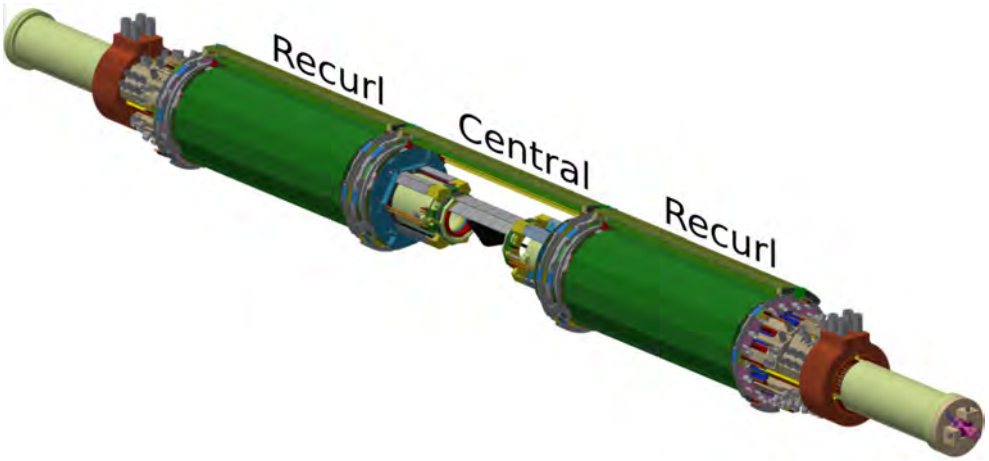

Figure 1.19: *3D schematic view of the Mu3e Pixel Tracker from [4]. The detector consists of a central tracker and two side stations (recurl stations) for tracks recurling outside of the central tracker.*

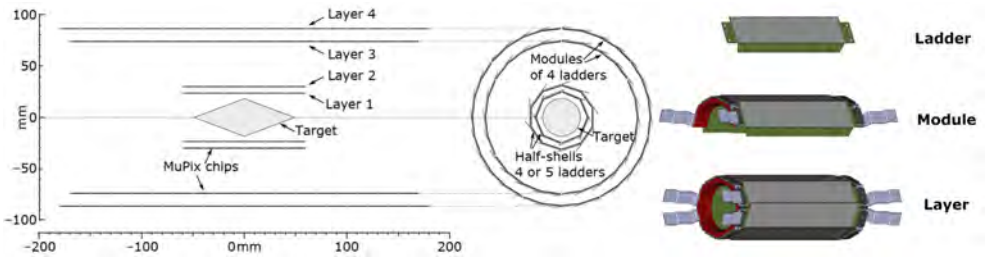

Figure 1.20: *Left: geometry of the central tracker. Right: 3D-model of each sub-component of Layer 1. From [4].*

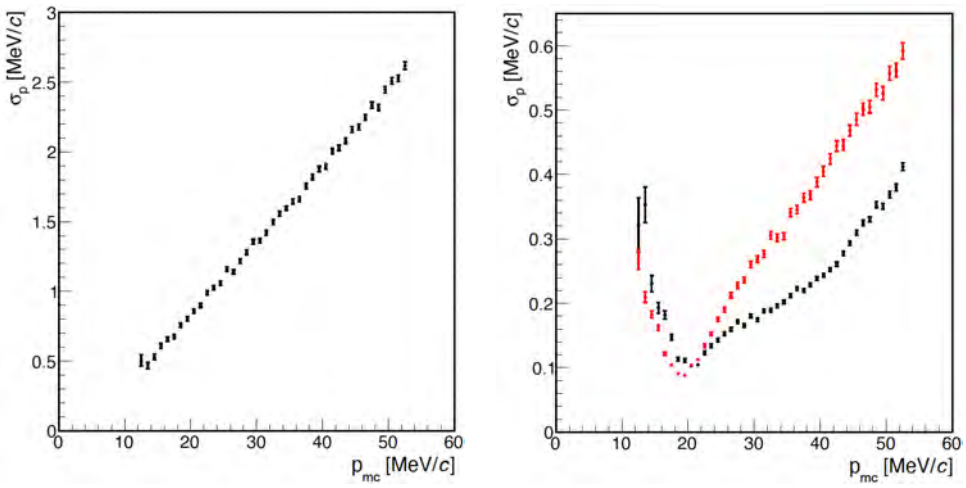

Figure 1.21: *Left: momentum resolution as a function of the generated momentum for tracks with 4 reconstructed hits (short tracks). Right: momentum resolution as a function of the generated momentum for tracks with 6 (black) and 8 (red) reconstructed hits (long tracks). From [4].*

1.4.2.4 The Scintillating Fibre detector

The timing in the central tracker is provided by the Scintillating Fibre detector (SciFi). An open view of the central tracker is shown in Figure 1.22.

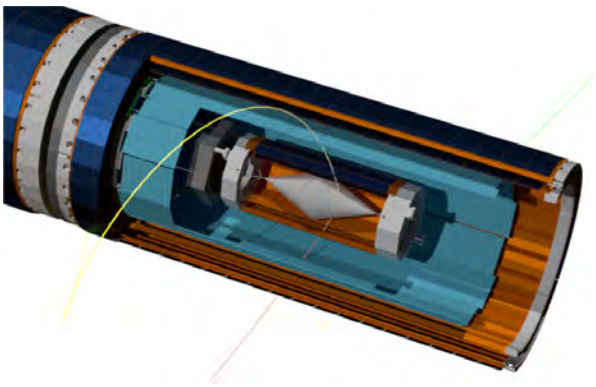

Figure 1.22: *Open view of the central pixel tracker enclosing the SciFi detector, in light blue, from [4].*

The SciFi detector is barrel shaped, with an inner radius of 61 mm and a length of 300 mm. It is composed of 12 *ribbons* of fibres, each 300 mm long and 32.5 mm wide. Each ribbon consists of 3 layers of 250 µm diameter round plastic fibres, staggered to provide maximum acceptance. Figure 1.23 shows a picture of a 4-layers ribbon prototype and its front view. SiPM arrays detect scintillation light on both ends of each ribbon.

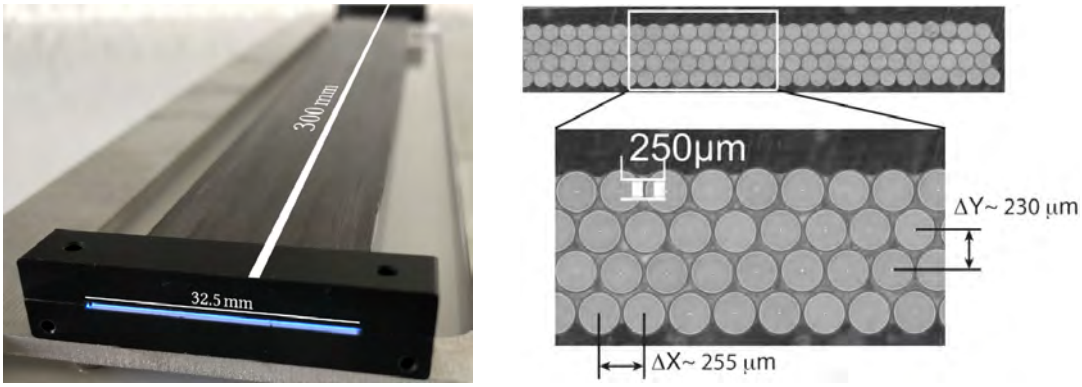

Figure 1.23: *Left: SciFi ribbon prototype. Right: front view of the SciFi ribbon prototype. From [4].*

For tracks recurling in the central tracker, the SciFi provides information on the charge of the particle through the correlation between the time difference of two consecutive crossings (Δt_{fibres}) and the length of the trajectory as

shown in Figure 1.24, allowing to assess the charge of the particle or reject mis-reconstructed tracks. The timing resolution is expected to be 250 ps.

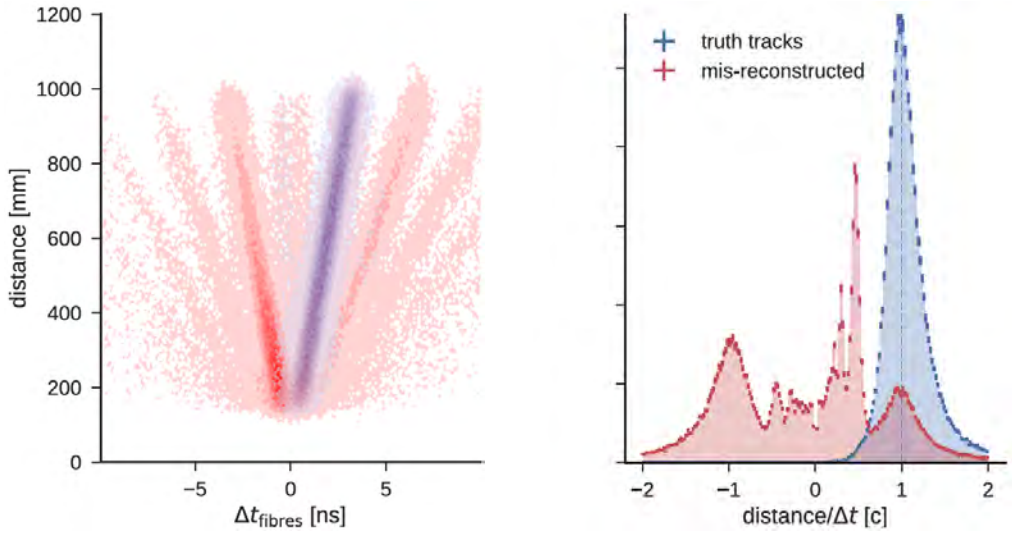

Figure 1.24: *Left: length of the reconstructed trajectory vs time between two consecutive fibre crossings. Right: reconstructed speed of recurling tracks. Tracks with wrong charge assignment and/or mis-reconstructed are shown in red. Correctly reconstructed charges are shown in blue. From [4].*

1.4.2.5 The Scintillating Tile detector

The Scintillating Tile (SciTile) detector is positioned inside the recurl stations, after tracking is performed. This allows to increase the material budget to achieve higher timing resolutions. Two 342 mm long SciTile stations are mounted inside each recurl tracker station. The detector is segmented in 52 tiles along the beam axis and in 56 tiles along the azimuthal angle. Each tile is a 6.3 mm × 6.2 mm × 5.0 mm plastic scintillator. The smallest mechanical unit, the *sub-module*, consists of 32 tiles and SiPM channels. The outer tiles of the sub-modules have the edges bevelled by 25.7°. 13 sub-modules are mounted on a water-cooled aluminum support to compose a *module*. The full detector consits of 7 modules mounted on two *endrings* connected to the beam pipe.
Figure 1.25 shows a 3-D rendering of the SciTile detector and its components. The time resolution measured for a single tile is $\sim$ 45 ps and decreases with the number of hits as shown in Figure 1.26.

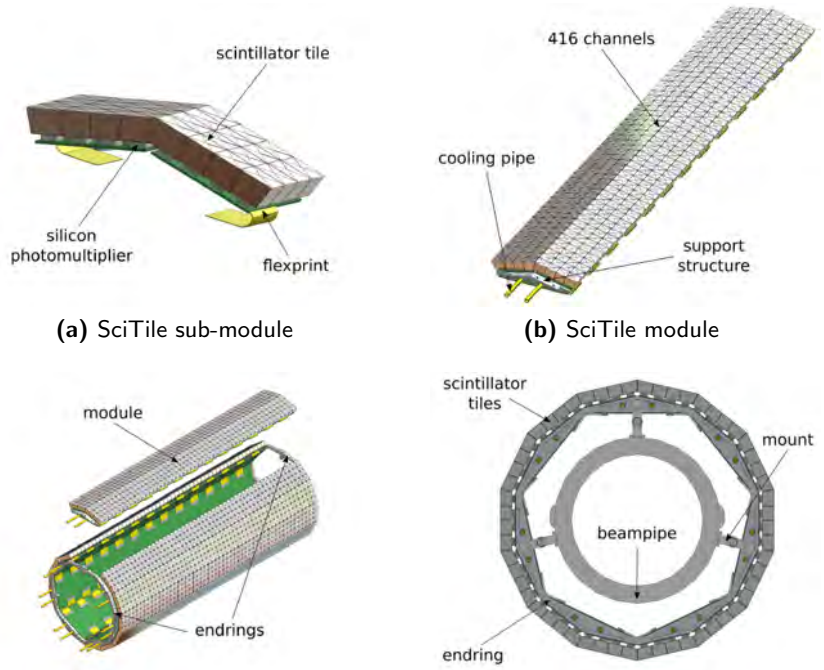

(a) SciTile sub-module

(b) SciTile module

(c) SciTile detector

(d) SciTile detector support, front view

Figure 1.25: *3-D CAD rendering of the SciTile detectors and its components from [4].*

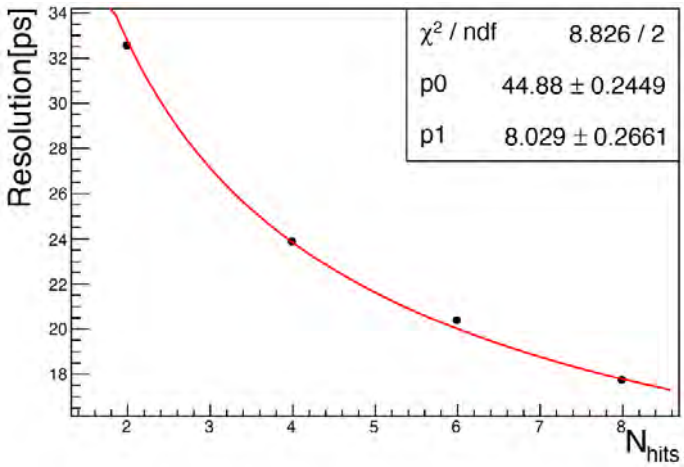

Figure 1.26: *Measured time resolution as a function of the number of hits from [4].*

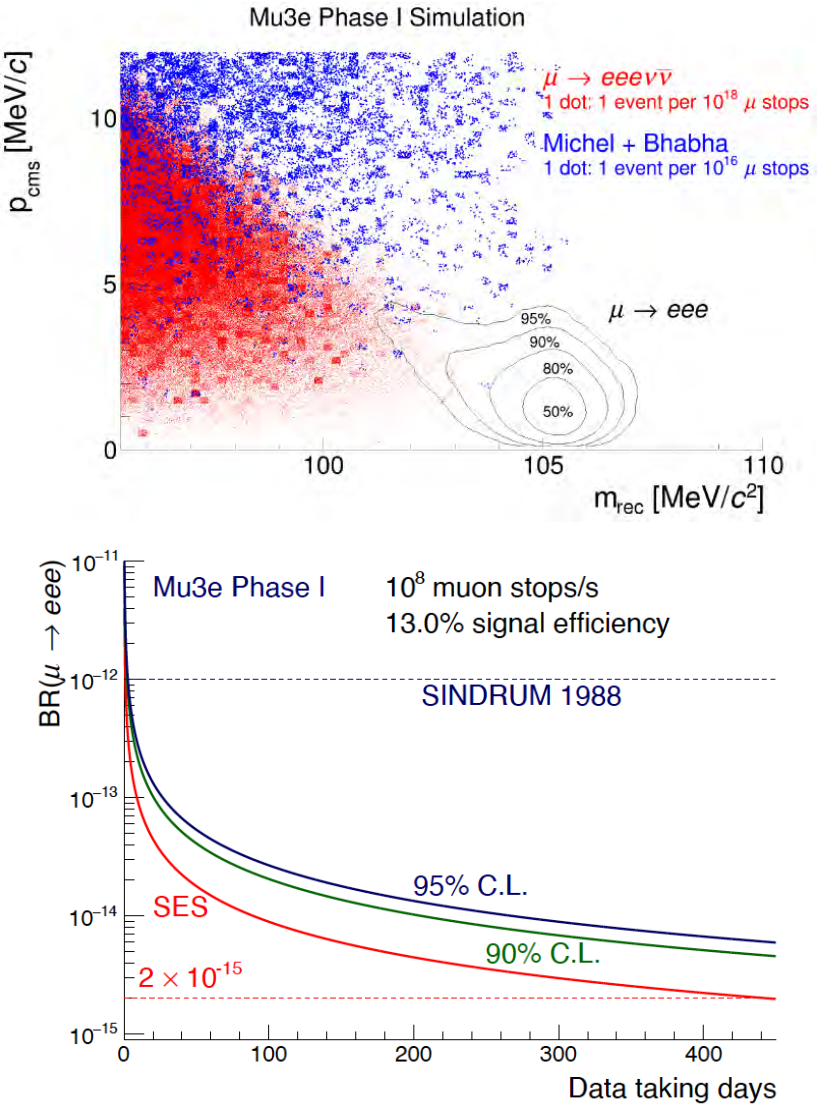

Figure 1.27: *Top: expected reconstructed mass versus the center of mass (CMS) momentum for the signal (solid black lines) and the main background (dots). In red, the internal conversion background. In blue, the accidental coincidences between Michel decays and Bhabha scattering. Bottom: expected single event sensitivity (SES) and corresponding* 90 % *and* 95 % *confidence level (CL) upper limits as a function of running time. From [4].*

1.4.3 Expected sensitivity

Figure 1.27 shows the expected reconstructed mass versus the CMS momentum for the signal and the background and the expected sensitivity as a function of running time.

In a wide signal box in the mass range from 103 MeV/c^2 to 110 MeV/c^2

with a center of mass (CMS) momentum $p_{cms} < 4\,\mathrm{MeV/c}$, $0.57(4)$ Radiative Michel Decays with internal conversion and $1.9(14)$ accidental coincidences of Michel and Bhabha event are expected in the signal region for 2.5×10^{15} muon stops. This corresponds to 300 days of data taking at 10^8 μ^+ stops/s.

1.5 Muon beams production at PSI

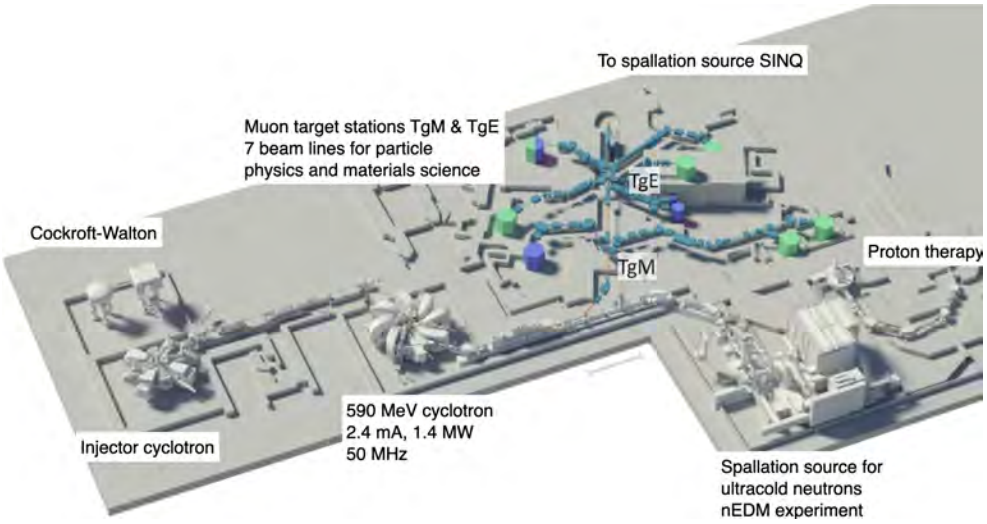

Figure 1.28: *Layout of the HIPA facility.*

As both MEG II and Mu3e are coincidence experiments, they both suffer from accidental background. Depending on the nature of the accidental event, the rate of such a background can scale with second or even third power of the muon stopping rate [1, 15]. If the average rate is kept constant, a pulsed beam will induce higher accidental backgrounds than a continuous beam.
The High Intensity Proton Accelerator (HIPA) facility at PSI delivers the highest continuous muon rates in the world, up to $10^8\,\mu^+/s$, making it a suitable host for both experiments.

1.5.1 The High Intensity Proton Accelerator facility

Figure 1.28 shows the layout of the HIPA facility. An Electron Cyclotron Resonance ion source (ECR) ionizes hydrogen. The first acceleration is provided by a high power Cockroft-Walton accelerator to 870 keV. The acceleration continues then at the Injector II (INJ2) cyclotron to 72 MeV and at the RING cyclotron to reach the terminal energy of 590 MeV. Up to 2.4 mA of protons can be delivered in continuous wave, allowing for beam powers up to 1.4 MW.

The beam can be either steered to the Ultra Cold Neutron (UCN) source or to the meson production targets:

- Target M (TgM): 5 mm thick polycrystalline graphite target. It serves a beamline for muon spin spectroscopy (μSR) and a high resolution pion beam line.

- Target E (TgE): 40 mm thick polycrystalline graphite target. It serves the highest intensity muon beamlines.

Both targets rotate at 1 Hz to allow for radiation cooling.

The remaining proton beam, ∼70 % of the initial power, is used for neutron production at the spallation target of the Swiss Neutron Spallation Source (SINQ).

1.5.2 Muon production

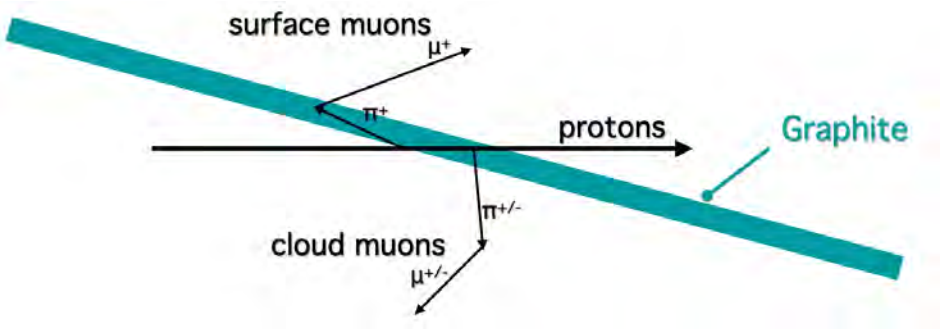

Figure 1.29: *Cartoon of the muon production at PSI. Protons impinge on the graphite producing charged pions, which then decay to muons. Muons produced in the target from the pion decay at rest are called surface muons. Muons produced by the pion decay in flight are called cloud muons.*

The muons are produced by the decay of pions generated at the two targets. Depending on where they are created, we classify:

- Surface and sub-surface muons (5-30 MeV/c): they are created inside the target from pions at rest as a monochromatic line of 29.8 MeV/c of momentum. Their energy depends only on their path inside the target allowing for high yields in a narrow momentum bite. As neutrinos are left-handed, they are fully polarized.

- Cloud muons: they come from pion decay in flight.

Figure 1.29 shows a cartoon of the muon production process. The time structure of surface muon beams depends on the proton beam bunching. At HIPA, the radio frequency cavities work at 50.6 MHz, making the bunch spacing ∼ 20 ns. Even though the pion production follows closely the proton bunching, this structure is washed out in the surface muon production due to the decay time of charged pions being 26 ns and due to the coherence loss along the muon transfer lines. The surface muon beam is therefore continuous.

In 2019, a slanted version of TgE was tested and then permanently installed in 2020 as TgE*. The upgrade consisted in the introduction of a slanting angle with the proton beam of 8° while keeping the material budget in the direction of the proton beam constant at 40 mm to not affect neutron production at SINQ. Because surface muons are generated in the epithermal region of the target, within the outer 200 µm – 400 µm [6], the slanting angle allows to reduce the volume of the target while keeping the surface constant. The muon yield increase depends on the muon emission angle and was measured to be 30 % – 50 % depending on the experimental area.

Chapter 2

Beam dynamics and matrix formalism

This work is focused on both the commissioning of the Compact Muon BeamLine (CMBL) in the context of the Mu3e experiment and on the optimization and evaluation of different beamline designs for the High Intensity Muon Beams (HIMB) project. A brief introduction on elements of beam dynamics is given in the following to set basic concepts needed in Chapter 3 and Chapter 5. When not explicitly stated, the reference for this chapter is [28].

This chapter serves as an introduction to the notions of beam dynamics needed for Chapter 3 and Chapter 5.

2.1 Hamiltonian formalism

As opposed to the Lagrangian formalism, the Hamiltonian formalism uses coordinates and momenta as canonical variables instead of coordinates and velocities. Whereas equivalent, these two formalisms highlight different underlying properties of a dynamical system:

- Lagrangian formalism is well suited for the description of systems with constraints and for the description of dissipative systems;
- Hamiltonian formalism is well suited for the decscription of systems with symmetries and conserved quantities, that can be handled through canonical transformations.

Particle beam dynamics is usually described using the Hamiltonian formalism, which allows to propagate particles through the accelerator lattice with symplectic operators. Further details are provided in Section 2.2.

The Hamiltonian of a charged particle in an electromagnetic field is given by:

$$H = e\varphi + \sqrt{c^2(\vec{p} - e\vec{A})^2 + m^2c^4} \tag{2.1}$$

with φ the electric potential, $\vec{A}$ the magnetic vector potential, m the mass of the particle, e its charge and $\vec{p}$ its momentum.

2.1.1 Frenet-Serret coordinates

A common approach to beam dynamics is to express the motion relative to a reference orbit using the so-called Frenet-Serret coordinates. In such case we can express an arbitrary trajectory as:

$$\vec{r}(z) = \vec{r}_0(z) + \Delta\vec{r}(z) \tag{2.2}$$

with $\vec{r}_0(z)$ been the ideal orbit and $\Delta\vec{r}(z)$ the local deviation from the ideal orbit in the coordinate system perpendicular to the reference orbit in z. The system is defined by the unit vectors:

$$\vec{u}_x(z) \quad \text{horizontal unit vector } \perp \text{ to the reference trajectory} \tag{2.3}$$
$$\vec{u}_z(z) \quad \text{unit vector } \parallel \text{ to the reference trajectory} \tag{2.4}$$
$$\vec{u}_y(z) \quad = u_z(z) \times u_x(z) \tag{2.5}$$

$\vec{u}_x(z)$ and $\vec{u}_y(z)$ define the so-called transverse plane. Figure 2.1 shows the coordinate system.

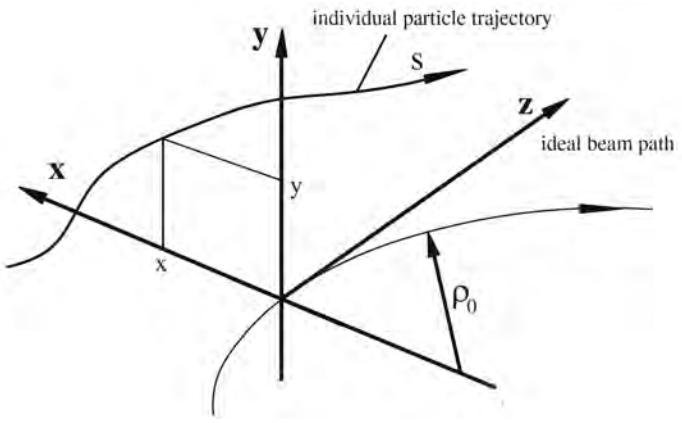

Figure 2.1: *Frenet-Serret coordinate system from [28].*

The change in unit vectors are determined by:

$$\frac{\mathrm{d}\vec{u}_x}{\mathrm{d}z} = \kappa_x \vec{u}_z \tag{2.6}$$

$$\frac{\mathrm{d}\vec{u}_y}{\mathrm{d}z} = \kappa_y \vec{u}_z \tag{2.7}$$

with κ_x and κ_y the curvatures of the reference trajectory in the horizontal and vertical plane respectively.
We can then write:

$$\vec{r}(z) = \vec{r}_0(z) + x(z)\vec{u}_x(z) + y(z)\vec{u}_y(z) \tag{2.8}$$

$$\mathrm{d}\vec{r} = \vec{u}_x \mathrm{d}x + \vec{u}_y \mathrm{d}y + \vec{u}_z h \mathrm{d}z \tag{2.9}$$

$$h = 1 + k_{0,x}x + k_{0,y}y \tag{2.10}$$

with $k_{0,x}$ and $k_{0,y}$ the curvatures of the reference trajectory in the horizontal and vertical plane respectively.

The reference $\vec{r}_0(z)$ does not need to be the trajectory of a reference particle, it could also be defined as the centerline of the beamline instead, that is to say the geometric axis of the beamline. This is an important point for those systems where the centerline is not a solution of the equations of motion, as in the case of HIMB.

Equation 2.1 can be expressed now in the local coordinate system:

$$H = e\varphi + c\sqrt{m^2c^2 + (p_x - eA_x)^2 + (p_y - eA_y)^2 + \frac{(p_z - eA_z h)^2}{h^2}} \tag{2.11}$$

We can now change the independent variable to z by solving the Hamiltonian for p_z and dividing it by the momentum p:

$$p = \sqrt{\frac{(H - e\varphi)^2}{c^2} - m^2c^4} \tag{2.12}$$

$$K = -\frac{p_z}{p} = -\frac{eA_z h}{p} + h\sqrt{1 - \frac{p_x^2}{p^2} - \frac{p_y^2}{p^2}} \tag{2.13}$$

which can be rewritten by using the slopes $x' = \mathrm{d}x/\mathrm{d}z = p_x/p_z$ and $y' = \mathrm{d}y/\mathrm{d}z = p_y/p_z$, which are the new conjugate momenta:

$$K = -\frac{eA_z h}{p} - h\sqrt{1 - \frac{x'^2 + y'^2}{1 + x'^2 + y'^2}} \tag{2.14}$$

The transverse components of the magnetic potential are neglected here as usual accelerator elements, like quadrupoles and dipoles, have a magnetic field that is perpendicular to the reference trajectory. For solenoids, where this is not the case, additional terms are added as perturbations to this Hamiltonian.

2.1.2 Paraxial approximation

Particle accelerators constrain the motion along the z axis, resulting in small deviations from the reference trajectory. In such regime, $x'^2 + y'^2 \ll 1$ and $p \approx p_z$ and therefore we can expand the square root to first order:

$$K \approx -\frac{eA_z h}{p} - h\sqrt{1 - x'^2 - y'^2} \tag{2.15}$$

Finally, we express the momentum of a charge particle by its deviation from the reference momentum p_0:

$$\delta = \frac{p - p_0}{p_0} \tag{2.16}$$

$$p = p_0(1 + \delta) \tag{2.17}$$

$$\frac{1}{p} = \frac{1}{p_0(1+\delta)} \approx \frac{1}{p_0}(1 - \delta) \tag{2.18}$$

The Hamiltonian takes then the form:

$$K \approx -\frac{eA_z h}{p_0}(1 - \delta) - h\sqrt{1 - x'^2 - y'^2} \tag{2.19}$$

The equations of motion are then:

$$\frac{\partial K}{\partial x} = -x'' = -\frac{ec}{cp_0}\frac{\partial A_z h}{\partial x}(1 - \delta) - k_{0,x}\sqrt{1 - x'^2 - y'^2} \tag{2.20}$$

$$\frac{\partial K}{\partial y} = -y'' = -\frac{ec}{cp_0}\frac{\partial A_z h}{\partial y}(1 - \delta) - k_{0,y}\sqrt{1 - x'^2 - y'^2} \tag{2.21}$$

One can compute the magnetic field in the Frenet-Serret coordinate system:

$$hB_y = -\frac{\partial hA_z}{\partial x} \tag{2.22}$$

$$hB_x = \frac{\partial hA_z}{\partial y} \tag{2.23}$$

$$\Rightarrow \quad x'' + \frac{ec}{cp_0}B_y h(1 - \delta) - k_{0,x}\sqrt{1 - x'^2 - y'^2} = 0 \tag{2.24}$$

$$\Rightarrow \quad y'' - \frac{ec}{cp_0}B_x h(1 - \delta) - k_{0,y}\sqrt{1 - x'^2 - y'^2} = 0 \tag{2.25}$$

These are the equations of motion of a charged particle in a magnetic field (B_x, B_y).

2.2 Matrix formalism

For highly relativistic particles, magnetic fields are preferred thanks to the linear scaling in β of the Lorentz force in the magnetic component. For lower velocities both electric and magnetic fields are used. Here only magnetic fields are considered.

In particle beam optics, a lattice of electromagnetic elements is used to restrict the motion of a beam of particles within a well specified region in space. This allows to simplify the problem by restricting the kind of fields employed to easy to handle ones, like pure multipolar components. An additional simplification usually adopted is to consider only magnetic fields transverse to the reference trajectory. In such case, solenoidal fields can be treated as perturbations to the main magnetic field.

Dipolar fields, hence uniform magnetic fields, are used to define the reference trajectory. From the expression of the Lorentz force, the bending radius ρ of a particle moving in a dipole is:

$$m\gamma v^2 \vec{k} + e\vec{v} \times \vec{B} = 0 \tag{2.26}$$

$$k_{x,y} = \frac{\mp eB_{y,x}}{m\gamma v} = \frac{\mp eB_{y,x}}{p} \tag{2.27}$$

$$\rho = \frac{p}{eB} \tag{2.28}$$

The quantity $B\rho$ is usually referred to as *rigidity*.

2.2.1 Equations of motion

We want now to simplify the equations of motion and to linearize them. Together with the paraxial approximation, another ideal assumption is that the momenta of the particles are close to that of the reference, i.e. $\delta \ll 1$. Starting from Equation 2.24, for beams propagated in the horizontal plane with no vertical coupling ($y = 0$):

$$
\begin{aligned}
x'' &= -\frac{ec}{cp_0}B_y h(1-\delta) + k_x\sqrt{1-x'^2-y'^2} && (2.29)\\
&\approx -\frac{ec}{cp_0}B_y h(1-\delta) + k_x\Big(1-\frac{1}{2}x'^2-\frac{1}{2}y'^2\Big) + \mathcal{O}(3) && (2.30)\\
&\approx -\frac{1}{\rho}(1-\delta)h + k_x + \mathcal{O}(3) && (2.31)
\end{aligned}
$$

here the expansion was truncated at second order in x, y, x', y' and δ.

With $h = 1 + k_x x$:

$$x'' \approx -\frac{1}{\rho} + \frac{1}{\rho}\delta + \frac{1}{\rho}(1-\delta)k_x x + k_x + \mathcal{O}(3) \quad (2.32)$$

We can expand the general curvature $1/\rho$ to second order in x:

$$\frac{1}{\rho} = k_x + k_1 x + \mathcal{O}(2) \quad (2.33)$$

where k_1 is the linear multipole of the magnetic field, or *quadrupole*.

To the first order, the equations of motion are:

$$x'' + (k_1 + k_x^2)x = k_x\delta + \mathcal{O}(2) \quad (2.34)$$

Analogously, for the vertical plane:

$$y'' + k_1 y = \mathcal{O}(2) \quad (2.35)$$

with $k_y = 0$. We derived the Hill's equations for a particle in a magnetic field. The homogeneous equation can be written as:

$$u'' + Ku = 0 \quad \text{, with } u = x, y \quad (2.36)$$

Assuming the initial conditions $u(z_0) = u_0$ and $u'(z_0) = u_0'$, the solution is:

$$
\begin{aligned}
u(z) &= C(z)u_0 + S(z)u_0' && (2.37)\\
u'(z) &= C'(z)u_0 + S'(z)u_0' && (2.38)\\
C(z) &= \begin{cases} \cos(\sqrt{K}z) & K \geq 0 \\ \cosh(\sqrt{-K}z) & K < 0 \end{cases} && (2.39)\\
S(z) &= \begin{cases} \frac{1}{\sqrt{K}}\sin(\sqrt{K}z) & K \geq 0 \\ \frac{1}{\sqrt{-K}}\sinh(\sqrt{-K}z) & K < 0 \end{cases} && (2.40)
\end{aligned}
$$

The restoring force K will be generally dependent on z. The solutions shown above can be generalized to such case. We substitute the solutions into Equation 2.36:

$$[S''(z) + K(z)S(z)]u_0 + [C''(z) + K(z)C(z)]u_0' = 0 \tag{2.41}$$

Solutions need to exist for any u_0 and u_0', so the need to vanish separately:

$$C''(z) + K(z)C(z) = 0 \tag{2.42}$$
$$S''(z) + K(z)S(z) = 0 \tag{2.43}$$

2.2.2 Transfer matrices

We can express Equations 2.37 and Equation 2.38 in matrix form:

$$\begin{bmatrix} u(z) \\ u'(z) \end{bmatrix} = \begin{bmatrix} C(z) & S(z) \\ C'(z) & S'(z) \end{bmatrix} \begin{bmatrix} u_0 \\ u_0' \end{bmatrix} \tag{2.44}$$

For each element of the lattice we obtain the so-called *transfer matrix*, allowing to propagate the initial conditions to any point of the accelerator. In a drift of length L, the transfer matrix is:

$$\mathcal{M}_{drift}(0|L) = \begin{bmatrix} 1 & L \\ 0 & 1 \end{bmatrix} \tag{2.45}$$

In a quadrupole magnet of length l and strength $k_1 > 0$, the transfer matrix is:

$$\mathcal{M}_{quad}(0|l) = \begin{bmatrix} \cos(\sqrt{k_1}l) & \frac{1}{\sqrt{k_1}}\sin(\sqrt{k_1}l) \\ -\sqrt{k_1}\sin(\sqrt{k_1}l) & \cos(\sqrt{k_1}l) \end{bmatrix} \tag{2.46}$$

Higher order terms are introduced as perturbations to the solution to the homogeneous Hill's equation. Dispersion is an example of such treatment. In general beams deviate from the monochromatic hypothesis and have indeed a finite momentum spread. Such deviation introduces variations in the curvature, causing for instance more rigid (higher rigidity) particle to be steered less and vice versa. The first order correction to this effect is shown in Equation 2.47:

$$x'' + K(z)x = k_x(z)\delta + \mathcal{O}(2) \tag{2.47}$$

The particular solutions to the perturbation can be found with the Green's function of the homogeneous equation:

$$G(z, \tilde{z}) = S(z)C(\tilde{z}) - C(z)S(\tilde{z}) \tag{2.48}$$
$$P(z) = \delta \int_{z_0}^{z} k_x(\tilde{z})G(z, \tilde{z})\mathrm{d}\tilde{z} \tag{2.49}$$
$$P(z) = \delta \int_{z_0}^{z} k_x(\tilde{z})\big[S(z)C(\tilde{z}) - C(z)S(\tilde{z})\big]\mathrm{d}\tilde{z} = \delta D_x(z) \tag{2.50}$$

The term $\delta D_x(z)$ is to be added to the homogeneous solution and is the shift in the transverse direction given by a particle with momentum deviation δ. $D_x(z)$ is the so-called *dispersion function*. In matrix form, we can expand the state vector to include the momentum deviation δ:

$$\begin{bmatrix} x(z) \\ x'(z) \\ \delta(z) \end{bmatrix} = \begin{bmatrix} C(z) & S(z) & D_x(z) \\ C'(z) & S'(z) & 0 \\ 0 & 0 & 1 \end{bmatrix} \begin{bmatrix} x_0 \\ x'_0 \\ \delta_0 \end{bmatrix} \tag{2.51}$$

2.3 Beam emittance

In mechanics, the space described by the coordinates and their conjugate momenta is called *phase space*. As shown above, in beam dynamics the conjugate momenta are approximated by the slopes of the single particle trajectories, from now on referred to as divergences. The slopes themselves are indeed the tangent of the angular divergence of the particles with respect to the reference orbit and in the paraxial approximation they can be approximated by such angles. For such reason, the divergences are expressed in radians.

It is usually convenient to not track each particle in a beam through the beam, but to describe the collective motion of their distribution. This is possible thanks to Liouville's Theorem: it can be shown that the density of particles in phase space is constant if under the influence of conservative forces. This is true for electromagnetic fields.
In the matrix formalism, such property is equal to requiring the transfer matrices to be symplectic.

Lioville's theorem means also that any closed surface in phase space at a given point along the lattice will be transformed into a closed surface enclosing an equal volume at any other point along the lattice. Such volume is usually called *beam emittance* and the surface definition might vary depending on the properties of the beam. If no correlation is present among the horizontal, vertical and longitudinal coordinates, the area of their subspaces is conserved as well, and the total emittance is given by their product. It is particularly convenient to use ellipses to define such surfaces:

$$\gamma_x x^2 + 2\alpha_x x x' + \beta_x x'^2 = \varepsilon_x \tag{2.52}$$

with α_x, β_x, γ_x and ε_x the ellipse parametrs. ε_x is the emittance and the area enclosed by the ellipse is $J = \pi\varepsilon_x$. The inclusion of π in the emittance is a possible notation as well and there is no uniformity in the field concerning the convention. To avoid confusion, in the following the emittance will be quoted in units of π. The parameters α_x, β_x and γ_x are also known as Twiss parameters. Figure 2.2 shows the ellipse in Equation 2.52.

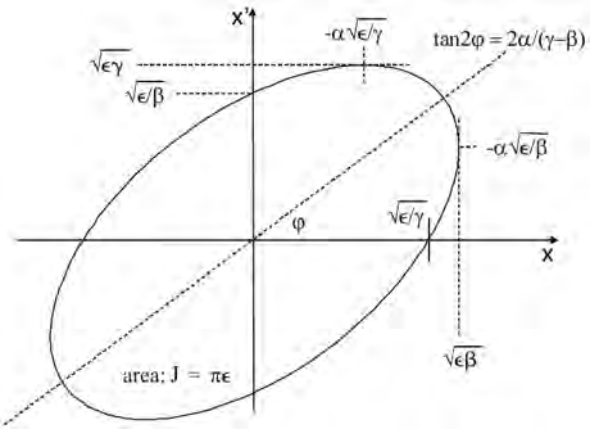

Figure 2.2: *Beam ellipse definition adapted from [28].*

A general ellipse in the $N-$dimensional space can be written as:

$$\vec{x}^T \Sigma^- 1 \vec{x} \quad = \quad 1 \tag{2.53}$$

Its volume is given by:

$$V_N = \frac{\pi^{\frac{N}{2}}}{\Gamma(N/2+1)} \sqrt{\det \Sigma} \tag{2.54}$$

with $\Gamma(x)$ the gamma function.

For simplicity we consider again only the horizontal coordinates:

$$\Sigma \quad = \quad \begin{bmatrix} \sigma_{xx} & \sigma_{xx'} \\ \sigma_{xx'} & \sigma_{x'x'} \end{bmatrix} = \varepsilon^2 \begin{bmatrix} \varepsilon_x & -\alpha_x \\ -\alpha_x & \beta_x \end{bmatrix} \tag{2.55}$$

$$V_2 \quad = \quad \pi \sqrt{\det \Sigma} = \pi \sqrt{\sigma_{xx}\sigma_{x'x'} - \sigma_{xx'}^2} = \pi \varepsilon_x \tag{2.56}$$

The beam matrix transforms as a bilinear operator. If we consider a transformation $\mathcal{M}$ mapping u_0 to u_1:

$$u_0^T \Sigma_0^{-1} u_0 = 1 \quad = \quad (\mathcal{M}^{-1} u_1) \Sigma_0^{-1} (\mathcal{M}^{-1} u_1) \tag{2.57}$$

$$= \quad u_1^T (\mathcal{M}^{-1})^T \Sigma_0^{-1} \mathcal{M}^{-1} u_1 \tag{2.58}$$

$$= \quad u_1^T \Sigma_1^{-1} u_1 \tag{2.59}$$

$$\Rightarrow \Sigma_1 \quad = \quad \mathcal{M} \Sigma_0 \mathcal{M}^T \tag{2.60}$$

In case of a gaussian beam, the contours of the distribution are ellipses with their matrices proportional to the covariance matrix. In a 2D space, the 1-σ ellipse encloses 46.6 % of the full distribution. Gaussian beams are of

particular interest due to their simplicity and because they provide a good description of a generic beam in the linear regime.

As a final remark, in general the horizontal, vertical and longitudinal phase space can be treated separately as long as there is no correlation among them. In absence of changes in p_0, the 4D transverse phase space is used. An example is given by solenoids in paraxial approximation, which introduce helicoidal motion to the particles, and therefore strongly correlating the motion in the horizontal and in the vertical planes. If the paraxial approximation does not hold, the 6D phase space has to be used.

Chapter 3

The πE5 Area

In the following chapter, a description of the πE5 area hosting the MEG II and Mu3e experiments, among others, will be provided together with the instruments and methods employed to tune the beamline. Then the focus will be put on the commissioning of the Compact Muon Beam Line (CMBL), serving Mu3e, and on the study performed to understand the phase space of πE5 aiming at a consistent modeling of the beamline dynamics.
The work presented in this chapter is a continuation of the work presented in [5] and in [6].

While the first section is mostly introductive, the rest of the chapter represents a big fraction of the work of the candidate as part of the MEG II and Mu3e teams tuning the πE5 beamline. The candidate has set up the measurements and performed the analysis.

3.1 The πE5 area

The πE5 area is served by a low-energy secondary beamline delivering pions and muons in the momentum range [10, 120] MeV/c. It has a 165° viewing angle with respect to the proton beam on TgE. Figure 3.1 shows the layout of the beamline from TgE up to the entrance in the experimental area.

For greater clarity in the following, Figure 3.2 shows the beam envelope of the surface muon beam in πE5 as evaluated with TRANSPORT [30] at second order in the transverse coordinates and divergences.

Muons and pions are produced by impinging protons on TgE (see Chapter 1) and are captured in the backwards direction by the AHSW41 dipole.

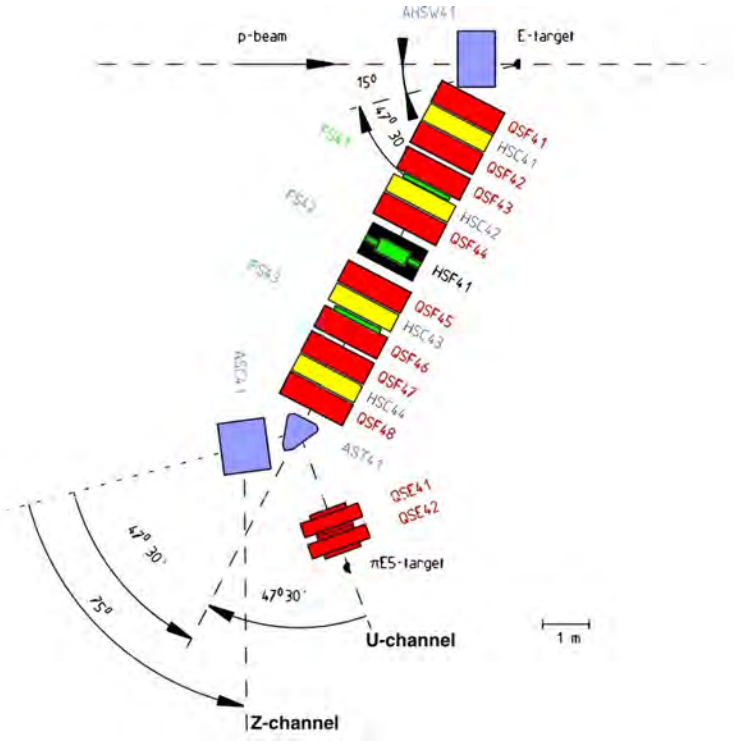

Figure 3.1: *πE5 beamline layout up to the entrance in the experimental area from [29]. The colors indicate the type of element: quadrupoles are red, sextupoles are yellow, dipoles are light blue and the slits are green. The proton beam impinges on TgE producing mesons as described in Chapter 1. They are then collected by the first dipole AHSW41, which defines the accepted central momentum.*

This magnet is part of the proton beamline and defines the momentum accepted by the πE5 beamline.

The mesons are deflected by 47.5° and coupled into a straight section consisting of quadrupoles (QSF4*) and sextupoles (HSC4*). Along this section three slit systems (FS41-42-43) are used to reduce the beam intensities delivered to the experimental area and to cut the momentum distribution. This is possible as dipoles introduce dispersion in the lattice and because the meson beams are not monochromatic and a correlation between the horizontal transverse coordinate of the beam and the momentum distribution arises: by cutting on the horizontal plane it is possible to cut the momentum distribution as well. More specifically, FS41 and FS43 are horizontal slits and are positioned in a high dispersion position to shape the momentum distribution, while FS42 can cut the beam at the same time in the vertical and in the horizontal direction and is positioned in a dispersion free point, allowing for beam intensity reduction without affecting the momentum distribution.

As both MEG II and Mu3e are stopping target experiment, FS41 is usually

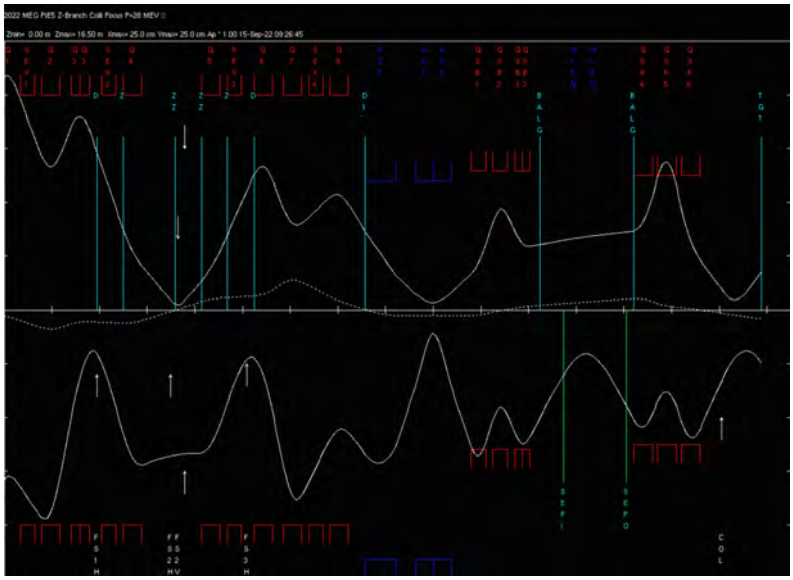

Figure 3.2: *Second order envelope (solid white lines) of the surface muon beam along the πE5 beamline up to the MEG II collimator computed with TRANSPORT. Top: vertical envelope. Bottom: horizontal envelope. The dashed line represents the dispersion along the beamline in case of a momentum higher than nominal by* 1 %.

used to reduce the beam intensity if required, as lowering the momentum distribution width results in a lower straggling at the target, and a higher stopping efficiency.

After QSF48, the AST41 dipole can be used to switch between two channels: channel Z, where both MEG II and Mu3e are connected, and channel U. When in channel Z mode the beam is transmitted through a second dipole, ASC41 that provides a 75° bend to then deliver the beam in the experimental area. In channel U mode instead, the beam is transmitted through a doublet of quadrupoles, QSE41-42, into the experimental area.

As the requirements for MEG II and Mu3e on the characteristics of the beam are similar, the first section of the beamline inside the experimental area is shared. As shown in Figure 3.3, the beam is coupled into a Wien filter (SEP41) through Triplet I, a quadrupole triplet (QSB41-42-43), to separate the muon beam from the positron background.
A Wien filter is a device providing transverse electric and magnetic fields perpendicular to each others. From the expression of the Lorentz force, it can be shown that such configuration does not affect particles with a velocity v_0:

$$F = q\,(E + v_0 \times B) = 0 \Rightarrow v_0 = \frac{E}{B} \tag{3.1}$$

with E and B the electric and magnetic field respectively. Any particle with

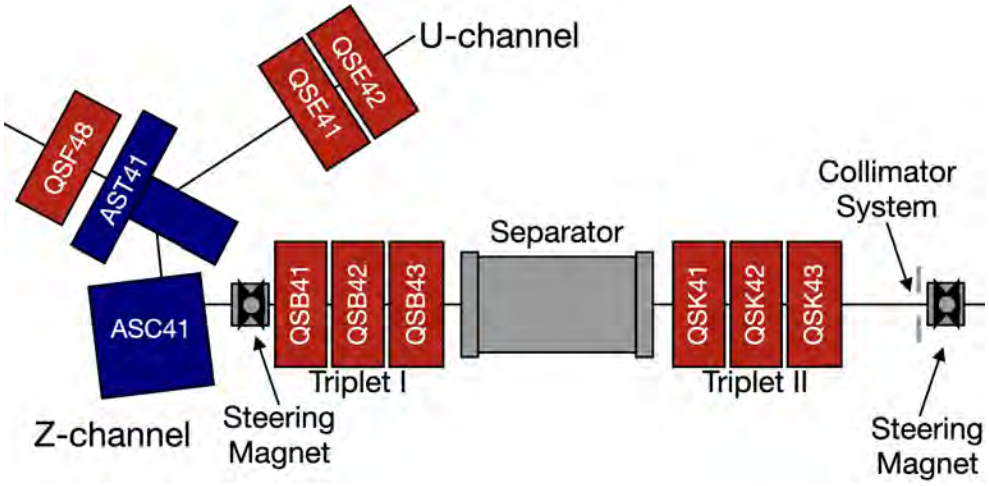

Figure 3.3: *πE5 beamline section connected to channel Z. The elements shown here are shared between the MEG II and the Mu3e experiments.*

a velocity different than v_0 will be deflected by the Wien filter, which is also called velocity selector or particle separator.

In πE5, the separation is performed vertically to deflect the positron beam downwards. Two metallic plates are set at a positive and negative high voltage to produce a vertical electric field pointed downwards. Two coils produce a magnetic field in the horizontal direction instead, pointing in the direction of the U-channel (see Figure 3.3).
The role of Triplet I is to shape the beam to be focused in the horizontal direction, as in the horizontal plane the Wien filter is a drift, and to be parallel in the vertical plane. The Wien filter in fact provides a kick to the beams that depends on the longitudinal velocity only. While the average kick is the same for both a divergent and a parallel beam, in the first case the longitudinal velocity distribution will be broader and therefore the beam spot in the separation direction at the end of the Wien filter overlap. Figure 3.4 shows a cartoon of the difference between these two cases. Further details about the Wien filter are given in Section 5.3.5.

The beam is then focused by Triplet II (QSK41-42-43) at a collimator, aimed at stopping the tails of the contaminant beams. During beam tuning campaigns in πE5 the first measuring point is right downstream of the collimator. Further details will be provided in the following sections.

As already stated above, up to this point the beamline is the same for both MEG II and Mu3e. The layout of the beamline in the two configurations is provided in the following two paragraphs.

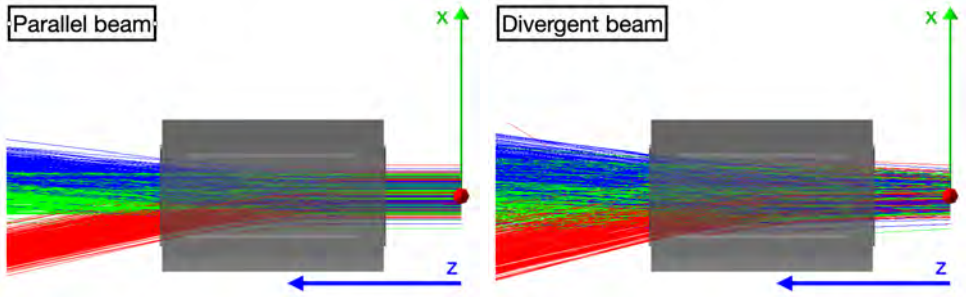

Figure 3.4: *Cartoon of the effect of the initial divergence distribution for three different particle beams: μ^+ in green, π^+ in blue and e^+ in red. For a parallel beam (left) the separation is better than for a divergent beam (right) as the final beam spot of the contaminants will be narrower.*

3.1.1 The Compact Muon BeamLine CMBL for the Mu3e experiment

The Compact Muon BeamLine (CMBL) is an extension of the πE5 channel Z to deliver the beam to the Mu3e solenoid. The design was studied to fit the beamline and the Mu3e spectrometer in the limited space available in the front part of the πE5 area. This is necessary as the rear part of πE5 is occupied by the MEG II experiment. Figure 3.5 shows a comparison between the layout of the πE5 area in the Mu3e and in the MEG II configurations. The CMBL starts after Triplet II described before.

The ASL41 dipole provides a 90° bending angle to fit the stringent space constraint and it is positioned only a few centimeters away from the concrete wall that separates the front and the rear part of πE5 in the CMBL configuration. A doublet of compact quadrupoles (QSO41-42) is used to couple the beam through the ASK41 dipole, that provides a final 65° bend. Before entering the Mu3e solenoid the beam is further shaped by a large aperture quadrupole, QSM41. The QSO doublet together with QSM41 form the so-called *split triplet*.

The beamline inside the Mu3e solenoid is bolted to its entrance flange and is gradually reduced in size to fit within the small amount of free space in the Mu3e detector. Figure 3.6 shows the G4bl model of the beam pipe inside the Mu3e solenoid. A 600 µm Mylar® moderator is included along the beamline to reduce the energy of the incoming beam before stopping it at the target. After the moderator, a collimator with a 40 mm diameter aperture reduces the number of muons hitting the innermost tracker layer due to scattering in the moderator. Finally, a 35 µm thick Mylar® window separates the vacuum in the beam pipe from the helium atmosphere inside the Mu3e solenoid (see Chapter 1).

Figure 3.7 shows the first order beam envelope of the surface muon beam for πE5 including the CMBL.

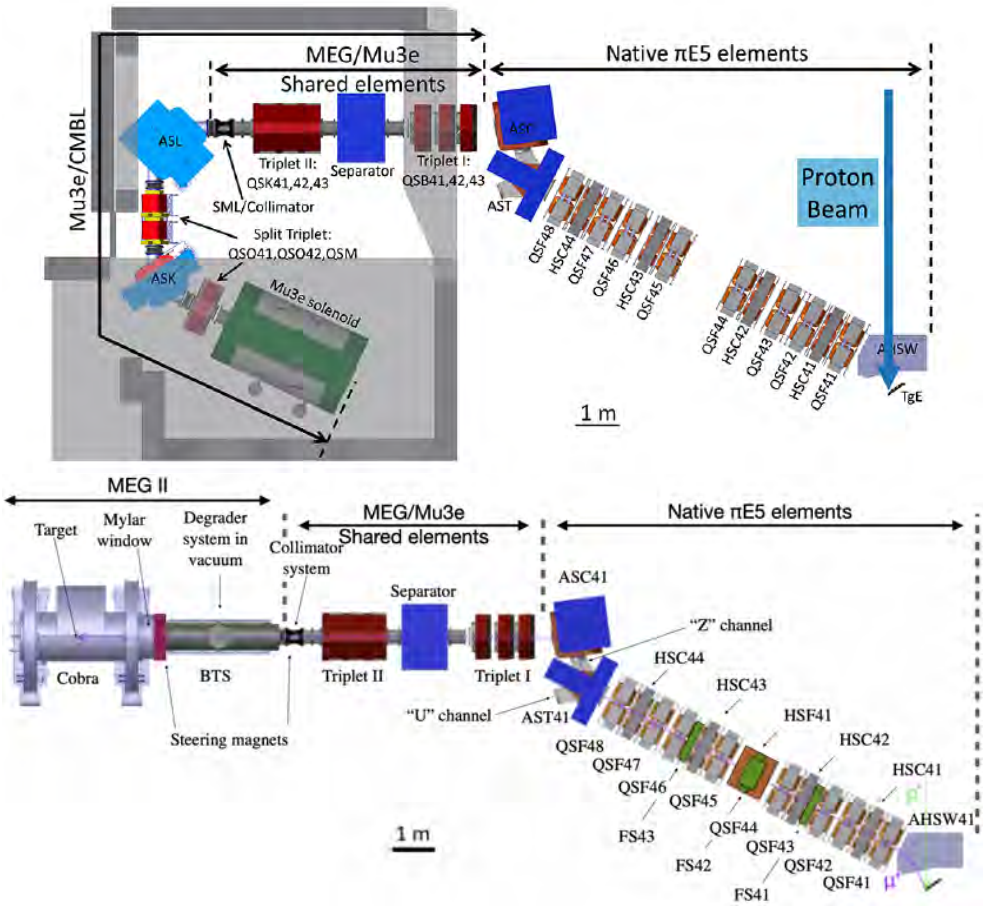

Figure 3.5: *Top:πE5 layout in the Compact Muon BeamLine configuration from [4]. Bottom: πE5 layout in the MEG II configuration adapted from [2].* As reported above, the section up to the collimator is shared by MEG II and Mu3e. In CMBL configuration the front part of the area hosting Mu3e is separated by the rear part of the area hosting MEG II by a concrete wall positioned close to the ASL41 dipole.

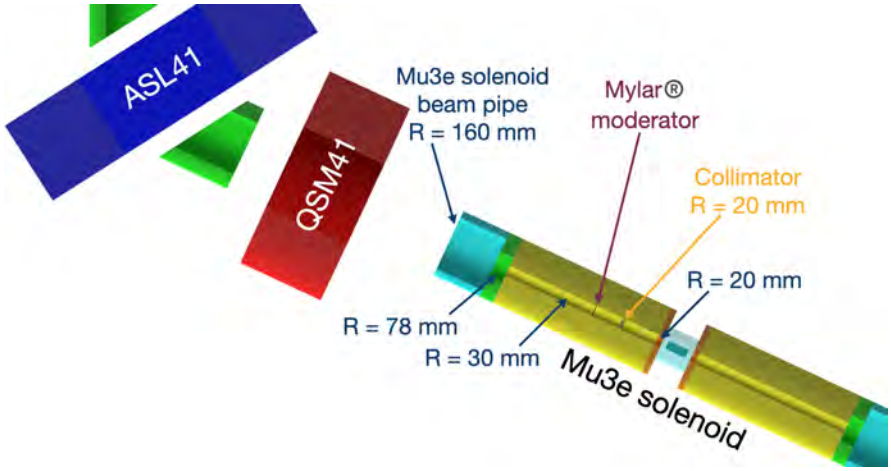

Figure 3.6: *G4bl model of the beam pipe inside the Mu3e solenoid. Right at the entrance of the magnet the radius of the beam pipe is* 320 mm.

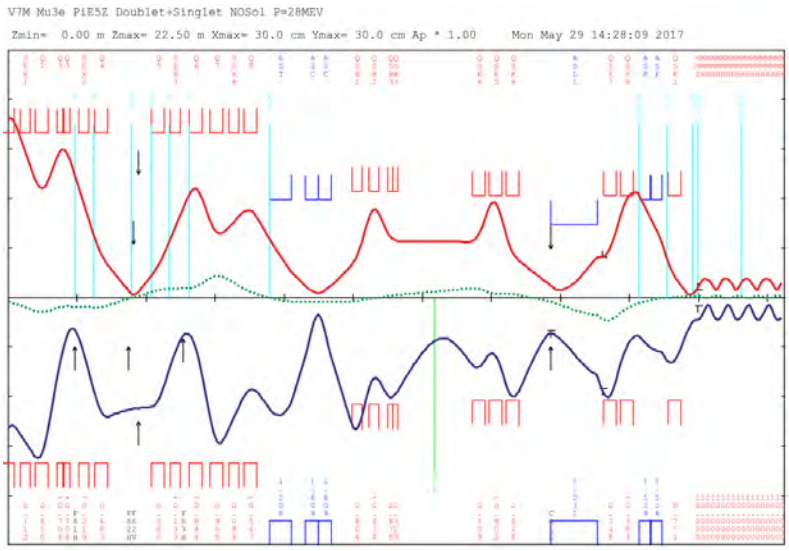

Figure 3.7: *First order envelope of the surface muon beam along the πE5 beamline in the Mu3e configuration using the CMBL [5]. Top: vertical envelope. Bottom: horizontal envelope. The dashed green line represents the dispersion along the beamline in case of a momentum higher than nominal by* 1 %.

3.1.2 The MEG II beamline

When the πE5 area is configured for the MEG II experiment (see Figure 3.5), Triplet II couples the beam into the Beam Transport Solenoid (BTS). There, a Mylar® moderator of 300 µm thickness is placed in a focus to minimise the effect of multiple scattering (see Figure 3.8). In fact, the multiple scattering on the moderator causes an increase in the divergence of the beam. In a focus, the beam spot is minimised at the expense of a higher divergence. A parallel beam instead has a minimal divergence at the expense of the size of the envelope. In both situation the contribution of multiple scattering will increase the divergence by the same amount, meaning that the relative change in divergence is smaller in a focus.

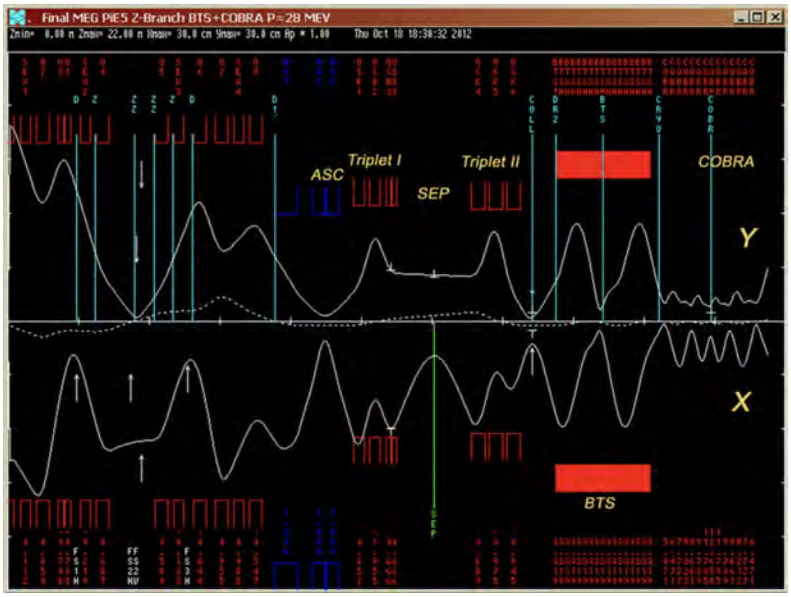

Figure 3.8: *Second order envelope of the surface muon beam along the πE5 beamline in the MEG II configuration computed with TRANSPORT from [31]. Top: vertical envelope. Bottom: horizontal envelope. The dashed line represents the dispersion along the beamline in case of a momentum higher than nominal by* 1 %

A 190 µm Mylar® window separates the vacuum in the beamline from the helium atmosphere inside the COnstant Bending RAdius (COBRA) magnet that delivers the beam to the MEG target. The field shape of the COBRA magnet is optimized to reduce the dependence of the bending radius on the emission angle of charged particles coming from the center of the experiment (see Chapter 1).

A further difference with respect to the Mu3e configuration lays in the position of the collimator after Triplet II: in MEG II configuration the collimator

is moved 200 mm upstream to accommodate the Scintillating Fibers (SciFi) detector. The SciFi detector is a beam monitor based on plastic scintillating fibers that can be inserted on demand in the beamline during data taking periods to measure beam parameters. It is part of the vacuum of the beamline and is moved with a motor system. Further details are provided later in this section.

3.2 CMBL 2022 commissioning

The commissioning of the CMBL started in 2014. The results of the campaigns carried out until 2018 can be found in [5] and in [6].
The commissioning of the CMBL relevant for this thesis has been performed during three beam time periods in 2021 (4 weeks), 2022 (3 weeks) and 2023 (3 weeks). In 2021 the CMBL was fully assembled, including for the first time the Mu3e solenoid: the main aim of the beam campaign was to tune the beamline to deliver the muon beam to a minimal version of the final detectors including some modules of the inner tracker and of the SciFi detector during the so-called *pre-engineering* run. The results of the beam tuning campaign will be shown later in this section.

Here the focus is put on the commissioning performed in 2022, during which the requirements in the Technical Design Report of Mu3e [4] were met and surpassed.

The 2023 campaign was needed in order to study the position of the moderator and the collimator inside the Mu3e solenoid and to study the impact of the HSC42 sextupole, that was not operational in 2022. The results of the 2023 campaign are summarized in Section 3.4.

The basic strategy during the different beam campaigns is the same: a first tuning of the beamline is performed right after the collimator downstream of Triplet II; the second measuring point is between QSM41 and the Mu3e solenoid, with the latter switched off; the final tuning is performed at the center of the Mu3e solenoid. Further details on the set-ups and detectors employed are reported in the following.

3.2.1 πE5 conditions in 2022

During the 2022 campaign three main conditions are worth to be mentioned:

- at the beginning of the beam campaign the amplifier of Resonator 4 of the INJ2 cyclotron broke. After repairing the proton beam current was kept at 1860 µA as opposed to the usual operation at 1950 µA. This did not affect the campaign as we usually quote the rates normalised to the proton current at a reference value, here 2.2 mA, and the muon rates scale linearly with the proton current;

- during the first week of commissioning the HSC42 sextupole was disconnected from power because of a water leak in the cooling circuit: as the cooling system was not properly working the magnet would heat up. The HSC42 magnet is included in the biological shielding and therefore any maintenance operation requires a few days simply to remove the concrete shielding. It was therefore decided to run the πE5 beamline without HSC42. A posteriori this was found to not affect the CMBL commissioning too much, but this was indeed affecting the optics of the MEG beamline (see Section 3.3).
- the power supply of the QSF43 was found to be malfunctioning, causing additional delays in the commissioning.

3.2.2 Beam commissioning set-up

The main aim of the beam commissioning of the CMBL was to maximise the transmission of the surface muon beam. In order to do so we employed two detectors:

- The Pill detector (see Figure 3.9a): a NE102 scintillator coupled to a small-sized PMT. This detector has a 2 mm diameter and is 2 mm thick. Particle ID is performed through energy deposition and this detector features the best separation between muons and positrons among our tools. As a photomultiplier is used to detect scintillation light the Pill can not be used to scan particle beams in an intense magnetic field.
- The Avalanche PhotoDiode (APD) detector (see Figure 3.9b): the particle detection is provided by a photodiode in proportional mode. Particle ID is performed in this case as well through energy deposition, but the initial separation deteriorated over time due to radiation exposure. This detector is used in high magnetic field conditions, such as beam scans at COBRA center or at the Mu3e solenoid center.

For measurements at the collimator, at QSM41 and at COBRA center, both types of detectors are mounted on a robotic arm controlled via LabView [32], able to move in the two transverse directions. For measurements at the focus of the Mu3e center a new moving stage has been built in 2021 and improved in 2022 based on piezoelectric motors, exploitable in high magnetic field, and controlled with a MIDAS [33–35] front-end. Further details will be provided in Section 3.2.5. A laser is used for aligning the detectors on the beamline centerline thanks to markers placed in the experimental area.

The signals from the PMT and the APD are processed with standard NIM modules. The signal is amplified and split to apply two different thresholds to discriminate muons and positrons: a *high threshold*, muons, and a *low threshold*, positrons + muons. The discriminated outputs are NIM pulses sent to a DRS4 evaluation board [36].

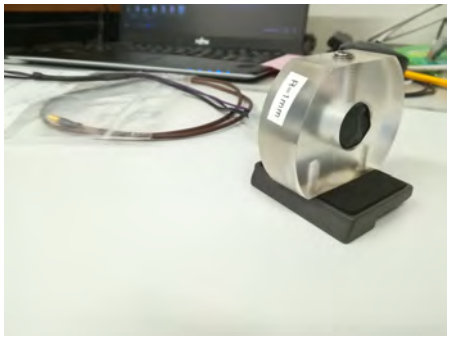

(a) Pill detector

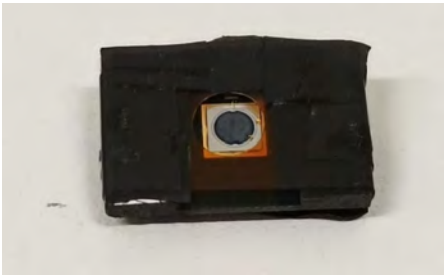

(b) APD detector

Figure 3.9: *Left: Pill detector. The PMT is held by a plexiglass housing, while the NE102 is glued on its front. The detector is covered with Tedlar® (polyvinyl fluoride) foil to make it light tight. Right: APD. The detector is covered in Tedlar® to make it light tight.*

Figure 3.10 shows the separation between muons and positrons as measured with the two detectors.

(a) Pill detector

(b) APD detector

Figure 3.10: *Separation in pulse height between muons and positrons as measured with the two detectors.*

The DRS4 evaluation board receives two further inputs: the *RF-signal* of the proton accelerator and the *proton current*. The former is used as a reference for time-of-flight (TOF) measurements: we define it as the time difference between the discriminated signals from the detectors and the next RF rising, or falling, edge. These measurements result in the TOF modulo the RF-period, which is 19.76 ns. This quantity can be used to distinguish lowly relativistic particles (muons and pions) from the ultrarelativistic electrons. At the surface muon momentum, the TOF measurement can also be used to discriminate the positron background generated at target through π^0 decay and pair creation on a much shorter time scale than the RF-signal period,

while surface muons have a continuous time structure as the charged pion life time is ∼26 ns. At 28 MeV/c the pion contribution is negligible. Lastly, positrons coming from muon and charged pion decays contribute to the continuous contribution of the TOF spectrum as well.

Figure 3.11 shows the TOF distributions as measured at MEG collimator at 28 MeV/c for SEP41 off and on tuned on muons and positrons. A continuous component with a width of ∼20 ns is clearly distinguishable. The tails of the distributions are both due to the finite resolution of the apparatus and to the time walk of the DRS4 evaluation board, which measures the time the signals exceed the threshold and not the time to reach a fraction of their maximum. The measurement shown here is used as an input to benchmark the G4beamline [37] model of the High Intensity Muon Beams beamlines in Appendix H.

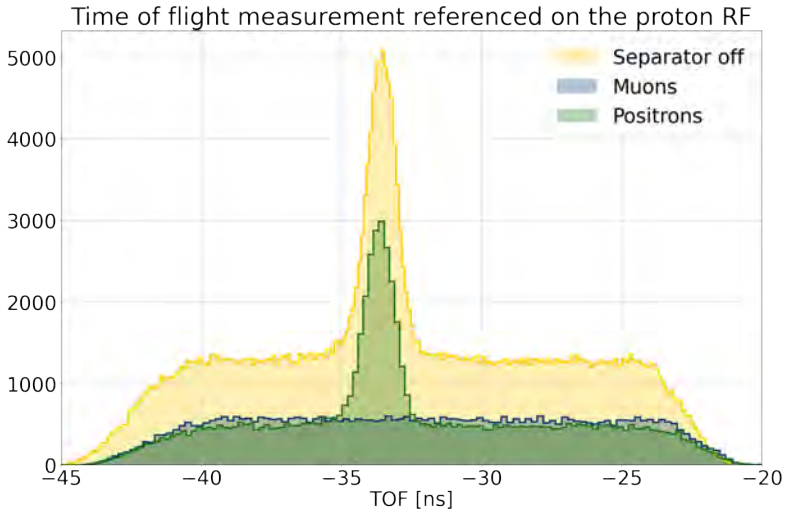

Figure 3.11: *Time of flight spectrum measured at collimator for different separator settings: off (yellow), muons (blue) and positrons (green). The TOF is defined as the difference between the discriminated Pill signals and the RF-signal. The scale does not represent the delivered rates. The tails of the distributions are due to the finite resolution of the apparatus and to the time walk of the DRS4 evaluation board, which measures the time the signals exceed the threshold and not the time to reach a fraction of their maximum.*

The beamline is tuned by keeping the detector fixed on the centerline axis and by iteratively scanning the beamline elements with OPTIMA; a program to automatically acquire the muon rate while scanning the currents of the elements within a given range.

After a few tuning iterations, the beam profile is measured through the so-called *Cross-scan*: the beam is scanned with a cross-like movement on the two transverse axes. The scan is performed twice: a first time with broader

steps to find the maximum of the beam distribution; a second time performing the cross-scan on the two axis passing through the beam maximum. The integrated rate is obtained assuming a non-correlated beam profile.

Once the tuning is finished we perform a *Raster-scan*: full point by point 2D scan of the beam profile. This measurement is the most accurate in evaluating the integrated beam rate, but it is rather long to perform as opposed to the Cross-scan.

The following convention is applied when changing the dipole currents along the beamline:

- if the current is reduced in absolute value, no particular action is taken;
- if the current would end up being higher in absolute value than the starting point, the dipole is first ramped to the closest absolute maximum (-130 A for example in the case of negative currents) and then changed to the wanted value.

This way, the dipoles undergo always the same hysteresis cycle. At the beginning of the commissioning, or if the hysteresis cycle is not correctly followed, the dipoles are cycled. The cycling is a procedure that consists in ramping the dipoles from -130 A to 130 A and back to -130 A three times in order to reset the hysteresis cycle.
Such an operation is not needed for quadrupoles.

3.2.3 Collimator focus

We started by tuning the beamline to obtain the maximum transmission to the collimator. Figure 3.12 shows a picture of the set-up at the collimator. To perform the measurement it is necessary to close the vacuum in the beamline and let the beam exit into air. This is done through a 190 µm Mylar® window.

As stated above, the beamline was fully assembled including the Mu3e magnet for the first time in 2021 and a first tune for it was found, but the transmission was limited compared to the expected performances [4], most likely because of non optimal transmission through the AST41-ASC41 double bend. In fact there is not a unique current setting to let the beam pass through AST41 and ASC41.
We therefore decided to start from the tune used at collimator for MEG II in 2019. Table 3.1 shows a comparison of the optimized setting as obtained in 2019, 2021 and 2022 together with the associated rate. The highlighted rows show the most relevant changes applied in 2022. An additional difference regards the meson production target, that was the standard straight TgE during the MEG II beamtime in 2019 and that was replaced with its slanted

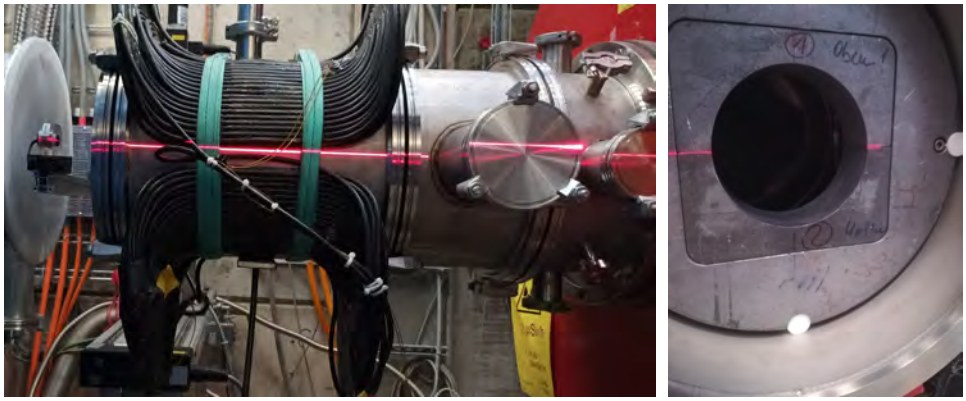

Figure 3.12: *Left: side view of the Pill set-up at the collimator in πE5. The last aluminum ring attached through the clamps in the figure is the support for the Mylar® window. Right: a view of the collimator inside its flange. The inner collimator has a* 130 mm *diameter and is enclosed in a* 160 mm *square housing.*

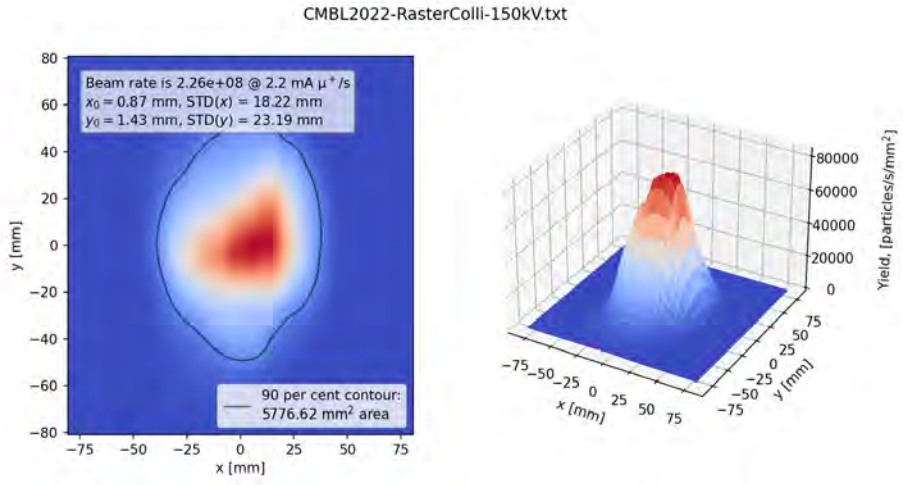

Figure 3.13: *Raster-scan at collimator. The currents are set to the optimum found at the end of the beam tuning.*

version TgE* right after. Since then, the slanted target has been used for all the beam campaigns. Further details are provided in Section 1.5.2.

Figure 3.13 shows the final raster-scan performed with the optimized currents on a 160 mm×160 mm grid with a spacing of 5 mm. The rate is obtained interpolating the data with bi-dimensional cubic splines with the *RectBivariateSpline* class from *scipy.interpolate* [38], finding 2.26×10^8 μ^+/s at a proton beam current of 2.2 mA. The rate is higher than measured in 2021 by 16 %, meaning that the transmission through the double bend AST41-ASC41 has been improved. The 20 % increase in rate with respect to the result obtained in 2019 is compatible with the upgrade of the meson pro-

Beamline element	Excitation currents [A]		
	2019	2021	2022
AHSW41	97.50	97.50	97.50
QSF41	-93.0	-93.3	-93.0
HSC41	-19.1	-19.1	-16.0
QSF42	84.00	82.6	82.3
QSF43	-65.0	-64.5	-64.5
HSC42	-29.9	-29.9	0.0
QSF44	82.0	81.8	82.0
QSF45	86.0	85.0	83.0
HSC43	45.0	45.0	40.0
QSF46	-81.5	-82.7	-82.8
QSF47	94.6	95.1	95.6
HSC44	-10.0	-10.0	-10.5
QSF48	-51.5	-50.6	-50.7
AST41	-97.4	-97.4	-97.4
ASC41	113.8	119.0	116.3
SSL41	-2.0	-5.2	-3.0
QSB41	37.8	39.0	39.0
QSB42	-48.0	-47.8	-47.8
QSB43	15.0	15.0	15.0
SEP41	-91	-92.8	-89.0
QSK41	18.2	15.0	14.0
QSK42	-40.7	-39.4	-39.5
QSK43	34.8	39.8	34.8
SML41	-10	0.0	0.0
Beam rate at collimator at 2.2 mA[μ^+/s]	1.89×10^8	1.94×10^8	2.26×10^8

Table 3.1: Beam tuning results at collimator for 2019, 2021 and 2022 beam campaign. The rows highlighted in blue show the most relevant changes applied in 2022.

duction target from TgE to TgE* (see Section 1.5.2).

By varying the current powering the dipole in SEP41 at fixed electric field it is possible to check on the separation between the muon and the positron beams. Figure 3.14 shows a net separation between the two beams on the interface of the program used for tuning, OPTIMA. The plates of SEP41 were biased with $\pm$ 180 kV.

The transported phase space was measured by performing a quadrupole scan: this is a standard technique based on measuring the beam profile for different quadrupole strengths, based on the assumption that the beam is

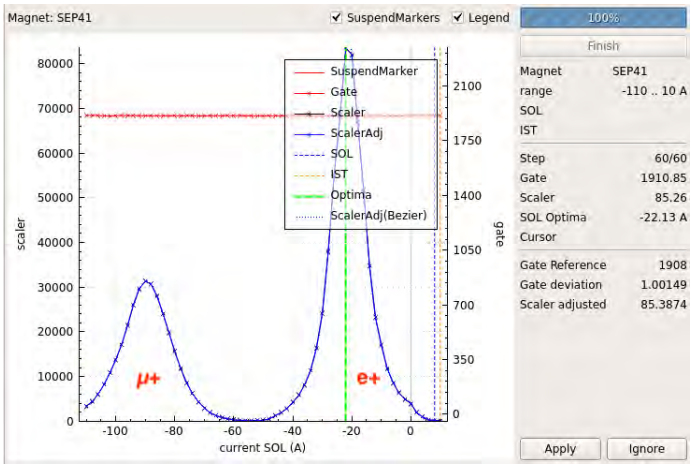

Figure 3.14: *Scan of the current exciting the dipole in SEP41 in the OPTIMA interface. The plates of SEP41 were constantly biased with a* $\pm$ 180 kV *voltage.*

gaussian. In fact, for a gaussian beam, the phase space can be represented with the 4D covariance matrix of the transverse coordinates. As an example, Equation 3.2 shows the sector linked to the horizontal phase space only:

$$\Sigma_x = \begin{bmatrix} \sigma_x^2 & \sigma_{x,x'} \\ \sigma_{x,x'} & \sigma_{x'}^2 \end{bmatrix} \tag{3.2}$$

As shown in Section 2.3, the sigma matrix Σ_x can be then evaluated at any point along the beamline by applying the transport matrix as shown in Equation 3.3:

$$\Sigma(s) = M(s_0|s)\Sigma(s_0)M(s_0|s)^T \tag{3.3}$$

As normal quadrupoles cannot couple horizontal and vertical motion, they can be studied independently. The 2D transport matrix for a thick quadrupole is:

$$M(s_0|s) = \begin{bmatrix} \cos\left(\sqrt{k}\ell_q\right) & \frac{\sin\left(\sqrt{k}\ell_q\right)}{\sqrt{k}} \\ -\sqrt{k}\sin\left(\sqrt{k}\ell_q\right) & \cos\left(\sqrt{k}\ell_q\right) \end{bmatrix} \quad \text{, for k} > 0 \tag{3.4}$$

$$M(s_0|s) = \begin{bmatrix} \cosh\left(\sqrt{|k|}\ell_q\right) & \frac{\sinh\left(\sqrt{|k|}\ell_q\right)}{\sqrt{|k|}} \\ \sqrt{|k|}\sinh\left(\sqrt{|k|}\ell_q\right) & \cosh\left(\sqrt{|k|}\ell_q\right) \end{bmatrix} \quad \text{, for k} < 0 \tag{3.5}$$

with k the quadrupole strength and ℓ_q the effective length of the quadrupole. Both depend on the magnet design and the first one is proportional to the excitation current. The only observables of the covariance matrix are the variances in the horizontal and transverse direction and they depend on the

full covariance matrix at the reconstruction point s_0. The sigma matrix has only three independent variables, and the problem can be fully constrained with three measurements. A common practice is to fit the dependence of σ_x and σ_y on the quadrupole strengths.

We set s_0 as the position of the Pill detector in the optimal transmission settings shown in Table 3.1. This is analogous to backpropagating the beam through the drift from the Pill to QSK43 and through QSK43 excited with 34.8 A to then transport it again through QSK43 and the drift with varying quadrupole strengths. Equation 3.6 shows the corresponding transport matrix:

$$M(s_0|s) = M_{\text{drift}}(s_1|s)M_{\text{QSK43}}(s_2|s_1)M^{-1}_{\text{QSK43,opt}}(s_1|s_2)M^{-1}_{\text{drift}}(s_1|s_0) \quad (3.6)$$

where M_{drift} is propagating the beam from the downstream face of QSK43 to the Pill position and M_{QSK43} propagates the beam through QSK43. The notation used is analogous to that used in Figure 3.15.

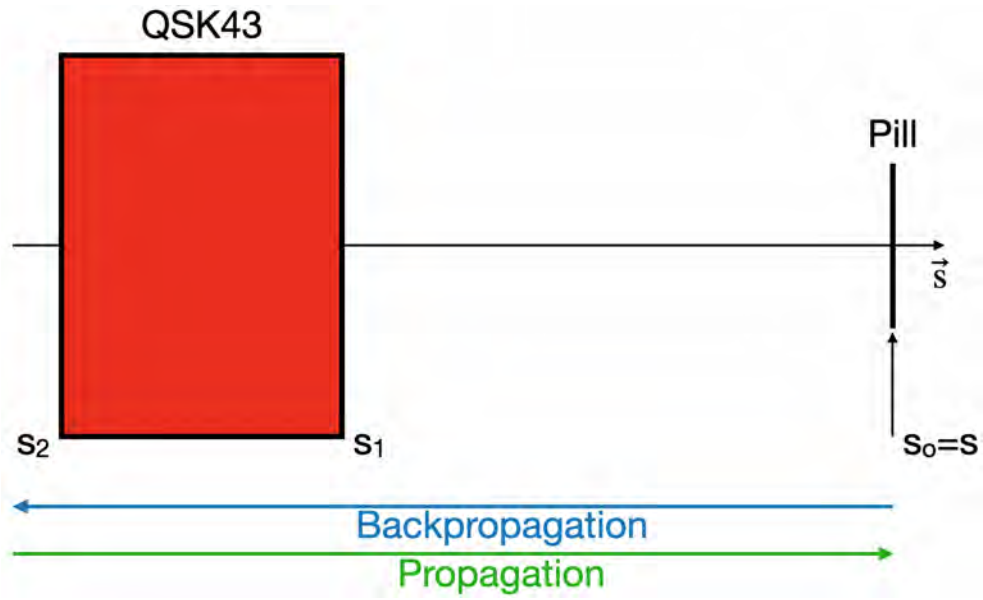

Figure 3.15: *Cartoon of the beamline corresponding to Equation 3.6. The inverse matrices correspond to backpropagating the beam (blue arrow).*

Figure 3.16 shows the quadrupole scan performed with QSK43 together with the reconstructed phase space. The points shown are the standard deviations in the two transverse directions obtained through cross-scans.

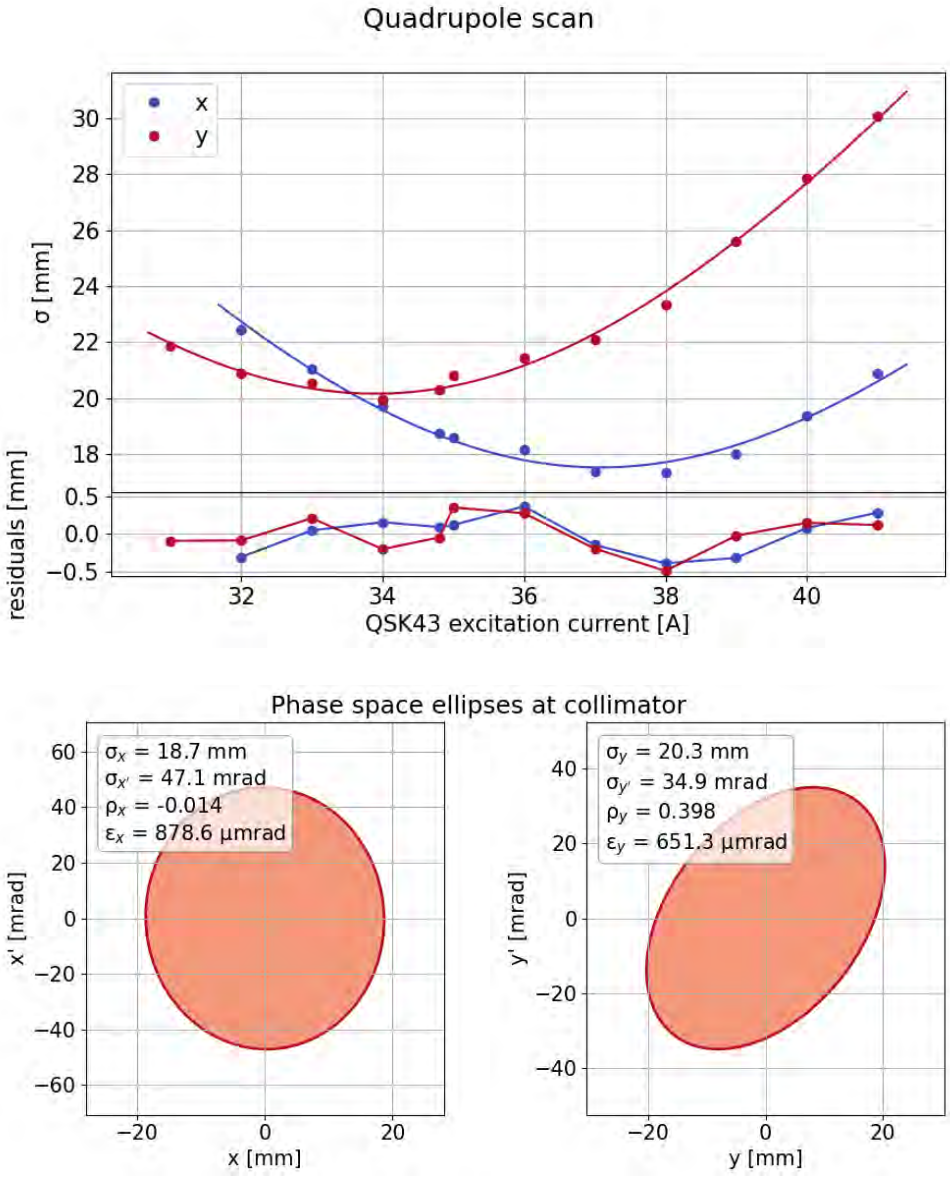

Figure 3.16: *Top: quadrupole scan. The markers show the measured standard deviation in the horizontal (blue) and vertical (red) directions. The solid lines are the best least square fit to the data points. Bottom: phase space ellipses as reconstructed at the collimator.*

3.2.4 QSM41 focus

After completing the tuning at collimator we moved downstream to the QSM41 quadrupole. Figure 3.17 shows a picture of the set-up. At this stage the Mu3e magnet is already in position but not powered. The presence of two bends between the previous measurement point and this one requires a different approach to tuning the dipoles: we decided to first tune the dipoles while switching of the QSK triplet, SML41 and QSO doublet and powering QSM41 with 210 A. This approach allows to propagate the beam through ASL41 and ASK41 without deviations induced from the focusing of the quadrupole tuplet. QSM41 is powered to focus the beam in the horizontal direction at the Pill position, otherwise the beam would be too wide to perform a meaningful tuning.

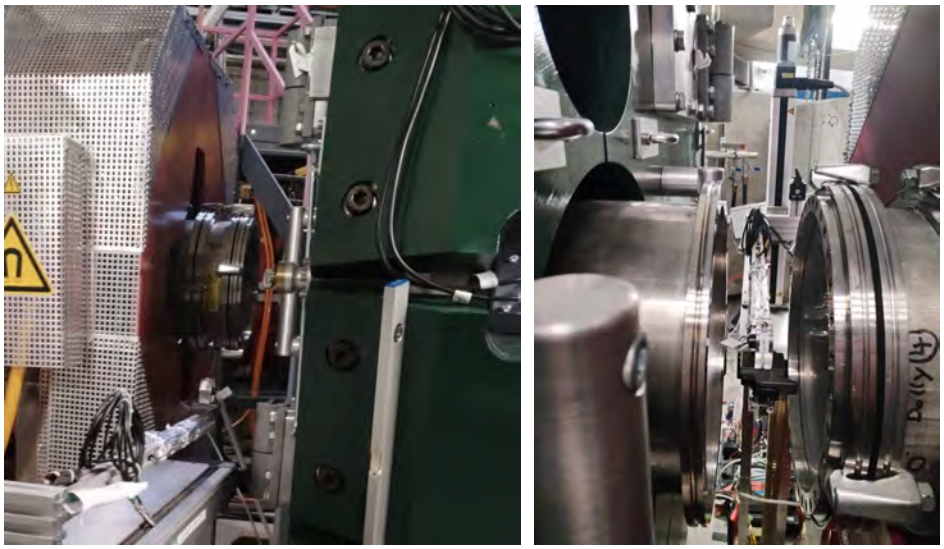

(a) Rear view of the Pill in parking position **(b)** Front view of the Pill on the centerline

Figure 3.17: *Views of the Pill detector between QSM41 and the Mu3e spectrometer.*

Then, the settings for ASC41, ASL41 and AST41 were fixed and the rest of the beamline tuned again. In this condition a rate of $1.43 \times 10^8\,\mu^+/\mathrm{s}$ was found.

We then removed the inner part of the collimator, leaving only the 160 mm aperture in the housing in position, leading to an increase in rate by 16 %. This was done because, due to the long drift between QSK43 and QSO41, after tuning at QSM41, the focus was shifted from the collimator to the center of ASL41 to maximize transmission, resulting in an increased beam size at the collimator. The rate increase confirms that the inner part of the collimator limits the transmission. No significant positron contamination was

observed, meaning that separation is still sufficient with the bigger opening. The result is shown in Figure 3.18. Because the beam is wider in the vertical direction than the grid set for the raster-scan, the outer part was extrapolated assuming gaussian tails and included in the rate estimate, finding $1.66 \times 10^8\,\mu^+/\mathrm{s}$. Compared to the rate of $1.10 \times 10^8\,\mu^+/\mathrm{s}$ obtained in 2021, the transmission from the collimator to QSM41 has improved from 57 % to 73 %, and the overall rate has improved by 51 %. Table 3.2 shows the comparison between the currents used in 2021 and in 2022 for the QSM focus.

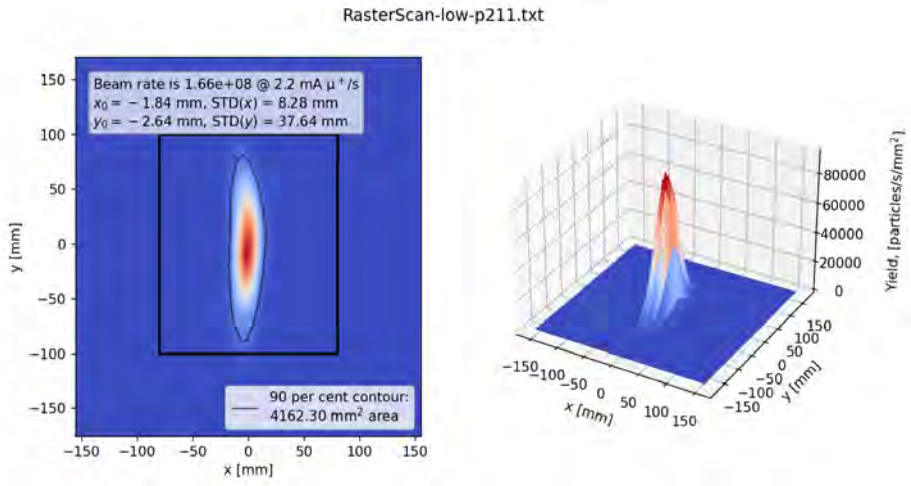

Figure 3.18: *Raster-scan at QSM41. The currents are set to the optimum found at the end of the beam tuning. The black square on the left shows the region where the scan was performed, while outside of it the tails are estimated with a gaussian tail.*

The quadrupole scan measurement was performed at QSM41 as well and is shown in Figure 3.19. While in Figure 3.16 the beam is focused in both the horizontal and in the vertical directions, here the beam is focused in the horizontal direction only, while in the vertical direction the beam is diverging. Additionally, a high divergence is observed in the horizontal direction as opposed to the vertical. Intuitively, the former point is due to the distance between QSM41 and QSO42, which is the element focusing in the vertical direction. The latter point instead is due to the short distance between QSM41 and the Pill detector. This behaviour is expected and can be observed also in the design TRANSPORT envelope in Figure 3.7.

	Excitation currents [A]	
Beamline element	2021	2022
ASC41	119.0	113.8
SEP41	-74	-88.0
QSK41	19	15.0
QSK42	-41.8	-34.0
QSK43	30.5	28.0
SML41	0.0	0.0
ASL41	75.0	74.7
QSO41	45.5	52.0
QSO42	-15.7	-23.0
ASK41	-92.8	-92.0
QSM41	170	210
Beam rate at QSM at 2.2 mA $[\mu^+/s]$	1.10×10^8	1.66×10^8

Table 3.2: Beam tuning results at QSM for 2021 and 2022 beam campaign. The rows highlighted in blue show the most relevant changes applied in 2022.

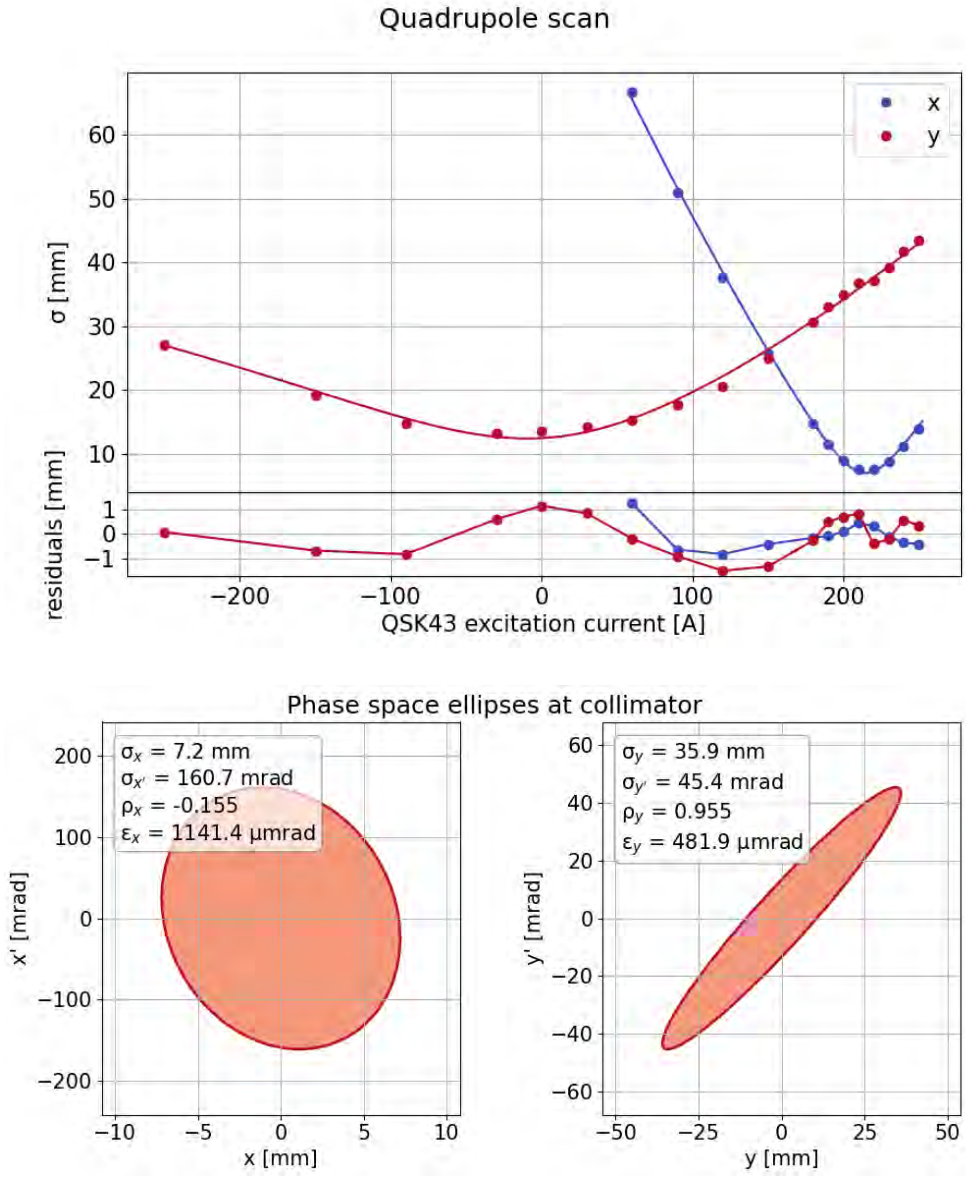

Figure 3.19: *Top: quadrupole scan. The markers show the measured standard deviation in the horizontal (blue) and vertical (red) directions. The solid lines are the best least square fit to the data points. Bottom: phase space ellipses as reconstructed at the QSM41.*

3.2.5 Mu3e focus

As reported above, the beamline inside the Mu3e magnet shrinks in diameter while approaching the target location. For the commissioning, a wider beam pipe with a diameter of 160 mm is used, to characterize the beam in full transmission conditions. At the end of the beam pipe, a 100 µm Mylar® window with a 100 mm aperture is used to separate the vacuum from the air in the spectrometer. An insert with a diameter of 60 mm is used to match the running conditions of Mu3e. Figure 3.20 shows a sketch of the beam pipe and of the insert used for the commissioning.

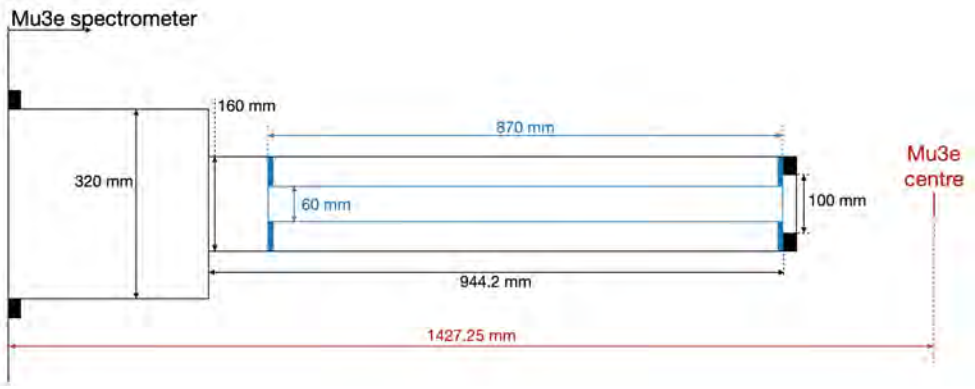

Figure 3.20: *Sketch of the beam pipe and of the insert used for the commissioning at Mu3e center. The beam pipe has a diameter of* 160 mm *and an exit window with a diameter of* 100 mm. *The insert has a diameter of* 60 mm.

We first started without the insert. The solenoid was powered to the Mu3e design value of 1 T. In such a high magnetic field environment the APD detector is needed, but the conventional stages used for beam tuning in πE5 cannot be used as they would not fit in the available space. For this reason a new stage based on two piezoelectric motors was developed in 2021 [7]. A front-end based on MIDAS was developed for the 2022 beamtime allowing for an online display of the ongoing scan. Both raster-scan and cross-scan are implemented. Figure 3.21 shows a picture of the stage and Figure 3.22 shows a screenshot of the MIDAS interface.

The focus in this configuration is shown Figure 3.23. This set-up is limited in movement by the length of the piezomotor axis and it is not possible to cover the full beam spot with a scan. The black rectangle shows the limits of the scan region. Any point outside of it is obtained with an extrapolation assuming a gaussian tail. The measured rate is $1.50 \times 10^8\,\mu^+/\mathrm{s}$, meaning that almost the full beam is transmitted through the beam pipe in this configuration.

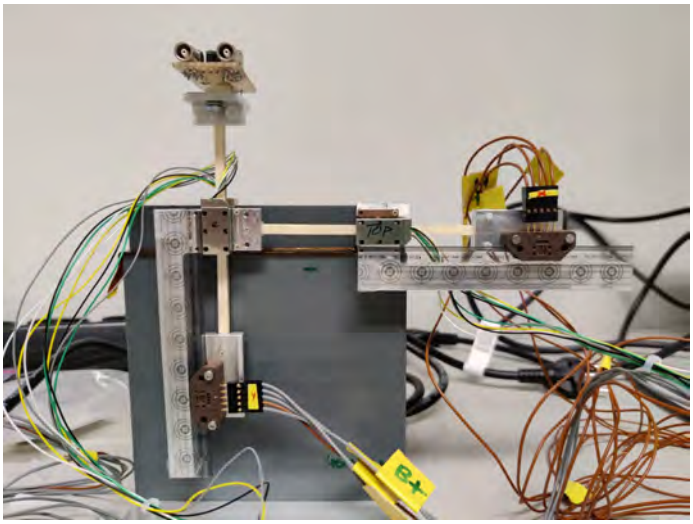

Figure 3.21: *Moving stage for the APD detector in high magnetic field environment. The stage is moved by piezoelectric motors and the position is determined with optical encoders.*

Subsequently, the tuning was repeated by including the insert in the beam pipe: the aperture is now reduced to 60 mm in diameter (Figure 3.24). The rate is now reduced to $9.46 \times 10^7\,\mu^+/\mathrm{s}$ and the size of the beam spot is reduced in size as well from $\mathrm{STD}(x) = 11.4\,\mathrm{mm}$ and $\mathrm{STD}(y) = 9.36\,\mathrm{mm}$ to $\mathrm{STD}(x) = 9.27\,\mathrm{mm}$ and $\mathrm{STD}(y) = 8.60\,\mathrm{mm}$.

In the final configuration, the vacuum window closing the Mu3e beam pipe has 40 mm of diameter which has been added to the insert to find the focus on the Mu3e target. At this stage, nor the moderator nor the collimator were present. The beam spot is shown in Figure 3.25. The rate is further reduced to $6.89 \times 10^7\,\mu^+/\mathrm{s}$. Compared to the rate of $4.40 \times 10^7\,\mu^+/\mathrm{s}$ achieved in 2021, the transmission from QSM41 to the center of Mu3e is compatible, but thanks to the improvements in transmission in the upstream section we now meet the design value quoted in the TDR [4]. Table 3.3 shows the comparison between the currents used in 2021 and in 2022 for the Mu3e focus.

The main limitation to the rate that can be delivered at the experiment is the size of the beam pipe, that needs to fit the available space in the detector. From the measurements reported above, the beam is collimated at the vacuum window reducing the rate by 27 %. We investigated the possibility to tune the field of the spectrometer itself to further increase transmission. We performed a cross-scan for different values of the magnetic field in the solenoid while keeping the other elements at the same settings. Figure 3.26 shows the total rates, therefore integrated on the full beam spot, and the rate within the radius of the Mu3e target (19 mm) as a function of the magnetic

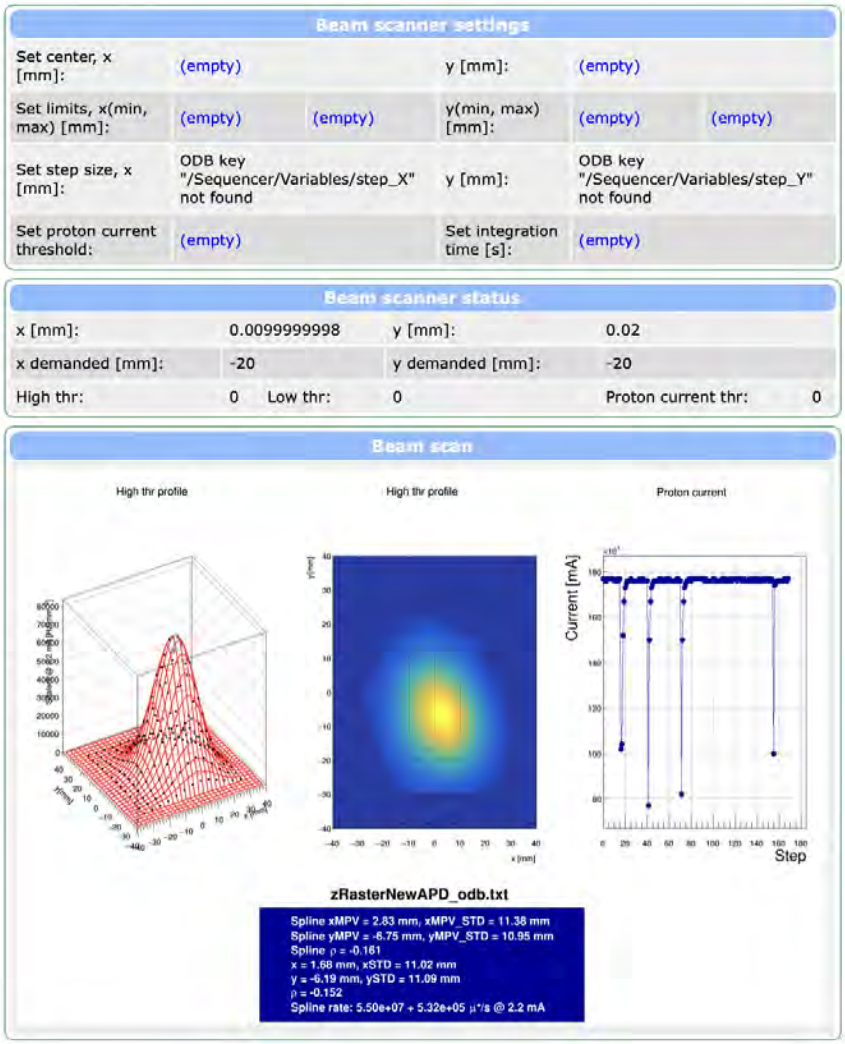

Figure 3.22: *MIDAS front-end interface to take a scan. The plot shown is updated online with the latest measured point.*

field. Each cross-scan was interpolated within the boundary of the scans with the CubicSpline class from the python3 package *scipy.optimize* [38] and extrapolated with gaussian tails outside of it. The single measurements are reported in Appendix A.

Two concurrent effects are introduced by varying the magnet field generated by the spectrometer:

- the envelope is reduced in size with increasing field
- the distance between two consecutive foci decreases with increasing field (dominating effect)

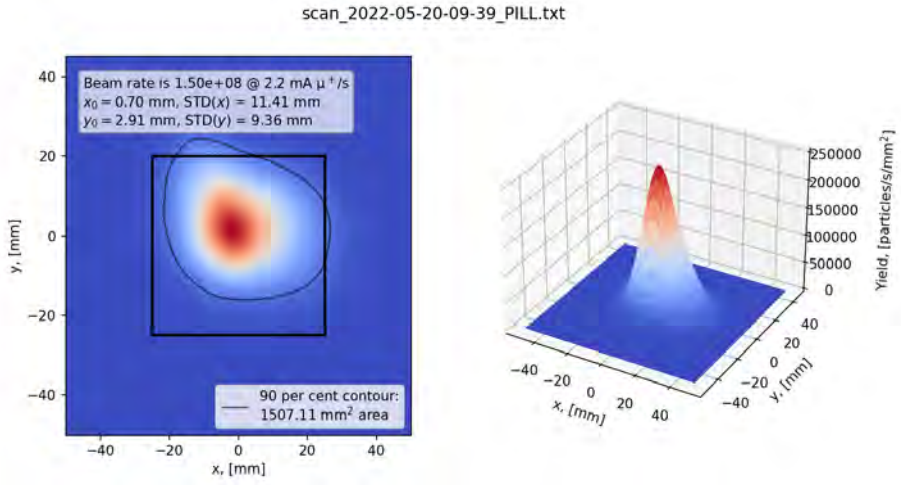

Figure 3.23: *Raster-scan at Mu3e center without beam pipe insert: the inner-most aperture of the beam pipe is* 160 mm *and the aperture of the exit window is* 100 mm.

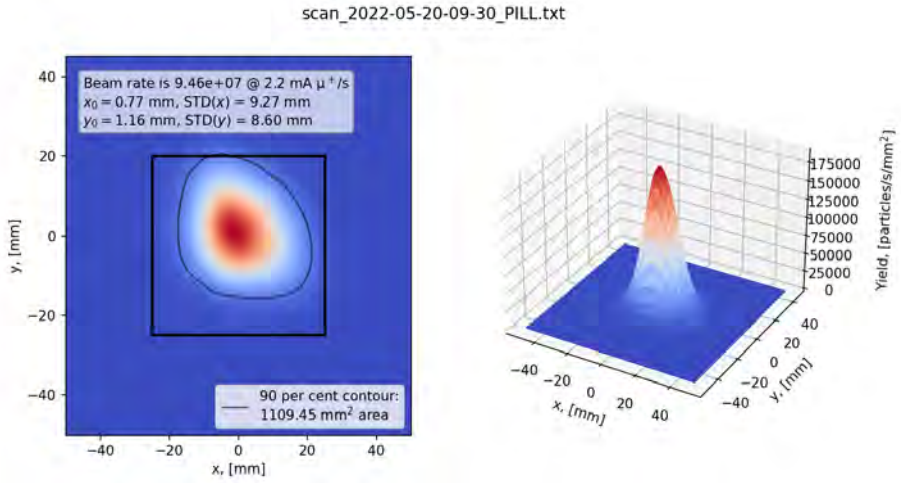

Figure 3.24: *Raster-scan at Mu3e center including the beam pipe insert: the inner-most aperture of the beam pipe is* 60 mm.

The first effect alone would cause a steady increase in rate with higher magnetic fields. The second effect alone would maximise or minimize the transmission through the vacuum window, where the aperture along the beam line is the smallest. The two effects affect differently the rate over the full beam spot and the rate on the target surface. Figure 3.27 shows the transmission at the center of Mu3e for different magnetic fields simulated with G4beamline [37], a toolkit based on Geant4 [39–41] for single particle tracking in electromagnetic fields. The simulation was set up by Felix Berg in the context of [5]. The phase space used as an input is obtained later in

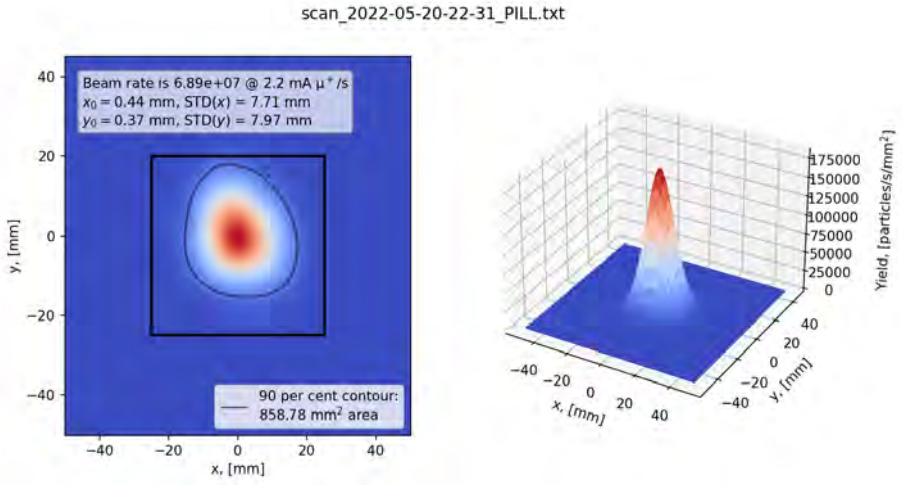

Figure 3.25: *Raster-scan at Mu3e center including the beam pipe insert: the inner-most aperture of the beam pipe is* 60 mm. *The* 40 mm *aperture of the design vacuum window is included as well.*

	Excitation currents [A]	
Beamline element	2021	2022
QSK41	19	4.8
QSK42	-41.8	-31.6
QSK43	30.5	28.8
SML41	-15	-14
ASL41	75.0	74.0
QSO41	47	53.5
QSO42	-8.0	-15.0
ASK41	-93.3	-92.0
QSM41	87.5	120
Beam rate at QSM at 2.2 mA[μ^+/s]	4.40×10^7	6.89×10^7

Table 3.3: Beam tuning results at Mu3e center, with beam pipe inserts, for 2021 and 2022 beam campaign. The rows highlighted in blue show the most relevant changes applied in 2022.

Section 3.3, but here it is used by way of example only.

As stated above, the dominant effect on the transmission is the shift of the foci along the beamline: in Figure 3.27a the first two foci are moved downstream w.r.t. to the corresponding ones in Figure 3.27b, and the third focus is barely visible because of the strong reduction in transmission at the vacuum window, where the beam is bigger than in Figure 3.27b. In Figure 3.27c the focus is moved upstream and the transmission is increased,

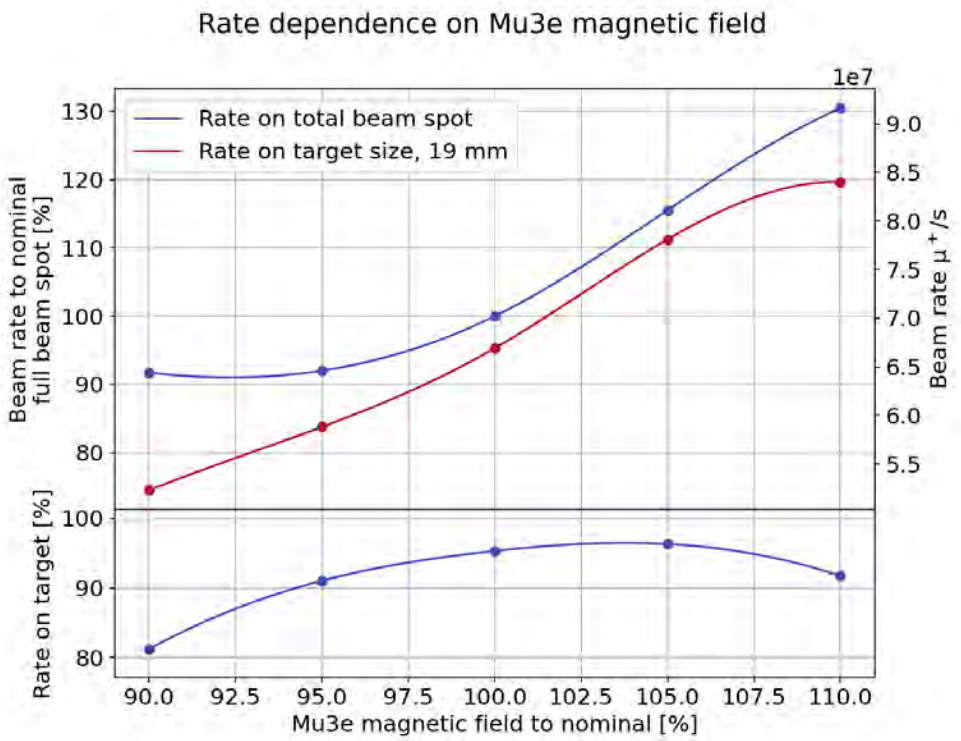

Figure 3.26: *Top: the rate estimated by integrating over the total beam spot (blue) and within the surface of the Mu3e target (red) at Mu3e center as a function of the magnetic field. Bottom: fraction of beam within the area of the Mu3e target. The points represent the measurements. The solid lines are their interpolation with cubic splines.*

but the beamspot at target is larger and is not contained within the surface of the target anymore.

Based on the results shown in Figure 3.26, we decided to improve the modeling of the phase space to study with G4beamline the optimal magnetic field of the spectrometer together with the position of the moderator and of the collimator inside the Mu3e magnet. The following section is focused on the measurement of the phase space at collimator performed during the MEG II beam time.

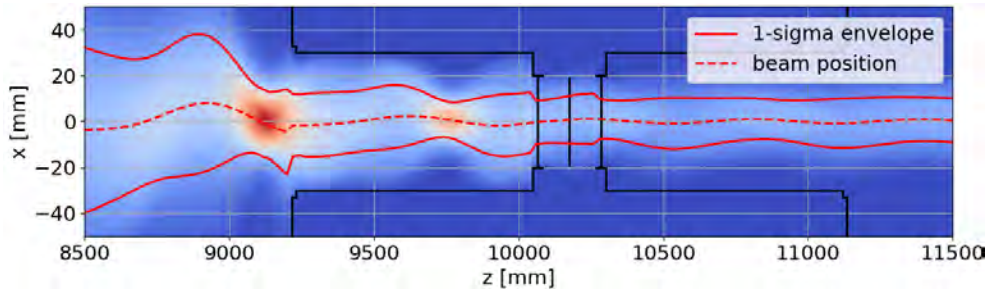

(a) Mu3e magnetic field at 90 % nominal

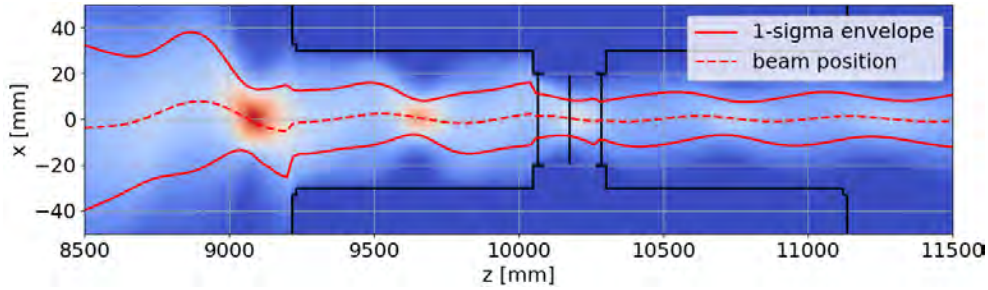

(b) Mu3e magnetic field at 100 % nominal

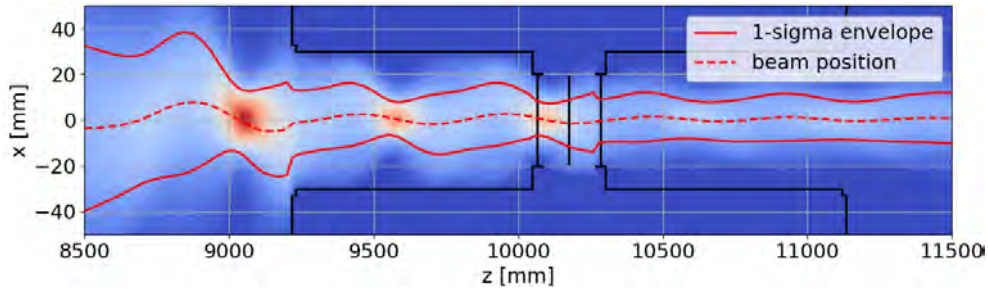

(c) Mu3e magnetic field at 110 % nominal

Figure 3.27: *Simulated density map of the horizontal distribution of the muon beam inside the Mu3e spectrometer. The transport is simulated with G4beamline. The red regions represent higher density points, i.e. foci.* The black solid line represent the beam pipe apertures and the target location. The transmission is simulated at 90 % (top), 100 % (center) and 110 % (bottom) of the nominal magnetic field. With increasing magnetic field the focus is moved upstream of the target location.

3.3 πE5 phase space studies during the 2022 MEG II beam tuning

The MEG II beamline is tuned once per year at the beginning of each beamtime. As the operation of the beamline is well established, the main focus is on measuring the beam properties at the nominal tune and to compensate for possible changes. The beam is first focused at collimator and then at COBRA center.

As soon as the requirements for the beam at COBRA center are met, we measure the integrated beam rate as a function of the aperture of FSH41 and FSH42, the slit systems in the first straight section of the beamline (see Figure 3.1). This is done to be able to vary the delivered intensity during the physics run without the need of setting-up the beam monitor.

The MEG II beamline and the CMBL share the same elements up to the MEG collimator, with the difference that it is moved 200 mm upstream in MEG configuration to accommodate the SciFi detector. During the MEG II beamtime we performed a direct phase space measurement with the pepper-pot technique [42], to be used as an input for the simulations of both experiments. In the current section, the phase space reconstruction with the pepper-pot technique is described and used as an input for the studies on the optimal position of the moderator inside the Mu3e solenoid for different excitation currents.

3.3.1 Pepper-pot measurement and parametrization

The pepper-pot measurement is a well established technique to measure the 4D transverse phase space of low energy beams. We consider first the mono-dimensional case or *slit scan*, as it is usually performed with slits, and generalise it to the case at hand.

The beam is transmitted through the aperture of a slit system, small enough compared to the size of the beam so that it can be considered as a point-like source, as shown in Figure 3.28. The slits are thick enough to completely stop any impinging particle. The fraction of the beam passing through the aperture, called *beamlet*, is measured at a screen after a drift of length L.

A particle in s_0 is transmitted through a drift with the matrix (see Section 2.2.2):

$$M_{drift}(s_0|s_0+L) \;=\; \begin{bmatrix} 1 & L \\ 0 & 1 \end{bmatrix} \tag{3.7}$$

A particle at the aperture will be therefore transmitted as:

$$M_{drift}(s_0|s_0+L)\,x(s_0) \;=\; \begin{bmatrix} 1 & L \\ 0 & 1 \end{bmatrix} \begin{bmatrix} x_0 \\ x_0' \end{bmatrix} = \begin{bmatrix} x_0 + L\,x_0' \\ x_0' \end{bmatrix} \tag{3.8}$$

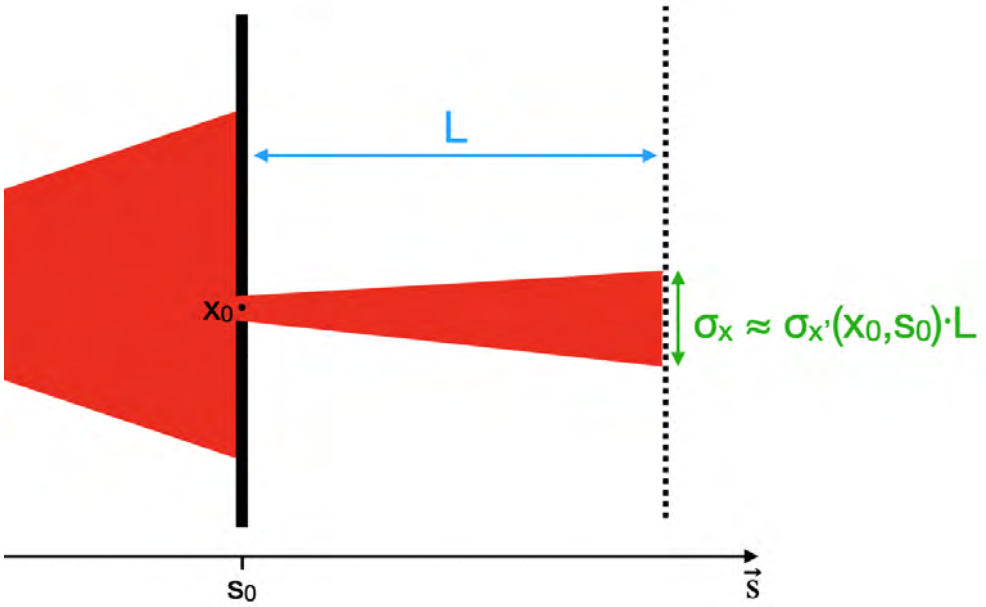

Figure 3.28: *Cartoon of the slit measurement principle. The particle beam, in red, is transmitted through a small aperture at a location s_0 along the beamline. x_0 is the position of the aperture along the transverse axis. The fraction of the beam transmitted through the aperture, beamlet, and its profile is measured with a detector after a drift of length L. The size of the beamlet at the end of the drift is proportional to the divergence of the beam in (x_0, s_0).*

The profile of the beamlet at the screen is therefore proportional to the divergence distribution of the beam in (x_0, s_0). Each profile is then shifted by the corresponding slit position and scaled with the drift length to be combined in a phase space plot: the result is a sliced phase space as in Figure 3.29.

The advantage of such a measurement over a quadrupole scan is that no assumption is required on the beam distribution and the result does not depend on the knowledge of the magnetic fields, but only on the geometry of the set-up. On top of that, the precision on the phase space reconstruction does not depend on the knowledge of the absolute position of the plate, but only on the relative position of the apertures.

A pepper-pot scan uses the same principle as a slit scan, but employing a plate with holes on a grid, allowing to:

- measure at once the 2D transverse divergence distribution at every hole position (including the vertical component and possible correlations)
- reduce the time needed for a measurement

This technique is suitable for low energy beams that can be stopped with

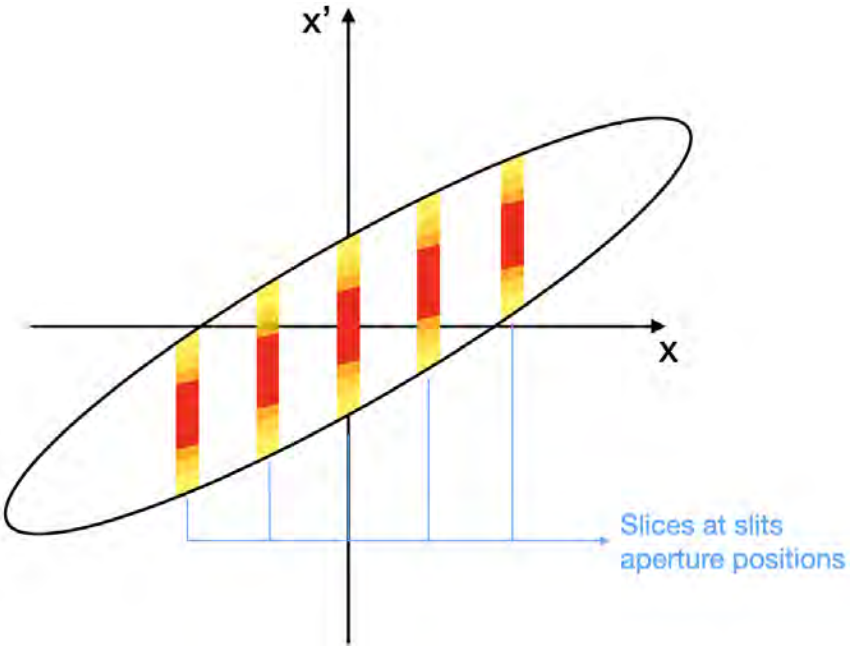

Figure 3.29: *Cartoon of the result of a slit scan. Each slice corresponds to a profile at a different aperture position after being shifted to the value of the measured divergence.*

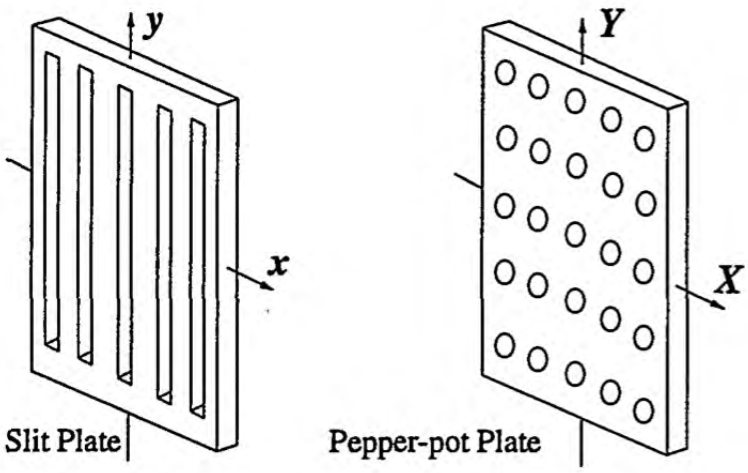

Figure 3.30: *Beam masks in emittance measurement: slit plate (left) and pepper-pot plate (right). From [42].*

plates thin enough to not cut on the divergence distribution and have been extensively used for diagnostics of electron, proton and ion beams. To date we have not found in the literature any application on muon beams.

Due to the limited time available, the set-up was designed to perform the scan with the Pill detector only along the horizontal and vertical axes. The geometry is based on the phase space measured with the quadrupole scan (see Figure 3.19) and on the position of the Pill monitor at the collimator: given that the beam divergence is $\sim$ 50 mrad in both transverse directions and that the expected drift between the grid and the Pill monitor is L $\sim$50 mm, we decided to have roughly 10σ of separation between adjacent beamlets, spacing the holes by 25 mm. Such a conservative geometry is justified by the dependence of the position of the center of the beamlet on the correlation of the phase space ellipse and on the inherent deviation from the gaussian model of the beam. The size of the holes was chosen to be 1 mm in diameter as a trade off between the rate observed after the grid for each beamlet and the expected size of the beamlets. Three aluminum plates 3 mm thick were prepared for this measurement. Figure 3.31 shows two of the construction drawings:

- normal plate: the holes are arranged so that one of them is on the centerline (Figure 3.31a)
- alternate plate: the holes are arranged so that they are staggered by 12.5 mm with respect to the normal plate. This way by combining the two scans one can have a shorter distance between beamlets without them overlapping during a single measurement (Figure 3.31b)
- blind plate: no holes are drilled. This is used to measure the positron background coming from the muons stopped in aluminum

A thing to be taken into account is that we currently do not have the possibility to perform measurements in vacuum: the pepper-pot grid is fixed on the aluminum ring holding the Mylar® window (see Figure 3.32), which means that the muons will propagate in air from the Mylar® window to the pepper-pot grid and then again propagate in air to the Pill detector.

The material budget in Figure 3.32 is present also during the beam measurements shown above and more specifically during the quadrupole scan in Figure 3.19, but the two phase space measurements are affected differently by Multiple Coulomb Scattering (MCS). In both cases the MCS increases the divergence of the beam after the Mylar® window:

- in a quadrupole scan this is going to increase the size of the beam spot by a negligible amount (up to $\sim$3 %), but not directly affecting the divergence measurement. As a matter of fact, even if the phase space can be propagated anywhere along the beamline with the matrix formalism, the quadrupole scan profile will depend only on the phase space at the entrance of the scanned quadrupole. Therefore the MCS contribution enters at a higher order: it enters only on the beam spot

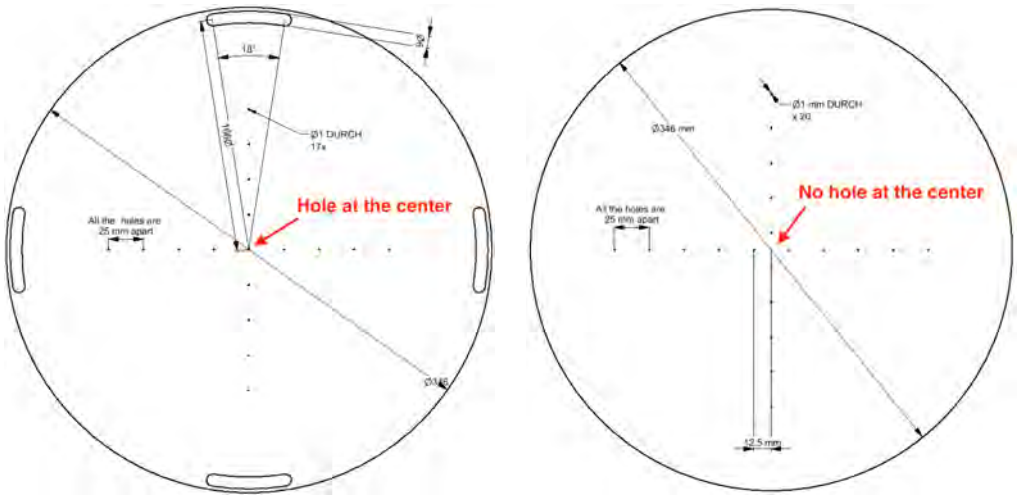

(a) Pepper-pot: normal plate **(b)** Pepper-pot: alternate plate

Figure 3.31: *Left: normal plate for pepper-pot measurement. The holes are arranged to have one hole on the beam centerline. Right: alternate plate for pepper-pot measurement. The holes are staggered by* 12.5 mm *with respect to the normal plate. The two separate measurements are overlapped to increase the number of beamlets while avoiding them to overlap during the measurement.*

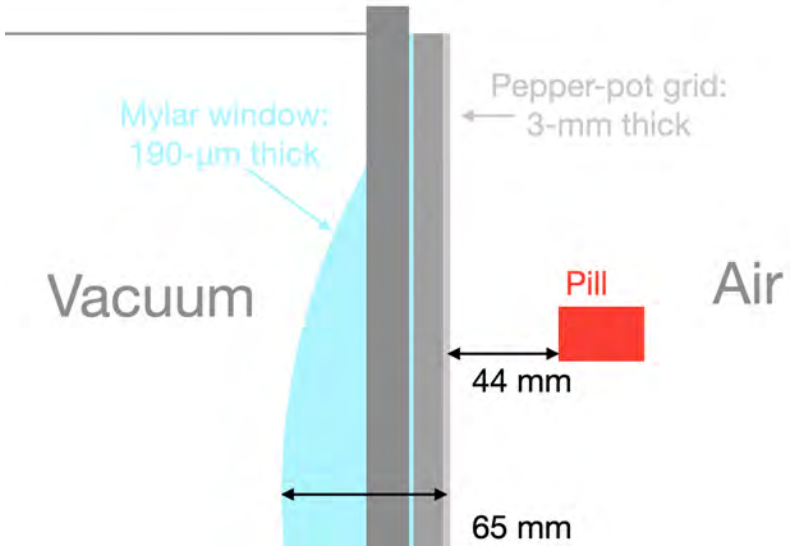

Figure 3.32: *Full material budget for the muon beam for the beam tuning set-up at the collimator.*

width at the Pill location which depends on the divergence through the drift length as $\Delta x = Lx'_0$.

- in a pepper-pot scan the final beam spots are a function of the di-

vergence at the grid location: an increase in divergence between the Mylar® window and the pepper-pot grid will result in a bigger phase space measurements by a factor that is proportional to the MCS contribution.

To account for that, the effect of MCS was fitted by simulating the propagation of the muon beam measured with the quadrupole scan in the gaussian approximation from the Mylar® window to the Pill scanner in G4beamline. The momentum spectrum is assumed to be gaussian centered around 28 MeV/c with a standard deviation of 3.5 %. The simulation includes:

- 190 µm Mylar® window modeled as the sector of a sphere
- air at standard conditions
- the normal pepper-pot plate in aluminum

Figure 3.33 shows the simulation layout.

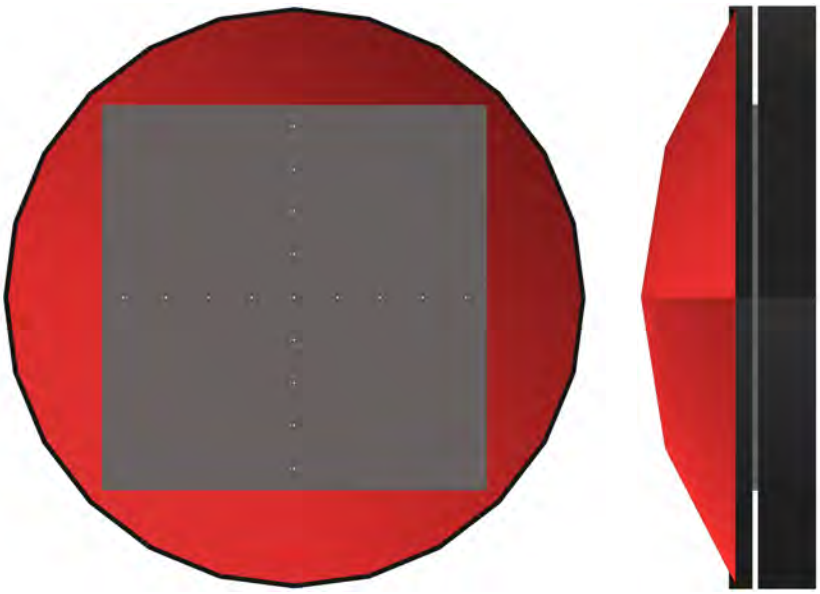

Figure 3.33: *Front (left) and side (right) view of the material budget included in the G4beamline simulation to evaluate MCS effect on the pepper-pot scan. In red is the Mylar® window, in dark grey air and in light grey the normal pepper-pot plate. The air is fitting the insides of the Mylar® dome as well. The detector is placed on the right of the side view, adjacent to the column of air.*

The simulation was run twice: once only with the pepper-pot plate and once with the whole material budget. Figure 3.34 shows the fit to the beamlets in absence of material budget: they are parametrized with the sum of two gaussians, to account for deviations induced by the acceptance of the holes.

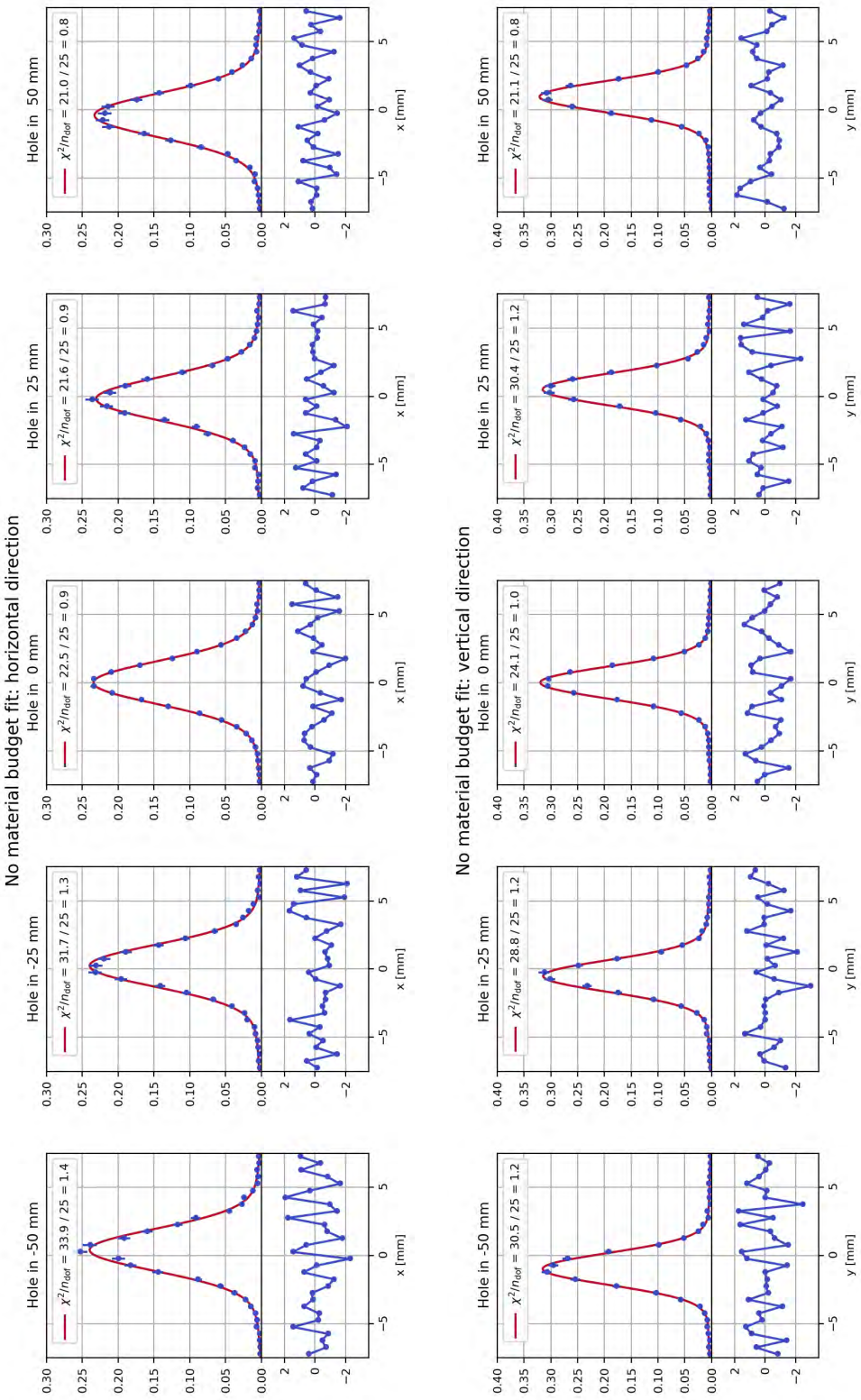

Figure 3.34: *Fit (red line) and normalized residuals to beamlets from G4beamline simulation (blue points) in absence of material budget. The error bars are the statistical errors on the single bin. Each beamlet is parametrized with the sum of two gaussians. Each beamlet is fitted in a window* 15 mm *wide centered on the respective hole location in the grid. The* χ^2/ndof *and the normalized residuals show reasonable agreement with the chosen parametrization.*

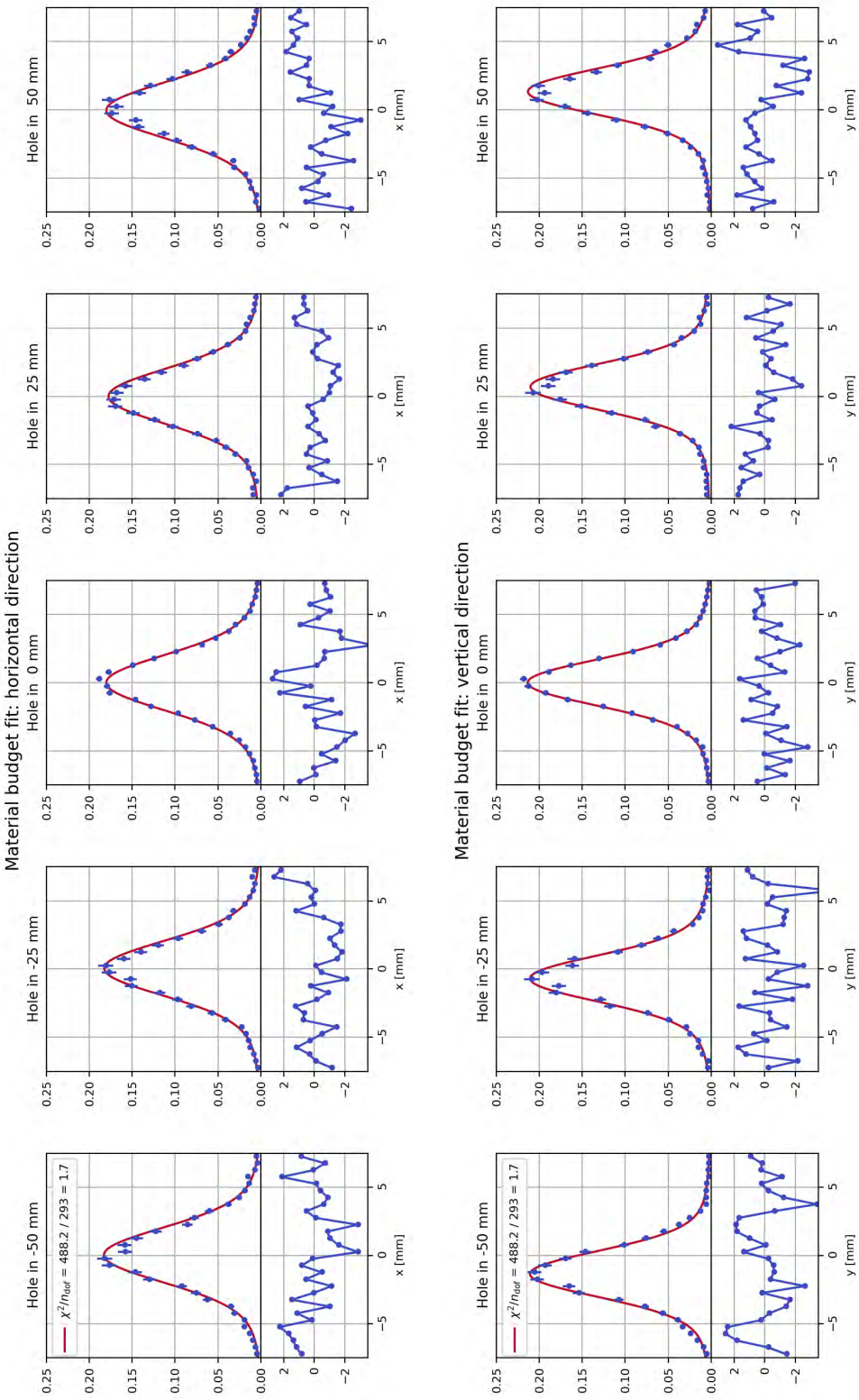

Figure 3.35: *Fit (red line) and normalized residuals to beamlets from G4beamline simulation (blue points) in presence of material budget. The error bars are the statistical errors on the single bin. Each beamlet is parametrized with Equation 3.11. The MCS parameters are constrained to be the same for all beamlets, which are fitted together at once. The* χ^2/ndof *and the normalized residuals show reasonable agreement with the chosen parametrization.*

The MCS contribution is modeled by displacing the beamlets linearly with the hole position and by convoluting the parametrized beamlets with the sum of two gaussians. This parametrization allows for an easy to handle combination of gaussians:

$$b_i = f\mathcal{N}(1,\mu_1,\sigma_1) + (1-f)\mathcal{N}(1,\mu_2,\sigma_2) \quad (3.9)$$

$$mcs = f_m\mathcal{N}(1,0,\sigma_{m,1}) + (1-f_m)\mathcal{N}(1,0,\sigma_{m,2}) \quad (3.10)$$

$$\Rightarrow b_{i,measured} = b_i(x + x_{hole-i}\cdot k) * mcs(x) \quad (3.11)$$

where b_i is the fit at the $i-$th hole in absence of material budget, mcs is the contribution of the MCS that broadens the divergence distribution of the beam and k is the linear coefficient that accounts for the displacement of each beamlets as a function of the hole position x_{hole-i}. Figure 3.35 shows the result of such fit: only the parameters linked to MCS are free to vary. The MCS parameters are shonw in Table 3.4.

$\sigma_{m,1}$ [mm]	$\sigma_{m,2}$ [mm]	f_m	k
1.288(12)	7.7(9)	0.939(3)	0.372 0 014

Table 3.4: MCS parameters from G4beamline simulation: $\sigma_{m,i}$ are the standard deviations of the two gaussians, f_m is the ratio between the integral of the first gaussian and the integral of the sum of the two, k is the linear coefficient for the displacement of the beamlets with respect to nominal.

The parameters found in this way are used to unfold the measured beamlets from the MCS contribution by fitting the measured beamlets with Equation 3.11.

Figure 3.36 shows the profiles measured with the normal and alternate pepper-pot plates. The solid areas are the profiles measured with the blind plate, that is to say the positron background to subtract from the muon beamlets.

Figure 3.37 shows the fit to the measured horizontal beamlets in the divergence space after subtracting the positron background. Figure 3.38 shows the comparison between the unfolded horizontal beamlets after removing the MCS contribution and the measured data points. The fit to the measured vertical beamlets are shown in Appendix B. The unfolded profiles are thinner, than the measured ones due to the subtraction of the MCS contribution, and are shifted depending on the plate with which they were measured.

In fact, in order to combine the results from the normal and the alternate pepper-pot plates, it is necessary to align the beamlets, which are shifted in the two scans because of the uncertainty in the plate positioning. This is done by fitting two straight lines to the average position of the unfolded

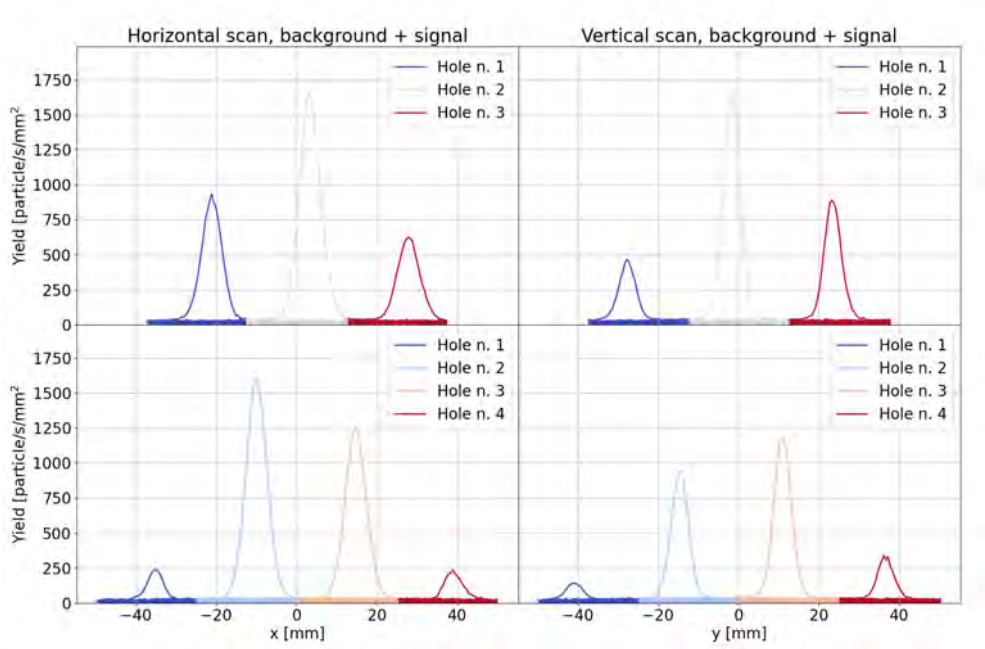

Figure 3.36: *Profiles measured after the pepper-pot grid. The points are spaced by* 0.5 mm *and measured in a* 5 s *interval. The left plots show the horizontal scans. The right polts show the vertical scans. The top plots show the normal pepper-plot scans. The bottom plots show the alternate pepper-plot scans. The solid areas on the bottom of each plot show the contribution from the positron background produced by Michel decays in the aluminum plates as measured with the blind plate.*

beamlets with the linear coefficient constrained to be the same. Figure 3.39 shows the result of such fit. The horizontal displacement is found to be 1.22 mm, while in the vertical profiles no misalignment is observed.

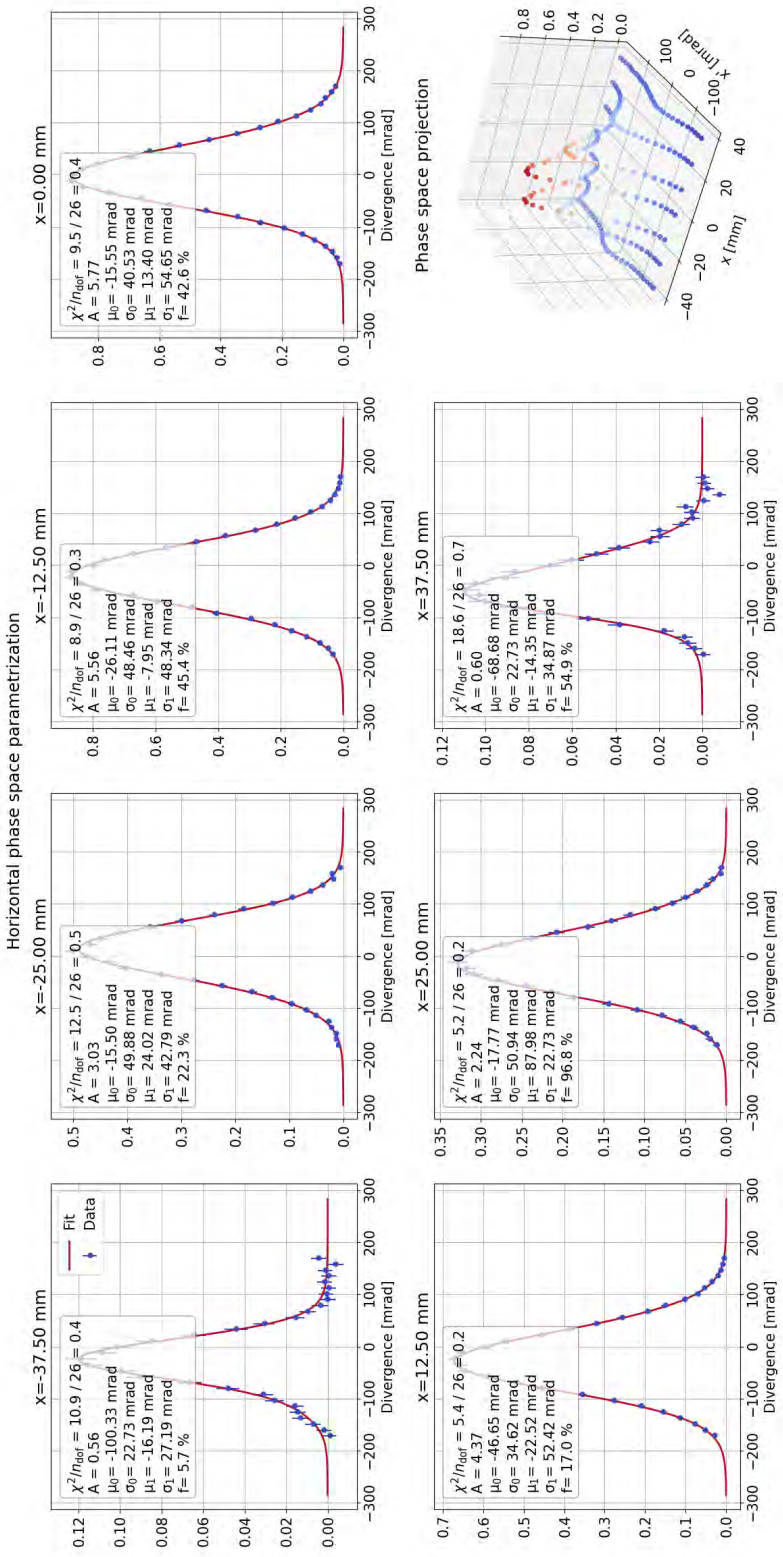

Figure 3.37: *Fit (red line) to the measured beamlets profiles (blue points) for the horizontal scans. The profiles are transformed to divergences through the distance between the pepper-pot plate and the Pill monitor. The error bars are the statistical error. Each beamlet is parametrized with Equation 3.11 fixing the MCS contribution to the parameters in Table 3.4. The 3d plot in the bottom-right corners show the combined beamlets in the transverse phase space.*

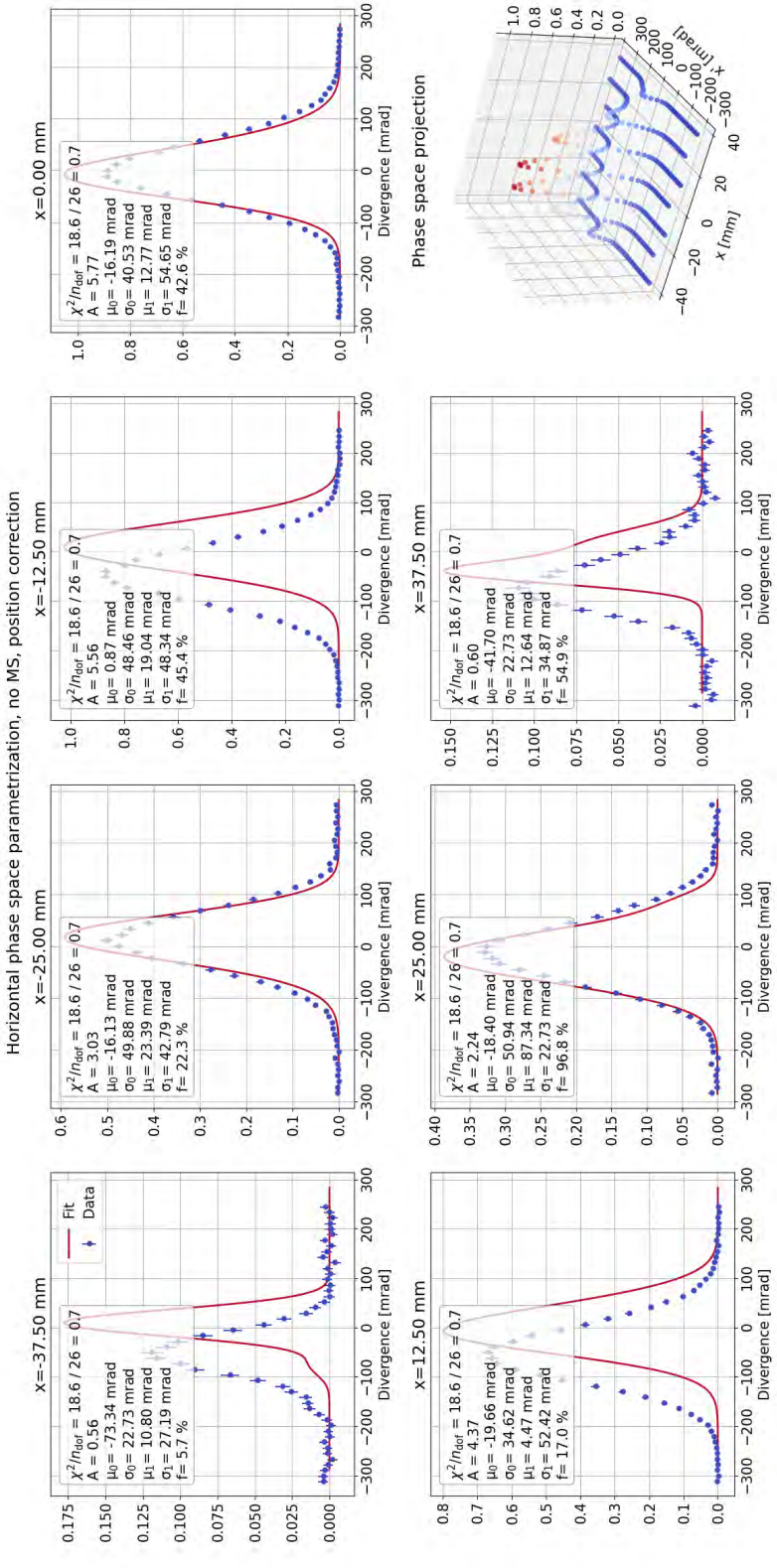

Figure 3.38: *Comparison between the measured beamlets (blue points) and the unfolded beamlets (red lines), after removing the MCS contribution for the horizontal scans.*

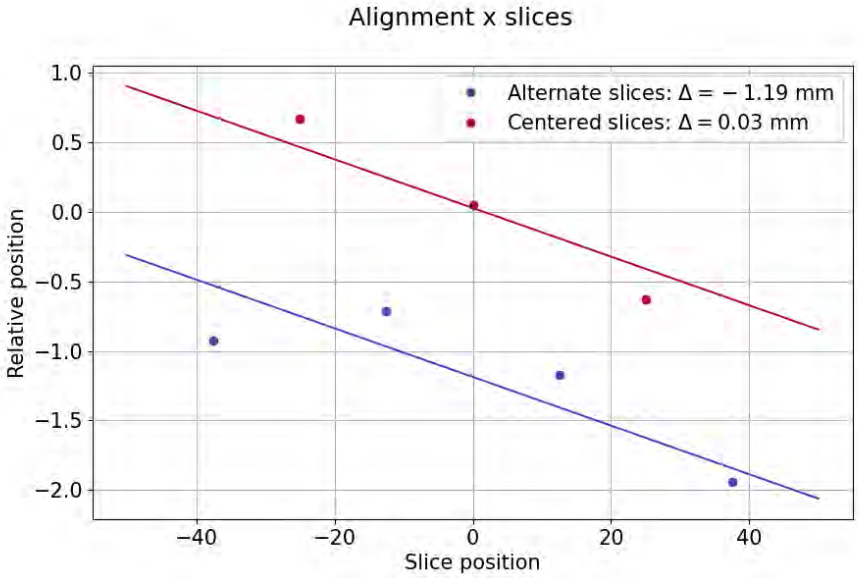

(a) Horizontal phase space

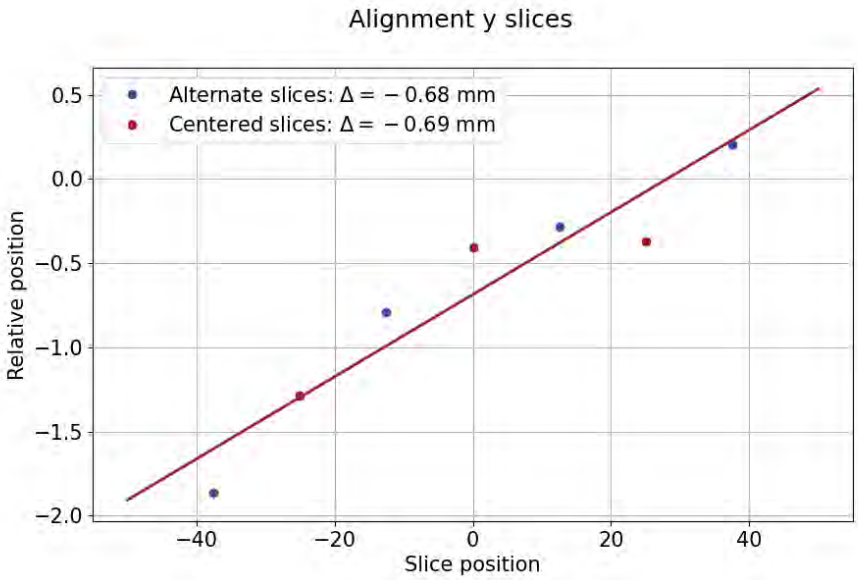

(b) Vertical phase space

Figure 3.39: *Fit to evaluate the shift of the normal (red points) and of the alternate (blue points) pepper-pot plates. Two independent fits are performed for the horizontal (top) and for the vertical (bottom) displacements. Each fit is performed by fitting two straight lines to the averages of the beamlets as a function of the corresponding hole position. The two straight lines are constrained to have the same linear coefficient and different offsets. In the fit performed on the horizontal profiles the relative displacement is found to be* $1.22\,\mathrm{mm}$*, while in the vertical profiles no misalignment is observed.*

At this stage, only the divergence at the aperture positions are available. To fill in the remaining phase space an interpolation is applied. Figure 3.40 shows a cartoon of the steps employed:

- the parametrized slices are evaluated in the full wanted range along the divergence axis
- a bivariate cubic spline interpolates the missing area
- a gaussian tail is matched in the configuration space to each side of the interpolated surface

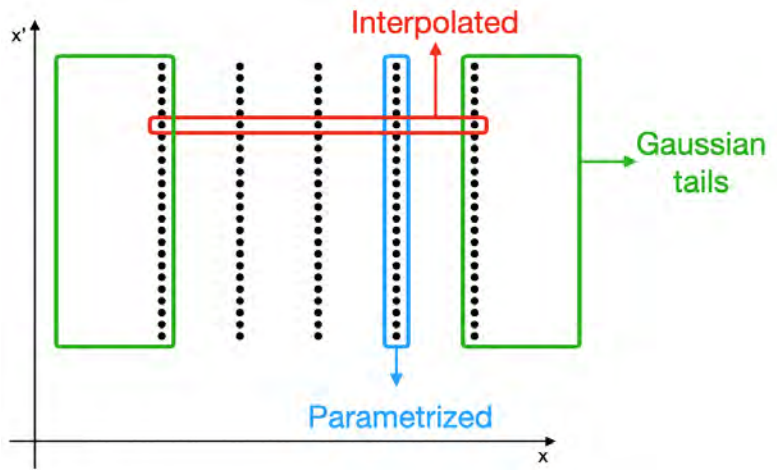

Figure 3.40: *Cartoon showing the steps of the phase space interpolation. The horizontal direction is the configuration space and the vertical direction is the divergence space. Each slice is parametrized with the fit shown above. The area within the slices is interpolated with a bivariate cubic spline. The tails in the configuration space are approximated with gaussian tails matched to the interpolation at the extreme slices.*

The resulting phase space is shown in Figure 3.41. To evaluate the emittance, the contour in the figure was obtained by ordering the bins in the figure by population size and summing them up to 46.5 % of the beam, which corresponds to the integral of a 2-dimensional normal distribution within the 1-sigma ellipse. The standard deviation on the mode was chosen as a measure of the population size to be consistent with the ordering used to evaluate the emittance. Table 3.5 shows a comparison between the phase space parameters as obtained with the pepper-pot scan and with the quadrupole scan. Even if a direct comparison is not possible, as the quadrupole scan assumes a normal distribution, while the result of the pepper-pot scan is a skew distribution, the reconstructed widths are comparable within 10 % and the emittances within 20 %.

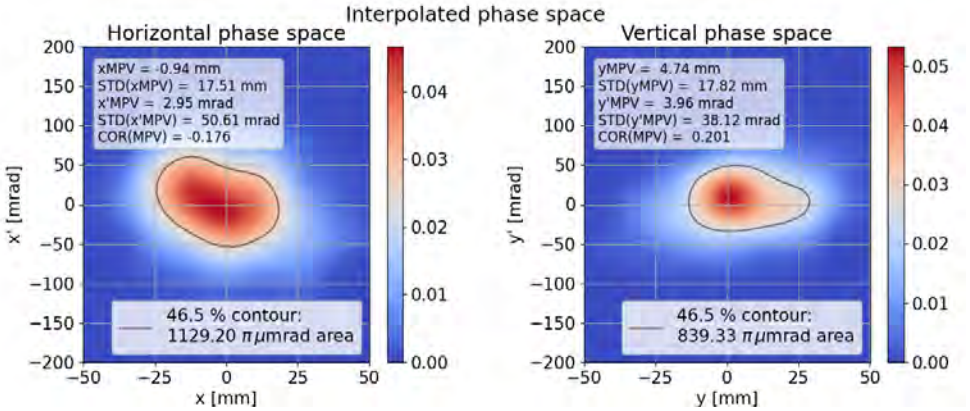

Figure 3.41: *Reconstructed phase space from the pepper-pot scan. Here MPV denotes the Most Probable Value, that is to say the maximum of the distribution. STD and COR denote the standard deviation and the correlation coefficient respectively, here computed with respect to the MPV of the distribution.*

Horizontal phase space				
	σ_x [mm]	$\sigma_{x'}$ [mrad]	ρ_x	ε_x [π μm rad]
Quad. scan	18.7	47.1	-0.014	878.6
Pepper-pot scan	17.5	50.6	-0.176	1129.2
Vertical phase space				
	σ_y [mm]	$\sigma_{y'}$ [mrad]	ρ_y	ε_y [π μm rad]
Quad. scan	20.3	34.9	0.398	651.3
Pepper-pot scan	17.8	38.1	0.201	839.33

Table 3.5: Transverse phase space parameters as measured with the quadrupole scan and with the pepper-pot scan.

3.3.2 Fit to momentum distribution

The phase space obtained with the pepper-pot scan can be used to sample the transverse phase space of the muon beam at collimator, but a further step is needed to have a through description of the beam dynamics in πE5: the modeling of the momentum spectrum. In fact the pepper-pot scan is inherently a measurement of the transverse phase space, giving no information on the longitudinal phase space. No dedicated measurement was performed, but the final beam spot at the center of the Mu3e solenoid is expected to depend on both the transverse phase space at collimator and on the momentum distribution. This is caused by the presence of the two bends along the CMBL which introduce dispersion and by the spectrometer itself through chromatic aberrations, that is to say the dependence of the position of a focus on the momentum of a particle.

A python class [43] was developed to fit phase space parameters to available

beam data using G4beamline models.

The parametrization for the momentum distribution is built as follows:

- the surface muon spectrum depends on the momentum to the power of 3.5: $pdf_{surface\,muons}(P) = \alpha P^{3.5}$
- the surface muon spectrum is convoluted with a gaussian of width $\sigma_1 = 74.4\,\mathrm{keV/c}$ to account for cloud muons
- the resulting distribution is multiplied by a gaussian distribution centered at $\mu_2 = 27.88\,\mathrm{MeV/c}$ and with $\sigma_2 = 1.23\,\mathrm{MeV/c}$ to model the beamline acceptance

The parameters listed above for the momentum distribution (see Figure 3.42) were found by fitting the histogram in Figure 2.44 of Reference [5]. At this stage these values are the initial parameters for the fit with the G4beamline model. Five additional parameters are added to the fit: the centroids of the transverse phase space and the first order correlation between the horizontal coordinate and the momentum.

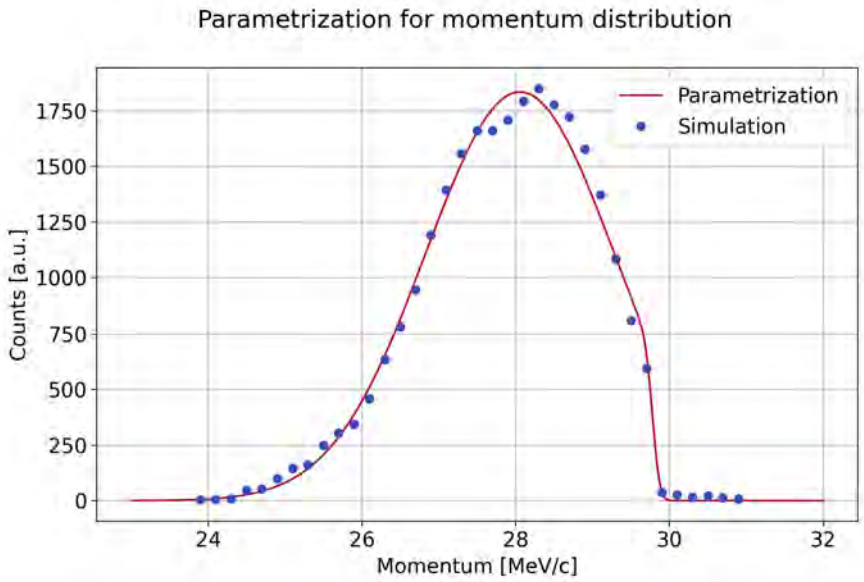

Figure 3.42: *Parametrization for the muon momentum spectrum. In blue the points from Figure 2.44 of Reference [5]. In red the parametrized distribution.*

After initialization with a configuration file, the class interpolates the available beam profiles with cubic splines and defines the phase space parametrization function (from the pepper-pot fit). Then a method evaluates a χ^2-like variable given a set of beam parameters by comparing the measured profiles with the result of a G4beamline simulation. The advantage in using

G4beamline is that it allows for single particle tracking, but the computation time needed for single evaluation strongly depends on the modelled beamline and on the required statistics. In general a time up to 20 min is needed to make an evaluation on the full CMBL. Due to the demanding computation time needed, standard minimization routines for fits like MINUIT [44] are not suitable.

In order to overcome this issue, the Non-dominated Sorting Genetic Algorithm II (NSGAII) [45], as implemented in the optuna package [46], was used instead. Together with other genetic algorithms, NSGAII is widely used to solve high-dimensional multi-objective optimization problems, delivering results in accelerator physics as well [47]. Genetic algorithms are metaheuristics inspired by the process of natural selection. A generic single-objective algorithm works as follows:

1. Generate starting population. Each individual is defined as the set of parameters to be optimized, in this case the beam parameters.
2. At each iteration of the algorithm:
   a) evaluate the fitness of each individual in the population. The fitness is the function to be minimized, so in our case the evaluation of the χ^2-like variable
   b) select the fittest individuals
   c) breed the fittest individuals through crossover and mutation and give birth to offspring
   d) replace the least-fit individuals with the new individuals

The different algorithms differ mainly in the choice of the sorting for fitness in case of multi-objective optimization. In this specific case, the sorting is trivial, and further details about NSGAII are reported in Chapter 5 where this point is of relevance.

For the CMBL, a G4beamline simulation developed in 2018 [5] was used. The geometry of the beam pipe inside the spectrometer was updated to the current version and an air atmosphere was used to reproduce the conditions of the measurement during commissioning.

Convergence showed to be slow for this minimization and after $\sim 7 \times 10^5$ trials, corresponding to $\sim$ 2 weeks on 350 cores, it was stopped. In Figure 3.43 the dependence of the objective function on the fitting parameters is shown.

The objective function is narrower along the centroid axes than along the momentum parameters axes: this is caused by the narrow acceptance of the QSO doublet, which cuts the tail of the momentum distribution, washing out the features of the initial momentum distribution. A slight trend can be seen

on the correlation axis, but as the points are sparse close to the minimum this could be an artefact of an early stop of the optimization routine.

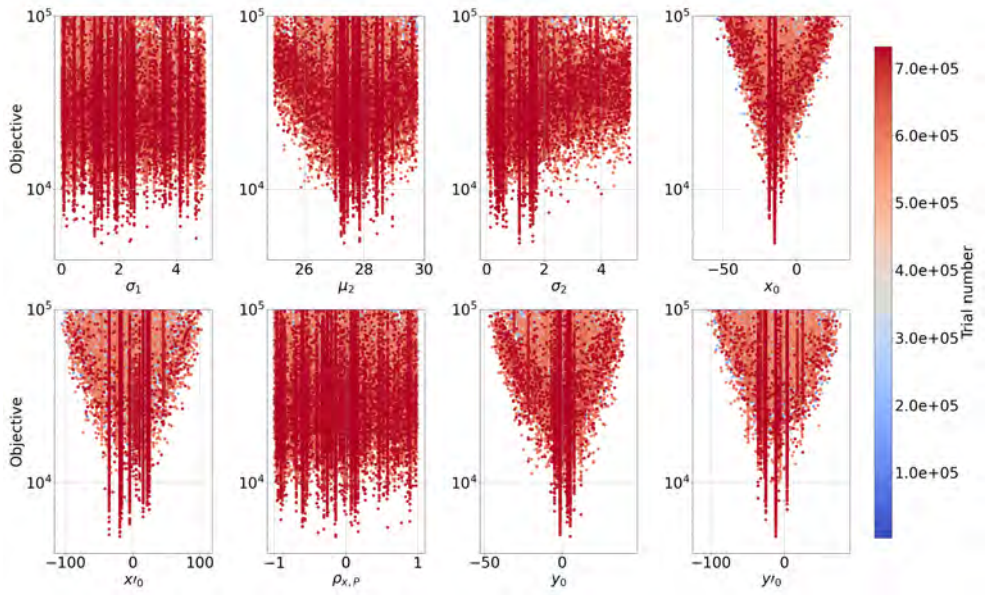

Figure 3.43: *Objective function dependence on fitting parameters. The centroid position in phase space is better resolved than the momentum distribution parameters.*

Figure 3.44 shows the comparison between the measured and fitted beam spots at the Mu3e center. The minimum value obtained from the optimization is $\chi^2/\text{ndof} = 4877/110$, but the main feature of the measured beam spot are reproduced. Due to the relevant amount of resources needed to obtain such agreement and given that the aim of this study is not to fine tune the beam phase space representation for Mu3e, no furhter optimization was carried out. This method has anyways proven to be valid for phase space inference, and further refinement can be carried out in the future after commissioning completion to aid the high-fidelity Monte Carlo simulations of the Mu3e apparatus.

3.3.3 Studies of the optimal magnetic field for the Mu3e focus and of the optimal position of the moderator and collimator

The beam reconstructed in the previous paragraphs was used to optimize the position of the Mylar® moderator along the beam pipe in the Mu3e spectrometer. Figure 3.45 shows the transmission to the beam monitor from the entrance of the solenoid. Air is included. 36.8 % of the beam entering the Mu3e solenoid is transmitted to the beam monitor. The losses are caused

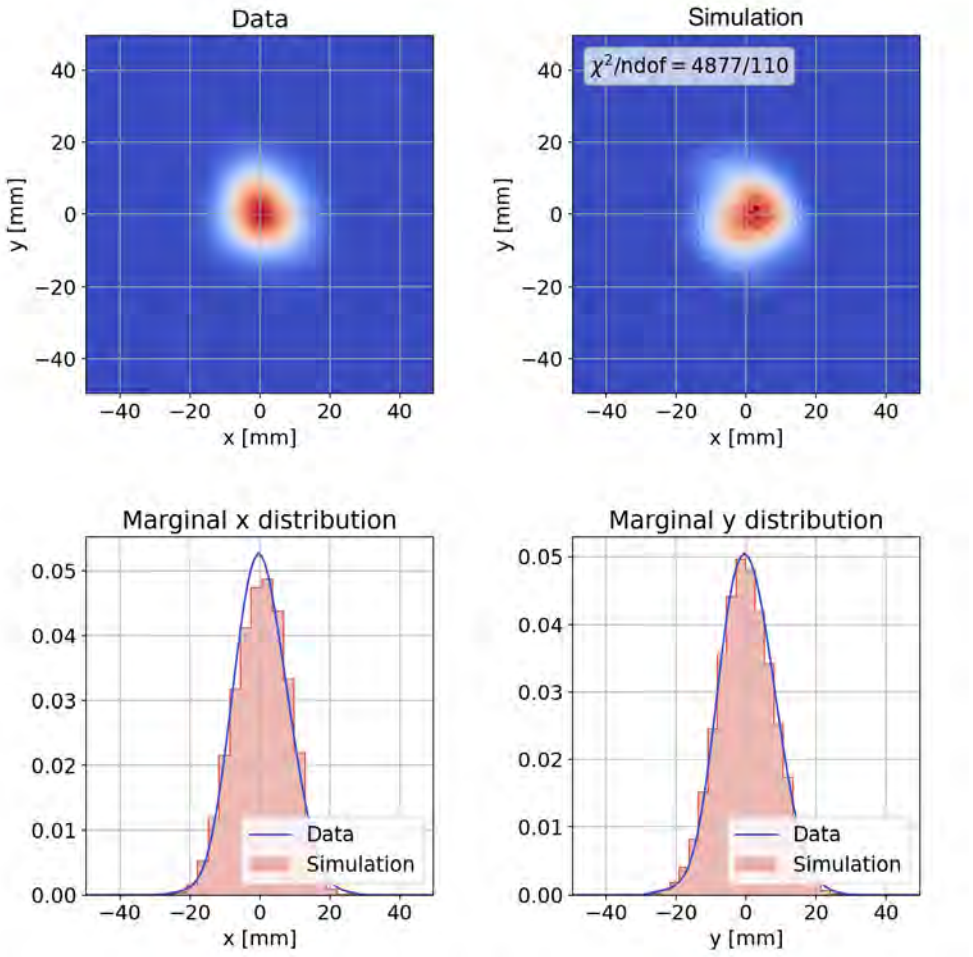

Figure 3.44: *Comparison between measured and fitted beam spot at the Mu3e center with the 2022 campaign tune. The minimum value obtained from the optimization is* $\chi^2/\mathrm{ndof} = 4877/110$. *The main features of the measured beam spot are reproduced.*

by the 60 mm aperture of the beam pipe and by the size of the final vacuum window and its holder, which is 40 mm in diameter. As expected, the beam is focused in both transverse directions close to the beam monitor.

As shown in Figure 3.26, a dependence of the transmission on the Mu3e field strength is expected: when increasing the magnetic field the waists of the envelope will be moved upstream allowing for higher transmission when the waists are located in correspondence of the vacuum window as shown in Figure 3.27. Figure 3.46 shows the simulated transmission for a magnetic field at 110 % of the nominal. At the vacuum window the beam spot is reduced in size allowing for a transmission of 45.34 %. On the other hand there is not a focus anymore at target position, leading to a wider beam and

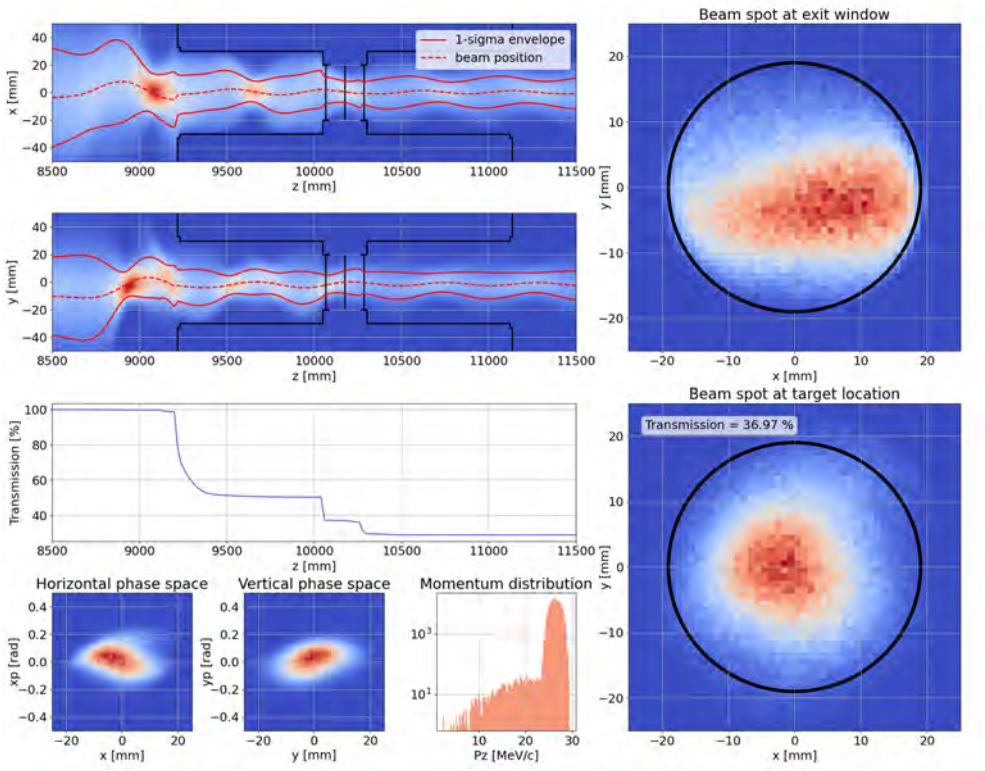

Figure 3.45: *Transmission to the center of the Mu3e spectrometer. On the left from the top: the envelopes in the horizontal and vertical plane, the black lines show the size of the beam pipe; the transmission from the entrance of the magnet; the phase space at the center of the Mu3e magnet. On the right from the top: the beam spot at the vacuum window and the beam spot at target location. The black circles show the size of the target cross section.*

a corresponding decrease of rate within the target cross-section, so that the whole CMBL should be retuned for a specific value of the magnetic field in the spectrometer.

Figure 3.47 shows the simulated transmission to the center of Mu3e as a function of the field strength, analogously to the measurement in Figure 3.26, without changing the currents that power the rest of the beamline: the simulation does not reproduce perfectly the measurements, but the overall behaviour is consistent. The agreement is better if considering the total rate only, while the discrepancies in the rate on target estimates are probably due to mismodeling of the centroids of the beam. The main aim of this study is to provide an input for the 2023 commissioning and the agreement reached with the current model is sufficient for such estimate.

From this point we can proceed with the optimization of the moderator position for different magnetic fields. The optimization is performed by opti-

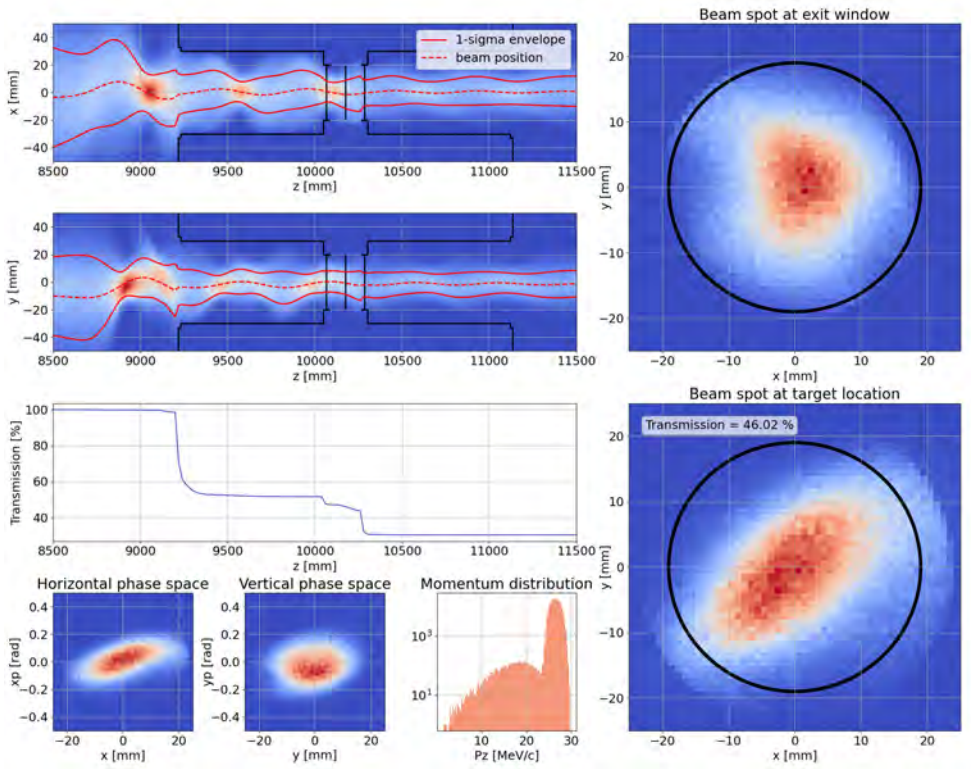

Figure 3.46: *Transmission to the center of the Mu3e spectrometer. The field strength is* 110 % *of the nominal. On the left from the top: the envelopes in the horizontal and vertical plane, the black lines show the size of the beam pipe; the transmission from the entrance of the magnet; the phase space at the center of the Mu3e magnet. On the right from the top: the beam spot at the vacuum window and the beam spot at target location. The black circles show the size of the target cross section.*

mizing the currents of the CMBL elements and the position of the moderator for three different values of the Mu3e magnetic field:

- nominal
- 110 % nominal
- 120 % nominal

The objective of the optimization is the number of muons transmitted from QSK41 to the center of Mu3e out of 10^5 generated particles. Only the particles within the radius of the Mu3e target (19 mm) are taken into account. Seven parameters are considered for the optimization: SML41, the QSO doublet, QSM41, ASK41 and ASL41 and the position of the moderator in the Mu3e 60 mm beam pipe. The atmosphere inside Mu3e in this case is made of helium, as it will be for the experiment. The optimization is performed

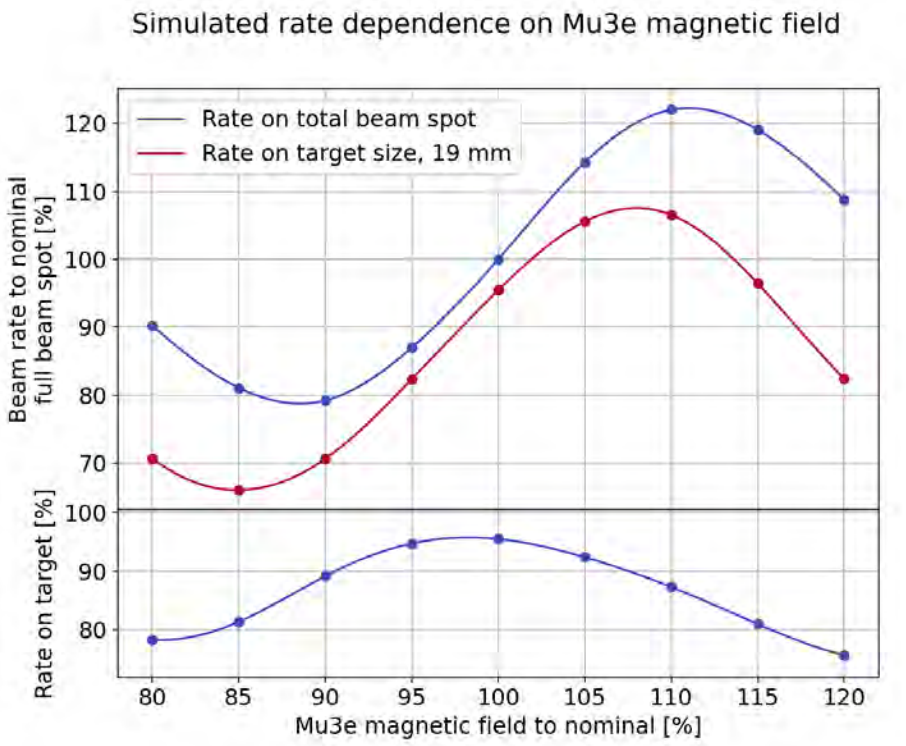

Figure 3.47: *Top: the simulated rate estimated by integrating on the total beam spot (blue) and within the surface of the Mu3e target (red) at Mu3e center as a function of the magnetic field. Bottom: simulated fraction of beam within the area of the Mu3e target. The points represent the simulations. The solid lines are their interpolation with cubic splines.*

using NSGAII with a population of 50 individuals.

The final parameters are shown in Table 3.6. The obtained tunes can be used to scan the collimator position between the moderator and the exit window to minimize the muon flux on the pixel tracker. Each simulation was run by transmitting 10^6 μ^+ to the Mu3e center. A hollow cylindrical VirtualDetector with a 23.7 mm radius was added to the G4beamline model to count the muons reaching the inner layer of the pixel tracker.

The position of the collimator is parametrized by the distance to the moderator divided by the moderator distance to the exit window and the figure of merit is the counts in the tracker divided by the counts within the radius of the Mu3e target: 0 % corresponds to having the collimator in contact with the moderator. The scan is performed in 10 % steps.

Figure 3.48 shows the transmission from the entrance of the Mu3e spectrometer to the Mu3e center, to the tracker and their ratio as a function of the collimator position. Although the 100 % and 110 % nominal tunes deliver similar transmissions to target, 27.04 % and 28.47 % respectively, a relevant

transmission increase is obtained with the 120 % nominal tune. The detailed transmission plot are reported in Appendix C.

The moderator position determined in this way was used during the 2023 campaign. Further details are reported in Section 3.4.

	Beamline parameters			
Beamline element	2022 tune	Mu3e 100 %	Mu3e 110 %	Mu3e 120 %
SML41 [A]	- 14	- 13.14	- 12.46	- 19.28
ASL41 [A]	74.	74.72	74.33	73.36
QSO41 [A]	53.5	52.70	52.78	49.52
QSO42 [A]	- 15.0	- 15.96	- 17.70	- 14.74
ASK41 [A]	- 92.0	- 91.19	- 90.84	- 89.99
QSM41 [A]	120	104.46	126.55	106.61
zMOD [mm]	-	9685.51	9691.40	9503.76
Moderator distance to Mu3e center [mm]	-	489.49	483.60	671.24
Transmitted particles	16390	16132	16349	17855

Table 3.6: Optimized parameters for muon beam transmission to the Mu3e center. The three optimizations include the positioning zMOD of the 600 µm Mylar® moderator as a parameter and they are compared to the simulated transmission using the nominal CMBL tune as obtained after 2022 campaign.

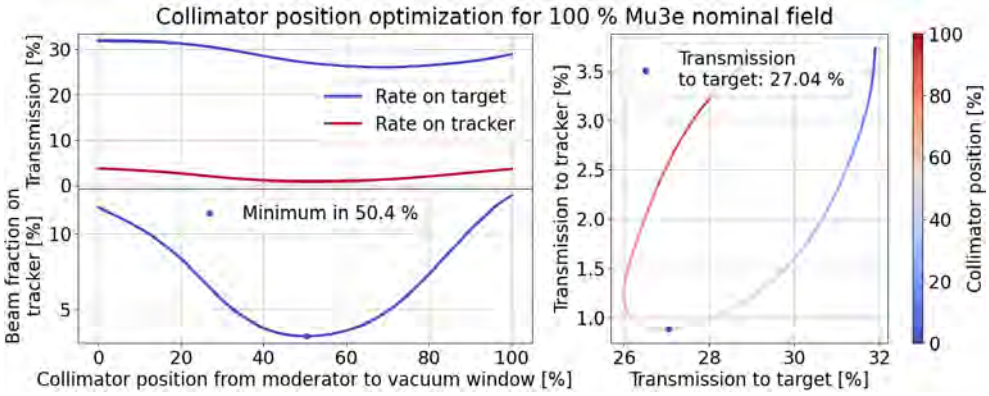

(a) Mu3e spetrometer at 100 % nominal current

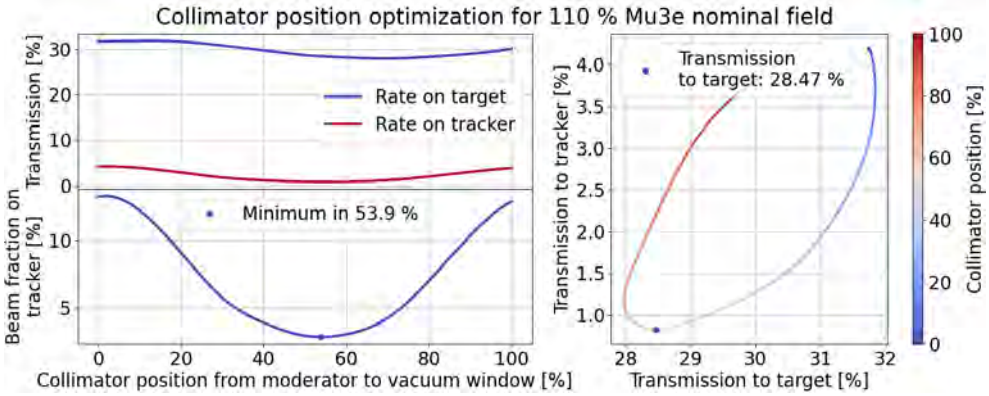

(b) Mu3e spetrometer at 110 % nominal current

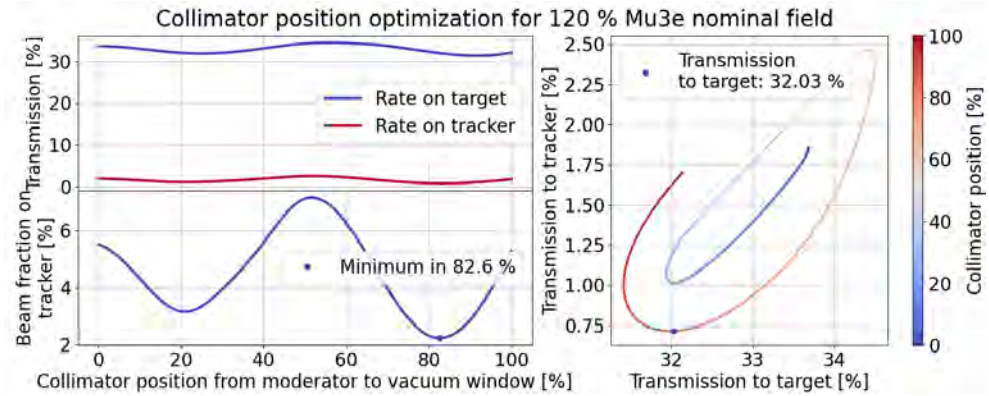

(c) Mu3e spetrometer at 120 % nominal current

Figure 3.48: *Collimator position scan for the* 100 %, 110 % *and* 120 % *nominal Mu3e spectrometer field tunes. Left top: transmission to Mu3e target (blue) and to the inner layer of the pixel tracker (red) vs collimator position. Left bottom: ratio between counts on tracker and on target vs collimator position. Right: transmission to tracker vs tranmission to target as a function of the collimator position (color coded).*

3.4 Final remarks and latest results

In this chapter, a description of the activities carried out between 2021 and 2022 to commission the CMBL for the Mu3e experiment was given, with particular emphasis on the 2022 campaign. The main results can be summarized as follows:

- 2021 campaign: the Mu3e solenoid was moved for the first time in the πE5 area and the muon beam was successfully transmitted to its center.
- 2022 campaign: whereas the HSC42 was not operational, the transmission through the CMBL was improved and surpassed the requirements stated in the Technical Design Report of the Mu3e experiment [4]. The characterization of the muon beam phase space was improved by performing a pepper-pot scan, allowing to determine the optimal position of the moderator and collimator for the data taking.

After the 2022 campaign, the HSC42 sextupole was fixed and the delivered muon rate was significantly improved during the 2023 campaign[1]. In 2023 the moderator was installed in the 60 mm insert. The beamline was first tuned for maximum transmission to the center of Mu3e without the insert. Then, a section with a length of 400 mm of the 160 mm diameter beam pipe was removed to measure the beam spot where the moderator would be installed, that is to say 487 mm upstream to the center of the Mu3e spectrometer. Such position was chosen as a trade off between the optimal position at nominal field and at 110 % of the nominal shown in Table 3.6. Figure 3.49 shows the beam spot measured at both the moderator position and Mu3e center. The beam spot at the moderator position is smaller than the one at Mu3e center, meaning that the chosen position is indeed a focus as expected.

Then, the 400 mm section was mounted again and the beamline was tuned with the 60 mm diameter insert in place. Finally the moderator and the collimator were installed in the insert and the 40 mm exit window was installed at the end of the beamline. Due to the 100 µm thick exit window being thicker than the 35 µm planned for the data taking, the moderator here was limited to a 550 µm thickness. The collimator was positioned in contact with the moderator so that the muon transmission would be maximal (see Section 3.3.3). Due to time constraints, the beam spot was not measured with the collimator in the position that minimizes the muon flux on the pixel tracker. Figure 3.50 shows the beam spot measured at Mu3e center with the moderator in position. The delivered rate is $7.50 \times 10^7\ \mu^+/s$, that is to say 8.7 % higher than the rate delivered in 2022 without the moderator.

[1] The 2023 beamtime happened at the time of writing this thesis, so only a brief summary of the activities is reported.

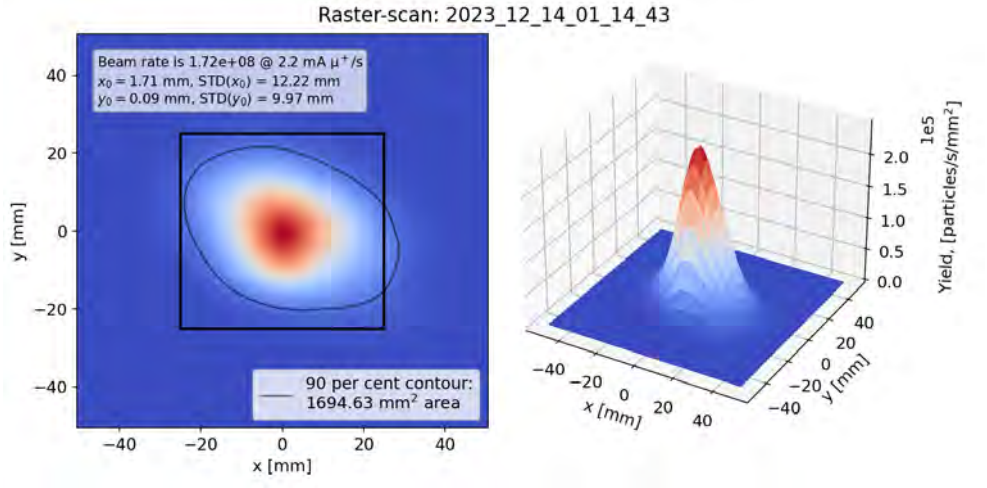

(a) Scan at Mu3e center

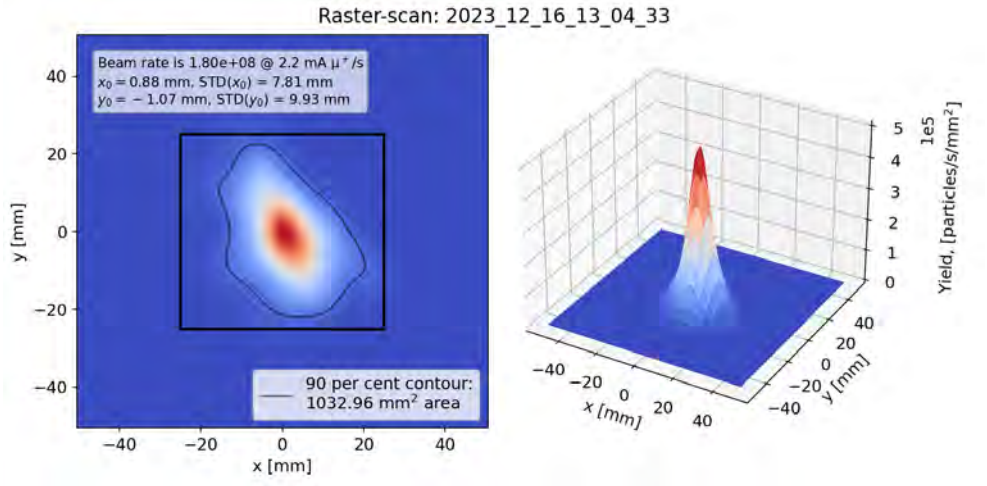

(b) Scan at the moderator position

Figure 3.49: *Raster-scan at Mu3e center (top) and at the moderator position (bottom) without beam pipe insert: the inner-most aperture of the beam pipe is* 160 mm *and the aperture of the exit window is* 100 mm. *To measure the beam spot at the moderator position, a* 400 mm *long section of the beam pipe was removed.*

Finally, Table 3.7 shows a comparison between the muon beam rates delivered to the collimator, to the QSM41 focus and to the center of the Mu3e spectrometer over the three commissioning campaigns.

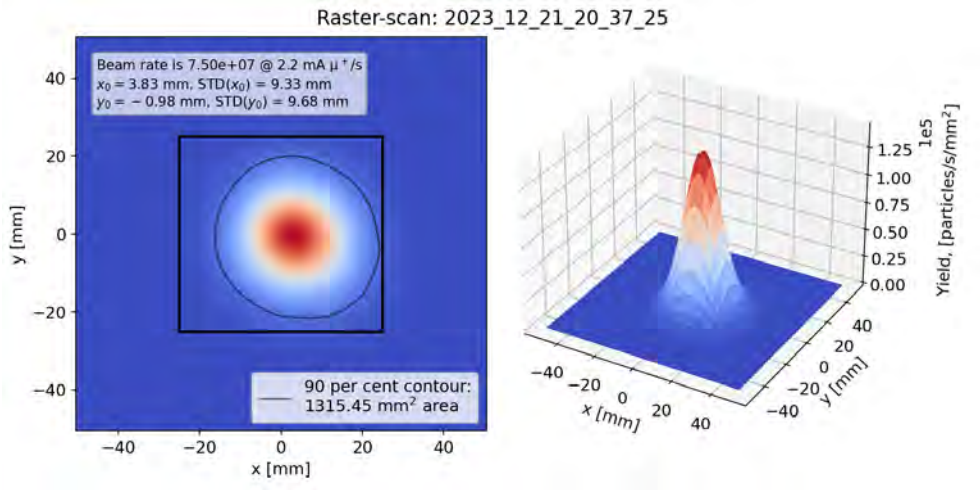

Figure 3.50: *Raster-scan at Mu3e center including the* 60 mm *beam pipe insert. The moderator and the collimator are installed in the* 60 mm *insert and the* 40 mm *exit window is present.*

CMBL commissioning rates comparison			
	Rate [μ^+/s]		
Year	Collimator	QSM41	Mu3e
2021	1.94 10^8	1.10 10^8	4.40 10^7
2022	2.26 10^8	1.66 10^8	6.89 10^7
2023	2.38 10^8	1.88 10^8	7.50 10^{7*}

Table 3.7: Final muon beam rates over the 2021, 2022 and 2023 CMBL commissionings. In 2023 (*), the measurement at Mu3e center was performed with the moderator in place.

Chapter 4

Exotic physics measurements performed with the MEGII apparatus

In 2016 the ATOMKI collaboration has found an excess in the relative angle distribution of the internal pair creation (IPC) pairs in the $^{7}\mathrm{Li}(\mathrm{p}, \mathrm{e}^{+}\mathrm{e}^{-})^{8}\mathrm{Be}$ reaction [8]. Until today, the absence of a nuclear model providing an explanation to such an excess has lead to the hypothesis of observation of new physics with the introduction of a boson of mass $16.95\,\mathrm{MeV/c^2}$ [48–50], therefore the name X17. Only another experiment [51] has claimed the observation of the anomaly at the time of writing, with similar detection technique and geometric acceptance to ATOMKI, and the MEG II collaboration has the possibility to perform an independent measurement.
A brief introduction of the anomaly is provided, followed by the description of the experimental set-up and of the measurement campaigns. Finally, the analysis strategy and framework are described.

The first two sections are introductory. The third and last section focuses on the analysis. The candidate has contributed to the testing and construction of the target volume, to the data taking, to the definition of the analysis and to the adaptation of the MEG II analysis framework to the X17 analysis.

4.1 The beryllium anomaly

The aim of the measurement performed in the ATOMKI laboratories in Debrecen (Hungary) was to perform a high precision measurement of the relative angle distribution of the internal pair creation pairs from nuclear de-excitation, to be then compared with the Standard Model prediction. The choice of the $^{7}\mathrm{Li}(\mathrm{p},\gamma)^{8}\mathrm{Be}$ reaction is due to the high energy of the γ

(≈18 MeV) emitted in the de-excitation of the ^{8}Be nucleus. Such feature lead as well the choice of the MEG experiment for it to be a calibration source for the energy scale of the XEC.

Two resonances are observed (see Figure 4.1) as a function of the proton energy E_p: $E_p = 441$ keV, the beryllium is excited to a 17.64 MeV state; $E_p = 1030$ keV, the beryllium is excited to a 18.15 MeV state. The beryllium is excited to spin-parity $J^P = 1^+$ and mixed isospin whose main components are $T = 1$ (Mostly IsoVector, MIV) and $T = 0$ (Mostly IsoScalar MIS) respetively [52]. Figure 4.2 shows a schematic of the relevant energy levels.

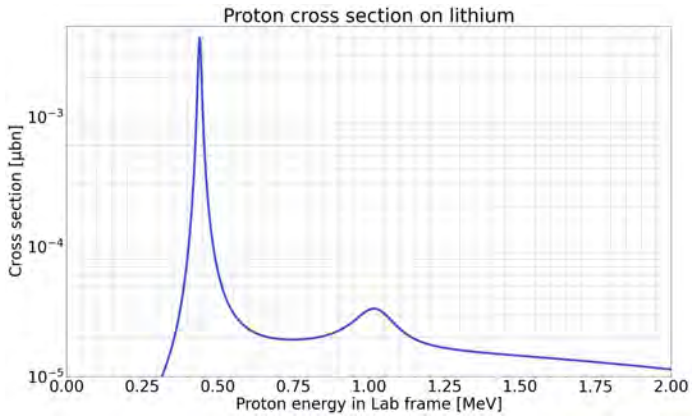

Figure 4.1: *Cross section of the ^{7}Li(p,γ)^{8}Be reaction as a function of the proton energy in the laboratory frame implemented in the Geant4 MEG II Monte Carlo simulation (GEM). The implementation is reported in [53] based on the calculations of Zhang and Miller [52].*

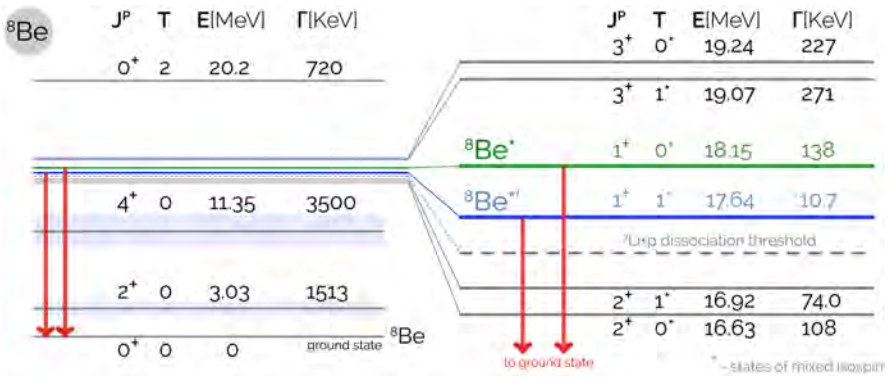

Figure 4.2: *Relevant ^{8}Be states from [52].*

The excited beryllium state can then either directly emit a photon or an electron-positron pair, leading to the so-called internal pair converion (IPC). IPC is produced with a branching ratio $\mathcal{B} \approx 3.9 \times 10^{-3}$ to the γ produc-

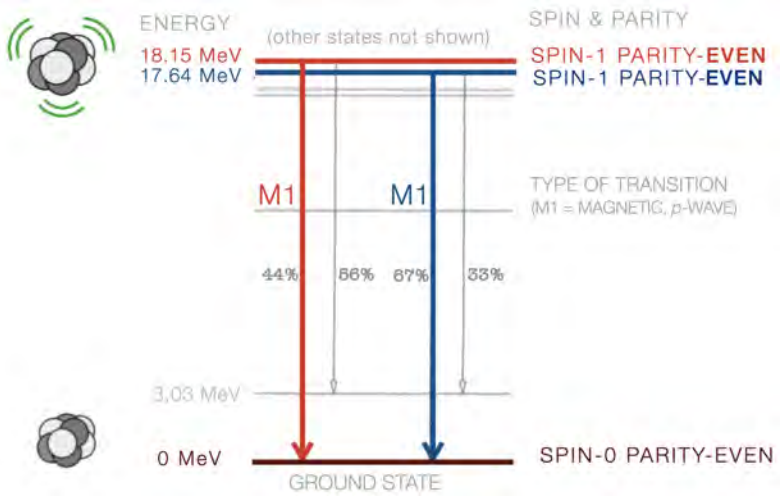

Figure 4.3: *Transition mixing to first ground state for MIS and MIV states, from [54].*

tion. In addition to the transition to ground state, both MIS and MIV can decay to the first excited state of 3.03 MeV. Figure 4.3 shows the fractions of transitions to ground and first exited states.

In 2016, the ATOMKI collaboration found an excess in the IPC relative angle at $\sim 140^\circ$ [8, 9]. In the distribution of the invariant mass of the pair, the excess corresponded to a mass of $16.70(51)\,\mathrm{MeV}/c^2$. The initial geometry was optimized to improve the resolution at 90° and later upgraded to measure the anomaly with higher precision [55] (Figure 4.4), measuring an invarian mass of $16.98 \pm 0.16(\mathrm{stat.}) \pm 0.20(\mathrm{syst})\mathrm{MeV}/c^2$. Later the anomaly has been confirmed at ATOMKI in the $^3\mathrm{H}(\mathrm{p},\gamma)^4\mathrm{He}$ process and in the $^{11}\mathrm{B}(\mathrm{p},\gamma)^{12}\mathrm{C}$ process [56, 57] with results consistent with the original anomaly. To date, the anomaly has been observed only by ATOMKI and by an experiment at the University of Sciences in Hanoi [51], and whereas the detector of ATOMKI has been upgraded and the latter group has independently conducted the experiment, the detection technique and the main features of the geometric acceptance did not change: every measurement has been performed only in the plane perpendicular to the proton beam axis. This poses a criticality and requires independent tests of the anomaly. Additionally, measurements in the full solid angle are needed to test the hypothesis of a new boson [58]. The MEG II apparatus is suitable for such a measurement allowing for a broader acceptance and a different detection technique.

In addition to MEG II, many experimental efforts are being carried out to directly or indirectly test the anomaly [59]. In the following paragraph, a general overview of such searches is given. The search of the beryllium anomaly with the MEG II apparatus is presented in the following sections.

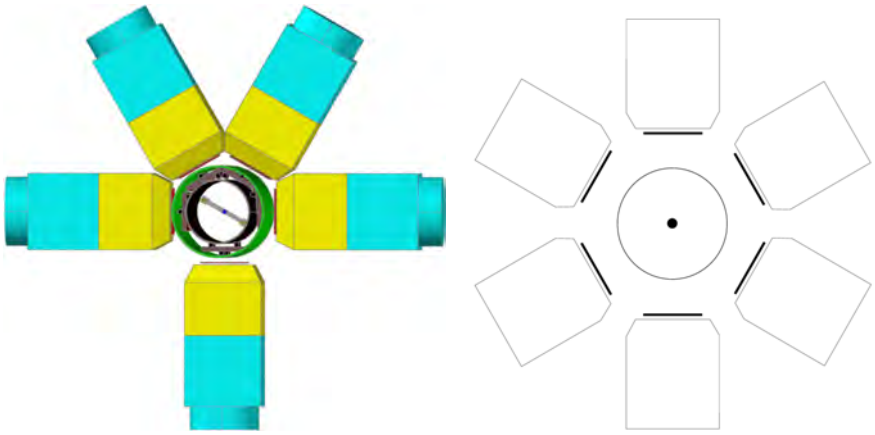

Figure 4.4: *Layout of the spectrometer used to measure the Berllium anomaly. Left: initial set-up. The telescopes are plastic scintillator $\Delta E - E$ detectors to perform particle ID and measure the energy of the pairs. The position of the hits was measured with multi-wire proportional chambers (MWPC). Right: upgraded set-up. The MWPCs were substituted with double sided silicon strip detectors (DSSD) [55].*

4.1.1 Searches for the X17 boson

In addition to the MEG II collaboration, other groups are working to test the anomaly [59] by measuring the IPC spectrum:

- At the Institute of Experimental and Applied Physics (IEAP) at Czech Technical University in Prague, a new experiment is being designed to measure IPC in different nuclear reactions with the COmpact Positron Electron spectrometer (COPE), based on silicon based Timepix sensors and gas detectors [60].
- A 2 MV Van de Graaff accelerator is available at the Laboratori Nazionali di Legnaro (LNL) with deliverable currents up to 1 µA, suitable to perform the measurement of the anomaly. The detector concept is similar to the one used by ATOMKI, but fully performed in vacuum and optimized to minimize multiple scattering [59].
- Due to the observation of the excess in the $^3\mathrm{H}(\mathrm{p},\gamma)^4\mathrm{He}$, the $^3\mathrm{He}(\mathrm{n},\gamma)^4\mathrm{He}$ reaction is considered to provide complementary information. An experiment has been proposed with the pulsed neutron beam generated at the nTOF facility at CERN to measure the IPC spectrum with a nearly 4π acceptance detector [61]. The same group is also working on measuring the $^3\mathrm{H}(\mathrm{p},\gamma)^4\mathrm{He}$ process at the LUNA-MV facility at Laboratori Nazionali del Gran Sasso (LNGS) with a similar detector geometry.
- A dedicated beamline has been installed at the UdeM 6 MV tandem at the Canadian Charged Particle Accelerator Consortium (CCPAC) in

Montreal to deliver a ^{3}He beam to a LiF target and measure the IPC from the nuclear de-excitation of both ^{8}Be and ^{10}Be. The detector is designed to have 95 % angular acceptance and is based on a multi-wire proportional chamber (MWPC) for tracking and scintillating bars for energy measurement [62].

Among these efforts, the MEG II experiment is the only one to have a fully operational set-up and a data-taking campaign has been performed in 2023.

Additional efforts aim to measure the anomaly in other processes:

- In case it exists, the X17 could be produced through the $e^{-}Z \rightarrow e^{-}ZX$ Bremsstrahlung reaction. The NA64 experiment at CERN has combined the data of the runs performed in 2017 and 2018 to set limits on the coupling of the X17 with the electron $1.2 \times 10^{-4} < \varepsilon_e < 6.8 \times 10^{-4}$ [63].
- The Positron Annihilation into Dark Matter Experiment PADME at Laboratori Nazionali di Frascati (LNF) is looking for the resonant production of X17 by impinging a positron beam on a diamond target [64].

A more comprehensive review of the experiments testing the anomaly can be found in [59].

4.2 X17 detection with the MEG II detector

The measurement of the IPC spectrum in the $^7\mathrm{Li}(\mathrm{p},\gamma)^8\mathrm{Be}$ process can be repeated with the MEG II apparatus with minor changes to the system. The target area, including the support and the vacuum hosting the target itself have been redesigned for the IPC measurement due to the high material budget of the standard set-up used for XEC calibrations. Only a subset of the available equipment is required:

- the pTC to trigger the acquisition;
- the CDCH and COBRA to track and measure the energy of the pair;
- two auxiliary γ detectors (see Figure 4.5) to monitor the photon production. A 4×4 Bismuth Germanate (BGO) matrix is used for the CEX measurement and a 3-inch Lanthanium Bromide crystal ($LaBr_3 : Ce$, or Brillance) both read out by PMTs.

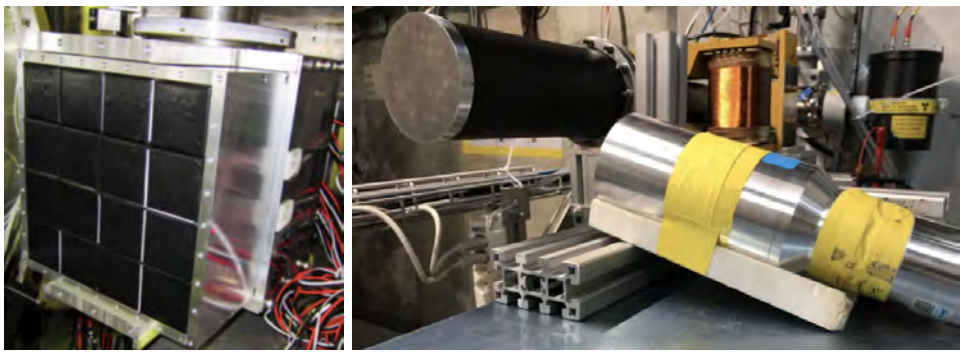

Figure 4.5: *Auxiliary detectors used for the X17 measurement. Left: the 4×4 BGO matrix used for the CEX measurement. Right: the 3-inch Brillance crystal next to the carbon fiber vacuum chamber (black) for testing.*

The Cockroft-Walton accelerator (CW) used for calibrations allows to perform the measurement independently on the schedule of the HIPA facility, letting us taking data during the shut-down periods in early 2022 and 2023. Ideally, the XEC would have been better suited to measure the photon spectrum through the data taking, but the X17 campaigns overlap with the period dedicated to anneal the MPPCs of the XEC. It was possible to still take $\sim$12 h of XEC data during the HIPA service days in May 2023 to improve the resolution on the photon spectrum.

In this configuration, the copper arm and support ring induce external pair conversion (EPC) of the γ from beryllium de-excitation. This effect contributes mostly at low relative angles, while the main expected contribution in the signal region is IPC. A possible X17 is produced with a boost, causing

the expected energy of the positron/electron pair to be:

$$E_{\text{min}} = 5.9\,\text{MeV},\ E_{\text{max}} = 12.2\,\text{MeV} \tag{4.1}$$

The CDCH is specifically designed to accept narrow momentum ranges, not allowing to cover the full interval. During the 2022 tests, data were taken by scaling the field of the COBRA magnet to 15 %, 16 % and 17 % of the value used for MEG II runs, not observing differences in the detector response. The scale for data taking in 2023 was then set to 15 %, accepting positron and electron energies between $\sim$7.5 MeV and $\sim$10.8 MeV.

4.2.1 Target area

The optimization of the target layout is reported in [53, 65]. The lithium target is held at 45° with the beam axis at the center of the COBRA spectrometer by a copper arm. The target is a lithium compound sputtered on a copper substrate which both provides support and heat and charge dissipation to the copper arm. Everything is enclosed in a carbon fiber cylinder with a 13 cm diameter and a 400 µm thickness (see Figure 4.6). The carbon fiber is glued to an aluminum flange and to an aluminum endcap. The chamber is vacuum tight. Three stainless steel rods hold three acrylic rings to reinforce the structure. Two target options have been tested during a run in early 2022:

- 2 µm LIPON (lithium phosphorous oxynitride) sputtered on a 25 µm copper substrate;
- 5 µm LiF (lithium fluoride) sputtered on a 10 µm copper substrate.

The LIPON is a class of compounds with the general formula $Li_xPO_yN_z$, where x, y and z depend strongly on the production process. It allows for micrometric deposits and it can be produced at PSI. The targets used for tests and data taking were all produced at PSI by the *Neutronenoptik und Wissenschaftliches Computing* with the formula $Li_3PO_4N_2$. The elements present in the compound do not introduce background at the energies of interest for this work. The production process does not allow to precisely control the uniformity of the target at such thickness. The LiF can be used to grow precisely depositions on the order of a few micrometers. Additionally, the reaction $^{19}F(p,\alpha\gamma)^{16}O$ is triggered, producing three γ lines of 6.13 MeV, 6.92 MeV and 7.12 MeV with relative yields which depend on the incoming proton energy [66]. This could serve as an additional calibration source for the auxiliary detectors. Due to the high rate associated with the fluorine γ line, the LIPON target has been chosen for the data taking, while the LiF target is used for calibration of the auxiliary detectors.

Figure 4.6: *Left: carbon fiber vacuum chamber. The carbon fiber cylinder is glued to an aluminum endcap and to an aluminum flange. Center: carbon fiber vacuum chamber, inside. Right: target insert. The copper arm is bolted to an aluminum ring which fits into the flange of the chamber. Three stainless steel rods hold acrylic rings to reinforce the structure of the vacuum chamber. The copper target is secured on the arm with a ring to connect to the copper support with screws.*

4.2.2 High fidelity Monte Carlo simulation

The X17 target station is included in the main MEG II Geant4 [39–41] simulation, the so-called GEM. The response of the detector is stored to ROOT [67] files and processed by the *bartender*, which converts the simulated response into waveforms based on measured templates. The waveforms are then processed by the same reconstruction chain used for data. The Zhang-Miller model has been implemented for the event generator as reported in [53]. The 15 MeV line is simulated with a 3 MeV width, while the 18.15 MeV is generated monochromatically. The excited beryllium is assumed to be at rest and the X17 is assumed to decay isotropically in the rest frame. This leads to a minimum relative angle of 134° in the produced pair in the case of a 17 MeV/c^2 invariant mass.
The Monte Carlo (MC) simulation is used to separately produce EPC, IPC and X17 samples and to optimize the reconstruction. While the latter two can be mass produced within a short amount of time, the EPC events are more challenging as they require to generate a γ and then convert. At the time of writing, the MC simulation is not yet final and the MC samples are not yet generated. The foreseen production consists of: 2×10^5 X17, 10^6 IPC18, 10^6 IPC15 and 10^9 γ events to produce EPC.
This work is based on the MC production done in July 2023.

4.2.3 Kinematic variables and observables selection

In the center of mass frame of the X17, the pair is produced back to back and the only degree of freedom is the emission angle of either of them. As-

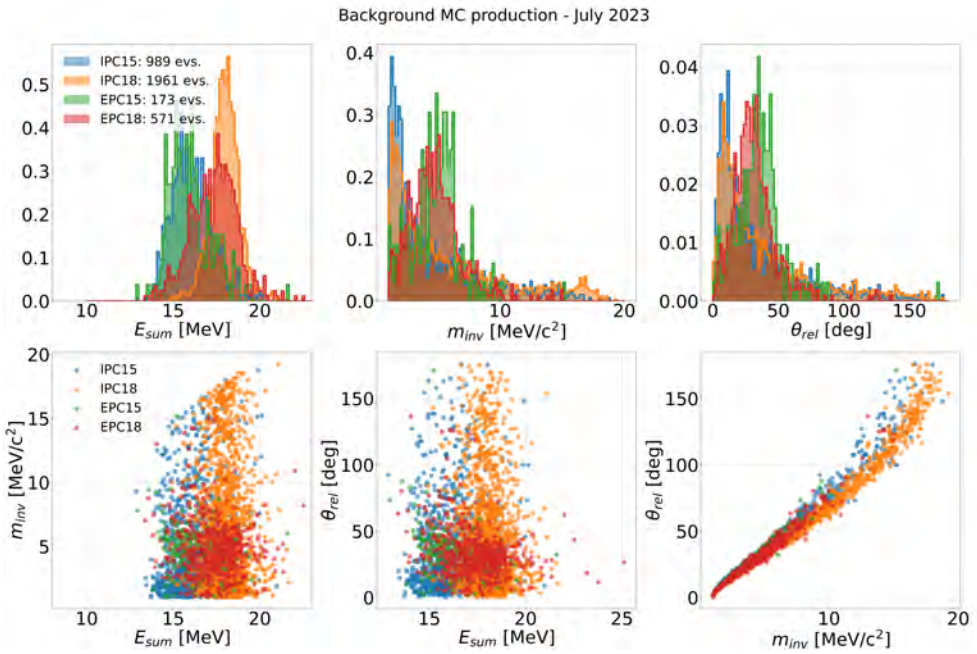

Figure 4.7: *Monodimensional and bidimensional distributions of the reconstructed kinematics variables obtained from the test MC production done in July 2023. Only backgrounds are shown: IPC 15 (blue), IPC 18 (orange), EPC 15 (green) and EPC 18 (red). Due to the nature of the EPC, which requires the interaction of a photon with the set-up to have proper kinematics, the statistics is limited to a few hundreds of events.*

suming the excited beryllium to be at rest, the X17 is generated with a boost $\beta = 0.35$ making the relative angle of the pair dependent on the emission angle in the center of mass frame with respect to the boost. The angular distribution depends on the quantum numbers of the X17, making it a suitable observable to determine its nature.
The sum of the energies of the electron and of the positron (energy sum) allows to discriminate events from the 18.15 MeV and 15.12 MeV lines, making it suitable for blinding.
As an alternative to the relative angle, the invariant mass is considered as well to perform the likelihood analysis for the X17. It is expected to be independent on its quantum numbers, which can be possibly studied in case of a discovery claim. In either case, for both EPC and IPC the invariant mass is expected to be strongly correlated with the relative angle, not providing additional benefits for either of the two.

Figure 4.7 shows the distributions and correlations of energy sum, relative angle and invariant mass of the different background populations with the currently available MC statistics.

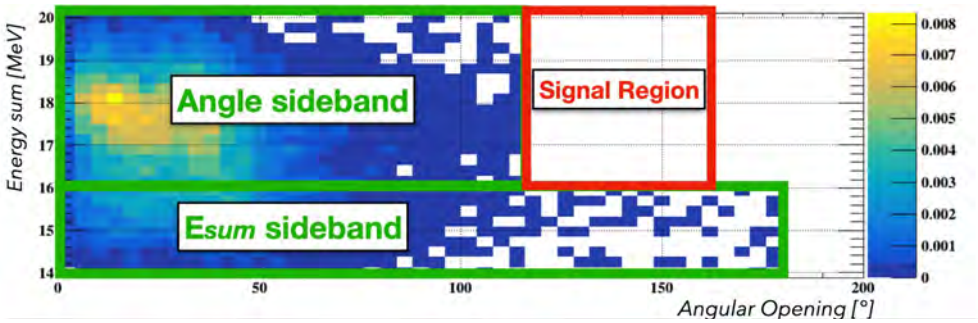

Figure 4.8: *Green: relative angle and energy sum side-bands. Red: blinded box corresponding to the signal region. Gentle courtesy of H. Benmansour, who wrote the track selection and pair reconstruction.*

4.2.4 Blinding strategy

Due to the delicate matter of possibly finding new physics, a main concern is to limit to the minimum extent possible the introduction of bias from the authors of the analysis. This in the years has come in different flavors depending on the nature of the observables [68]. We decided to introduce the same strategy used for MEG II creating a blinded box around the signal region. The box is defined in the energy sum and relative angle space, with the following boundaries:

- $16\,\text{MeV} < E_{\text{sum}} < 20\,\text{MeV}$
- $115^\circ < \theta_{\text{rel}} < 160^\circ$

The choice is based on the $17\,\text{MeV}/c^2$ mass hypothesis and that its width is negligible with respect to MEG II resolution $\sim$590 keV/c^2 [65].

Two side-bands are then defined:

- Energy sum side-band: here the MC production can be compared and benchmarked in the full relative angle range.
- Relative angle side-band: here the probability density functions (PDFs) based on the match in the energy sum side-band can be compared with the data.

Together they provide a first estimate for the population size of the different backgrounds.
Figure 4.8 shows the blinded box and the side-bands. Limited statistics from the dataset (5 % of the total) is included for comparison.

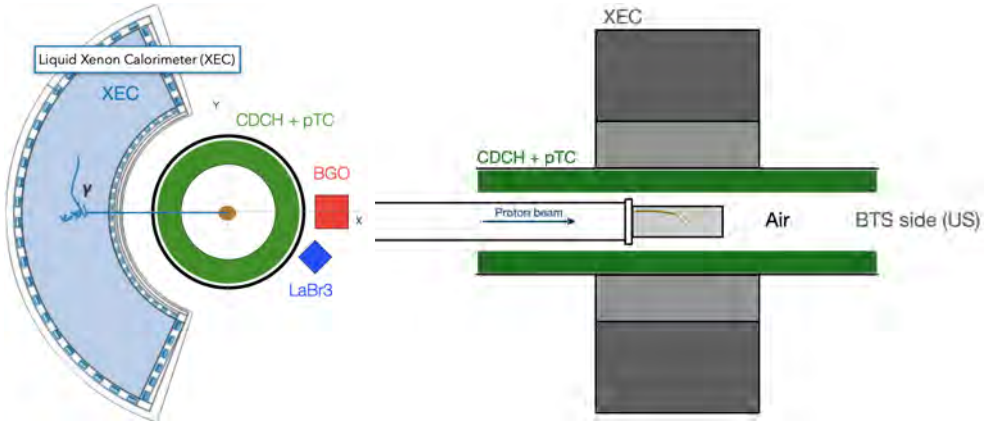

Figure 4.9: *Schematic, not in scale, of the set-up for the X17 measurement. Left: view from the downstream side of the beamline. The proton beam propagates in the direction entering the figure. Right: side view of the set-up. The target is slanted by* 45° *with respect to the proton beam.*

4.2.5 2023 data taking

In February 2023, a data-taking campaign has been carried out to measure the IPC spectrum. A schematic of the layout is shown in Figure 4.9. The measurement was performed in air in absence of the insertion system, which is usually used to push upstream the helium volume in the CDCH to insert the CW beamline.
The trigger required at least 18 hits on each end of the CDCH, so requiring that a signal should have been read on 18 wires per end. At this stage we could not impose the wire to be the same for the hits on the two ends, as it would have needed additional work on the FPGAs of the TDAQ. Furthermore, at least one hit in the pTC was required. The data taking lasted four weeks and the CW current was kept at $\sim$10 µA. With such set-up the trigger rate was $\sim$50 Hz. A few datasets with the LiF target were taken to compare with the expected cross sections and our MC simulation. BGO data have been taken as well for different positions along the beam axis to study the photon asymmetry, which is expected in the MIS state, but not in the MIV. Figure 4.10 shows the γ spectrum as measured with the BGO detector. The calibrations and the analysis of such samples are beyond the scope of this work, but one further point is worth mentioning: during the analysis of the first auxiliary detectors datasets we found the beryllium peak at a energy lower than 18.1 MeV, at 17.8 MeV, which was later confirmed with the XEC. A possible explanation of this effect can be found in diffusion of lithium to the copper substrate either during production or induced by the heat load of the proton beam. Due to energy loss in copper, the substrate causes the access to the 441 keV resonance as well, resulting in a mix of the MIV and MIS states. The investigation of this effect is ongoing.

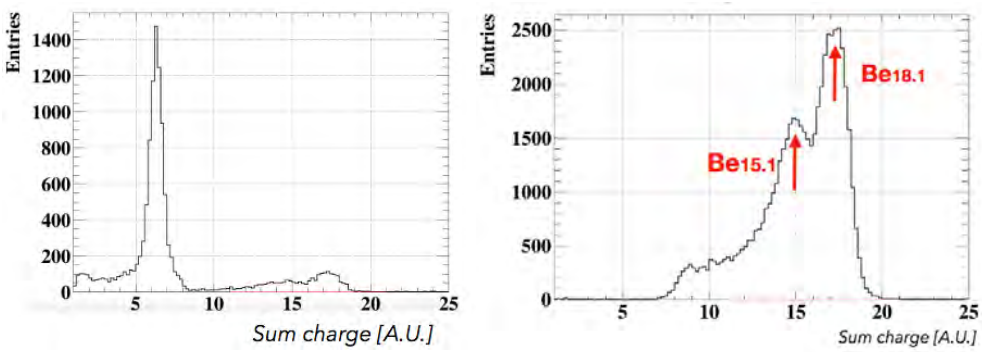

Figure 4.10: *Gamma spectrum as measured with the BGO detector for $E_p = 500\,\text{keV}$ on LiF (left) and for $E_p = 1080\,\text{keV}$ on LIPON (right). Gentle courtesy of H. Benmansour, who wrote the track selection and pair reconstruction.*

In the following, the analysis is presented assuming that only MIS is produced, but such effect needs to be accounted for.

4.2.6 Track reconstruction and pair selection

The track reconstruction of MEG II is optimized positron tracks and was adapted to reconstruct pairs. The fitting procedure is run twice on each event, once with the actual magnetic field orientation and once with opposite polarity, allowing to reconstruct electrons as positrons. Due to multiple scattering in air, most reconstructed tracks cannot be backpropagated to the target. To select event candidates the point of closest approach (POCA) to the beam axis is used instead. A track candidate is selected if the following requirements are met:

- the number of (good) hits in the track is at least 10;
- the longitudinal coordinate of the POCA (z_{POCA}) is closer than 2.5 cm to the target center;
- $t_{0,\text{last hit}} > t_{0,\text{first hit}}$, with t_0 the time of the hit minus the estimated drift time of the ionization cloud;
- $(z_{\text{last hit}} - z_{\text{first hit}}) \cdot z_{\text{first hit}} > 0$, analogous to saying that the track is directed away from the target;
- the propagation length from the first hit to the vertex should be smaller than 35 cm, in case the first turn in the CDCH is not reconstructed;
- if $11 <$ number of good hits < 16, the track density is required to be greater than 1.1 hits/cm. This is a quality check on tracks that do not escape the CDCH volume within the first turn. Figure 4.11, shows the correlation between track density and number of good hits for tracks

that do not escape the CDCH, that do a full turn and that do two full turns together with the cut described here;

- not escaping tracks, should have hit density $> 0.8\,\text{hits/cm}$ and track score = number of good hits $+ 10 \cdot$ hit density > 20;
- the standard deviation of the propagation length between two consecutive hits should be smaller than $0.9\,\text{cm}$ for tracks which do not escape the CDCH to ensure that most hits are included in the reconstruction;
- $|z_{\text{first hit}}| > 2.5\,\text{cm}$;
- all z_{hit} should be in the same half of the CDCH, so they should have the same sign;
- $|z_{mean}| > 2.0\,\text{cm}$, with z_{mean} the mean of the z_{hit} for all good hits, to ensure the track propagates far enough from the target;
- $|z_{mean} \cdot (\theta - 90°)| < 0$, with θ the polar angle of the track at the POCA vertex with the longitudinal direction, to ensure the track is not perpendicular to the beam axis.

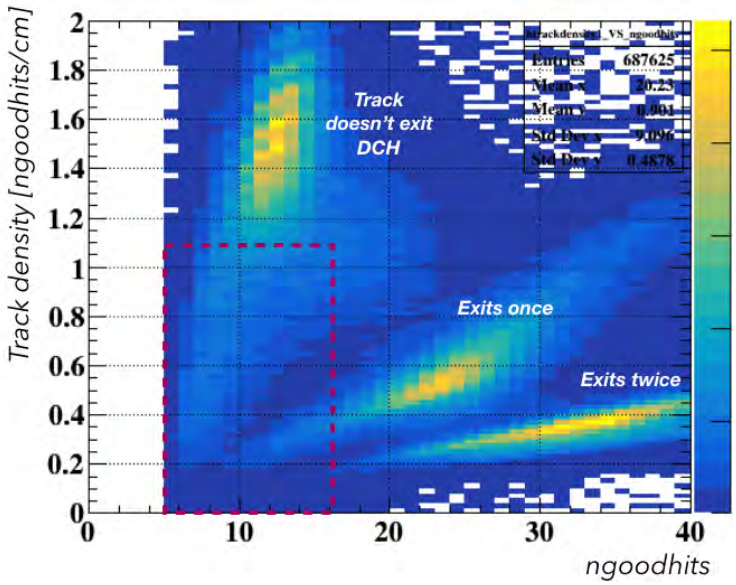

Figure 4.11: *Correlation between track density and number of good hits. Three populations can be distinguished: tracks that do not escape the CDCH; tracks that do a full turn; tracks that do two full turns. An additional cut is shown in red to improve the quality of the population of tracks that do not escape the CDCH. Gentle courtesy of H. Benmansour, who wrote the track selection and pair reconstruction.*

If in the same event, a positron and an electron pass the selection, a pair is defined if:

- the two selected tracks have no hits in common;

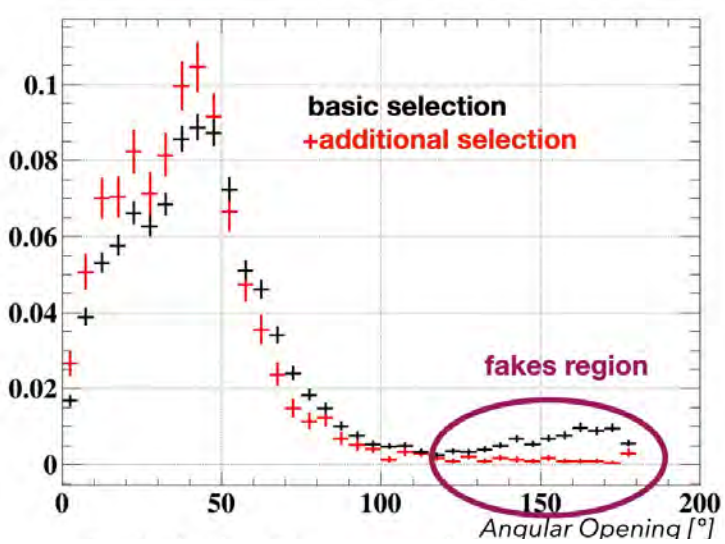

Figure 4.12: *E_{sum} distributions of the X17 data with a basic event selection (black) and the selection described here. Shown is a subsample of the energy sum side-band described in Section 4.2.4. Gentle courtesy of H. Benmansour, who wrote the track selection and pair reconstruction.*

- the distance between the two POCA vertices is lower than 3 cm.

Figure 4.12 shows the effect of such cuts on fake pairs rejection. Based on dedicated MC studies, 1.4 % of the collected data meets the selection criteria.

Due to multiple scattering in air, the reconstucted polar and azimuthal angles at the POCA vertex of the single track and its position are correlated as shown in Figure 4.13 and Figure 4.14. Such effect is mitigated through vertexing: for each pair, a common vertex is imposed with a beam spot constraint using the RAVE tool (Reconstruction in Abstract Versatile Environments) [69] available in GENFIT (Generic Track-Fitting Toolkit) [70]. The beam spot is defined as gaussian, identified by its position on the target and the correlation matrix in the three directions. The position and size of the beam spot on the target was obtained by fitting the single track data to dedicated MC samples:

$$x_{\text{beam spot}} = -2\,\text{mm},\ y_{\text{beam spot}} = -3\,\text{mm} \tag{4.2}$$

$$\sigma_{x,\text{beam spot}} = \sigma_{y,\text{beam spot}} = 3\,\text{mm} \tag{4.3}$$

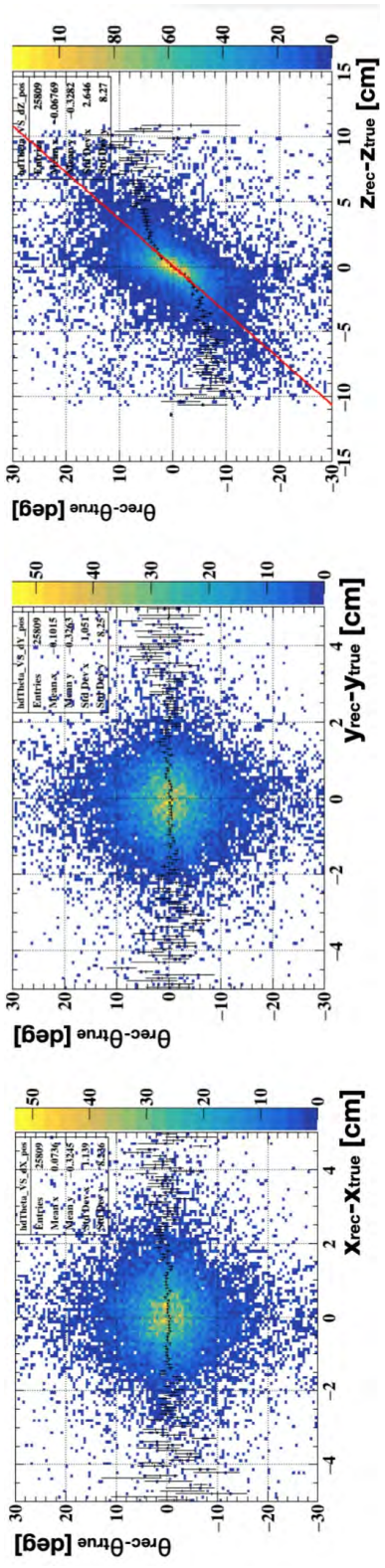

Figure 4.13: *Correlation between the reconstructed polar angle of the track and the position at the POCA vertex.*

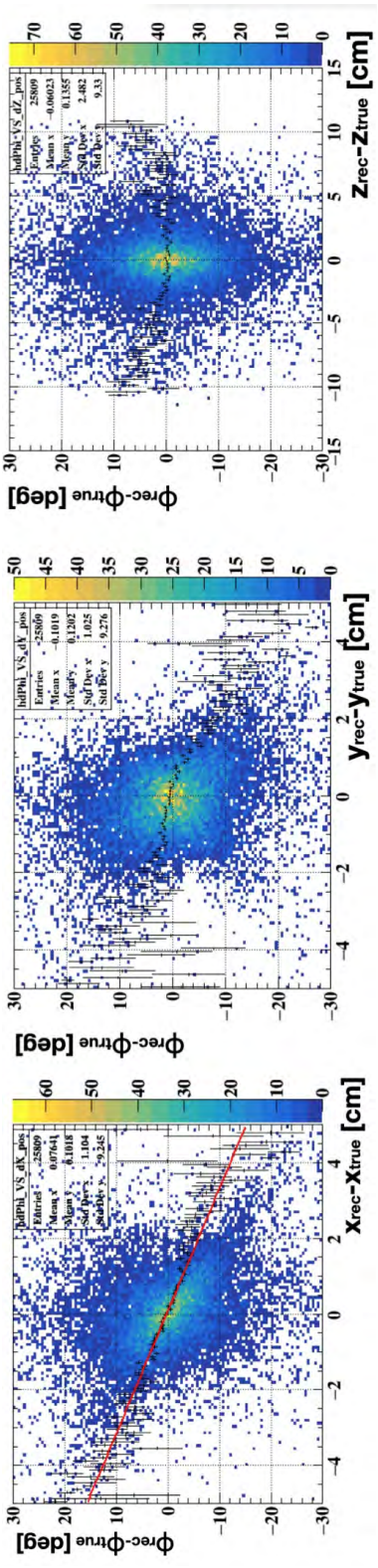

Figure 4.14: *Correlation between the reconstructed azimuthal angle of the track and the position at the POCA vertex. Gentle courtesy of H. Benmansour, who wrote the track selection and pair reconstruction.*

4.3 Likelihood analysis framework

Here, the changes to the framwork used to analyse the data of the MEG II experiment for the X17 analysis are presented.
The aim of the analysis is to provide 90 % confidence bands on both the branching ratio of the X17 to the 18 MeV line and its invariant mass with a full Feldman-Cousins construction [71].
The probability density functions (PDF) for the considered backgrounds are built by parametrizing the spectra computed with GEM, which is benchmarked in the side-bands in Section 4.2.4. Such approach, deepened (see Section 4.3.1), is found to suffer from the limited available MC statistics to model the EPC backgrounds.
A more robust alternative is outlined in Section 4.3.2, where background PDFs are implemented as histogram templates and their statistical uncertainty is included with the Beeston-Barlow (BB) likelihood [72].

4.3.1 Likelihood definition - parametrized background PDFs

Including the signal, five populations are expected to contribute to the likelihood:

- X17;
- internal and external pair creation from the 18.15 MeV line (IPC18 and EPC18);
- internal and external pair creation from the 15.12 MeV line (IPC15 and EPC15).

Due to the overlap between the MEG II experiment and the X17 studies, the development of the analysis framework has started in an early stage before a definitive decision on the strategy to pursue was selected, requiring the framework itself to be flexible and easy to extend. The analysis can either use a binned or unbinned likelihood and it can be run in the 2D space of the invariant mass/relative angle and energy sum, or in the mono-dimensional invariant mass/relative angle.
The unbinned likelihood is then defined as:

$$\begin{aligned} \mathcal{L} &= \mathcal{L}(\mathbf{x}|\hat{\mathcal{N}}_S, \hat{\mathcal{N}}_{EPC15}, \hat{\mathcal{N}}_{IPC15}, \hat{\mathcal{N}}_{EPC18}, \hat{\mathcal{N}}_{IPC18}, m_{\mathrm{X17}}) \\ \mathcal{L} &= \frac{\hat{\mathcal{N}}^{\mathcal{N}} e^{-\hat{\mathcal{N}}}}{\mathcal{N}!} \prod_{i=1}^{m} \Big(\sum_{j=0}^{4} \frac{\hat{\mathcal{N}}_j}{\hat{\mathcal{N}}} pdf_j(\mathbf{x}_i) \Big) \end{aligned}$$

with the index j running between 0 and 4 meaning respectively: X17, EPC 15, IPC 15, EPC 18, IPC 18. Here $\mathbf{x}_i$ is to be intended as the kinematic observables of the event i-th used in the fit. The free parameters are the X17 mass m_{X17} and the expected number of pairs for each population, with their sum distributed as a Poisson.

Analogously, the binned likelihood is defined as:

$$\mathcal{L} = \frac{\hat{\mathcal{N}}^{\mathcal{N}} e^{-\hat{\mathcal{N}}}}{\mathcal{N}!} \prod_{i=1}^{m} \Big(\sum_{j=0}^{4} \frac{\hat{\mathcal{N}}_j}{\hat{\mathcal{N}}} pdf_j(\mathrm{x}_i) \Big)^{N_i} \tag{4.4}$$

with i now running over the bins of the histogram.

Systematic effects are accounted for in the likelihood by introducing nuisance parameters distributed with a gaussian penalty term centered around their expected value:

$$\mathcal{L}_{\text{syst.}} = \mathcal{L} \cdot \prod_{k=1}^{N} \frac{1}{\sqrt{2\pi}\sigma_k} e^{-\frac{(\theta_k - \theta_{k,0})^2}{2\sigma_k^2}} \tag{4.5}$$

with k the index running on the nuisance parameters, θ_k the observed value of the nuisance parameter and $\hat{\theta}_k$ its true value. At the time of writing, the main source of systematics has been identified to be the shape of the PDFs of the EPC events due to the limited available Monte Carlo statistics. Additional sources of systematics are under study.

In case the analysis is run on the mono-dimensional invariant mass or relative angle, the energy sum distribution is fitted separately to estimate the number of pairs in each population. This information is then included in the likelihood analysis to constrain the populations by multiplying the likelihood with a Poisson penalty term for each type of background event:

$$\mathcal{L}_{\text{const}} = \mathcal{L} \cdot \prod_{j=1}^{4} \frac{\hat{\hat{\mathcal{N}}}_j^{\hat{\mathcal{N}}_j} e^{-\hat{\mathcal{N}}_j}}{\hat{\mathcal{N}}_j!} \tag{4.6}$$

with $\hat{\hat{\mathcal{N}}}_j$ the yield estimate of the j-th population from the fit in the energy sum side-band. Due to the analogy with the treatment of nuisance parameters, in the following only the bidimensional analysis case will be shown without constraints.
The basic principle behind the Feldman-Cousins construction (FC) is to define a grid in the space of the parameters of interest, so in this case the branching ratio and the X17 mass, and build the distribution of the likelihood ratio for each point by running a toy Monte Carlo (ToyMC) experiment. Each toy experiment is composed of a number of ToyMCs, generated as follows:

1. if systematics are included, each nuisance parameter is profiled using the *a priori Highland-Cousins* prescription [73, 74], where each nuisance is sampled around its expected value from the gaussian penalty term;
2. the size of each background population is sampled from a Poisson distribution with average equal to the corresponding value from the maximum likelihood fit;

3. from the PDFs of each population, possibly with the generated systematics, the kinematic observables are sampled if the likelihood is unbinned, or the population of each bin of the histogram of the kinematic variables is sampled with a multinomial distribution.

At this point, the likelihood ratio λ_{LR} is computed by profiling the nuisance parameters and any other parameter which is not of interest, like the yields of the backgrounds:

$$\lambda_{LR} = -2[\ln(\mathcal{L}(\hat{\hat{\theta}}, \theta_{k,0})) - \ln(\mathcal{L}(\hat{\theta}))] \tag{4.7}$$

where the double hat parameters now are the best values from the fit with the k parameters fixed to the values $\theta_{k,0}$ in the FC grid. For each toy experiment, the single ToyMCs are sorted by λ_{LR}. The likelihood ratio is then computed for data and the local Confidence Level (CL) is found as the fraction of ToyMCs with a lower likelihood ratio than data. The confidence belts are then built by selecting the iso-CL curves. Here, the 90 % CL belts are considered. The number of ToyMCs per toy experiment determines the accuracy to which the CL is computed. The uncertainty on the CL can be estimated locally with the standard deviation of the binomial distribution:

$$\sigma_{\hat{\mathrm{CL}}} = \sqrt{\frac{\hat{\mathrm{CL}}(1-\hat{\mathrm{CL}})}{N_{\mathrm{ToyMC}}}} \tag{4.8}$$

with $\hat{\mathrm{CL}}$ being the local estimate of the CL and N_{ToyMC} the number of ToyMCs in the current toy experiment.
To compute the significance of a possible signal, it is sufficient to perform a toy experiment for a null branching ratio and the p-value is the local CL. For a signal strength greater than $5\,\sigma$ this process can be demanding on the computing resources. In such a case, the p-value would be lower than 3×10^{-7}. To claim such a discrepacy, more than 10^7 MC are required, based on Equation 4.8. Currently our strategy is to perform the test by generating at most 10^7 ToyMCs and, if the likelihood ratio of the experimental dataset keeps on being lower than that of the ToyMCs, estimating the p-value based on the asymptotic λ_{LR} distribution of the data. Wilks' theorem [75] cannot be used in case the null hypothesis does not depend on one of the fitting parameters. In this case, the null hypothesis does not depend on the X17 variables, like the mass. The global p-value is computed with the trial factors technique [76]. Additional details are reported in Section 4.3.2. The likelihood is fitted using the MINUIT algorithm [77] implemented in the TMinuit class from ROOT [67].

If compared with the analysis of MEG II, the framework has been extended to higher dimensional parameter grids and the binned likelihood analysis has been added.
The PDFs can be selected from a dedicated database, allowing for a good versatility.

4.3.1.1 Test PDFs

For the tests presented here, the PDFs are parametrized based on the limited MC production done in July 2023 (see Figure 4.7). A sample of 10^4 EPC18 events, comparable in size to the expected final production given in Section 4.2.2, is sampled from the so-obtained PDF and is used to estimate the expected statistical uncertainty on the PDF parameters for the FC construction. The same is done for the EPC15 PDF.
Table 4.1 shows the yields of each population estimated by comparing the measured and simulatted BGO trigger rates during 2023 data taking. These numbers are to be considered provisional.

	X17	EPC 15	IPC 15	EPC 18	IPC 18
Population size	450	3.75×10^4	2.75×10^4	1.35×10^5	5×10^4

Table 4.1: Population sizes used for the likelihood analysis tests.

Figure 4.15 shows an example of ToyMC dataset. A cut in energy sum above 16 MeV is also shown. For the 2D analysis, the monodimensional PDFs are considered to be uncorrelated. Further MC statistics is required to confirm this assumption. Possible alternatives are 2D PDF parametrizations or building a likelihood by multiplying the total marginal distributions in energy sum and either relative angle or invariant mass. An example of binned likelihood fit is shown in Figure 4.16.
The parametrization and the parameters with their uncertainties are collected in Appendix D.

Of particular relevance are the PDF employed to model the EPC spectra. The energy sum E_{sum} is modelled with an asymmetric gaussian:

$$\begin{aligned} pdf_{EPC}(E_{\text{sum}}) &= (E_{\text{sum}} < \mu_E) \cdot \mathcal{G}(E_{\text{sum}}|\mu_E, \sigma_{E,L}) && (4.9) \\ &+ (E_{\text{sum}} \geq \mu_E) \cdot \mathcal{G}(E_{\text{sum}}|\mu_E, \sigma_{E,R}) && (4.10) \end{aligned}$$

with $\mathcal{G}$ the gaussian distribution and the subscripts L and R standing for left and right respectively. The relative angle θ_{rel} is modelled as a gaussian with asymmetric asymptotes:

$$\begin{aligned} pdf_{EPC}(\theta_{\text{rel}}) &= (\theta_{\text{rel}} < \mu_\theta) \cdot \exp\Big(-\frac{1}{2}\frac{(\theta_{\text{rel}} - \mu_\theta)^2}{\sigma_\theta^2 + \alpha_L^2 \cdot (\theta_{\text{rel}} - \mu_\theta)^2}\Big) && (4.11) \\ &+ (\theta_{\text{rel}} \geq \mu_\theta) \cdot \exp\Big(-\frac{1}{2}\frac{(\theta_{\text{rel}} - \mu_\theta)^2}{2\sigma_\theta^2 + \alpha_R^2 \cdot (\theta_{\text{rel}} - \mu_\theta)^2}\Big) && (4.12) \end{aligned}$$

The shape of the PDFs in the signal region is crucial, specially due to the lack of EPC statistics from the MC simulations. No EPC events are expected in the signal region, but a wrong parametrization can affect the sensitivity of the analysis. Based on this considerations, a ranking of the systematic

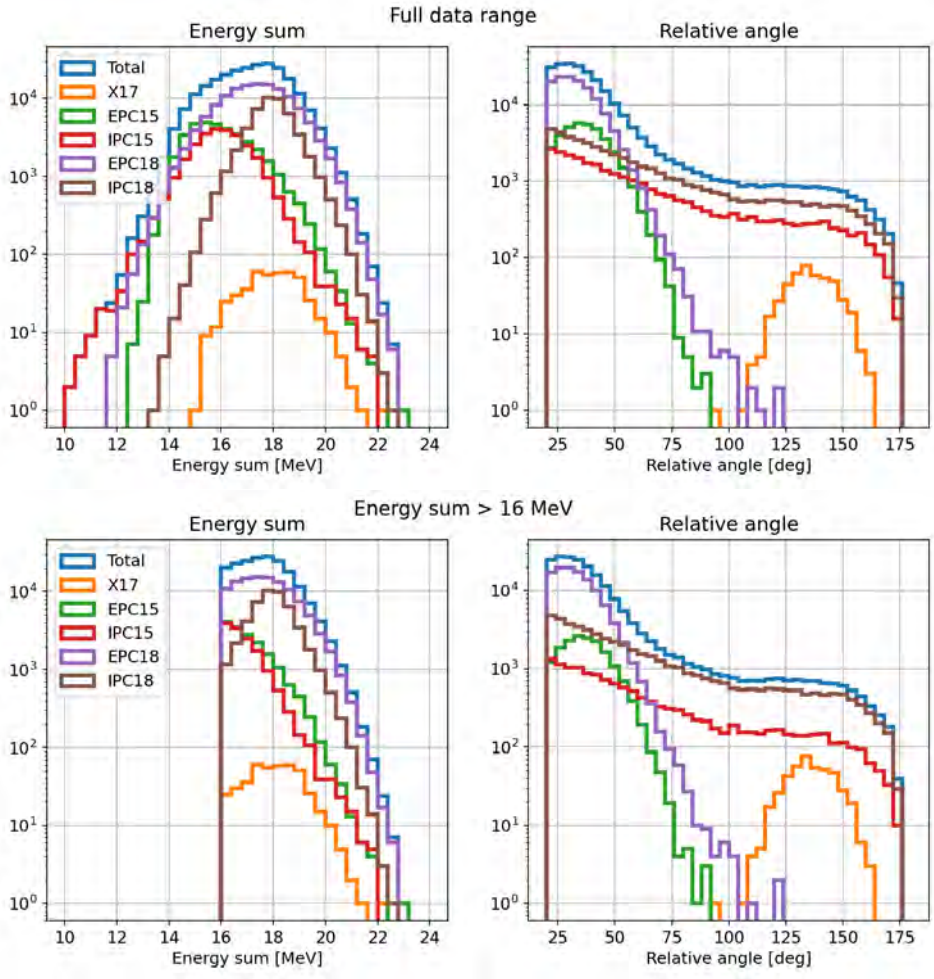

Figure 4.15: *Energy sum (left) and relative angle (right) spectra of the expected pair populations produced from the PDF estimate described in the text. Top: total marginal distributions. Bottom: marginal distributions with an energy sum cut above* 16 MeV.

effects was developed and four possible sets of systematics are considered for the final fit:

- OPTION 0: only the systematics not related to the shape of the EPC PDFs are fitted, e.g. signal normalization;
- OPTION 1: OPTION 0 plus α_R of both EPC 15 and EPC 18 are included;
- OPTION 2: OPTION 1 plus σ_θ of both EPC 15 and EPC 18 are included;
- OPTION 3: OPTION 2 plus the energy sum parameters of both EPC 15 and EPC 18 are included.

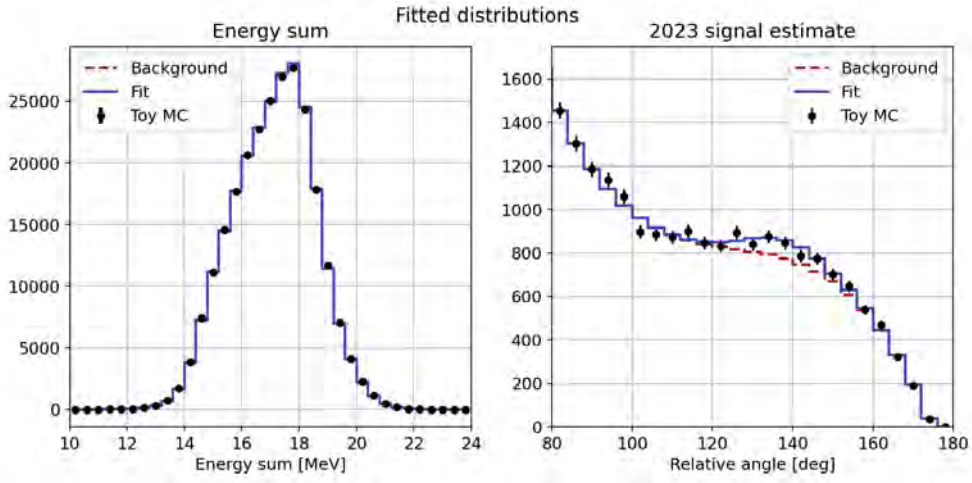

Figure 4.16: *Example of binned likelihood fit of the ToyMC (black) sample in Figure 4.15. No nuisance parameters are included. Here the marginal distributions are shown. The fit is performed with the binned likelihood using 2-dimensional PDFs in E_{sum} and θ_{rel}. The best fit is shonw in blue. The sum of the background PDFs is shown in red.*

4.3.1.2 Preliminary tests

Figure 4.17 shows a comparison between the estimators from the unbinned and binned likelihood analysis on 500 ToyMC samples. The nuisance parameters are fixed to the expected values. The yields of the backgrounds are summed to improve readability.
The analysis is performed on the relative angle between 20° and 180° and on the energy sum between 10 MeV and 24 MeV. The histograms for the binned analysis are built with 40 bins in relative angle and 35 bins in energy sum. Whereas the distributions of the estimators are compatible, the binned analysis runs on average in 0.8 s, while the unbinned analysis requires on average 62 s. The former is therefore preferred for the FC construction, as it allows for a faster data processing and a bigger ToyMC production.
In the following, the tests shown are carried out with the binned likelihood analysis only.

Figure 4.18 shows the distribution of the estimators when the nuisance parameters are included in the fit. OPTIONS 1, 2 and 3 in Section 4.3.1 are tested by sampling 500 ToyMCs to show the effect of the uncertainty on the parametrization of the PDFs of EPC15 and EPC18. For each ToyMC, the free nuisance parameters are sampled as described in Section 4.3.1. OPTION 1 and OPTION 2 do not introduce sensible changes to the estimators. OPTION 3 instead causes the signal yield to be always compatible with zero. The overpopulated bin in the background yield is due to the minimizer reaching the allowed range for the signal parameters. This is likely linked

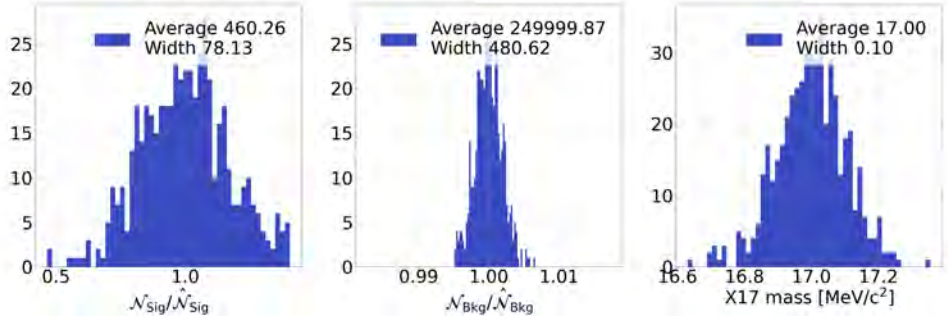

(a) Unbinned likelihood analysis

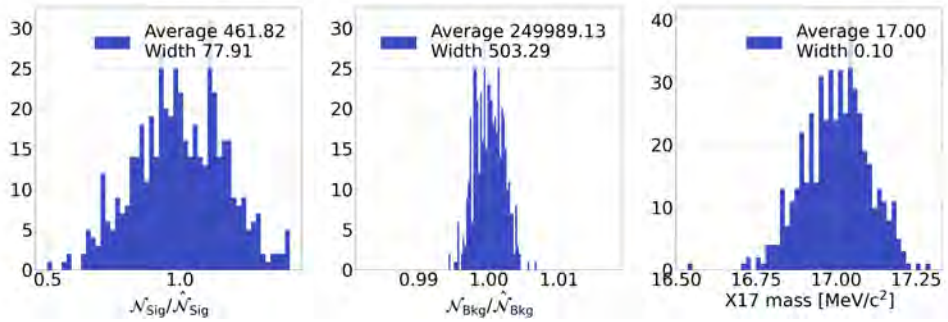

(b) Binned likelihood analysis

Figure 4.17: *Distributions of the yield estimators and of the X17 mass estimator generated by fitting 500 different ToyMCs with the unbinned (top) and binned (bottom) likelihood. The yields are normalized to their averages and the background yields are summed to improve readability. The estimators are unbiased and compatible between the two analysis. Because the binned analysis is faster, it is preferred for the FC construction.*

to the parametrization chosen for the E_{sum} EPC PDFs and therefore to the low MC production this study is based on. As shown in Figure 4.7, the original MC production resulted in a few hundreds of EPC events for both the 15 MeV and the 18 MeV lines. The chosen parametrization correctly reproduces the behaviour of such sample, but the lack of statistics in the tail can have lead to an improper parametrization.
Further tests are required when the final MC production will be available, but the statistics is expected to be on the same order of magnitude, if not lower, than the expected population size in data.
Moreover, the current strategy does not account for possible correlations between energy sum and relative angle, which cannot yet be excluded.

To tackle both issues, a different approach was proposed and is described in the following.

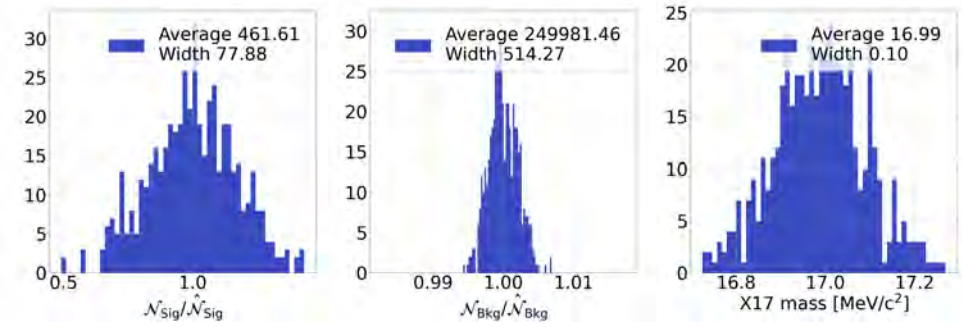

(a) OPTION 1

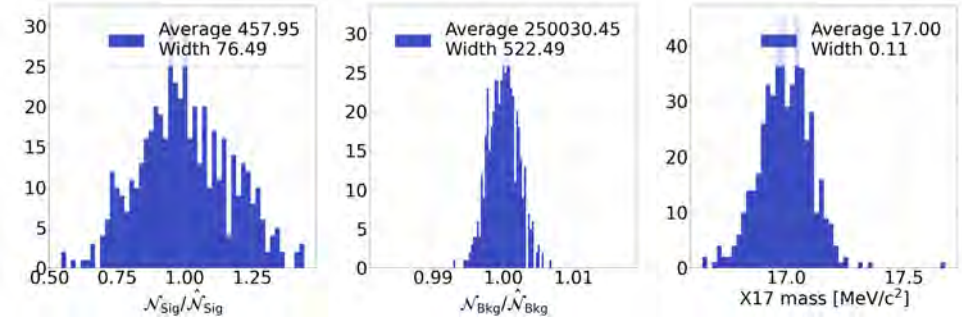

(b) OPTION 2

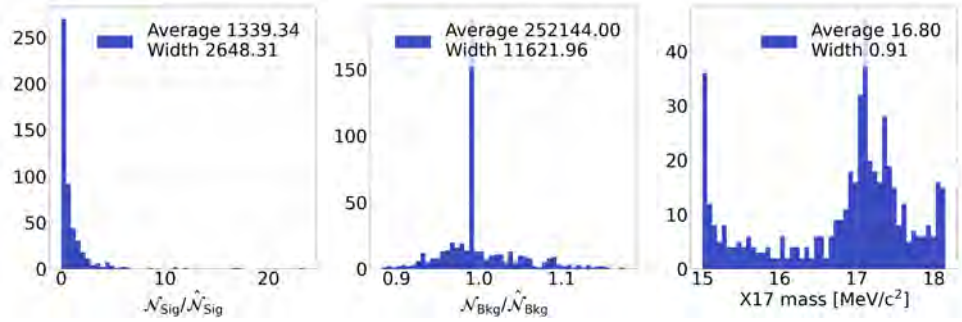

(c) OPTION 3

Figure 4.18: *Distributions of the yield estimators and of the X17 mass estimator generated by fitting 500 different ToyMCs with the binned likelihood. The yields are normalized to their averages and the background yields are summed to improve readability. The effect of the nuisance parameters linked to the EPC PDFs is shown. OPTION 1 (top) and OPTION 2 (center) reported in Section 4.3.1 do not introduce changes with respect to the estimators in Figure 4.17. OPTION 3 (bottom) instead causes the estimated signal yield to be always compatible with zero. The overpopuletd bin in the background yield is due to the minimizer reaching the limits of the allowed range for the signal parameters.*

4.3.2 Likelihood definition - template background PDFs

Due to the low MC statistics currently available ($\sim 5 \times 10^2$ EPC, $\sim 10^4$ IPC) to study the estimators from the likelihood analysis and to the low statistics ($\sim 10^4$ EPC, $\sim 10^5$ IPC) that will be available from the final MC production with respect to the expected population size in data (see Table 4.1), an alternative likelihood has been defined.
In [72], the authors derive the complete binned likelihood for template fits including the effect of low MC statistics. The population of each bin is distributed with a Poisson distribution around their true value. The likelihood is the sum of a term describing the data ($\mathcal{L}_{data}$) and of a term describing the templates ($\mathcal{L}_{nuisance}$):

$$\ln \mathcal{L} = \ln \mathcal{L}_{data} + \ln \mathcal{L}_{nuisance} \tag{4.13}$$

$$= \sum_{i=1}^{n} D_i \ln f_i - f_i + \sum_{i=1}^{n} \sum_{j=1}^{m} a_{ji} \ln A_{ji} - A_{ji} \tag{4.14}$$

with:

- n is the number of bins
- m is the number of populations
- D_i is the population in the data i-th data bin
- f_i is the estimated population in the i-th bin
- a_{ji} is the observed statistics in the j-th MC sample in bin i
- A_{ji} is the estimator of a_{ji}

This approach introduces one nuisance parameter per bin per population. The nuisance parameters A_{ji} are used to estimate f_i:

$$f_i = \sum_{j=1}^{m} p_j A_{ji} \tag{4.15}$$

$$p_j = \frac{\hat{\mathcal{N}}_{j,data}}{\mathcal{N}_{j,MC}} \tag{4.16}$$

The figure p_j is called *population strength* and it is more relevant than the population yield in this case as it embedds not only the amount of events in data, but it also the difference in statistics between the generated MC and the data.

The maximum of the likelihood is found by differentiating it with respect to p_j and A_{ji} and setting the derivatives to zero:

$$\frac{\partial \ln \mathcal{L}}{\partial p_j} = \sum_{i=1}^{n} \frac{D_i}{f_i} A_{ji} - A_{ji} = 0 \quad \forall j \tag{4.17}$$

$$\frac{\partial \ln \mathcal{L}}{\partial A_{ji}} = \frac{D_i}{f_i} p_j - p_j + \frac{a_{ji}}{A_{ji}} - 1 = 0 \quad \forall i, j \tag{4.18}$$

leading to $m \cdot (n+1)$ equations to be solved simultaneously.
Equation 4.18 can be rewritten as:

$$1 - \frac{D_i}{f_i} = \frac{1}{p_j}\Big(1 - \frac{a_{ji}}{A_{ji}}\Big) \quad \forall i, j \tag{4.19}$$

The left hand side term depends only on i, and it is usually defined as t_i:

$$t_i = 1 - \frac{D_i}{f_i} \tag{4.20}$$

Equation 4.18 can then be solved for A_{ji}:

$$A_{ji} = \frac{a_{ji}}{1 + t_i \cdot p_j} \tag{4.21}$$

meaning that for a given set of p_j, only one nuisance parameter per bin is free, t_i. If $D_i = 0$, $t_i = 1$. If $D_i \neq 0$, Equation 4.17 can be written as:

$$\frac{D_i}{1 - t_i} = f_i = \sum_{j=1}^{m} p_j A_{ji} = \sum_{j=1}^{m} p_j \frac{a_{ji}}{1 + t_i \cdot p_j} \tag{4.22}$$

which is a set of independent non-linear equations in the t_is.

To maximize the likelihood, the authors propose to either solve the system of equations numerically or to use a minimizer like MIGRAD to minimize with respect to the p_js only, while for each set of p_js, the t_is are computed by solving Equation 4.22.
Here the latter approach is used. The likelihood was implemented in python and the minimization is performed with the MINUIT algorithm [77] in the implementation of the *iminuit* [77] package. Equation 4.22 is solved with the BRENT algorithm [78] in the implementation of the *brentq* function from the *scipy* [38] package.

Special care is needed to handle bins where the a_{ji}s are zero. In case $D_i = 0$, $t_i = 1$. Otherwise, 4.19 gives:

$$t_i = -\frac{1}{p_k} \tag{4.23}$$

with k running on the populations with $a_{ki} = 0$. Such solution is problematic as it leads to inconsistencies when different templates are null in the same bin. Action is required only if the discrepacy between D_i and f_i is statistically significant. This can happen only when the *strongest* population, the population with maximum p_k, has a null a_{ki}. In such a case, only A_{ki} is inflated to compensate for the discrepacy. This is justified by the fact that the strongest population is the one for which a variation in A_{ki} is expected to have the largest effect on the likelihood.
In such a case, the nuisance parameter is set to:

$$t_i = -\frac{1}{p_{max}}, \quad \text{if} \quad a_{ki} = 0 \quad \text{and} \quad p_k = p_{max} \tag{4.24}$$

Equation 4.22 can then be solved for A_{ki}:

$$A_{ki} = \frac{D_i}{1 + p_{max}} - \sum_{j \neq k}^{m} \frac{p_j \cdot a_{ji}}{p_{max} - p_j} \tag{4.25}$$

If $A_{ki} > 0$, the discrepacy between D_i and f_i is significant and the correction is needed. The other A_{ji}s are computed from Equation 4.21. If $A_{ki} <= 0$, the discrepacy is not significant. In case there are some $a_{ji} \neq 0$, Equation 4.22 is solved normally, otherwise A_{ji} is set to 0.

Such approach allows to correctly include the effect of limited MC statistics in the likelihood and is easily adapted for N-dimensional binning, therefore naturally accounting for possible correlations between the kinematic variables.
In the case of the X17, the mass is an additional parameter to be included to the fit. Here, the templates are used for the background, while a parametrization is used for the signal. The expression of the likelihood stays the same, but no A_{ji} or a_{ji} is defined for the signal. This is analogous to include a template for the signal in the limit for $p_{\text{signal}} \to 0$, so that no correction is applied to it:

$$a_{ji} = pdf_{j,i} \quad \text{if} \quad j = \text{signal} \tag{4.26}$$

$$A_{ji} = p_j \frac{a_{ji}}{1 + t_i \cdot p_j} \approx p_j a_{ji} \quad \text{if} \quad j = \text{signal, for } p_j \to 0 \tag{4.27}$$

4.3.2.1 Preliminary tests

Two scenarios are considered:

- *ideal statistics* scenario: each MC template is populated on average with 10^5 events
- *current statistics* scenario: each EPC template is populated on average with 10^4 events, while each IPC template is populated on average with 10^5 events

An example of fit for both scenarios is shown in Figure 4.19. The binning has been reduced here to 20 bins between 20° and 180° in θ_{rel} and 14 bins between 10 MeV and 24 MeV in E_{sum} to speed up convergence. The t_is are shown as well. A negative t_i results in an inflation of the corresponding template bins, while a positive t_i results in their reduction. As expected, where $D_i = 0$ the t_i is set to 1.

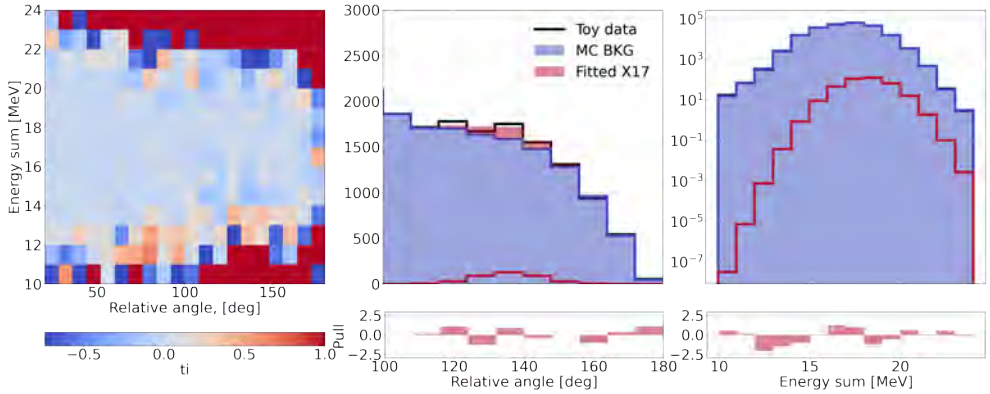

(a) Ideal statistics scenario

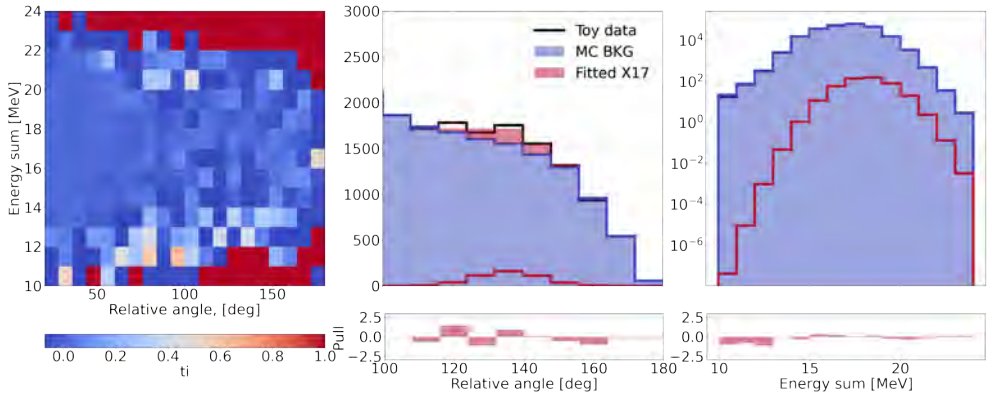

(b) Current statistics scenario

Figure 4.19: *Example of maximum likelihood fit for the template likelihood. The fit is performed on the same toy data sample in the ideal and in the current statistics scenarios. The heatmaps on the left show the fitted value of the t_i nuisance parameters. In the ideal statistics scenario, each template is populated on average with 10^5 events. In the current statistics scenario, each EPC template is populated on average with 10^4 events, while each IPC template is populated on average with 10^5 events. The fit is performed in the full data range, but only the signal region is shown to ease the interpretation of the results. The pull distribution on both relative angle and energy sum is shown below their respective histograms. Whereas here only the marginal distributions are shown, the fit is performed in the 2D space.*

To estimate the significance, the theorem of Wilks cannot be used due to the fact that the likelihood does not depend on the X17 mass when the signal

yield is set to zero. To estimate the significance, 10^2 toy MC with no signal where generated. For each toy MC, the templates were sampled as well. For each iteration, the test statistics $q(m)$ was computed:

$$q(m) = \lambda_{LR}(m) = -2[\ln(\mathcal{L}(m, \hat{\hat{\theta}}, \theta_{k,0})) - \ln(\mathcal{L}(m, \hat{\theta}))] \tag{4.28}$$

Then, as described in [76], the number of *up-crossing* is computed for each iterations as the number of times $q(m)$ passes over a certain value c_0. The value of c_0 is chosen to be $DOF - 1$ (degrees of freedom), with $DOF = 2$ (signal yield and mass) to maximize the average number of up-crossings. Figure 4.20 shows an example of such iteration. The average number of up-crossings is then used to compute the global p-value:

$$P(q(m) > c) \leq P(\chi^2_{DOF} > c) + \langle N(c_0) \rangle \Big(\frac{c}{c_0}\Big)^{\frac{DOF-1}{2}} e^{-\frac{c-c_0}{2}} \tag{4.29}$$

where c is the observed value of $q(m)$ for the data. With this approach it is possible to make an estimate of the asymptotic likelihood ratio distribution with a limited number of ToyMCs.
In principle the average number of up-crossings depends on the set of templates, so that the full procedure should be repeated for each sample separately. Due to the heavy computational cost and to the PDFs being provisional, here the average number of up-crossings is computed for two reference set of templates only, one for the ideal and one for the current statistics scenario and assumed to be the same for all generated sets.
The average number of up-crossings for $c_0 = 1$ is shown in Table 4.2. Figure 4.21 and Figure 4.22 show the distributions of the estimators for the population yields and for the X17 mass in the ideal and current statistics scenarios respectively, obtained by running $\sim 10^3$ ToyMCs for each scenario. At each iteration both the templates and the data histograms were sampled from the PDFs shown in Section 4.3.1.2. The yields are normalized to the average of their respective distributions to improve readability. The X17 yield is Poisson sampled around 500 as an example. The time needed for the template fit is maximum when no X17 events are injected in the ToyMCs and on average it is 6.4 s for the current statistics scenario and 8.8 s for the ideal statistics scenario to run.

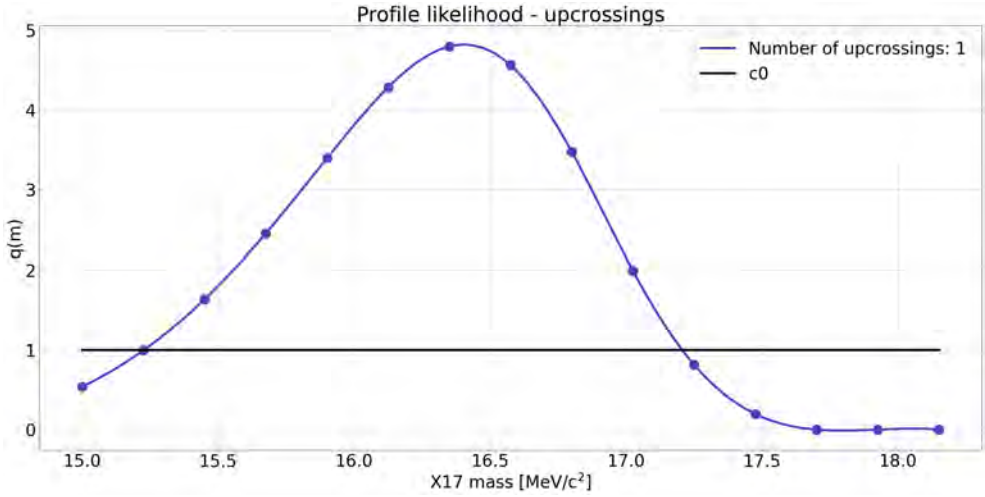

(a) Ideal statistics scenario

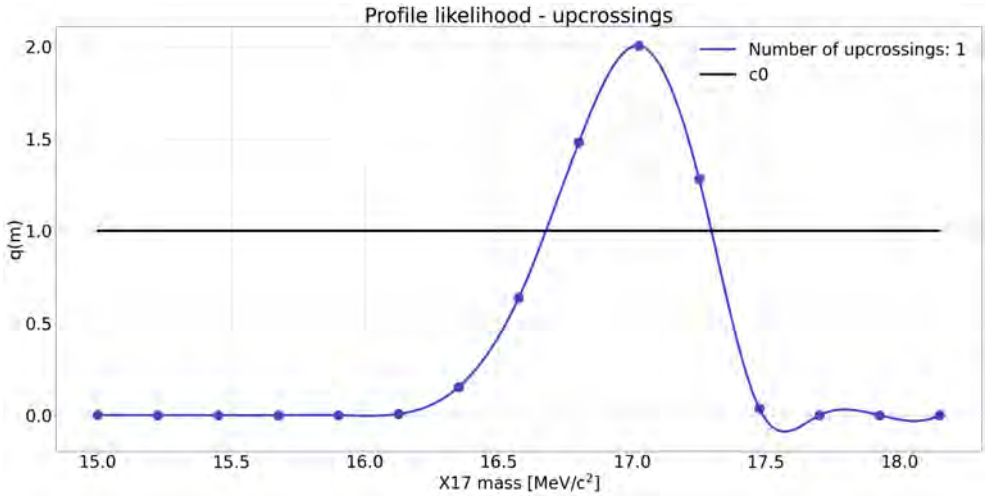

(b) Current statistics scenario

Figure 4.20: *Example of up-crossing computation for the template likelihood. The same ToyMC data sample is shown for the two template scenarios: ideal statistics (top); current statistics (bottom). The shape of the likelihood depends on the templates as well, so a direct comparison is not possible. In both cases the likelihood crosses the threshold, registering one up-crossing each.*

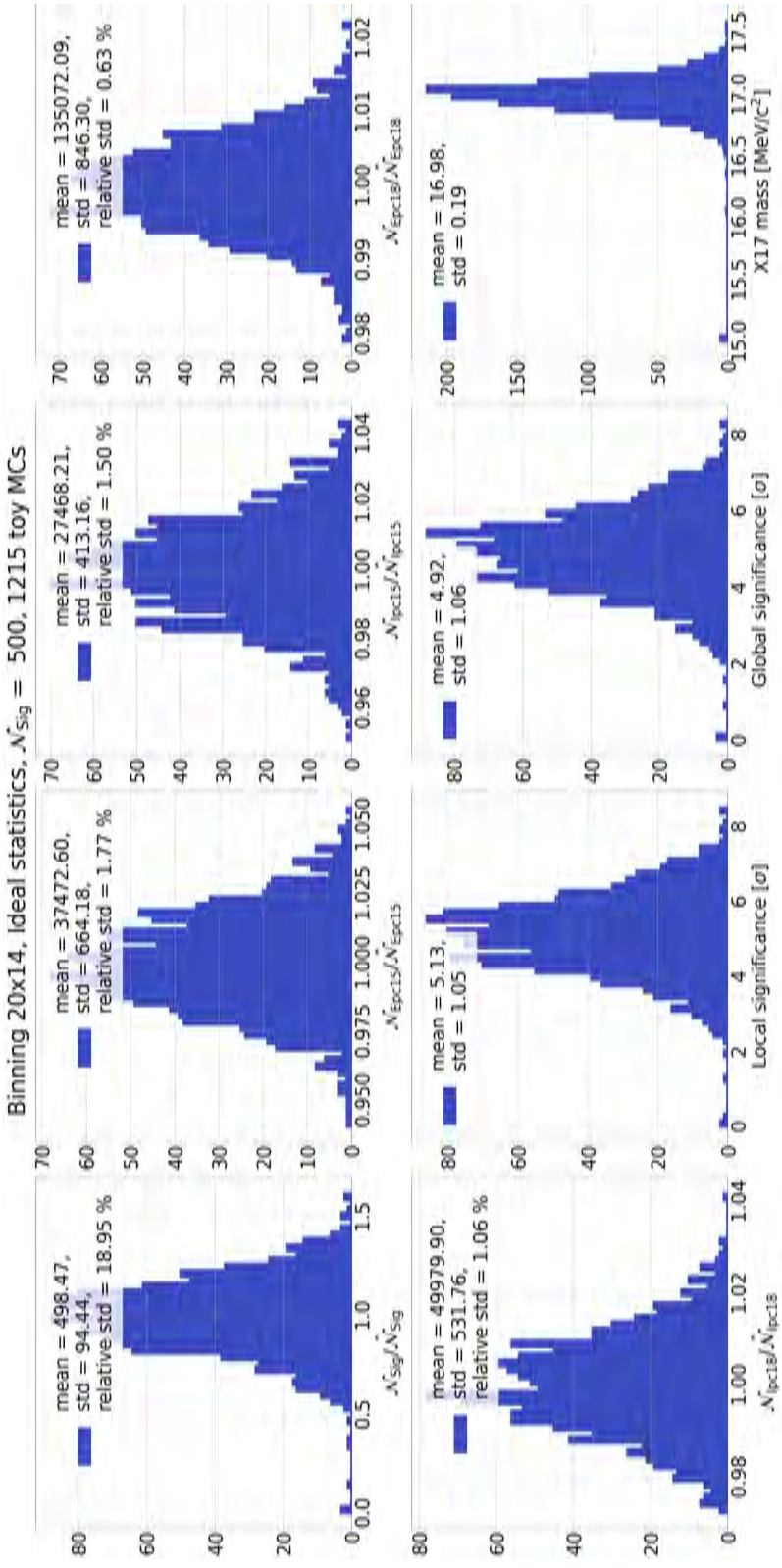

Figure 4.21: *Distribution of the yield and X17 mass estimators in the ideal statistic scenario. The yields are normalized with the average value of the respective distributions to improve readability. The local and global significance distributions are shown as well.*

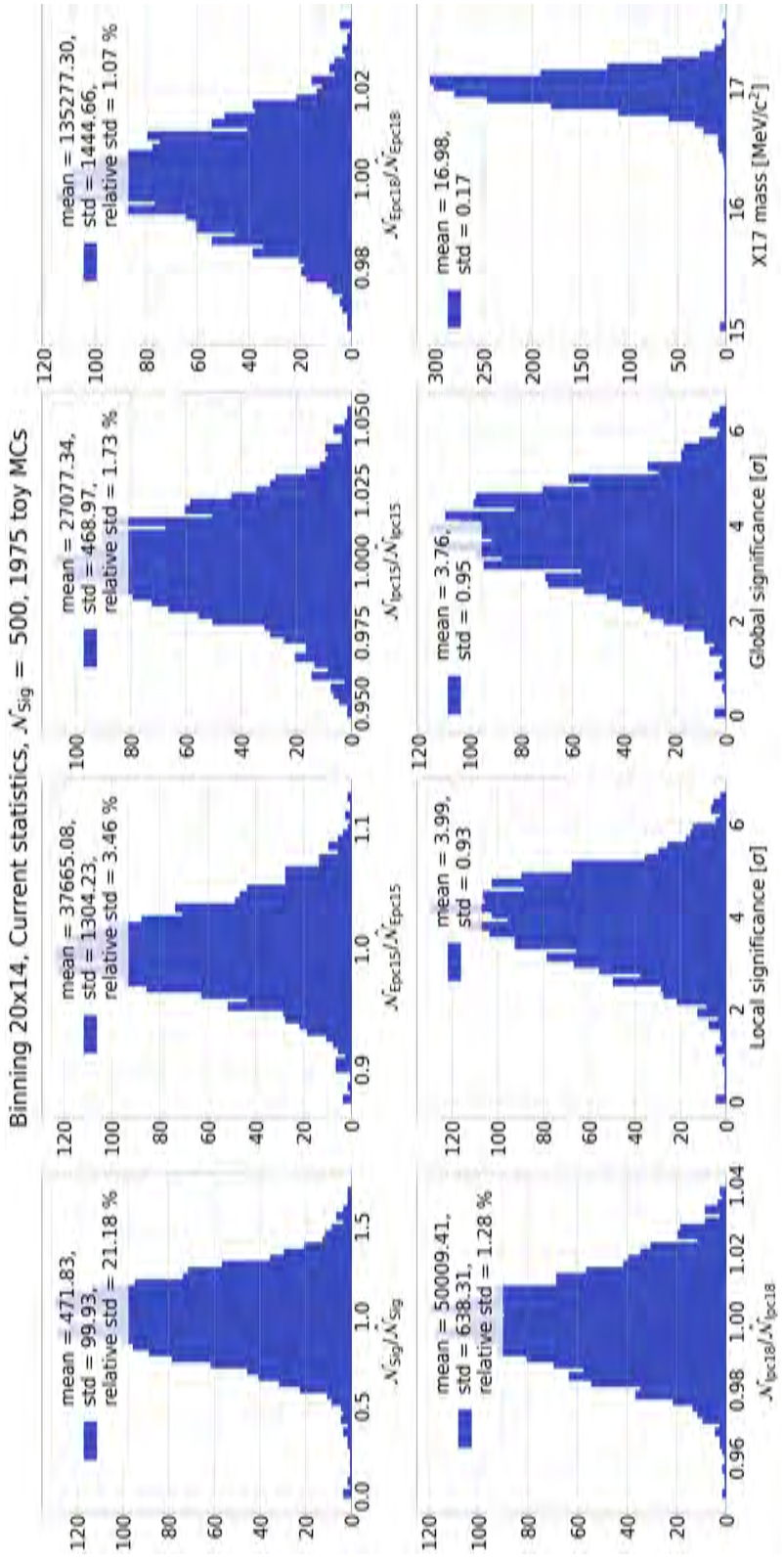

Figure 4.22: *Distribution of the yield and X17 mass estimators in the current statistic scenario. The yields are normalized with the average value of the respective distributions to improve readability. The local and global significance distributions are shown as well. Compared to Figure 4.21, when decreasing EPC template statistics by factor ten, the significance is reduced by* 0.5σ.

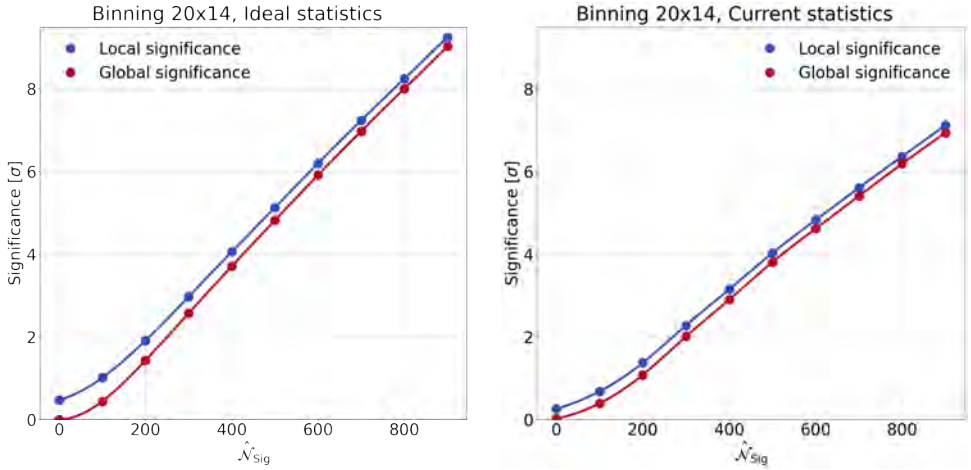

(a) Ideal statistics scenario **(b)** Current statistics scenario

Figure 4.23: *Medians of the local and global significances as a function of the real number of signal events. For each point,* 2×10^3 *ToyMCs were generated as it was done for Figure 4.21 and Figure 4.22.*

Figure 4.23 shows the medians of the local and global significance distributions as a function of the true X17 yield. When reducing the average EPC template population by a factor 10, the average signicance is reduced by 21 %. For the hypothesis of ATMOKI of 450 X17 events, the median global significance is expected to be $4.27\,\sigma$ in the ideal case and $3.36\,\sigma$ in the current statistics case.

	Ideal statistics	Current statistics
Average number of up-crossings	0.44	0.21

Table 4.2: Average number of up-crossings for $c_0 = 1$ for the ideal and current statistics scenarios. 100 ToyMCs were generated for each scenario.

4.3.2.2 CL estimate

The FC construction is performed as described in Section 4.3.1. The a priori Highland-Cousins prescription is naturally extended to sample the templates: at each ToyMC generation, the bins of the Toy templates are sampled with a Poisson distribution centered around the population in the corresponding bin of the reference template. The distribution of λ_{LR} is computed on a 15×15 grid between 0 and 900 average X17 events and between $15\,\mathrm{MeV/c^2}$ and $18.15\,\mathrm{MeV/c^2}$ X17 mass. For each point in the grid, the ToyMC generation and fitting was performed for 1 h. This delivered an inhomogeneous number of ToyMCs produced per point on the grid as the

convergence time depends on the strength of the signal. Each point in the grid has a generated statistics ranging between ∼130 and ∼350 ToyMCs. The grid was generated for both scenarios and used for the following tests.

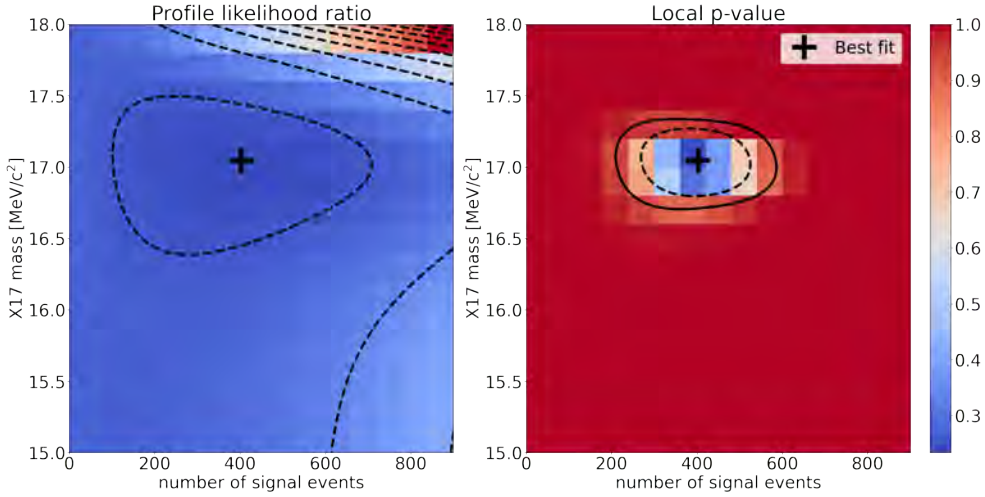

(a) Ideal statistics scenario

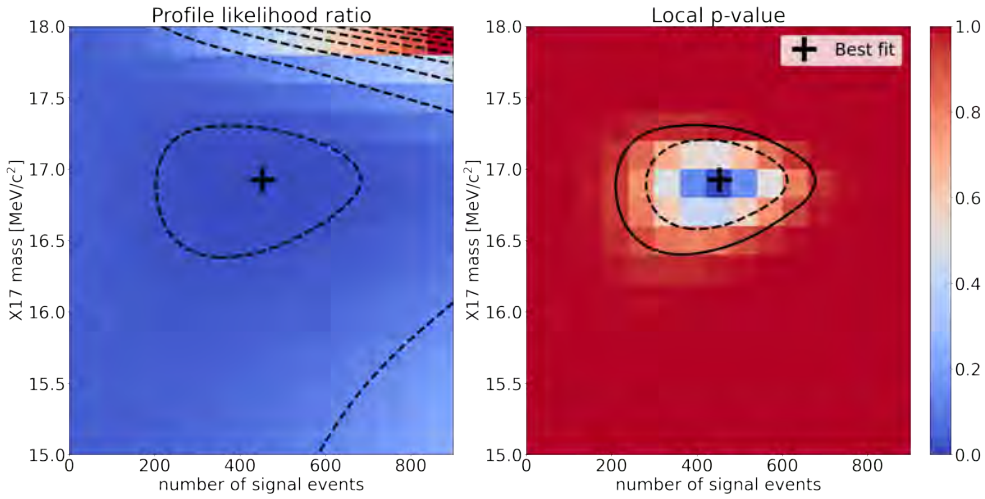

(b) Current statistics scenario

Figure 4.24: *Example of profile likelihood ratio in the ideal (top) and current (bottom) statistics scenarios. The true value of the X17 yield here is set to 500 events. The likelihood ratio is computed on the same ToyMC for both scenarios. On the left, the profile likelihood is shown. On the right, the local p-value estimated with Wilks' theorem is shown. The solid and dashed black lines show the* 90 % *and the* 68 % *p-value level respectively.*

In order to compute the CLs, the likelihood on the data sample, which is in this case a reference ToyMC sample, is profiled in the grid points and the

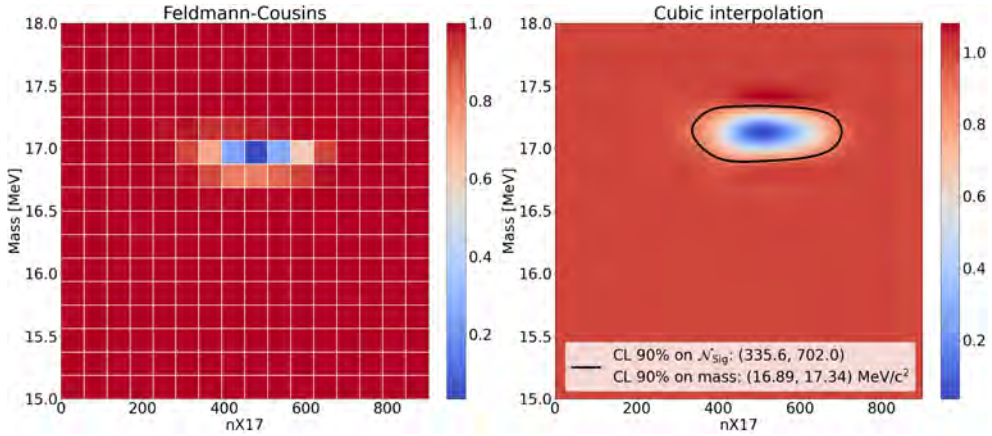

(a) Ideal statistics scenario

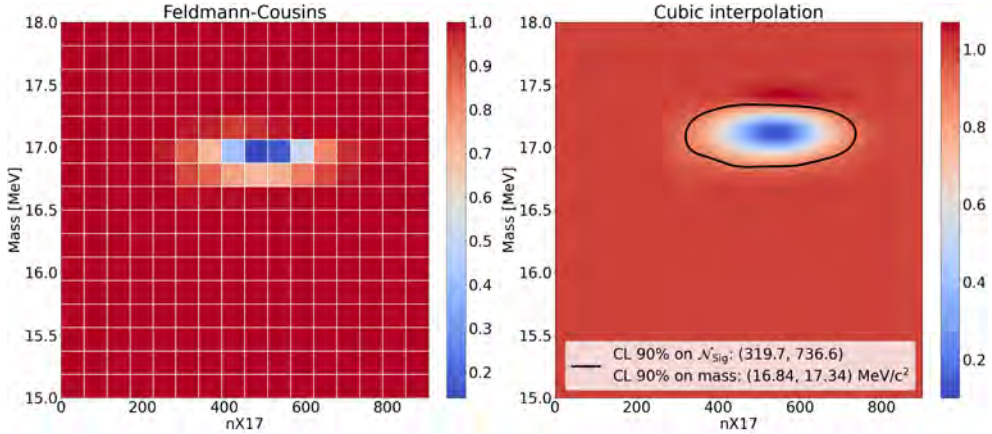

(b) Current statistics scenario

Figure 4.25: *Example of full FC construction in the ideal (top) and current (bottom) statistics scenario. The true value of the X17 yield here is set to 500 events. The FC construction is done on the same ToyMC for both scenarios. On the left, the grid points are shown. On the right, a cubic spline interpolation is shown. The solid black line shows the* 90 % *CL belt. By reducing the statistics of the EPC templates by a factor 10, the limits on the X17 yield increase by* 14 % *and the limits on the X17 mass increase by* 11 %

λ_{LR} is computed. For each grid point,the λ_{LR} is ranked giving the local CLs. As an example, Figure 4.24 shows the profile likelihood in both scenarios for the same ToyMC data sample, and Figure 4.25 shows the result of the FC construction for both scenarios for the same ToyMC data sample. The procedure is then repeated 100 times by resampling the dataset and computing the profile likelihood for each iteration for different values of the average X17 yield. The median of the upper and lower limits and of the best fit estimates are shown in Figure 4.26 as a function of the average X17 yield. Such estimates depend on the template used, resulting in a bias on the best fit

and on the quoted limits. In Figure 4.26 the bias is clearly visible, leading to a median yield of 400 X17 events for both scenarios when the true value is 450. The two scenarios have a similar bias due to the IPC populations being the same.

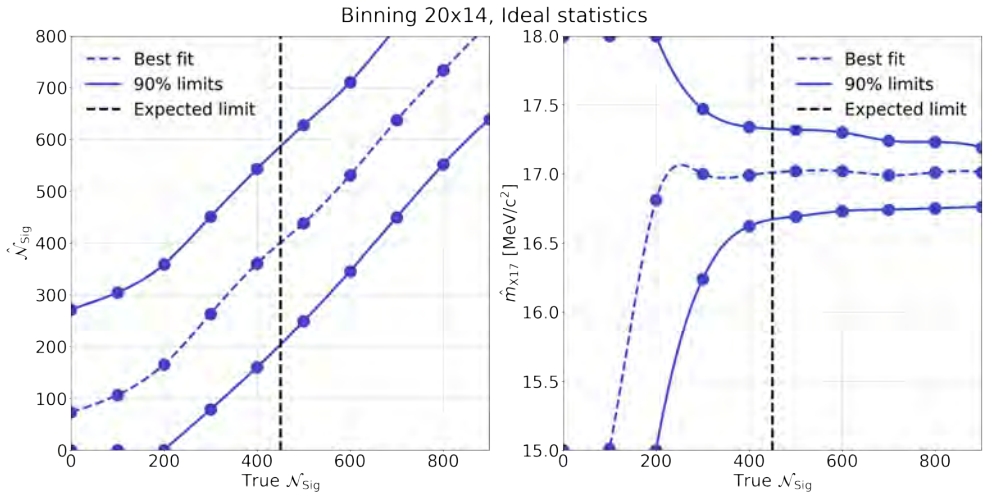

(a) Ideal statistics scenario

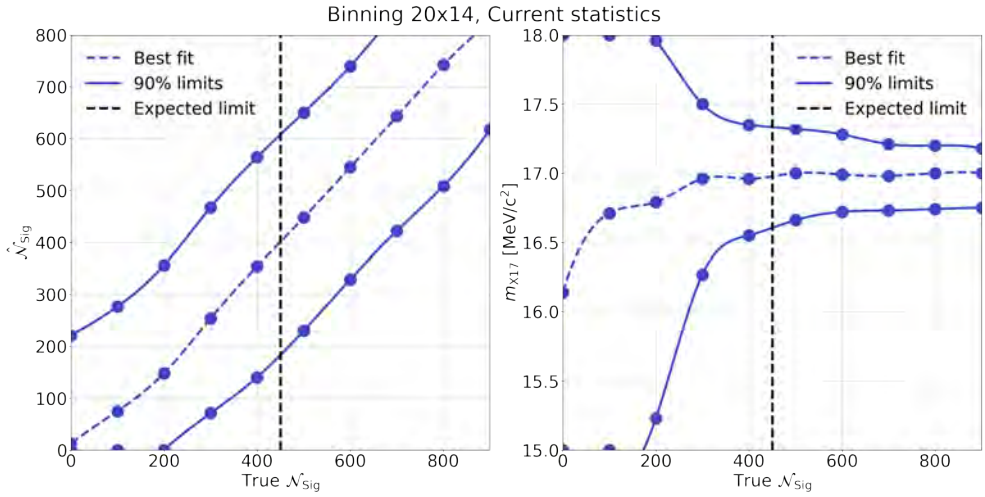

(b) Current statistics scenario

Figure 4.26: *Median* 90 % *CLs and best fits expected as a function of the true X17 yield in the ideal (top) and current (bottom) statistics scenarios. The limits are shown both in the estimated X17 yield (left) and mass (right). The bias on the best fit and on the limits is caused by the template. The biases in the two scenarios are similar due to the IPC templates being the same and to the fact that only few EPC events are expected for high relative angles.*

The sensitivity in the two scenarios is obtained by repeating the procedure in the null signal scenario 100 times with different templates. The distribution

of the so obtained medians is shown in Figure 4.27. The sensitivity is quoted as the average of the medians of the upper limits obtained with the different templates. It is $275(4)$ X17 events in the ideal case and $272(4)$ X17 events in the current statistics case to be compared to the expected 450 events assuming ATOMKI's hypothesis. The uncertainties quoted here are the standard deviations on the sample average. The two cases are compatible, meaning that in the null hypothesis case the lack of statistics in the MC EPC populations is not problematic. The same test has been repeated assuming the branching ratio measured by ATOMKI, therefore 450 signal events on average (see Figure 4.28). In that case, the average of the median upper and lower limits at 90 % CL are respectively $657(6)$ and $271(6)$ X17 events in the ideal statistics scenario and $638(6)$ and $215(6)$ in the current statistics scenario. Whereas the estimate of the upper limits are still compatible within statistical uncertainty, in the ideal statistics scenario the confidence interval is $\sim$10 % smaller.

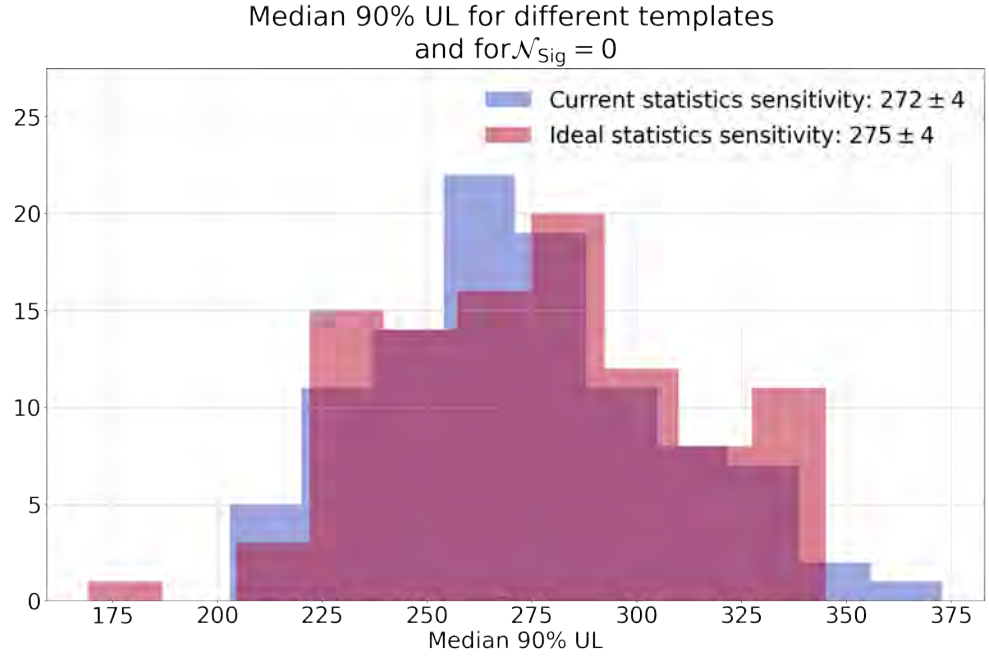

Figure 4.27: *Distribution of the median 90 % upper limit (UL) on the X17 yield for the ideal (red) and current (blue) statistics scenarios for $\hat{\mathcal{N}}_{\text{Sig}} = 0$. Each point is computed by repeating the FC construction 100 times. A different template is used for each point. The sensitivity is quoted as the average of the medians of the upper limit obtained with the different templates. The quoted uncertainty is the standard deviation on the sample average.*

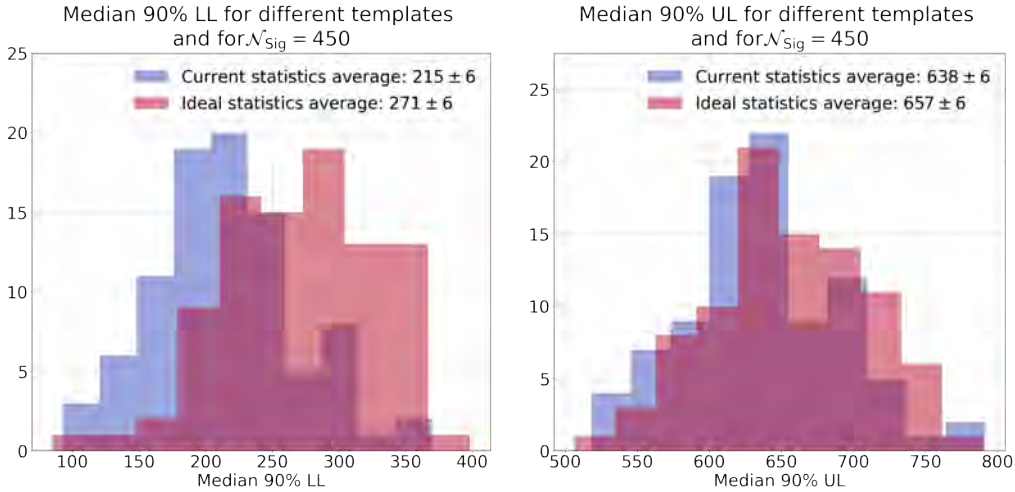

Figure 4.28: *Distribution of the median* 90 % *lower limit (LL, left) and upper limit (UL, right) on the X17 yield for the ideal (red) and current (blue) statistics scenarios for* $\hat{\mathcal{N}}_{\mathrm{Sig}} = 450$. *Each point is computed by repeating the FC construction 100 times. A different template is used for each point. The quoted uncertainty is the standard deviation on the sample average.*

4.4 Final remarks

A data taking campaign to test the beryllium anomaly has been carried out in 2023 with the MEG II detector. At the time of writing, the accuracy of the high fidelity MC simulation is investigated in the side bands and the MC production is ongoing.
The MEG II analysis framework has been adapted to perform a full Feldman-Cousins [71] construction of the 90 % Condifence Levels on the X17 anomaly yield and mass with a likelihood definition based on MC templates. The effect of the limited MC statistics that can be produced given the resources available to the collaboration has been included with the Beeston-Barlow likelihood [72].
The sensitivity expected on the 2023 data sample is estimated to be of 272(4) X17 events, to be compared with 450 assuming the hypothesis of the ATOMKI collaboration. The estimated significance of an anomaly compatible with the measurements from ATOMKI is $3.36\,\sigma$. A significance of $4.27\,\sigma$ could be achieved if the EPC MC statistics could be increased by a factor 10.

Chapter 5

The High Intensity Muon Beams project HIMB

In the following chapter, the High Intensity Muon Beams (HIMB) project is presented. A general overview of the motivations behind it together with its requirements will be given. The focus is subsequently put on the optimization strategy for the two beamlines MUH2 and MUH3.

The first three sections are included as an introduction to the optimization of the HIMB beamlines. The candidate has substantially contributed to the optimization of the MUH2 and MUH3 beamline designs and evaluated their performances in the full accepted momentum spectrum.

5.1 Motivations and requirements

Thanks to the HIPA facility (see Chapter 1) the Paul Scherrer Institut has been leading the high intensity frontier in both particle physics [79] and condensed matter [80–85] for decades by delivering surface muon beam rates of up to a few $10^8\,\mu^+/s$. The High Intensity Muon Beams project aims at exceeding the current intensity limits by two orders of magnitude, reaching rates of $10^{10}\,\mu^+/s$. Such an increase would push the sensitivity of cLFV searches with muons and improve the limitations of the current μSR technique. The next generation of proton drivers to deliver beam powers higher than 1.4 MW require significant research and development, so the HIMB projects focuses on improving the surface muon yield with a new target geometry [6, 86] and on increasing capture and transmission with a large-aperture solenoid-based beamline.

Figure 5.1 shows the layout of the HIPA facility including the HIMB beam-

lines. The new target station TgH will substitute the current TgM and the two HIMB beamlines will be positioned at 90° with respect to the proton beamline. The MUH2 beamline will replace the πM1 area and will be devoted to particle physics delivering the highest muon intensities: the focusing elements will be solely solenoids. The MUH3 beamline will serve μSR instruments and will replace the current πM3 areas: the capture and the first section of the beamline will be based on solenoids, while the coupling into the spin rotator and the transfer to the experiment will be done with two quadrupole channels. A detailed description of the beamlines will be provided in the following.

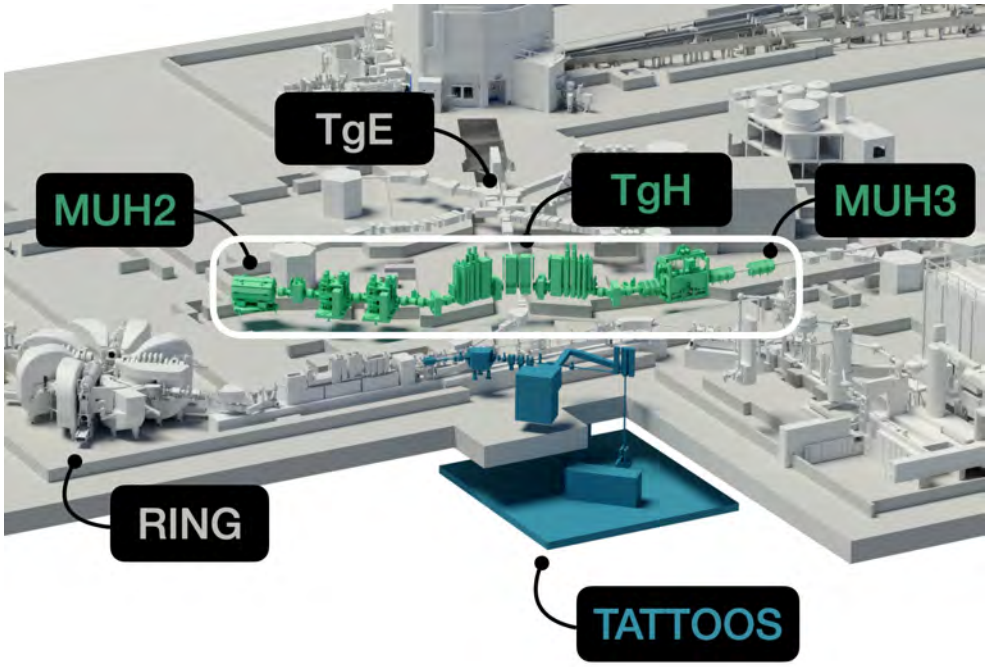

Figure 5.1: *Overview of the HIPA accelerator complex including the HIMB beamlines and the new isotope production target station TATTOOS. The new target station TgH will replace the current TgM and the beamlines will replace πM1 and πM3. Adapted from [87].*

The HIMB project is part of the Isotope and Muon Production using Advanced Cyclotron and Target Technologies project (IMPACT) [87], whose other goal is the construction of a new radionuclide production target for an online isotope separation facility: the Targeted Alpha Tumour Therapy and Other Oncological Solutions (TATTOOS) project.

5.1.1 Fundamental research applications

The importance of muons as sensitive probes for Beyond Standard Model physics has already been covered in Chapter 1. Figure 5.2 (already included in Chapter 1) shows the history of limits for the cLFV golden channels branching ratios, together with the expected sensitivity of MEG II, searching the $\mu^+ \to e^+\gamma$ decay, Mu3e, searching the $\mu^+ \to e^+e^+e^-$ decay, and Mu2e, searching the $\mu^-N \to e^-N$ transition.

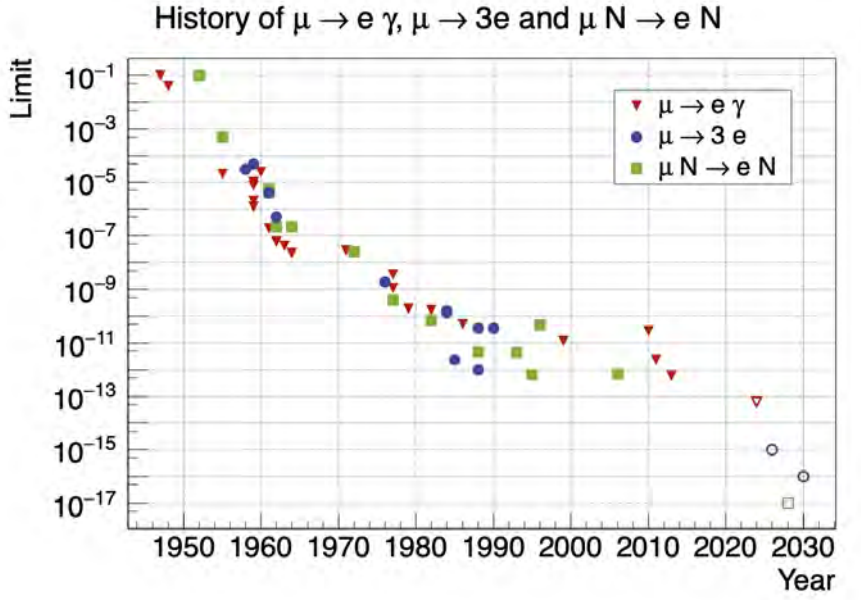

Figure 5.2: *The history of limits for the cLFV golden channels branching ratios. The open markers indicate projected sensitivities. Plot modified from [18].*

The MEG II and Mu3e experiments require continuous muon beams to minimize the accidental background, therefore PSI was chosen as the host facility, but within 5 years of data taking, they will exhaust their statistical reach in πE5. In particular, the phase II of Mu3e requires muon beam rates $\sim 10^9\ \mu^+/s$ to reach its sensitivity goal of $\mathcal{B} \sim 10^{-16}$ (see Chapter 1).

In conjunction with a cooling stage like muCool [88–91] the HIMB beams could be compressed in phase space by ten orders of magnitude with an efficiency of 10^{-4}-10^{-3}, allowing for sub-electronvolt sub-millimeter muon beams that can be reaccelerated. Such phase space would aid muonium production for muonium spectroscopy and antimatter gravity experiments like LEMING [91, 92].

A more comprehensive list of the new opportunities for particle physics

experiments at PSI enabled by the HIMB upgrade can be found in [91].

5.1.2 μSR applications

The spin spectroscopy technique (μSR) allows to probe the local magnetic properties of matter down to nanometer scales. This is done by implanting polarized positive muons in a sample and then measuring the direction of the outcoming decay positron. The measured time spectrum will depend on the interaction of the muon magnetic moment with the sample. The depth at which the sample is probed depends on the energy of the incoming muon. Figure 5.3 shows the calculated muon stopping range in copper as a function of the muon energy.

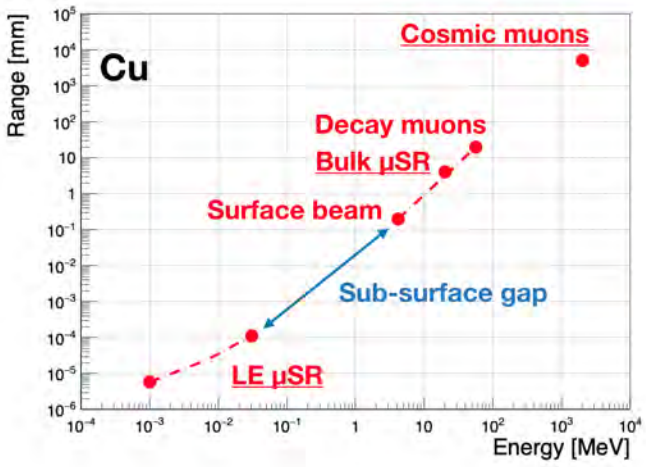

Figure 5.3: *Calculated muon stopping ranges in copper (Cu) as a function of the incoming muon energy. Plot modified from [91]. Typically used muon energies for μSR measurements restrict the probed ranges to either* $< 200\,\mathrm{nm}$ *(low-energy muons, LE-*μ^+*) or* $\geq 100\,\mu\mathrm{m}$ *(surface- and decay-muon beams).*

The red lines in Figure 5.3 show the available energy ranges for such measurements:

- ranges $> 100\,\mu\mathrm{m}$: muons in this range are surface-muons and decay-muons. The rates in this range are limited by the detection technique that measures one muon at a time: a few $10^4\,\mu^+/\mathrm{s}$.
- ranges $< 200\,\mathrm{nm}$: muons in this range are the so called low-energy muons (LEμ^+). The surface-muon beam is moderated on a thin film of a solid rare gas (argon or neon) [93, 94] to produce epithermal muons ($\sim$15 eV). The foil is biased with a high voltage, allowing to accelerate them up to 30 keV. The rates in this range are limited by the efficiency of the moderation process ($\sim 10^{-5}$-$\sim 10^{-4}$) to $\sim 5 \times 10^3\,\mu^+/\mathrm{s}$.

The gap in range is referred at as the sub-surface gap, because it corresponds to the energy range of subsurface muons. In this region of the muon spectrum the population decreases quickly with the kinetic energy and the currently achievable rates do not allow for reasonable data taking periods. Additional limitations arise due the standard μSR detection scheme, where a 200 μm scintillator is employed to measure the arrival time of the muons plus additional material in the radiation shield of the cryostat where the sample is located. Overall the muons lose tens to hundreds of keV in energy.

The HIMB beamlines would allow to increase the rates of LEμ^+ and surface muon beams and to give access to the sub-surface gap. Additionally, together with the development of vertex detectors based on silicon pixel sensors [91]:

- resolving the muon vertex at the millimeter level would reduce pile-up and allow for higher rates in the set-up
- smaller samples could be measured, down to cross sections of $\sim$1 mm^2. This would be 20 times better than the current limits and would allow for probing multiple samples in parallel

A more comprehensive list of the new opportunities for μSR at PSI enabled by the HIMB upgrade can be found in [91].

5.2 Target station upgrade: target H

As shown in Chapter 1, the introduction of an angle with respect to the proton beam increases the muon yield at TgE*. For the HIMB upgrade, TgM will be substituted with TgH, a thinner version of TgE*. The slanting angle with the beam will be 10° and the thickness in the proton beam direction is fixed to 20 mm. With such a geometry the surface muon yield is expected to be the same as a non-slanted TgE with a thickness of 40 mm. The material chosen for the target is polycriystalline graphite and the cooling will be radiative.

Figure 5.4 shows a section of TgH.

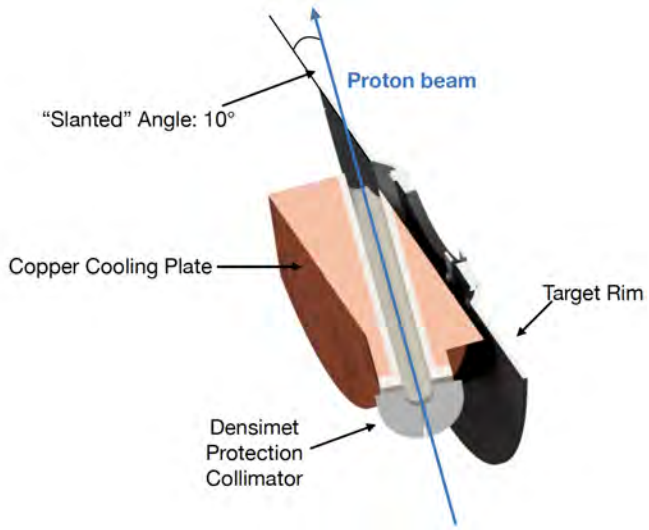

Figure 5.4: *Cross-section of TgH from [95].*

The proton beam will impinge on the back of the target, passing through a water-cooled copper plate acting as local shielding against the intense heat radiated off the target. A Densimet® (tungsten alloy) protection collimator will be used in order to protect against the proton beam hitting directly the copper cooling plate.

To allow for such a configuration, the proton beam trajectory will be lower than the rotation axis of the target, or it would intersect the rotation shaft. Additionally, a lower trajectory allows the use of a flat target, providing more usable space and further reducing heat and radiation load on the target insert. A more detailed view of TgH is shown in Figure 5.5.

The target rim will be 3.5 mm thick and 100 mm wide. The target will be composed of two different disks with 12 blades each. When the two disks are

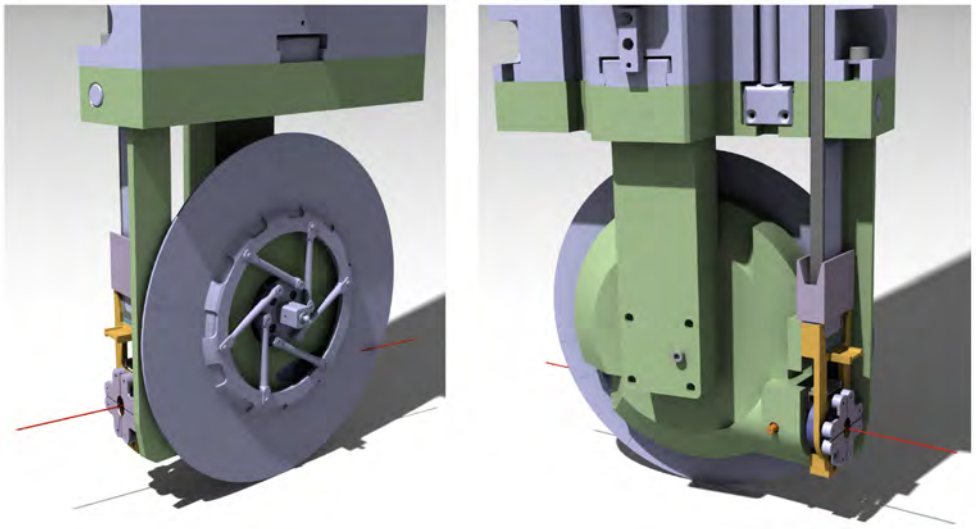

Figure 5.5: *Detailed view of the TgH insert.*

overlaid on on top of each other, the blades combine in a wheel. This design was preferred because it allows for a thicker graphite support at the center, where the disks overlap, without the need of machining a gradually varying thickness of the graphite. Additionally, it allows to precisely introduce gaps to keep distorsions and thermal stress under control. Figure 5.6 shows a schematic of the two disks.

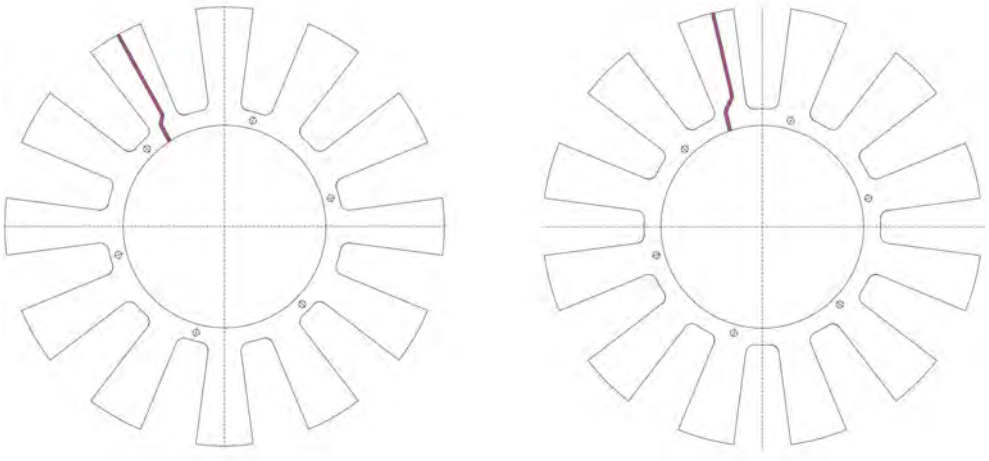

Figure 5.6: *Schematic of the two disks composing TgH from [87]. Each disk has a thickness of* 3.5 mm *and sustains 12 blades. Once overlaid the two disks combine in a wheel. This design was preferred because it allows for a thicker graphite support at the center, where the disks overlap, without the need of machining a gradually varying thickness of the graphite. Additionally, it allows to precisely introduce gaps to keep distorsions and thermal stress under control.*

Figure 5.7: *TgE remote-handling exchange flask in the HIPA facility experimental hall.*

To allow for maintainance, the elements along the proton beamline are organised in inserts that can be independently extracted with so-called *exchange flasks*. The aim of such devices is to shield the elements during extraction and transport. Due to the harsh radioactive environment along the proton channel, the exchange flasks are bulky and are designed to handle as many inserts as possible. Each exchange flask is a steel case equipped with grippers and motors to remotely extract the inserts. In case of TgH the insert was designed to fit the same exchange flask as TgE, allowing for easier operations and reducing the number of needed spare components. Figure 5.7 shows the TgE remote-handling exchange flask in the HIPA facility.

The distance between the target and the coil of the capture solenoid (see below in Figure 5.13) will be 250 mm to enhance the acceptance of the beamlines. The short distance sets stringent requirements on the design of the target station which needs to be enclosed in the same vacuum chamber as the capture solenoids. Figure 5.8 shows the target station with the two capture solenoids.

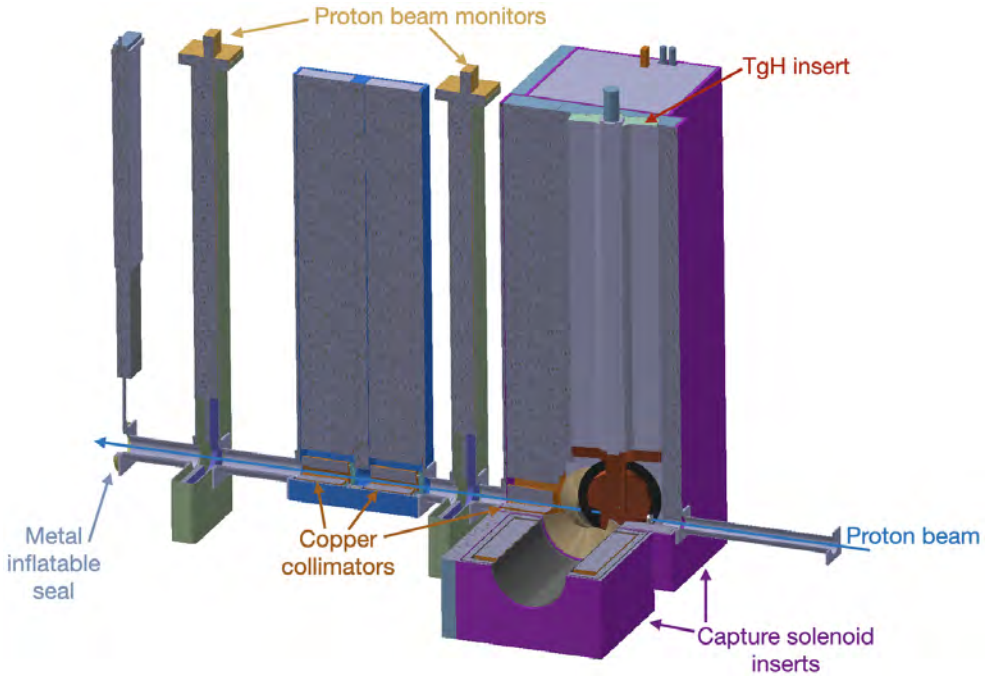

Figure 5.8: *Detailed view of the TgH station. The insert of TgH is enclosed in the same vacuum chamber as the two capture solenoids (purple).*

5.2.1 Particle spectra at TgH

To design and optimize the HIMB beamlines, a set of ROOT files containing the distributions of the particles of interest close to the target was prepared. The distributions were produced with a G4beamline [37] simulation using a square polycrystalline graphite slanted target with a side of 100 mm and a thickness of 3.47 mm. The proton beam impinges at the center of the target at a 10° angle, resulting in a 20 mm effective length for the proton beam. The proton beam is sampled with no divergence and a round beam spot with $\sigma_x = \sigma_y = 1$ mm. The proton energy is a monochromatic line at 590 MeV.

The secondary particles are detected by two VirtualDetectors[1] on the sides of the target 15 mm away from its center: at such a short distance the effect of the fringe fields from the capture solenoids are expected to be negligible. Due to the slanted geometry of the target, the distributions on the MUH2 and MUH3 sides are different and separate beam files have been generated for the two sides. While for MUH3, only positive muons are of interest, the species considered for the optimization of MUH2 are:

- μ^+, μ^-: species of interest for experiments

[1] A VirtualDetector is a G4beamline element that allows to record the particles entering its physical volume.

- e^+, e^-: main contamination to muon beams and possible calibration sources for the experiments (see Section 1.3.2.3)
- π^+, π^-: possible calibration sources for the experiments (see Section 1.3.2.2) and additional contribution to muon rates due to decays in flight

Figure 5.9 shows the graphic output of the G4beamline model, while Figure 5.10 and 5.11 show the momentum distributions respectively on the MUH2 and on the MUH3 side at target normalized to a proton current of 2.4 mA.

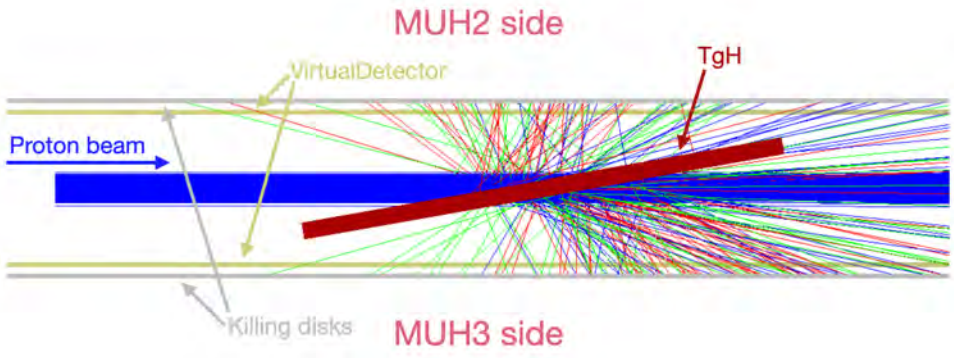

Figure 5.9: *Zoom-in of the graphic output of the particle production at TgH from G4beamline. The target is seen from above. The secondary beams are produced by impinging 1000 protons (blue straight lines) on a simplified version of TgH (red). The particles are detected with two VirtualDetectors (light yellow) on the sides of the target and then absorbed by the two 'killing disks' (light grey).*

5.3 Beamline elements

This section comprises a list of the elements composing MUH2 and MUH3 together with their main features. Their layouts are described in Section 5.4.1 and Section 5.5.1 respectively. A main characteristic of the HIMB beamlines is the extensive use of solenoids to maximize transmission. The advantage of solenoids over quadrupoles is linked to their optical properties: a single solenoid magnet is sufficient to focus both transverse directions of a particle beam, while at least two quadrupoles are needed to obtain the same effect, as they focus in one transverse direction and defocus in the other. Such characteristic introduces additional losses in the defocused direction. Because of the intrinsic high emittances of secondary particle beams together with the muons decaying in flight while transported to the experiments, the length of the beamlines is a crucial parameter to achieve high rates.

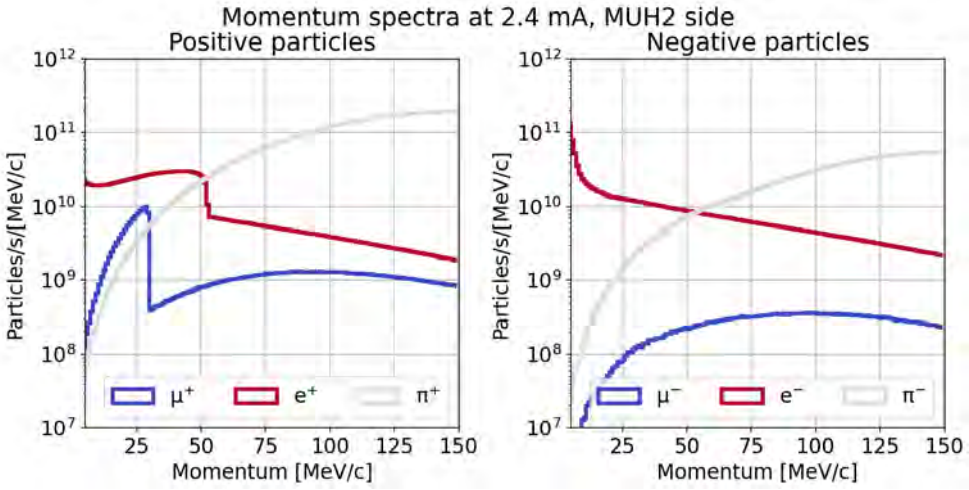

Figure 5.10: *Momentum spectra* 15 mm *away from TgH center on MUH2 side.* 2×10^{11} protons *were simulated. On the left: positive particles. The surface muons form the peak near* 30 MeV/c *in the muon spectrum (blue). The kinematic edge of the Michel distribution can be clearly seen at* 52.8 MeV/c *in the positron spectrum (red). On the right: negative particles.*

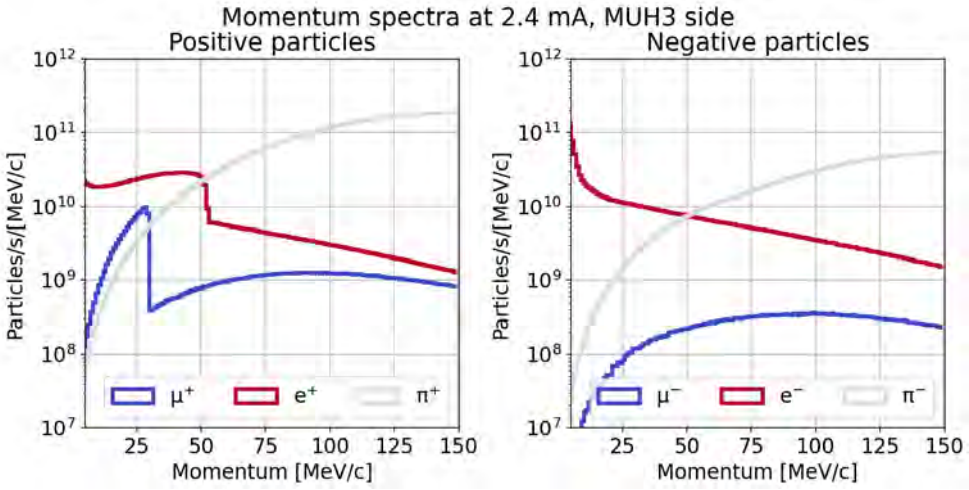

Figure 5.11: *Momentum spectra* 15 mm *away from TgH center on MUH3 side.* 2×10^{11} protons *were simulated. On the left: positive particles. The surface muons form the peak near* 30 MeV/c *in the muon spectrum (blue). The kinematic edge of the Michel distribution can be clearly seen at* 52.8 MeV/c *in the positron spectrum (red). On the right: negative particles.*

On the other hand, the focusing length of a solenoid magnet is quadratic with the rigidity of the beam [96], which means that the operation of solenoids as focusing elements is constrained by the currents that can be used to excite them. This is the main limitation at momenta higher than that of surface muons.

The fieldmaps of the new elements for the G4beamline simulation were com-

puted by the magnet group of PSI with ANSYS [97] and COMSOL [98].

5.3.1 The capture solenoid

A common approach to capture charged particles produced at a target is to completely enclose it in a solenoid magnet to maximize the acceptance. This solution is not straightforward to apply for the HIMB beamlines as the proton beam is not stopped at the target. As shown above, the proton beam crosses two targets and is then stopped at the spallation target of the SINQ.

In order to avoid major changes to the proton beam optics to compensate the high magnetic field required, a double solenoid capture field was preferred (see Figure 5.12). Two independent capture solenoids are positioned sideways to the target at an angle of 90° with respect to the proton beam direction. The iron yoke around the coils reduces the magnetic field at target to around 0.1 T and two additional correction dipoles are added to the proton beamline to compensate for it. Because of the harsh radioactive environment, normal conducting magnets were preferred. Pyrotenax® (mineral-insulated copper-clad cable) coils are chosen to withstand the high radiation load, and the water cooling is indirect to avoid the corrosion of the coils. The design is similar to the capture solenoid already used in the μE4 beamline at PSI [93].

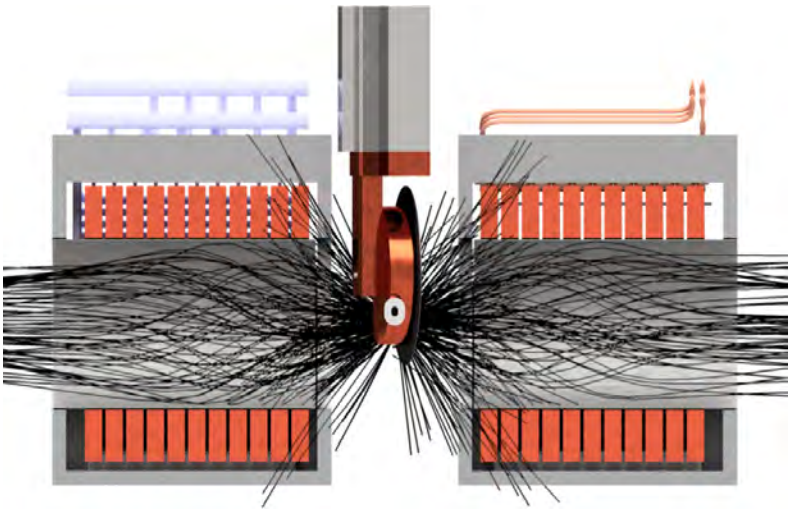

Figure 5.12: *Schematic of the target region from [91]. The two capture solenoids are collecting muons (black lines) sideways of TgH.*

After the capture solenoids, a dipole is placed in both MUH2 and MUH3 to avoid a direct line of sight from TgH to the experiment. This is needed to keep under control the neutron dose and to reduce neutron transmission along the transfer lines. To allow for optimal transmission through the first

dipole to the next solenoid, the beam should be focused in the vicinity of the dipole. On the other hand to maximize capture a high magnetic field close to the target is preferred, but this reduces the focal length at capture, reducing the overall transmission. To maximize both capture and transmission at once, the capture solenoids are composed of three *pancakes* of coils that can be powered independently. The idea behind this design is to initially capture the muons with a high magnetic field as close as possible to the target and then reduce the magnetic field along the centerline (see Section 2.1.1) to adjust the focus position. The upstream wall of the iron yoke, or mirror plate[2], further shapes the field moving the peak closer to the target while still keeping the stray fields low.

As an example, Figure 5.13 shows the transmision through the MUH2 capture solenoid when the currents energizing the three pancakes are optimized for transmission through the first dipole bend (plot on the left) and when the peak fields of the three coils are equal (plot on the right). In the latter case, the currents were scaled so that the integral of the magnetic field on the centerline is equal to the optimized case. The 1-standard-deviation (1-STD) envelope of the transmitted particles is shown overlayed to the graphic ouput of the G4beamline simulation. The optimized version allows for stronger focusing in the first coils to then obtain a parallel beam at the exit, while the uniform version produces a focus closer to the exit and reduces the capture from 14.5 % to 11.7 %.

The first two coils and the upstream mirror plate have a reduced radius to increase the magnetic field at the entrance of the solenoid and to reduce it at the proton target.
The radius of the aperture is 200 mm at the entrance and 220 mm at the second coil to not affect the acceptance. Two iron plates are positioned between the pancakes to further shape and terminate the fields of the different pancakes. Figure 5.14 shows the axial component of the magnetic field in the horizontal plane. The final aperture of the solenoid is 500 mm.

[2]The effect of the mirror plate on the field produced by a coil is analogous to that of a magnetic field produced by a coil mirrored with respect to the plate, hence the name.

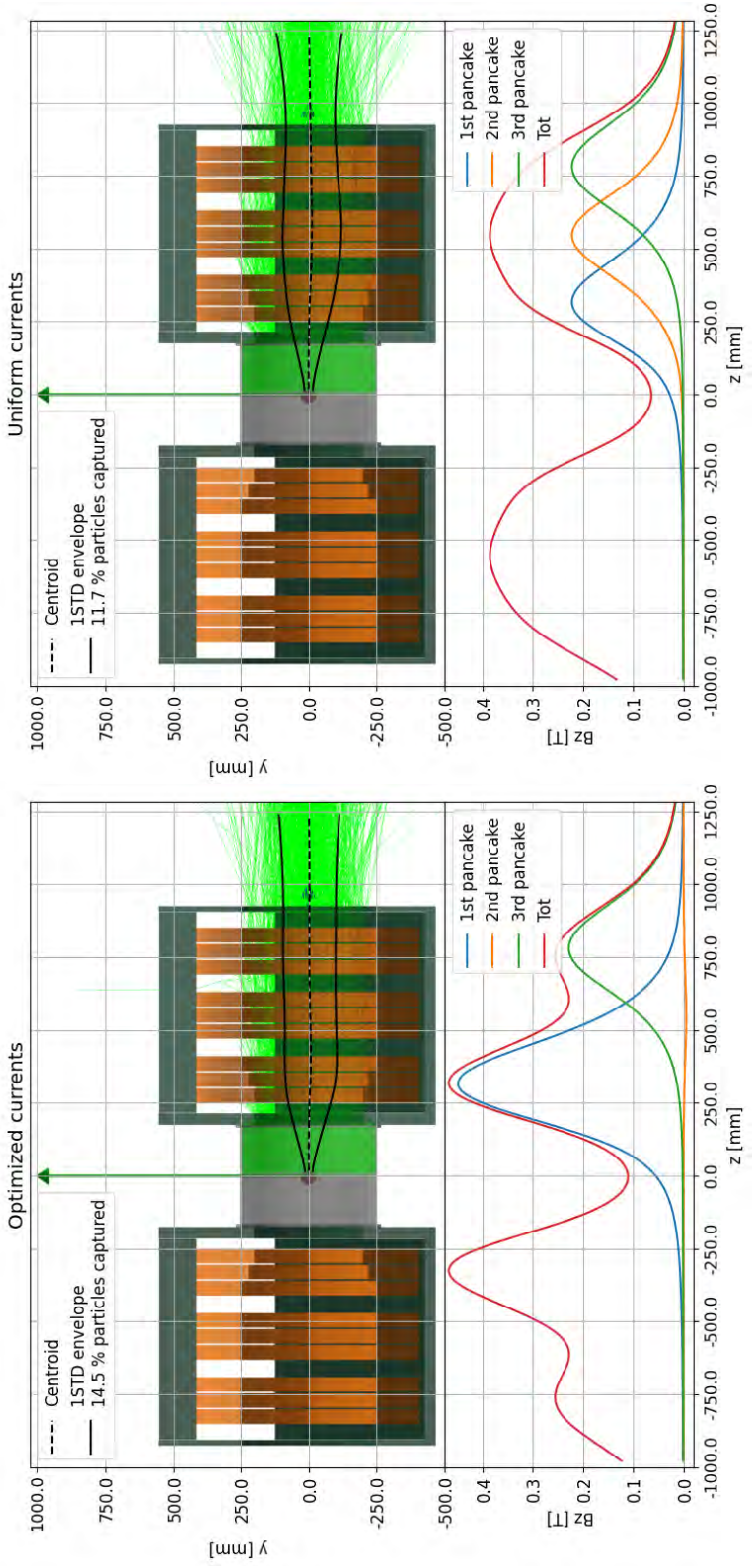

Figure 5.13: *Top: 1-standard-deviation (1-STD) envelope overlayed on the graphic output of the G4beamline simulation of the capture solenoids. The envelope is computed on the transmitted particles only. Bottom: axial component of the magnetic field on the centerline. Left: the currents energizing the coils are optimized for surface muon transmission through the first dipole in MUH2. 14.5 % of the μ^+ are transmitted. Right: the currents energizing the coils are chosen so that the peak fields are the same for the three pancakes. The field integral on the centerline is equal to that in the optimized version. 11.7 % of the μ^+ are transmitted.*

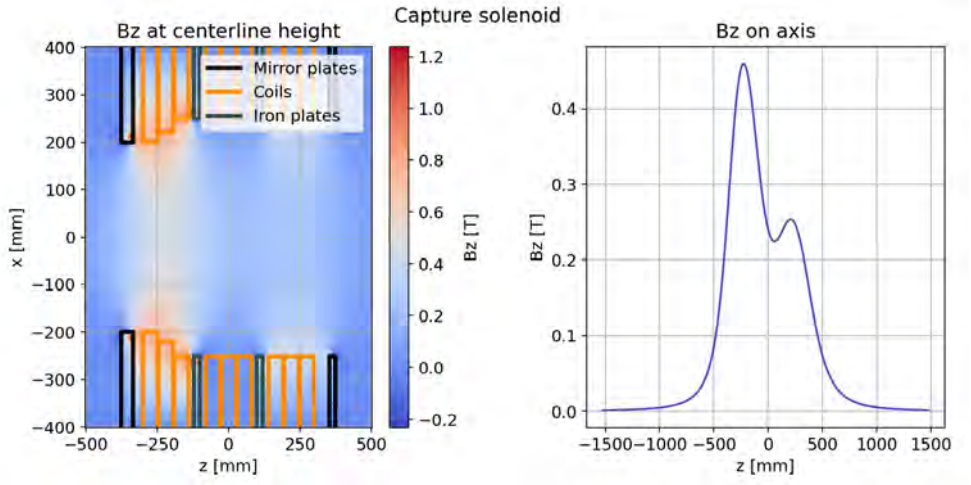

Figure 5.14: *Left: axial component of the magnetic field in the capture solenoid. The mirror plate facing the target is thicker to reduce the fringe fields affecting the proton beam. The aperture of the coils increases in the first pancake from left to right to increase the field strength close to the mirror plate. Right: axial component of the magnetic field in the capture solenoid along the axis.*

5.3.2 Pyrotenax dipoles

The first dipoles in both MUH2 and MUH3 are equipped with Pyrotenax® coils to sustain the harsh radioactive environment. The iron yoke is in the classical H-type shape, 710 mm long. As stated above, optimal transmission can only be granted for momenta lower than 30 MeV/c, nonetheless the dipoles are designed for rigidities up to 80 MeV/c, allowing for greater versatility. As an example, the MEG II experiment uses positron beams at 52.8 MeV/c and negative pion beams at 70 MeV/c for calibrations (see Chapter 1). Figure 5.15 shows the vertical component of the magnetic field in the horizontal plane for a 36° bend at 28 MeV/c.

In MUH3 the second (ASH32) and the fourth dipole (ASH34, see Section 5.5.1) have the same design, but with ASH34 featuring non-radiation hard coils.

5.3.3 Dipoles with slits

The second bend in MUH2 (ASH2) is performed with a non-radiation hard dipole which includes a slit system at its center. The design of the slit system follows the designs currently used at the secondary beamlines and is adapted to the larger aperture of the HIMB beamlines: they are 50 mm thick Densimet® plates in the vicinity of the beam, welded to a 50 mm thick copper plate. To lighten the weight of the slits, alternative designs are under study. Figure 5.16 shows the range of μ^+, π^+ and e^+ transmitted from TgH to ASH2 with G4beamline in Densimet® and copper when the beamline

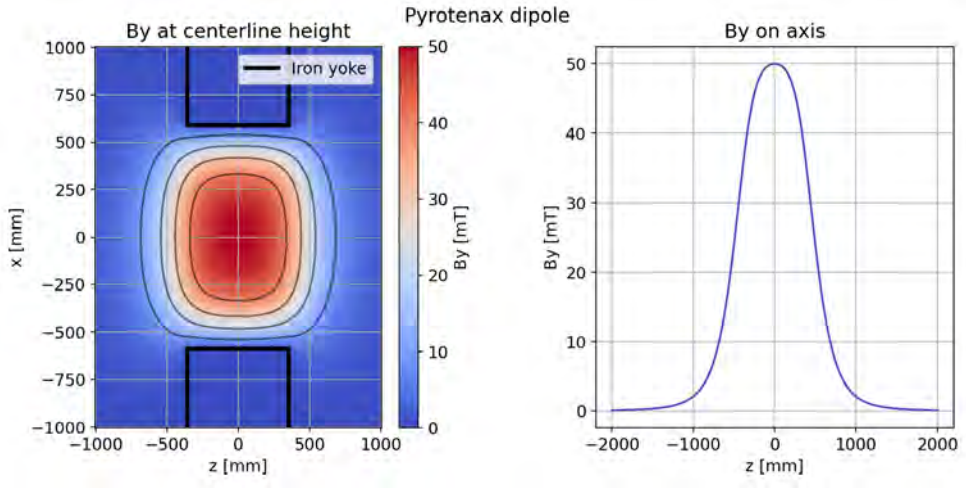

Figure 5.15: *Left: vertical component of the magnetic field in the radiation hard dipoles. The contours shown correspond to* 20 %, 40 %, 60 % *and* 80 % *of the field at the center. Right: vertical component of the magnetic field in the radiation hard dipoles along their axis.*

is tuned for a central momentum of 70 MeV/c. The simulations show that 20 mm of Densimet® or 40 mm of copper are sufficient to completely stop all the particles.

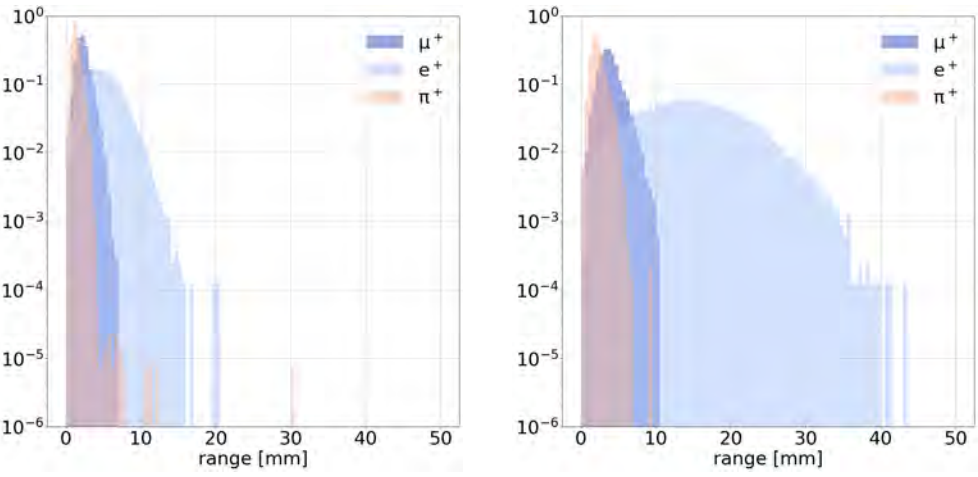

(a) Densimet® **(b)** Copper

Figure 5.16: *Range of* μ^+, π^+ *and* e^+ *with a momentum of* 70 MeV/c *in Densimet® (left) and copper (right) simulated with G4beamline. Particle decays are not included. The histograms are normalized to have unit area.*

The slits can be used to adjust the delivered rates and to adjust beam properties depending on their position along the beamline. Because of the big

acceptance and because they are included in a bend, the slits have a limited effect on the momentum distribution, but they can be used to reduce the positron contamination for surface muon beams as their momentum distributions have different features. This point will be further explored in the following section. Additionally, this design allows to include the slits without increasing the beamlines length and the spacing between elements.

The design of the dipole is analogous to the pyrotenax version, with a rectangular aperture on both sides of the iron yoke to accommodate the slits. This feature affects the magnetic field close to the yoke as shown in Figure 5.17 introducing however negligible effects close to the centerline.

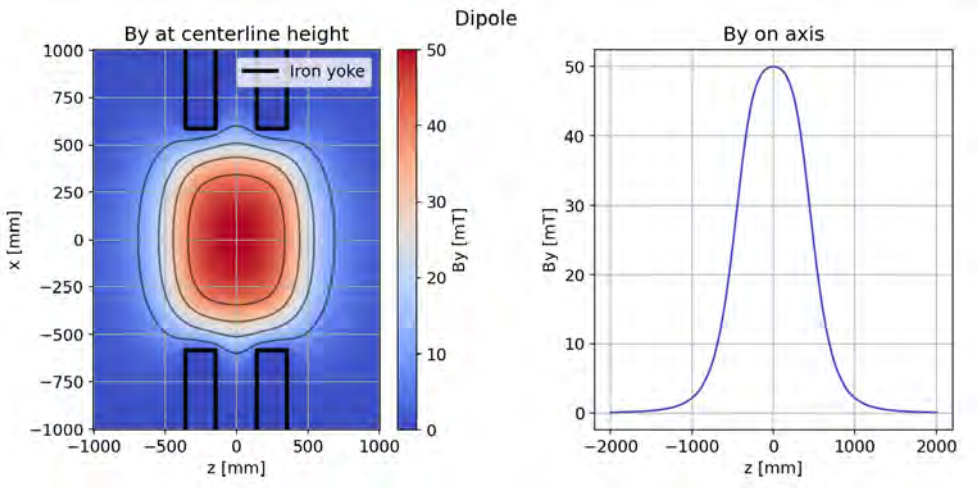

Figure 5.17: *Left: vertical component of the magnetic field in the non-radiation hard dipoles with a slit system. The contours shown correspond to* 20 %, 40 %, 60 % *and* 80 % *of the field at the center. Right: vertical component of the magnetic field in the non-radiation hard dipoles with a slit system along the axis.*

5.3.4 Transport solenoid

After capture, the solenoids along the beamline are referred to as *transport solenoids*. They exist in a radiation hard version with Pyrotenax® coils and a non-radiation hard version, but they are otherwise identical for the optics. The radiation hard coils are used for both MUH2 and MUH3 in the straight section after the first dipole magnet. The coils of the transport solenoids are uniformly powered and the aperture radius is kept constant through the full length of the solenoid to a value of 250 mm and no iron plates are employed. Figure 5.18 shows the axial component of the magnetic field in the horizontal plane.

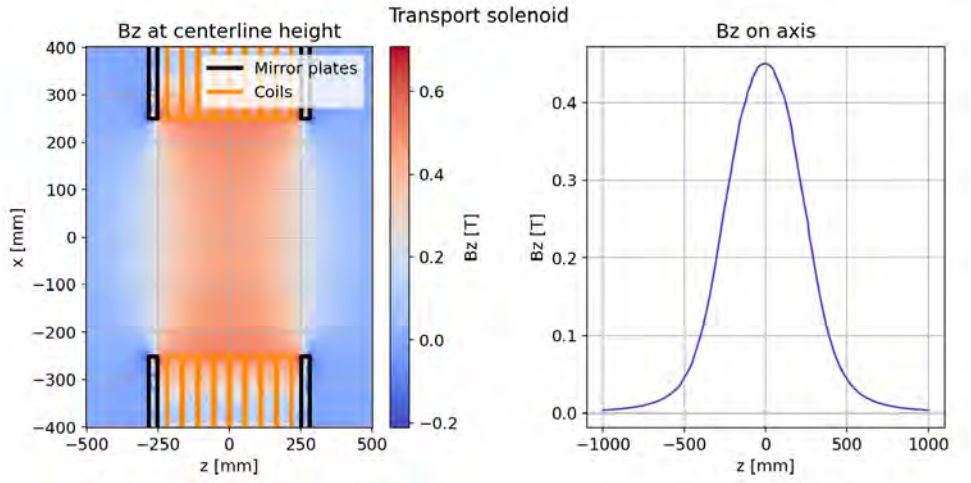

Figure 5.18: *Left: axial component of the magnetic field in the transport solenoids. As opposed to the capture solenoid, the transport solenoids are symmetric with respect to the vertical plane. Right: axial component of the magnetic field in the capture solenoid along the axis.*

5.3.5 MUH2 Wien filter

As shown in Figure 5.10 and 5.11, muons are not the only particle types produced, and whereas this is a desirable feature for a variety of applications, e.g. calibrations, this introduces a problem when a clean beam is preferred. In a Mu3e search for example, positrons are a source of background when they scatter on the target. In MEG II they could reach the Radiative Decay Counter (RDC) and trigger a veto (see Chapter 1). In the case of HIMB, due to the big acceptance of MUH2, the problem is more relevant than in the beamlines currently available at PSI: for surface and sub-surface muon beams, positrons are delivered with a yield $\mathcal{O}(10)$ times higher while pions are negligible; for negative muons electron contamination is $\mathcal{O}(100)$ times higher; for higher momenta, pions become more important. Depending on the experimental set-up, the beam-related backgrounds can be reduced by veto systems relying on the energy loss through thin foils or based on TOF referenced to the proton RF, or by introducing a Wien filter.

For MUH2, the introduction of a Wien-filter is foreseen, but the *vetoing* solutions can be employed as well.

The Wien-filter was quickly mentioned in earlier chapters when describing the πE5 area. The basic idea is to select the velocity of charged particle beams by utilizing static electric and magnetic fields in a cross-field configuration so that the electric and magnetic components of the Lorentz force have opposite directions. This way the resulting kick will depend on the velocity of the particle only:

$$F_x = q(E_x - v_z B_y) \tag{5.1}$$

Usually, the electric field is kept at the highest value that can be reached by the device (strictly depending on the separator design and on the available power supplies), while the magnetic field is tuned to cancel the net force for the desired particle.

This, combined with the momentum selection carried out by the dipole, discriminates particles with different masses. The effectiveness of the separation depends on the length of the Wien-filter, on the strength of the electric field and on the velocity of the particles. At first order, the deflections by the electric and magnetic contributions are respectively [99, 100]:

$$\theta_E[\text{mrad}] = \left(\frac{V \cdot L_{eff}}{d \cdot P_0 \cdot \beta}\right)[\text{kV, m, MeV/c}] \tag{5.2}$$

$$\theta_B[\text{mrad}] = \left(\frac{30 \cdot L_{eff} \cdot B}{P_0}\right)[\text{m, G, MeV/c}] \tag{5.3}$$

where V is the voltage difference between the plates, L_{eff} is the effective length for the considered field, d is the distance between the plates, P_0 is the central momentum, β is the particle velocity and B is the magnetic field. The typical Wien-filter separators used at PSI are effective up to $\sim 40\,\text{MeV/c}$, limited by the voltage difference that can be applied between the plates.

An additional effect to be considered is the transmission of such an element: even if a weak focusing is provided in the deflection plane by the plates [101], in the vertical plane the element is at first order a drift, and a trade off between its length and separation power must be made.

The initial design was based on the existing Spin Rotator 1 used in πM3, with the distance between the high voltage (HV) plates increased from 200 mm to 500 mm, causing a reduction of the electric field, and their length reduced from 3 m to 2 m. Including the vacuum ports the overall length of the element is 2.9 m. With such a design, the transmission is only 26 % [87] making the $10^{10}\,\mu^+/\text{s}$ goal impossible to reach.

The current solution to this problem is to use two shorter Wien-filters with intermediate solenoidal focusing to increase transmission keeping the positron contamination for surface muons lower than 20 % while allowing for rates higher than $10^{10}\,\mu^+/\text{s}$.

In the most recent design, the distance between the plates is 430 mm and their length is 900 mm. The achievable electric field will depend on the available power supplies. Currently the maximum HV achievable with the power

supplies employed at PSI is 300 kV, but devices providing up to 350 kV are potentially available commercially. The results reported in the following are obtained assuming a ±320 kV biasing on the two plates, leading to an electric field of 1.488 MV/m.

In this work, the simulations were performed assuming *perfect* transverse electric and magnetic fields, with no fringe fields and only transverse components. Recently, a complete mechanical design together with corresponding realistic electric and magnetic field maps has been finalized showing improvements with respect to its previous simplified version. The electric and magnetic field components of that design are shown in Figure 5.19.

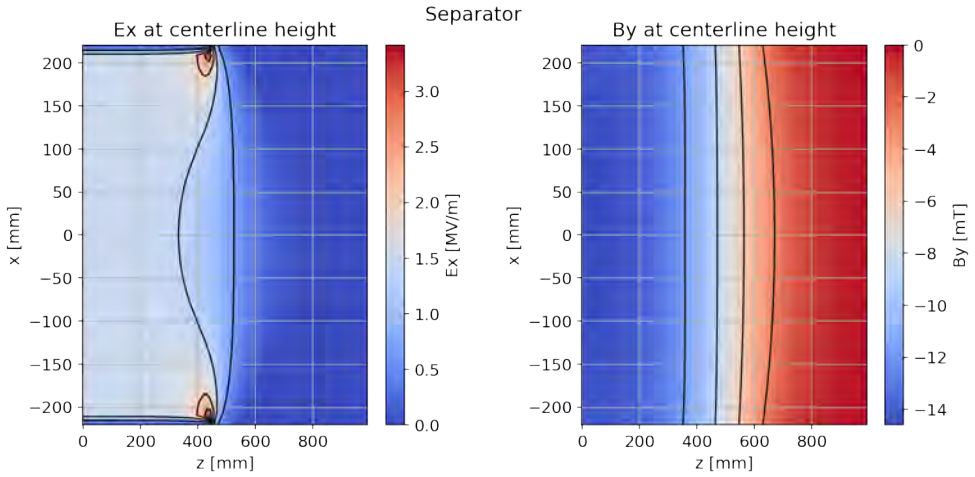

Figure 5.19: *Transverse electric (left) and magnetic (right) field components relevant for charged particle separation as produced by the short Wien-filter version. The fieldmaps are limited to the region between the high voltage plates. The fieldmaps are scaled here to select surface muons, with* ±320 kV *applied to the plates. The contours shown correspond to* 20 %, 40 %, 60 % *and* 80 % *of the maximum (absolute) field.*

5.3.6 MUH3 spin rotator

A Wien-filter can also be used to rotate the intrinsic spin polarization of the muons, with respect to their momentum vector, and this feature is of interest for some μSR techniques. For MUH3, the existing Spin Rotator 1 (SpinRot1) will be used. The plates, as briefly touched on in the previous paragraph, are 3 m long and have a gap of 200 mm. In the case of MUH3, transmission through the spin rotator is not a main concern as most of the phase space is cut when coupling into the quadrupole triplet immediately upstream to it. Because of that cut, the overall transmission through Spin Rotator 1 is 70 %. The maximum suppliable voltage is 300 kV. For 28 MeV/c muons the maximum spin rotation angle is 77.1° [87].

5.3.7 MUH3 beamline quadrupoles

As stated above, the MUH3 beamline is a hybrid solenoid-quadrupole beamline aimed at μSR applications. The capture and first straight section will be analogous to MUH2 employing radiation-hard solenoids, with a first dipole after capture to avoid a direct sight to TgH to reduce the neutron transmission. After the straight section, a dipole is included as in MUH2 but then the beam couples into a quadrupole section. The details on the layout will follow. Currently for πM3 three types of quadrupoles are used: a QSM triplet couples the beam into SpinRot1; QSL and QSE quadrupoles deliver the beam to the two experimental areas. At the time of writing the final layout of the MUH3 beamline is not yet defined, but the quadrupoles will be chosen among the three types mentioned above. The layout optimized in the following employes QSM quadrupoles only, but it is possible to translate the focusing strength employed for the QSM quadrupoles to the other two types.
Table 5.1 summarizes the main features of the quadrupoles employed in MUH3. As shown in Chapter 2, the first order transfer matrix of a perfect quadrupole is univoquely defined by the product of its gradien k_1 and its length. This expression can be generalized to include the effect of fringe fields by defining the effective length:

$$L_{eff} = \frac{1}{k_{1,max}} \int_{-\infty}^{\infty} k_1(s) ds \tag{5.4}$$

where $k_{1,max}$ is the maximum gradient of the quadrupole along its axis, namely at its center. It is not possible to generalize a conversion from a quadrupole type to another due to the $\sqrt{k_1}$ terms in the off-center elements of the matrix in Equation 5.5:

$$\mathcal{M}_{quad}(0|L_{eff}) = \begin{bmatrix} \cos(\sqrt{k_1}L_{eff}) & \frac{1}{\sqrt{k_1}}\sin(\sqrt{k_1}L_{eff}) \\ -\sqrt{k_1}\sin(\sqrt{k_1}L_{eff}) & \cos(\sqrt{k_1}L_{eff}) \end{bmatrix} \tag{5.5}$$

An approximated formula can be derived for thin lenses:

$$\mathcal{M}_{quad}(0|L_{eff}) \approx \begin{bmatrix} 1+\mathcal{O}(2) & \mathcal{O}(3) \\ -k_1 L_{eff}+\mathcal{O}(3) & 1+\mathcal{O}(2) \end{bmatrix} \tag{5.6}$$

The gradient for an alternative quadrupole can then be found by keeping $k_1 L_{eff}$ fixed with the values in Table 5.1. For thick lenses, as in this case, the approximation is not perfect, but can provide a starting point to match the new quadrupoles to the other elements.

MUH3 quadrupole parameters			
Quadrupole type	QSM	QSL	QSE
Max excitation current [A]	500	435	500
Gradient @ max current [T/m]	1.93	6.16	5.22
Effective length [mm]	400	590	366
Aperture diameter [mm]	400	250	254
Mirror plate thickness [mm]	20	20	-

Table 5.1: Parameters of the quadrupoles included along the MUH3 beamline as measured by the magnet group at PSI. No mirror plate thickness is reported for the QSE model because it does not have one.

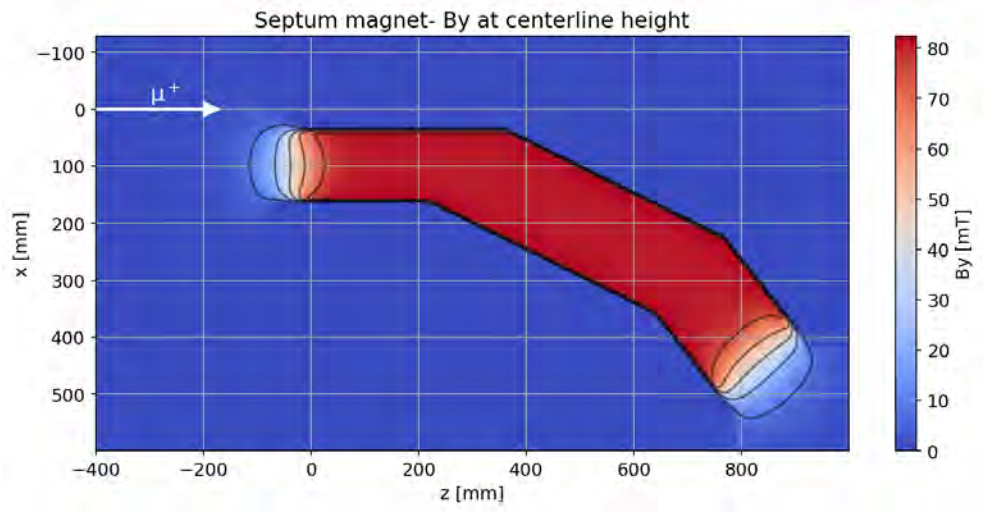

Figure 5.20: *Vertical component of the magnetic field in the septum magnet. The field is confined in a region close to the beamline axis, allowing to provide beam to either MUH3.2 or MUH3.3 or to both of them depending on the position of the beam with respect to the septum. The contours shown correspond to* 10 %, 30 %, 50 %, 70 % *and* 90 % *of the maximum field.*

5.3.8 Septum magnet

MUH3 can deliver muon beams to two experimental areas, MUH3.2 and MUH3.3, either providing beam to one area at a time or in a shared mode. This is done by means of a septum magnet, ASS31.
A septum magnet provides a dipolar magnetic field in a confined area in the vicinity of the beamline axis. The field is confined by the presence of a thin iron wall close to the beam trajectory, allowing to split the beam depending on its position. Figure 5.20 shows the vertical component of the magnetic field in the horizontal plane.

5.3.9 Beam blockers

A beam blocker (BB) is a device used to completely stop any radiation transmitted through the beamline when access to the experimental area is required. The design of the BB is based on the existing installations adapted to the larger aperture of the HIMB beamlines: they are constructed as two sandwiches of 90 mm copper, 120 mm stainless steel and another 90 mm copper which can be remotely moved into the beamline to stop the beam.

5.4 The MUH2 beamline

In the following, the optimization of the MUH2 beamline is described.
Whereas a dedicated framework was developed to easily optimize different versions of the beamline, different particle beams and different momenta, here only a limited selection is shown. To date, the latest design is MUH2 v7c, which is the one that will be described in detail in the following. To compare the performances of two different optimization algorithm for transmission, namely a Bayesian algorithm and NSGA-II, an additional version of the beamline is included: MUH2 v6a. The main features are listed below:

- MUH2 v6a: first model including two beam blockers, the transport solenoids in the first section are not yet radiation hard, graded field capture solenoid modeled without an iron yoke
- MUH2 v7c: the transport solenoids are radiation hard, the graded field capture solenoid is modeled with a fieldmap based on the latest design available

5.4.1 Beamline layout

The MUH2 beamline is designed to deliver the highest surface muon rates for particle physics experiments and it is therefore based on solenoid elements. The naming scheme for the magnets is not yet defined and the one presented here is to be considered provisional. As quickly mentioned

above, the length of the beamline severely affects the deliverable muon rates, so shorter beamlines are preferred. An additional constraint on the design is given by the neutron dose caused by the interaction of the proton beam with TgH and two bends are included along MUH2 to avoid a direct line-of-sight from the target to the experimental area. To further reduce the dose in the experimental area below the safety limit of 10 µSv/h to allow access, two beam blockers (BB) are positioned in the first straight section after the first bend (ASH1) of 36°.
Due to the big emittance transmitted, it is not possible to have the two BBs one after the other without losing a sizeable fraction of the beam as each of them needs ∼0.5 m of space. For the same reason a solenoid is needed between a BB and a bend. Therefore the first section is composed of three radiation hard solenoids (TSBL1, TSBL2, TSBL21) alternated with the BBs. After a second bend (ASH2) of 40° a solenoid (BL3) focuses the beam for transmission through a vacuum pump station. An additional solenoid (BL32) couples the beam into the first Wien filter. The BL4 solenoid is used to increase transmission through the separators. After the second Wien filter two additional solenoids (BL41 and BL5) are used to transmit through another vauum pump station and perform the final focusing.
Figure 5.21 shows the graphical output of the G4beamline simulation of MUH2 v7c used to optimize and characterize the design.

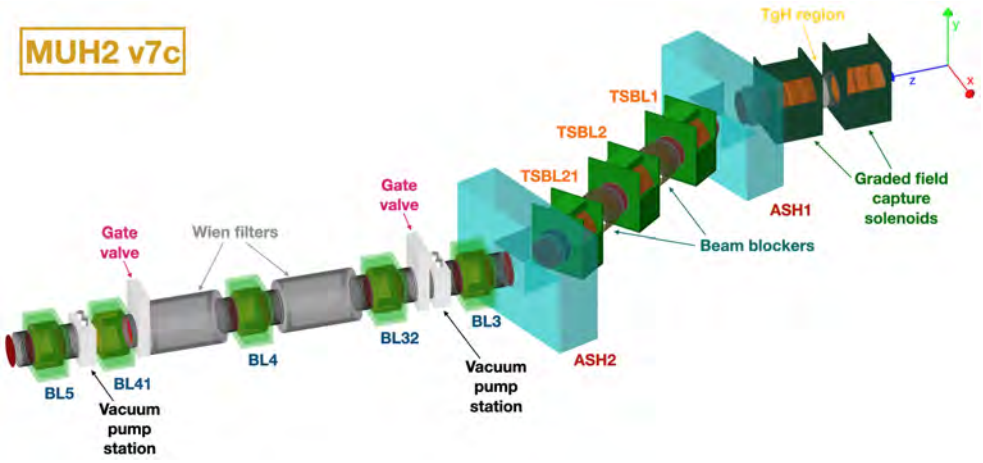

Figure 5.21: *MUH2 model in G4beamline. The layout is the most recent to date. The reference system is shifted from the target along the muon beam axis (z-axis in blue) for clarity. The proton beam impinges on TgH antiparallel to the x-axis. The MUH3 capture solenoid is included and set to the surface muon tune. The labelling is to be considered provisional and useful only in the context of this thesis to address the parameter space: ASH1 is a radiation hard dipole; the TSBL elements are radiation hard transport solenoids; ASH2 is a non-radiation hard dipole with slit system; the BL elements are non-radiation hard solenoids. Mock version of the two beam blockers, the pump stations and the gate valves are included to show their occupancy.*

5.4.2 Optimization strategy

The main figure of interest when comparing different design options for MUH2 is the delivered particle rate, however a number of additional parameters like the beam spot size or the contamination of the beam need to be considered as well. The first approach to this problem has been to sequentially optimize surface muon transmission from capture to the end. This is the current strategy for the optimization of the surface muon beams as carried out by Peter-R. Kettle [87], who is also working on the beamline layout and the optimisation of its performance. This approach is useful in case the available resources are limited but it is not easiliy scalable and it does not give information on the dependece of the properties of the beam on the tune, as the explored parameter space is limited. Additionally, it is prone to convergence to the first local maximum found. It is important to assess the properties of the delivered beam in the full available momentum spectrum, ranging from 0 MeV/c to 80 MeV/c. Already at 27 MeV/c, some elements of the beamline are energized with currents close to the allowed limit (details will follow). This prevents linear scaling of the tune to higher momenta and it therefore results in the need to optimize the beamline for cloud muons as well. To do so, the tune has been found independently for surface muons and for cloud muons constraining the central momenta to: 30 MeV/c, 40 MeV/c, 50 MeV/c, 60 MeV/c and 70 MeV/c. These optimizations have been repeated for positrons and pions as well, leading to 18 tunes to be found overall. Many changes have been applied to the initial design, and in order to give swift feedbacks on them for each tune, alternative optimization approaches were explored. A preference has been given to algorithms suitable for High Performance Computing, like Bayesian optimization [102] and genetic algorithms [45]. In the following paragraphs, an outlook of the optimization algorithms tested is provided.

Whereas the initial designs have been studied using optical modeling programs like Graphic Transport [30], such programs are not suitable for transmission evaluation. G4beamline [37] has been preferred for modelling as it allows to evaluate beam losses and to import high-fidelity fieldmaps, by which non-linearities are naturally treated.

5.4.2.1 Single-objective optimization

Many approaches have been developed to find global extrema of expensive-to-evaluate functions and it is not possible to determine a priori the most suitable for a given problem. The zoo of possible algorithms depends also on the number of figures of merit, or *objectives*, to be optimized. Two algorithms have been tested for the optimization of the transmission through MUH2:

- Bayesian optimization [102]

- Non-dominated Sorting Genetic Algorithm II (NSGA-II) [45]

Bayesian optimization was specifically designed to optimize expensixe functions whose behaviour in the parameter[3] space is generally unknown due to the lack of information. As such, this algorithm treats the objective function, which is the function to be optimized, as a probability distribution function assigning a prior distribution to it. At each iteration, the *black box* function is evaluated in a point in the parameter space and the prior is updated to a posterior function as done for Bayesian inference. The next point to be evaluated is obtained through the so-called *acquisition function*. There are a few different acquisition functions in literature, but the basic idea behind them is to find a point in the parameter space that would increase the information about the maximum of the objective function. A common approach is to use the *expected improvement* (EI) as acquisition function. It is defined as the expectation value of:

$$max(f(x) - f_n^*, 0), \quad x \in \text{search space} \tag{5.7}$$

where f is the objective function and f_n^* is the highest evaluation up to iteration n. The EI is generally faster to evaluate than the objective-function and standard approaches are based on first- or second-order derivatives [103]. For this work, the chosen implementation is that in the optuna python package [46]. The prior is built using the Tree-structured Parzen Estimator (TPE), which represents the prior distribution with a non-parametric density [104, 105]. Bayesian optimization is better suited for problems with less than 20 parameters [103]. This limit has been set empirically and it actually depends strongly on the problem and on the surrogate function[4] used for the priors, but finding the best parametrization for a given problem is by itself an optimization problem which might require an extensive use of resources.

Genetic algorithms have already been introduced in Chapter 3 and can be adapted to solve higher dimension problems, both in the parameter and objective space, simply by increasing the population size. Initially the Bayesian optimizer was used to maximize rate while, NSGA-II was used for the multi-objective optimization. With MUH2 v6a, shown here only to compare the two algorithms, the number of parameters to be optimized increased and the Bayesian optimizer performed worse than the sequential approach. Figure 5.22 shows MUH2 v6a: the layout is similar to v7c, the main differences are due to the number of elements along the beamline and the design of the graded field solenoids, which were just introduced. The parameters comprise 17 currents to energize the beamline, a shift in the position of each

[3] Here and in the following the term *parameter* is used to address the variables on which the objective function depends.

[4] A surrogate function is an approximation of another function which is generally less precise but much faster to evaluate. In this context, the Bayesian optimizer builds a surrogate of the G4beamline simulation which is quicker to optimize.

dipole and the two distances between the solenoids in the first straight section. All together the model is defined by 21 parameters. As an alternative to the Bayesian optimizer, NSGA-II was tested for single-objective optimization. Figure 5.23 shows a comparison between the optimization of MUH2

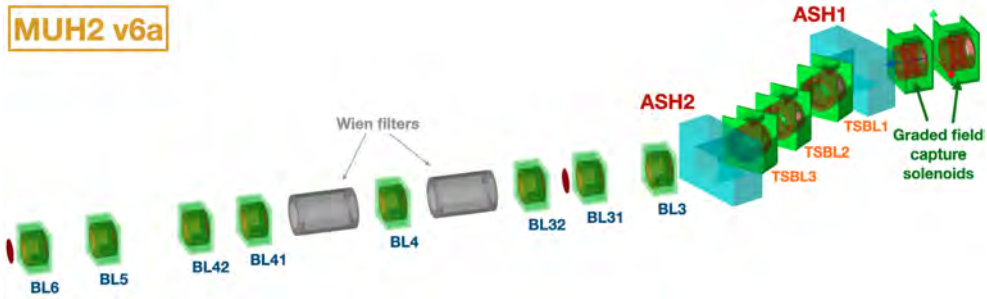

Figure 5.22: *MUH2 v6a model in G4beamline. First layout including the graded field solenoids. The MUH3 capture solenoid is included and set to the surface muon tune. The labelling is to be considered provisional and useful only in the context of this thesis to address the parameter space: ASH1 is a radiation hard dipole; the TSBL elements are radiation hard transport solenoids; ASH2 is a non-radiation hard dipole; the BL elements are non-radiation hard solenoids. Mock version of the two beam blockers, the pump stations and the gate valves are included to show their occupancy.*

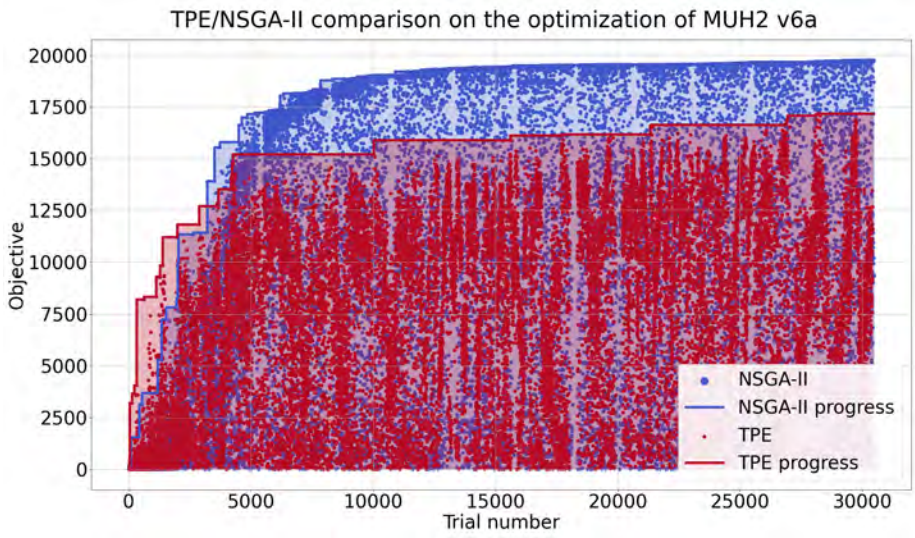

Figure 5.23: *Comparison between the optimization of MUH2 v6a with the TPE and NSGA-II. The TPE has a faster progress in the early trials, but does not approach the maximum, unlike NSGA-II which finds a maximum higher by* $\sim$15 %.

v6a with the two algorithms: the TPE has a faster progress in the early trials, but does not approach the maximum, unlike NSGA-II which finds a max-

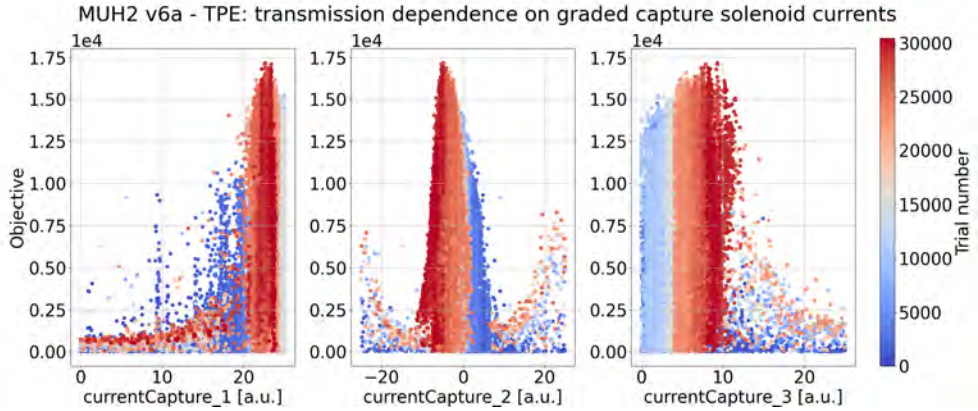

(a) TPE optimization: the trials are distributed in the full parameter space.

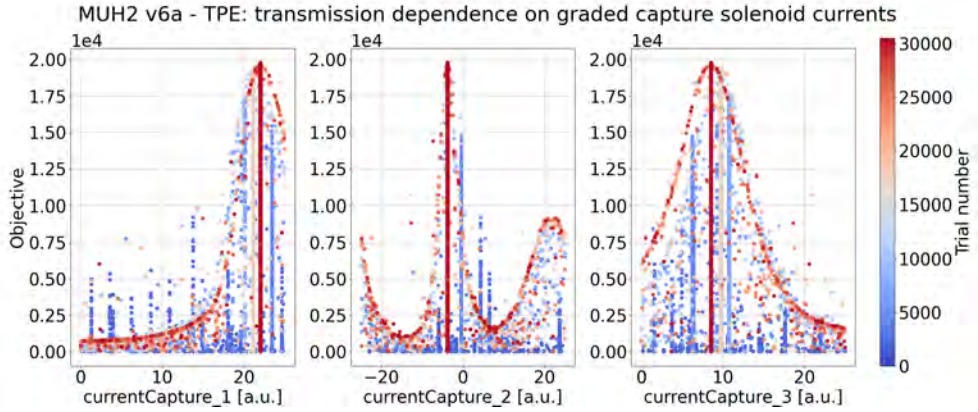

(b) NSGA-II optimization: the trials crowd the parameter space close to the found maximum.

Figure 5.24: *Muon transmission through MUH2 v6a as a function of the currents energizing the pancakes of the capture solenoid.*

imum higher by ∼15 %. The two optimizations were run on the Merlin6 cluster at PSI for 1750 core − hours on 350 cores. For later designs, NSGA-II has been used for both single- and multi-objective optimization.

Figure 5.24 shows the number of muons transmitted through MUH2 for each trial as a function of the currents energizing the three pancakes in the capture solenoid: in the top plot the TPE is used; in the bottom plot NSGA-II is used. There is a clear difference in the sampling: the TPE is covering a wider region of the parameter space, which at higher dimensions in the parameter space does not allow for a robust convergence; the NSGA-II, after convergence, by construction populates the region close to the maximum, causing the profilation on the parameter axes. This can be interesting to investigate the weight of each parameter on the final transmission.

5.4.2.2 Multi-objective optimization

A general overview of genetic algorithms for single-objective optimization has been given in the previous section. The main difference with multi-objective optimization relies in the ranking of the individuals to be selected for the next epooch. For single-objective functions the definition of fittest individuals is anlogous to sorting them by their fitness value, that is to say the value of the function. In multi-objective optimization the ranking is what differentiates different algorithms. The Non-dominated Sorting Genetic Algorithm uses the dominance as the first ranking criteria. An individual A dominates another individual B if:

- A is not worse than B in all objectives
- A is better than B in at least one objective

where *better* and *worse* are defined depending on what is the goal of the optimization. After the non-dominated points are found, they are removed from the set to be sorted and the procedure is repeated. The final result is a set of curves ranked by dominance as shown in Figure 5.25 with increasing ranking and the best being rank 0. The best trade-off curve is defined as the non-dominated set of points in the full parameter space. The aim of the multi-objective optimization is to find these curves. The dominance can be used to make a first selection of individuals, but the size of each rank is not defined and it is common to have more individuals with a given rank than the number needed to fill the population for the next epoch. The NSGA-II algorithm uses as a second selection criteria the crowding distance, which is a measure of how close an individual is to its neighbours. Different algorithms can be used to define this parameter, a common implementation consists in summing the distances to the closest neighbours on each axis. The individuals with the bigger crowding distance are then selected. While dominance is the analogous of fitness in natural selection, the crowding distance is analogous to diversity: a higher crowding distance will lead to a more diverse population and a better exploration of the parameter space.

5.4.3 Transmitted particle beam spectra

The starting point for the optimization of the particle spectra was to maximize surface muon transmission. Additionally to the magnet parameters, the position and the angle of the two dipoles were optimized and then kept fixed for the other optimizations. The search space includes 24 parameters, of which four categorical[5]:

- currentCapture_i: three currents, one for each coil pancake, to characterize transmission in the capture solenoid.

[5] A categorical variable can take on one of a limited number of possible values.

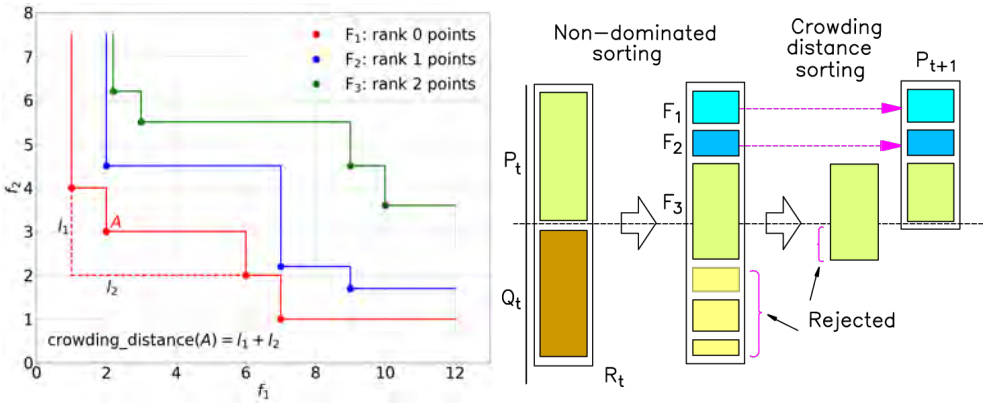

Figure 5.25: *Left: example of non-dominated sorting adapted from [106]. The f_i are the objectives to be minimized. The F_i are the pareto fronts shown with their ranking. F_3 has the highest ranking and it is dominated by the other two fronts. The crowding distance of point A is shown. Right: example of the iteration of the NSGA-II algorithm from [107]. At iteration t, P_t are the initial population. Then, the offspring population Q_t is created and is combined with P_t in the combined population R_t. The individuals are selected based on non-dominated sorting from the fronts F_i. When the individuals with a given rank are more than those needed for the next epoch, like in front F_3, they are sorted by crowding distance. The selected individuals are then used to create the next population P_{t+1}.*

- BField1: the field in ASH1.
- currentTSBLi: the current for each of the three radiation hard transport solenoids (TSBL).
- BField2scale: the ratio between the field in ASH2 and the field in ASH1, scaled with the increased bending angle. If set to 1, the ratio of the two fields is analogous to that of the maximum found with the sequential approach.
- currentBLi: the current for each of the five non-radiation hard solenoids (BL).
- WienB: the magnetic field in the two Wien filters. The two Wien filters are assumed to be identical and are oriented horizontally with the same polarities. The HV plates are set to $\pm 320\,\mathrm{kV}$ and the electric field is $1.488\,\mathrm{MV/m}$ directed so that the positrons are deflected towards negative x.
- MUH2sign: the sign of the MUH2 capture solenoid. It multiplies each of the three currents energizing the pancakes. This is a categorical parameter because the options are finite: positive and negative.
- MUH3sign: the sign of the MUH3 capture solenoid. It multiplies each of the three currents energizing the pancakes (categorical).

- FirstSSectionSign: sign of the solenoids in the first straight section. It multiplies each currentTSBLi (categorical).
- SecondSSectionSign: sign of the solenoids in the second straight section. It multiplies each currentBLi (categorical).
- ASH1dx, ASH1dz, ASH1dTheta: the shift in the position of ASH1 along the x and z axes and the tilt around the y axis.
- ASH2dx, ASH2dz, ASH2dTheta: the shift in the position of ASH2 along the x and z axes and the tilt around the y axis.

The parameter space is defined by the following ranges:

- [0 T, 0.45 T] for currentCapture_1, currentCapture_3 and currentTSBLi
- [−0.45 T, 0.45 T] for currentCapture_2
- [0.75 ·nominal, 1.25 ·nominal] for BField1. Nominal is 0.05 T from the sequential optimization
- [0 T, 0.55 T] for currentBLi. A higher field than for radiation hard solenoids is possible because of the different design
- -1 or 1 for the categorical parameters
- [−500 mm, 500 mm] for ASH1dx, ASH1dz, ASH2dx, ASH2dz
- [−18°, 18°] for ASH1dTheta
- [−20°, 20°] for ASH2dTheta

The range for the dipole rotation correspond to the total bending angle in the two arcs. The nominal position of the dipoles is chosen to have their center in correspondence of the centerline by applying a shift along their transverse axes and they are rotated by half their bending angle. The total number of parameters is 24 and the population size was chosen to be 100. The definition of the optimal population is by itself an expensive optimization problem. Here, 100 individuals were empirically found to perform well.

For each trial 10^5 μ^+ were transmitted. The input beam was obtained by selecting positive muons in the [17 MeV/c, 37 MeV/c] momentum range from the particle spectrum shown in Figure 5.10. Figure 5.26 shows the progress of the optimization: due to the high number of parameters, the latest trials still show a slow linear increase with time. The optimization was stopped after 6000 core − hours.

The best parameters for the positioning of ASH1 and ASH2 do not differ much from the nominal ones, as shown in Figure 5.27. The total rate is found by propagating the full available μ^+ spectrum (3×10^6 μ^+) through the beamline. The total rate is 1.23×10^{10} μ^+/s, which is 2.5 % higher than the maximum found with the sequential approach. In the following, the

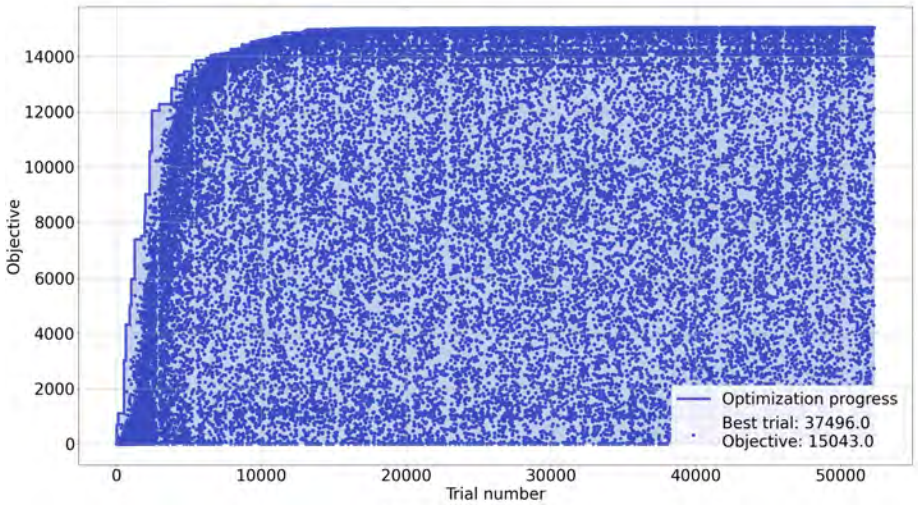

Figure 5.26: *Progress of the optimization of MUH2 v7c with NSGA-II on surface muons. The convergence is fast up to trial $\sim 10^4$ to then progress slower due to the high number of parameters.*

parameters for the dipole positioning are fixed to the values in Figure 5.27 and the single-objective optimizations is repeated for μ^+, e^+ and π^+. The central momenta were defined by fixing the BField1 scaled accordingly. For each optimization a selection on the particle spectra at target was performed centered on the nominal momentum and with a width of 5 MeV/c. Due to the lower number of parameters convergence was found faster and 2000 core − hours per optimized beam were sufficient. The full optimization ran in $\sim$5 days on 350 cores. The results are shown in Figure 5.28: each spectrum represents the maximum achievable rate at a given momentum. The rates of negative particle beams was computed by flipping the sign of each element. Additionally to the particles generated at target, muons and pions will decay through the beamline, contributing to the final rates. This contribution is not negligible for both μ^+ and μ^- and is included in Figure 5.28 labelled as *deep (D.) muons*. Deep muons are the biggest fraction of the delivered cloud muon spectrum.
For future reference, the tunes for maximum transmission are collected in Appendix E.

In the following, emphasis is put on improving the final beam spot of muons in the full momentum spectrum and on minimizing positron contamination for surface muon beams. The beam spot of Mott positrons and of π^- for a potential CEX reaction are included as well. The framework developed for these studies can be easily adapted for additional figures of merit, such as the accepted momentum bite by including in the parameter space the aperture of the slit system integrated in ASH2.

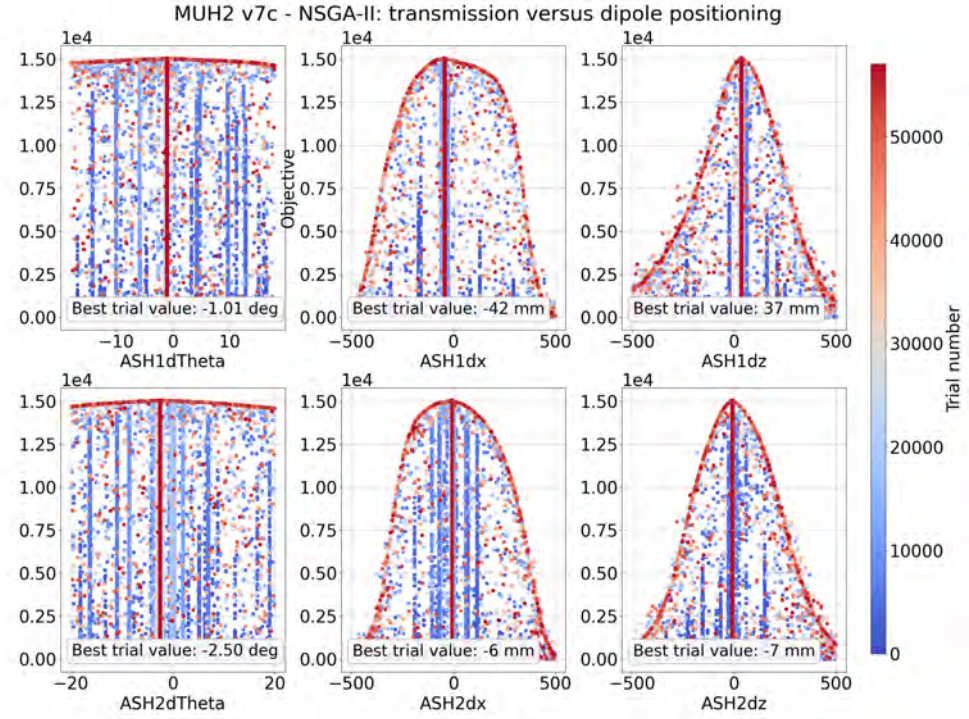

Figure 5.27: *Muon transmission through MUH2 v7c as a function of the position of the two dipoles. A positive shift along the x-axis for ASH1 is directed towards the outer side of the bend. The opposite goes for ASH2.*

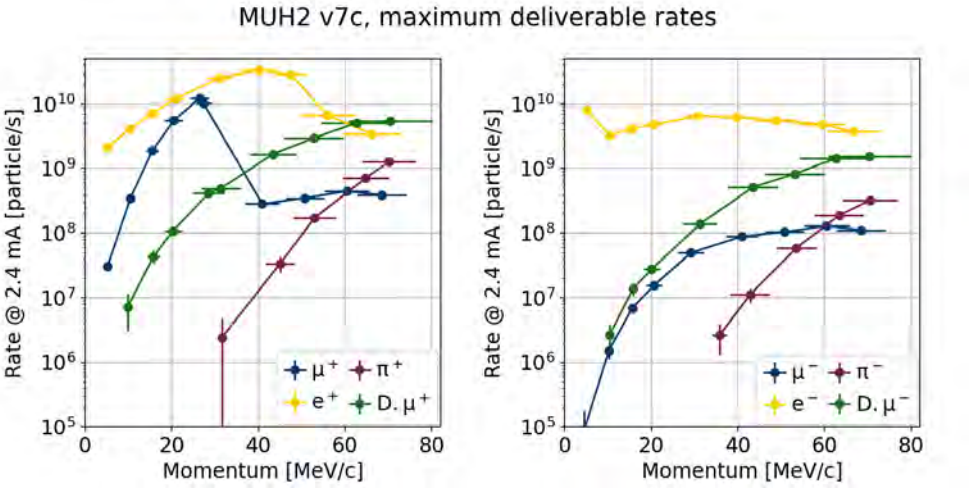

Figure 5.28: *Maximum deliverable rate in MUH2. The rate was maximized for the positive particle beams and computed for the negative ones by flipping the sign of each element. Deep (D.) muons are shown in green. The error bars in the vertical direction are the statistical uncertainty on the computed rates. The error bars in the horizontal direction correspond to ± 1 standard deviation of the transmitted momentum spectrum.*

5.4.3.1 Transmitted particle spectra for optimized beam spots

Whereas increasing the deliverable muon rates is the main goal of the HIMB project, the maximization of rate only does not set constraints on additional figures of merit such as the final beam spot size, the focus position or the width of the transported momentum distribution. Depending on the requirements of the experimental set-ups, a trade-off is necessary. Genetic algorithms in general were designed for such applications and they are very well suited to explore the parameter phase space and find the trade-off surfaces, that is to say the pareto front.

Here an example of such application is shown for the full muon spectrum, for 50 MeV/c positrons and for 70 MeV/c. The latter two were chosen as they are currently employed in MEG II as calibration sources and a next-generation MEG experiment might benefit from such input.

The optimization of the final beam spot does not require the tuning of the full beamline and the parameter space can be limited to the second straight section while keeping the other parameters fixed to the values found in the single-objective optimization. A focus is defined as a point where the correlation between the dispersions and the transverse positions is zero. In case there is no correlation between the motion in the horizontal and vertical transverse planes, there are two such correlations and a quadrupole doublet is enough to provide focusing. Whereas solenoids couple the horizontal and vertical motion, in the Larmor frame the motion in the two resulting axes is uncoupled and a solenoid doublet can be used for focusing [96]. The usage of additional elements provides additional degrees of freedom to compensate possible higher order contributions and it allows to lower the fields required for focusing. The parameter space comprises the five BL solenoids, the Wien filter magnetic field and the dipole fields reducing the search to an eight-dimensional problem. ASH1 and ASH2 are included to optimize the centering of the beam on the centerline. The objectives for the optimization are:

- particle rate: the number of particles transported to the end of the beamline as for the single-objective optimization (maximized)
- average radius r_{avg}: the average of the radial distribution at the focus. As solenoids focus in both transverse planes, the beam spot is expected to be circular and the radial size of the beam spot is a good approximation of the size in both planes. This figure embeds additionally information about the potential offsets of the beam (minimized)
- beam centering $\hat{N}_{center}$: the number of particles close to the centerline is maximized. For each BL solenoid the number of particles that are transmitted to the end and that cross their center within a 50 mm ra-

dius is counted. The average over the five solenoids is the objective (maximized)

The allowed range for solenoid currents and the Wien filter is the same as in the previous paragraph. The range for the dipole fields is reduced from 25 % to 10 % around the value found in the single-objective optimization: only minor corrections are expected for centering. For each optimization, only particles within $\pm 5\,\mathrm{MeV/c}$ are used. At each iteration, 10^5 particles are simulated. Due to the higher dimensionality of the objective space, the time needed per optimization increased to $20\,000\,\mathrm{core-hours}$ for surface muons and to $6000\,\mathrm{core-hours}$ for the other optimizations. The difference in computing time is due to the higher transmission efficiency for surface muons, which require a longer simulation time.

For surface muons, positron contamination is included as an additional objective: at each trial 10^5 positrons are propagated through MUH2 with the same tune as for surface muons. The number of positrons transmitted to the end is minimized.

Figure 5.29 shows the correlation between r_{avg} and $\hat{N}_{center}$ with the transmission relative to the maximum deliverable rate for each momentum spectrum. In r_{avg} vs transmission, the solid lines represent the 2D pareto front. In $\hat{N}_{center}$ vs transmission, the solid lines are the maximum $\hat{N}_{center}$ at a given transmission. The black-circled points are the trials chosen for each momentum bite. The ratio behind the choice is one of the possible trade-offs that can be made: the average radius was chosen to be lower than 45 mm and the point with maximum transmission and centering was chosen.

The total delivered rates for the chosen muon settings are shown in Figure 5.30. Here, the positron and pion rates represent the contamination at the end of the beamline. Table 5.2 shows the rate and phase space parameters of prompt antimuons only for each muon beam tune together with positron contamination and deep muon rates. As expected, the separation power decreases rapidly with increasing momentum. The emittance here is defined as the area enclosing 90 % of the beam. Figure 5.31 shows the envelope of surface muons as an example. Only trajectories delivered to the end of the beamline are shown. The dashed red line is the average of the transverse distribution for each given z. The solid red lines represent the ± 1 standard deviation with the respect to the average for each given z. The black lines represent the dispersion along the beamline. Appendix G shows the calculation of the dispersion.

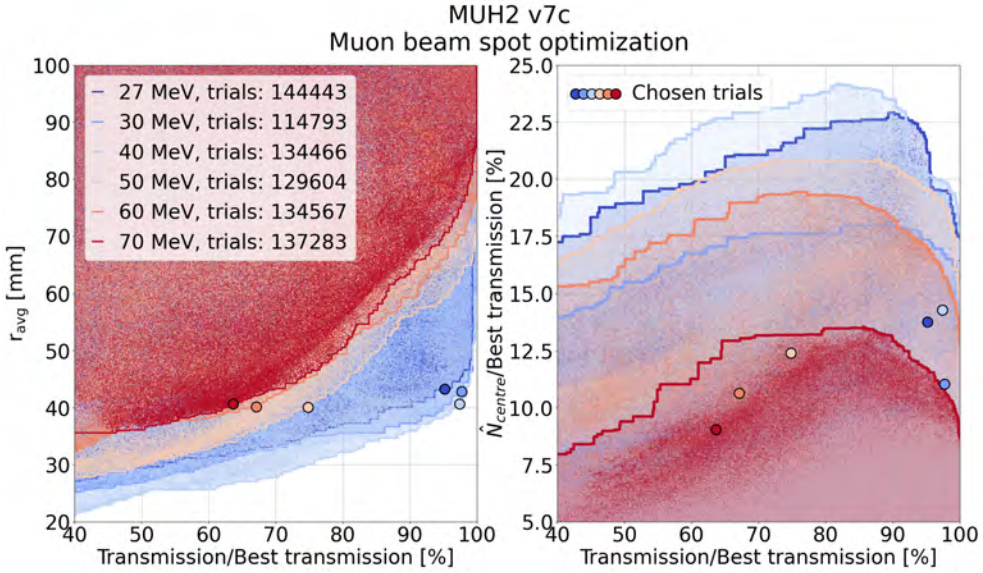

Figure 5.29: *Left: r_{avg} vs transmission relative to the maximum deliverable rate. The solid lines represent the 2D pareto front in this subspace of the objectives. Right: $\hat{N}_{center}$ vs transmission both normalized to the maximum deliverable rates. The solid lines represent the maximum centering at a given transmission. The 2D pareto is therefore a subset of such curves. The black-circled points are the trials chosen as an example for each central momentum.*

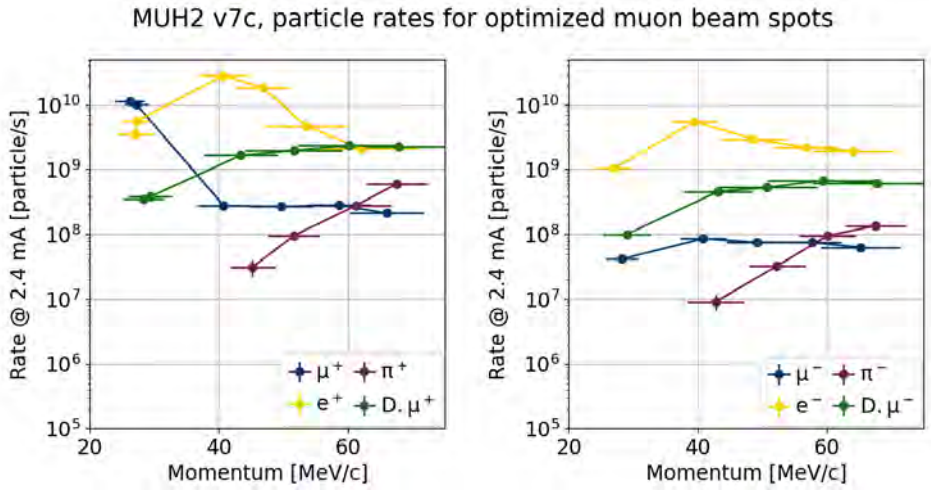

Figure 5.30: *Delivered rates in MUH2 for optimized muon beam spot settings. The rates for negative particle beams are obtained by flipping the sign of each element. Deep (D.) muons are shown in green. The error bars in the vertical direction are the statistical uncertainty on the computed rates. The error bars in the horizontal direction correspond to ± 1 standard deviation of the transmitted momentum spectrum.*

	27 MeV/c	30 MeV/c	40 MeV/c	50 MeV/c	60 MeV/c	70 MeV/c
Prompt muon Rate [μ^+/s]	1.12×10^{10}	9.94×10^{9}	2.86×10^{8}	2.69×10^{8}	2.77×10^{8}	2.08×10^{8}
Deep muon Rate [μ^+/s]	3.51×10^{8}	3.85×10^{8}	1.67×10^{9}	1.98×10^{9}	2.40×10^{9}	2.27×10^{9}
$\hat{x}$ [mm]	7.79	-1.61	13.43	-3.67	-5.12	-7.50
STD(x) [mm]	34.37	31.29	37.55	34.75	40.11	39.48
$\hat{x'}$ [mrad]	16.40	-23.91	-19.24	60.9	-46.04	6.70
STD(x') [mrad]	165.09	171.95	163.96	112.72	108.25	88.52
$\hat{y}$ [mm]	-2.57	5.64	1.75	2.12	0.36	4.40
STD(y) [mm]	33.14	32.02	32.27	36.76	34.58	40.74
$\hat{y'}$ [mrad]	0.91	-27.01	29.29	33.59	10.35	18.44
STD(y') [mrad]	176.69	165.15	159.93	105.19	86.78	90.35
$\hat{Pz}$ [MeV/c]	25.87	26.78	40.28	49.09	58.15	65.56
STD(Pz) [MeV/c]	2.16	1.88	3.98	4.71	4.98	5.59
$\varepsilon_x(90\,\%)\pi$ rad mm	20.28	17.58	16.99	13.04	12.19	10.38
$\varepsilon_y(90\,\%)\pi$ rad mm	19.51	18.08	15.43	12.48	9.83	11.07
e^+ contamination	3.07×10^{-1}	5.47×10^{-1}	1.46×10^{1}	8.10×10^{1}	1.75	8.39×10^{-1}

Table 5.2: Phase space parameters and positron contamination of prompt antimuons propagated with the tunes for optimized beamspot. The phase space parameters of deep muons are not shown as they are consistent with those of prompt muons. The contamination is normalized to the total transmitted muon rate.

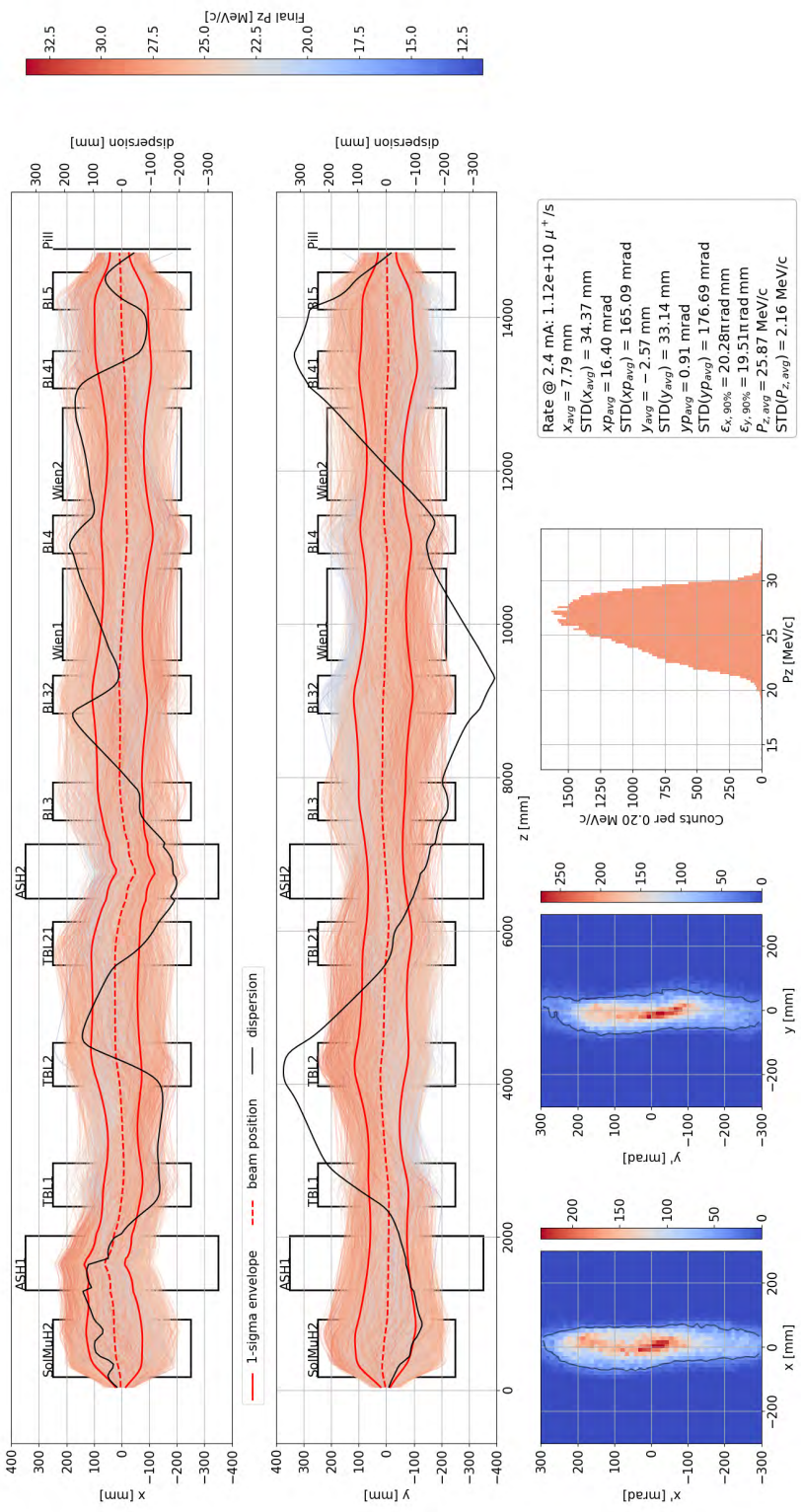

Figure 5.31: *Prompt surface muon beam envelopes and phase spaces. The dispersion curves shown here are computed based on the correlation between the position and the longitudinal momentum at each position. TgH is positioned at the origin of the coordinate system.*

The beam spot sizes obtained are consistently between 30 mm and 40 mm depending on the dispersion at the end of the beamline. The mechanism by which the beam spot sizes are reduced at higher momenta is based on lowering the currents in the second straight section and focus at maximum current with the last two solenoids. This allows to exploit the acceptance of the beamline to continuously and efficiently collimate the beam through the full lattice. The positron contamination in the case of surface muons is still high at 30.7 %. In the following an example of improved contamination will be shown. For future reference, the chosen tunes for optimized beam spot are collected in Appendix F.
Now, a few paragraphs will follow looking at the optimization of the positron contamination for surface muons and on the optimization of the beam spot for 50 MeV/c positrons, here Mott positrons (see Section 1.3.2.3), and for 70 MeV/c pions, here Charge EXchange (CEX) pions (see Section 1.3.2.2).

Surface muons Of particular importance for fixed target experiments like MEG and Mu3e is to reduce as much as possible the positron contamination, which would possibly increase the size of accidental background. For surface muons, as stated above, positron contamination was added as a figure of merit to be minimized with NSGAII. For each trial 10^5 μ^+ and 10^5 e^+ where propagated through MUH2. Figure 5.32 shows the 3D pareto front on transmission, average radius and positron contamination (colored markers) together with the full statistics of the study (grey markers). Two tunes are highlighted with a red and a black marker: the red point is the optimized beam spot tune for surface muons shown in Figure 5.31; in black the selection criteria include a cut on contamination. Whereas the muon rate is reduced only by 12 %, positron contamination is suppressed by a factor $\sim$12.

Table 5.3 shows the parameters of the two tunes. On a qualitative side, to keep the contamination low, the optics is changed so that most positrons are lost in the second Wien Filter by lowering the current in BL4 and reduce the divergence up to BL41. As the phase space is conserved, this causes an increase of the muon envelope, which is compensated by a stronger field in BL3. This behaviour is shown in Figure 5.33, where a steeper drop in the positron transmission is observed in the second Wien filter when positron contamination is minimized.

Due to the high contamination suppression, the tune presented here is also very interesting for negative muons in the same momentum range: only cloud muons contribute to negative moun rates and the rates are much lower than for positive muons. Electron production instead, is only a factor 2 lower in rate than positrons, as shown in Figure 5.10. Figure 5.34 shows the envelope of prompt negative muons for the same tune.

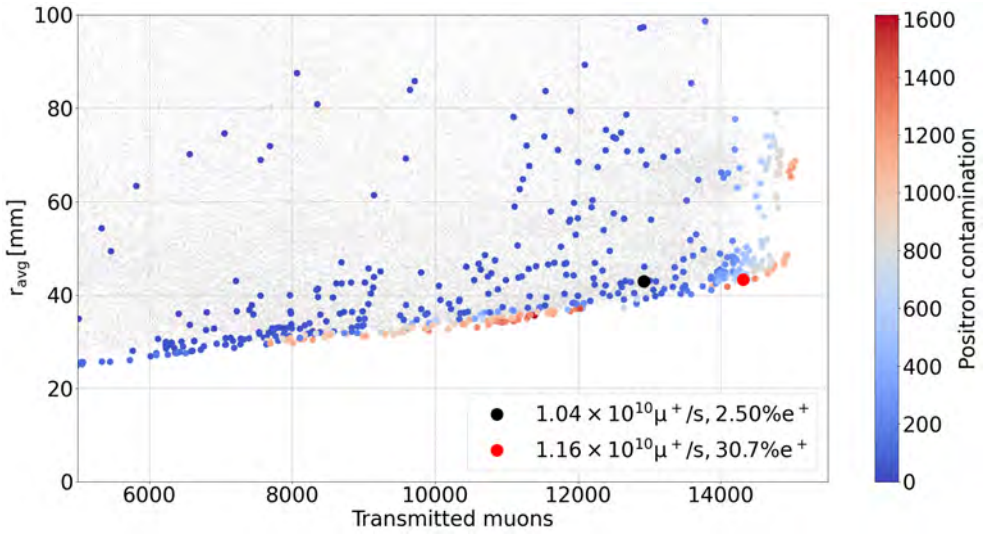

Figure 5.32: *Grey markers: full statistics of the optimization of the beam spot for surface muons. Colored markers: 3D pareto front on transmission, average radius and positron contamination. The red point is the optimized beam spot tune for surface muons shown in Figure 5.31; in black the selection criteria include a cut on contamination.*

	Peak fields [T]	
	Beam spot tune	Beam spot tune + contamination cut
BField1	0.0521	0.0521
BField2cur	0.952	0.952
WienB	-0.0158	-0.0165
currentBL3	0.207	0.269
currentBL32	0.236	0.236
currentBL4	0.263	0.203
currentBL41	0.225	0.151
currentBL5	0.364	0.364

Table 5.3: Peak fields for the optimized beam spot settings. On the left, the criterion for the parameter choice does not include positron contamination. On the right, a cut in positron contamination is included.

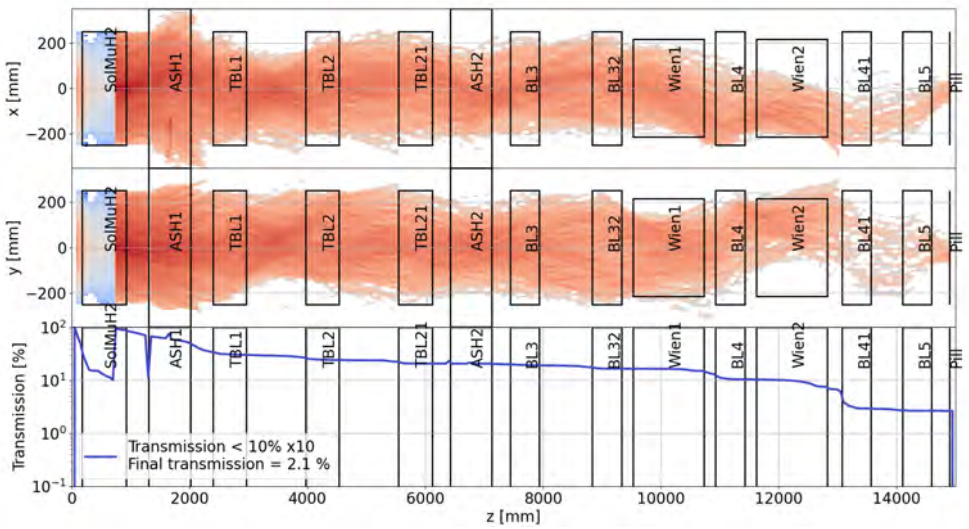

(a) Beam spot tune

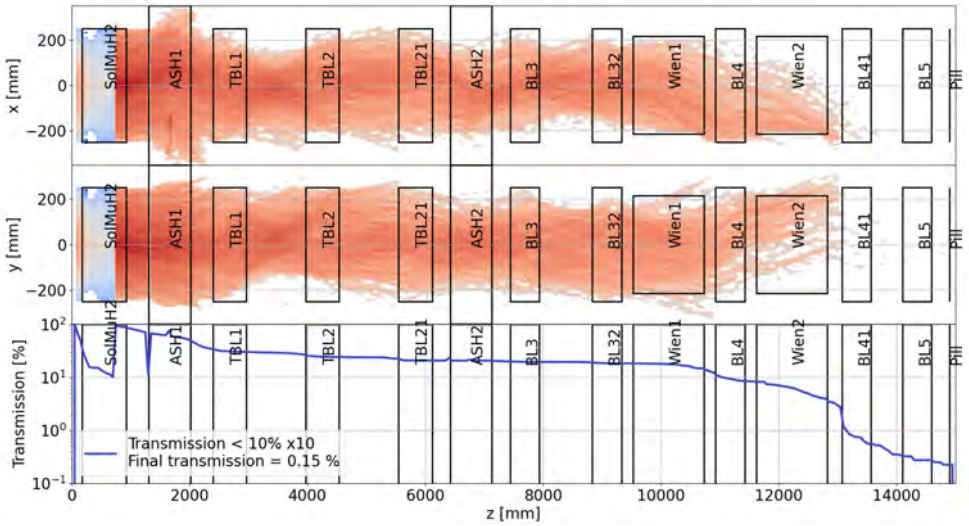

(b) Beam spot tune + contamination cut

Figure 5.33: *Positron transmission along MUH2. The heat maps represent the track density along MUH2, while the solid line plots are their integral along the transverse directions. Top: beam spot tune. Bottom: beam spot tune with contamination cut. The transmission is normalized on the propagated statistics,* $5 \times 10^4\,\mathrm{e}^+$*. When lower than* $10\,\%$*, transmission is multiplied by 10 to improve readability of the heat maps.*

	Beam spot tune + contamination cut		Beam spot tune	
	Prompt	Deep	Prompt	Deep
Rate [μ^-/s]	2.87×10^7	8.18×10^7	3.60×10^7	1.05×10^8
$\hat{x}$ [mm]	17.80	29.69	8.36	17.00
STD(x) [mm]	39.25	40.91	39.39	46.24
$\hat{x'}$ [mrad]	-17.60	-39.83	-25.38	-65.55
STD(x') [mrad]	212.69	196.91	181.49	170.38
$\hat{y}$ [mm]	9.15	-3.43	4.58	13.28
STD(y) [mm]	30.62	32.81	34.48	34.38
$\hat{y'}$ [mrad]	32.99	28.37	12.36	9.79
STD(y') [mrad]	162.27	176.49	164.42	165.43
$\hat{P}z$ [MeV/c]	26.63	26.93	26.46	27.21
STD(Pz) [MeV/c]	2.54	3.38	2.55	3.30
$\varepsilon_x(90\,\%)\pi$ rad mm	24.75	22.30	26.26	22.01
$\varepsilon_y(90\,\%)\pi$ rad mm	19.50	18.86	22.14	18.62
e^- contamination	8.16×10^{-1}		1.50×10^1	

Table 5.4: Phase space parameters and electron contamination of negative muons propagated with the surface muon tunes with inverted magnetic fields. On the left, the tune for optimized beam spot and low contamination is used. On the right, the tune optimized on beam spot only is used. Electron contamination is normalized to the total transmitted muon rate.

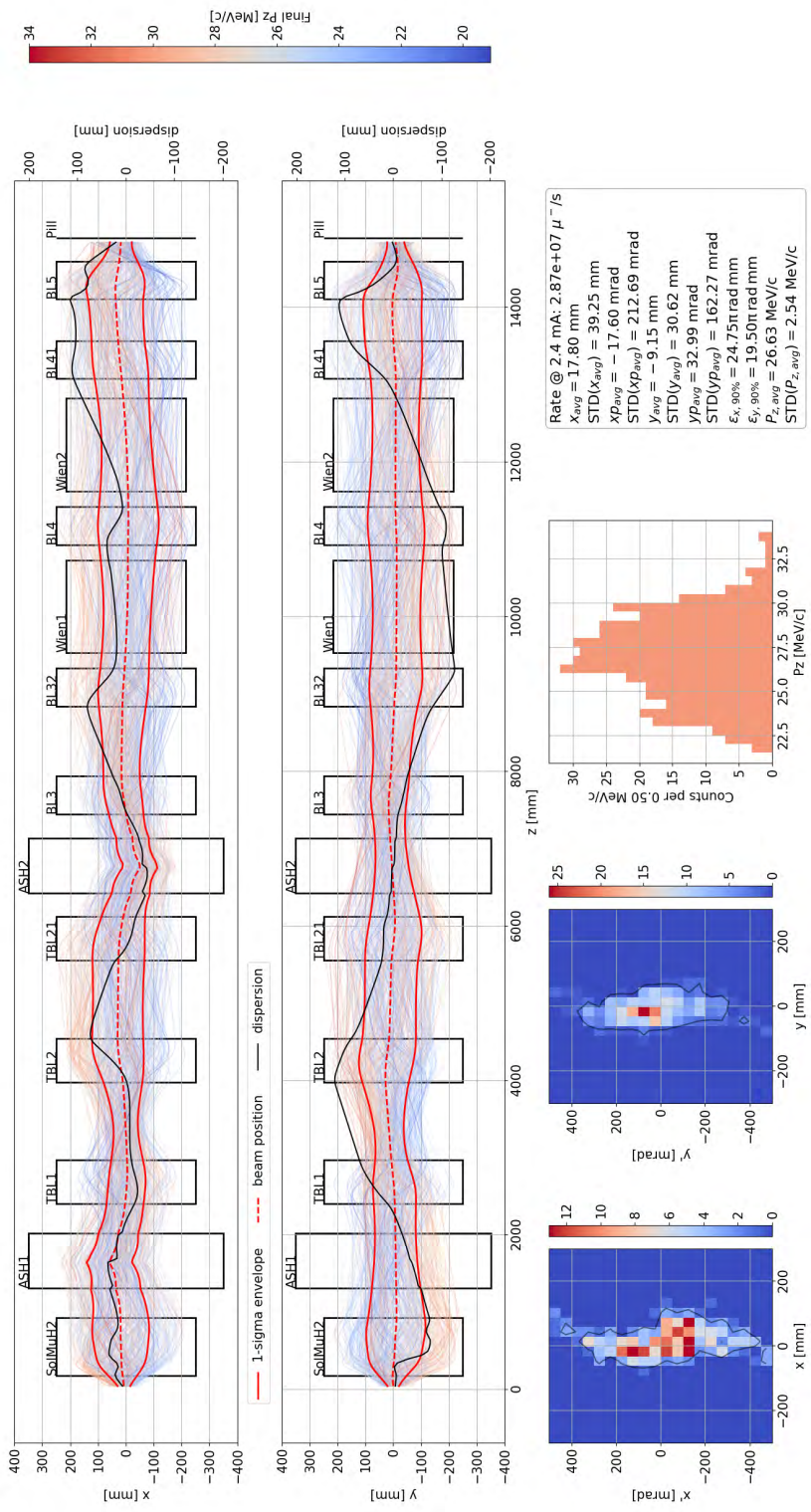

Figure 5.34: *Prompt negative muon beam envelopes and phase spaces. The dispersion curves shown here are computed based on the correlation between the position and the longitudinal momentum at each position. TgH is positioned at the origin of the coordinate system.*

The prompt muon rate is $2.87 \times 10^7\,\mu^-/\mathrm{s}$. The total rate, accounting for pion decays deep into the capture solenoid is $1.11 \times 10^8\,\mu^-/\mathrm{s}$ with an electron contamination of $1.03 \times 10^8\,\mathrm{e}^-/\mathrm{s}$. If compared with rate and contamination obtained with the tune optimized on beam spot only, the rate is $1.42 \times 10^8\,\mu^-/\mathrm{s}$, higher by 27 % and the contamination is $2.12 \times 10^9\,\mathrm{e}^-/\mathrm{s}$. The suppression factor of the contamination cut therefore amounts to $\sim$22. Table 5.4 shows the phase space parameters and the electron contamination for the studied tunes. As mentioned for positron contamination in Section 5.3.5, the electron contamination shown here is expected to overestimate the actual contamination due to the absence of fringe fields in the fieldmaps used to model the Wien filter.

Due to the low negative muon yield, the separation is not sufficient to allow for a clean negative muon beam. However, it would be possible to further reduce the electron background by exploting their time distribution: due to their large velocity spread at creation, negative muons have a flat distribution and only a small fraction of the electron beam is created by decay in flight of muons and pions within the acceptance of MUH2, while the majority of the electrons is created directly in the target. Figure 5.35 shows a comparison of the time of flight distribution of muons and electrons modulo the proton RF at the end of MUH2 for the two tunes, analogously to what is shown in Figure 3.11 in Chapter 3. Electrons are here distinguished in *Michel*, if created more than 5 ns after the interaction of the proton at TgH, and *Prompt*, if created within the first 5 ns after interaction. In this study the time structure of the proton beam is inclued by smearing the time of flights with a gaussian of width 0.25 ns, but no assumption is made on the possible resolution of the veto system. For both tunes, the electrons are well localized and a 3.5 ns window is sufficient to completely suppress the background. As a comparison, the proton RF has a period of 19.73 ns. Assuming such a setup and perfect transmission to an experiment, a continuous muon rate of $9.13 \times 10^7\,\mu^-/\mathrm{s}$ with an electron contamination of $3.78 \times 10^5\,\mathrm{e}^-/\mathrm{s}$ is achievable. Further details on the modeling of TOF spectra with G4beamline are presented in Appendix H.

Mott positrons Figure 5.36 shows the 3D pareto front for the optimization of the beam spot of Mott positrons. The tune chosen was found by imposing a cut on the average radius of 45 mm. The calibration based on Mott scattering performed in MEG requires a beam with a narrow momentum spread. Further details on the technique can be found in [65]. In πE5 such a condition is achieved by reducing the opening of the first slit system FSH41 (see Section 3.1), where the dispersion is at its maximum. For the tune here, and in general for MUH2, such a condition is not easily achievable. Due to the presence of solenoids, the horizontal dispersion couples into the vertical one and the only points which keep a non-zero dispersion independently

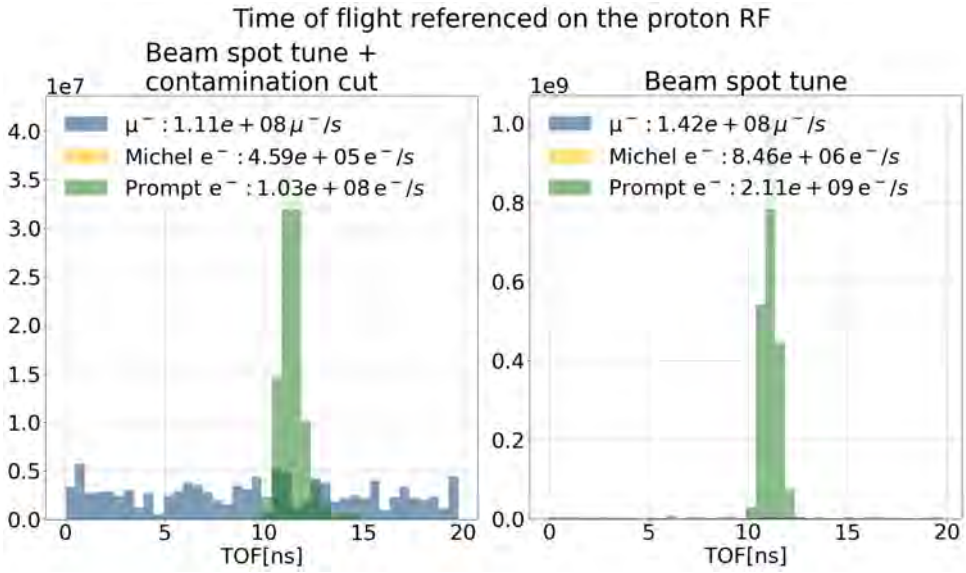

Figure 5.35: *Spectrum of the time-of-flight modulo the period of the proton RF at the end of MUH2 for negative muon settings separated by type: negative muons in blue, Michel electrons in yellow and Prompt electrons in green. The distribution of negative muons is flat due to their large velocity spread at creation. Electrons are discriminated based on their creation time after proton interaction: Michel electrons are created after* 5 ns*; Prompt electrons are created within the first* 5 ns*. The scale does no represent the delivered rates. Left: beam spot tune with contamination cut. Right: beam spot tune.*

from the tune are the dipoles. These are therefore the only points where a slit system would consistently affect the momentum distribution. The first dipole is not suitable to host a slit system due to the complicated mechanics and the harsh radiation environment, leaving ASH2 as the only possible location. Here, as shown in Apendix I, the dispersion is non-zero, but it is not sufficient for the requirements of a Mott calibration. For the sake of comparison, the rate and momentum spread as a function of the aperture of the slit system in ASH2 is shown in Figure 5.37. The calibration currently carried out for the MEG II experiment exploits a beam with a momentum spread of $\sigma \approx 140\,\mathrm{keV/c}$, while with the tune shown here the minimum achievable spread is 3.79 MeV/c, with a slit opening of 50 mm and a beam rate of $4.95 \times 10^9\,\mathrm{e^+/s}$. With maximum slit opening, the momentum spread is instead 4.10 MeV/c and the rate is $2.38 \times 10^{10}\,\mathrm{e^+/s}$. Whereas the optimization presented here is not exhaustive and a better tune cannot be excluded, in general MUH2 is designed to have a wide acceptance at the cost of a low momentum resolution, which is not compatible with the requirements of a Mott calibration.

Charge EXchange pion beam Figure 5.36 shows the 3D pareto front for the optimization of the beam spot for CEX pions. The tune chosen was found

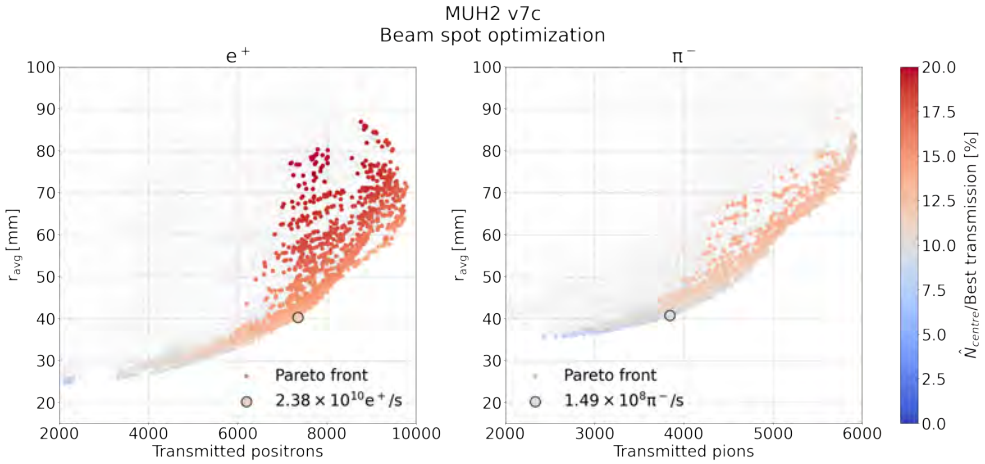

Figure 5.36: *Beam spot optimization for Mott positron beam (left plot) and CEX pion beam (right plot). Grey points: full statistics of the optimization of the beam spot. Colored markers: 3D pareto front on transmission, average radius and $\hat{N}_{center}$/Best transmission. The bigger markers are the trials chosen as a possible trade-off between the objectives.*

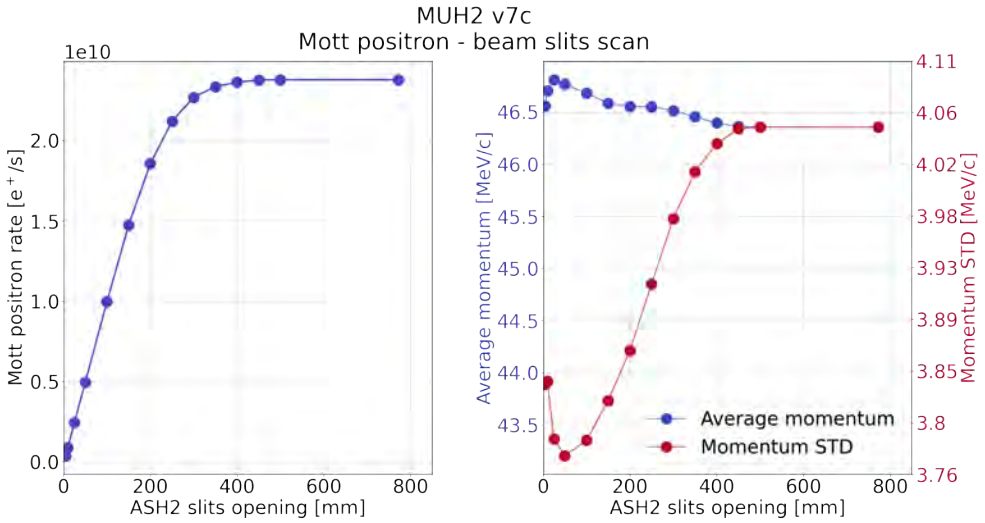

Figure 5.37: *Left: positron rate as a function of the aperture of the slit system in the ASH2 dipole for the Mott positron beam tune. Right: momentum average momentum (blue) and standard deviation (red) as a function of the aperture of the slit system in the ASH2 dipole.*

by imposing a cut on the average radius of 45 mm. Table 5.5 shows the peak fields for such a tune. Due to the field limits imposed (0.55 T) maximum transmission is granted when all solenoids are running at maximum current. The solenoids cannot be energized enough to keep the optics of the surface muon tune. The reduction of the beam spot size is provided as reported above, by effectively cutting the phase space. The focusing in the second straight section is relaxed with BL32 set to 0.25 T and BL4 set to 0.28 T. The

envelope is shown in Appendix J. A negative pion beam with a final beam spot of STD(x) $\approx$ STD(y) $\approx$ 35 mm is therefore obtained. The beam rate is $1.49 \times 10^8\,\pi^-/\mathrm{s}$.

	Peak fields [T]
currentBL3	0.548
currentBL32	0.248
currentBL4	0.284
currentBL41	0.544
currentBL5	0.547
BField1	0.137
BField2cur	0.986
WienB	-0.00976

Table 5.5: Peak fields for the optimized negative pion beam for a potential CEX calibration. Even though for high momenta, maximum transmission is obtained for maximum magnetic fields, here BL3 and BL4 are set to a lower value to reduce focusing to induce beam collimation with the acceptance of the beamline. Such strategy results in cutting the emittance of the final beam to reduce the size of the final beam spot.

5.4.3.2 Final remarks

A set of tunes suitable for different experimental application was found and it was shown that it is possible to reduce the beam spot size and to a limited extent the momentum spread of the beams in MUH2. Additionally, the possibility to strongly reduce the positron contamination in surface muon beams by means of dedicated optics was explored. It is important to underline that the commissioning of such beamline would need a detailed optical modeling and a dedicated tuning strategy. The results presented here should be intended as a proof of principle that the beamline can be optimized for different applications.

5.5 The MUH3 beamline

The framework developed for MUH2 was used for the optimization of the MUH3 beamline layout presented here. As in the previous section, a limited selection of results is shown. The optimization of the design is still ongoing at the time of writing this thesis and the model presented here was defined in October 2023.

5.5.1 Beamline layout

The MUH3 beamline is designed for μSR applications, which do not require to reach the $10^{10}\,\mu^+/\mathrm{s}$ but have more stringent requirements on the quality

of the delivered beam. As a matter of fact, the statistics required for such application is much lower than for particle physics experiments, while the main requirements consist of a 20 mm beam spot (σ_x, σ_y) and a high polarization. The layout and elements of MUH3 are inherited from the πM3 beamlines, with an upgraded capture scheme.

As for MUH2, the capture is performed with a graded field solenoid. The beam is then bent by 36° by a radiation hard dipole (ASH31) and coupled into a section consisting of two radiation hard solenoids (TSBL1 and TSBL2). Two Beam Blockers (BB) are used here as in MUH2 to keep the neutron dose below the safety limit when access is required to the experimental areas. The coupling into the next straight section is done by means of two non-radiation hard dipoles with an interposed non-radiation hard solenoid (here BL3). The two bends of 42° (ASH32) and 22° (ASH33) allow for a smoother transition to the following section and, together with the intermediate additional focusing, a wider acceptance. A slit system is implemented in ASH33 to reduce the muon beam rate on demand.
The next straight section comprises: two non-radiation hard solenoids, BL4 and BL5; the QSM quadrupole triplet; the Spin Rotator SpinRot1; two QSL quadrupole doublets; two SSL steering magnet, of which one horizontal (SSL32) and one vertical (SSL33); and a QSL triplet. The septum magnet ASS31 can be energized to split or direct the beam to two different μSR instruments. A dipole magnet bends (49.5°) the output of ASS31 to the MUH3.2 area. Alternatively, the beam continues to a QSL triplet and is then bent by 30° into the MUH3.3 area. The final focusing in both experimental areas is provided by a QSE quadrupole triplet.

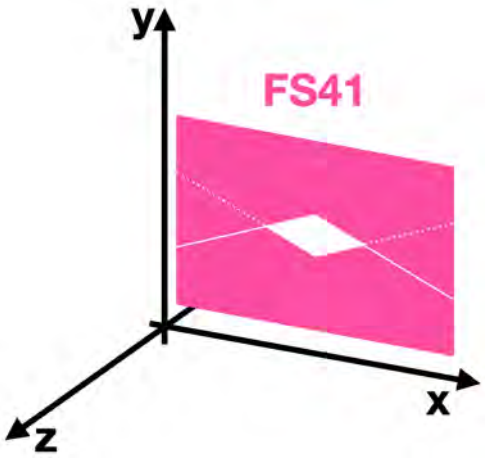

Figure 5.38: *Sketch of the FS41 slit system . The slits move along the horizontal direction and can select muon beam transmission to either MUH3.2 of MUH3.3 experimental areas.*

A slit system (FS41) is positioned in front of ASS31. Figure 5.38 shows a

sketch of FS41. The profile of the two slits is shaped so that, when overlapping, the aperture between the two slits is a square rotated by 45°. Such shape allows to collimate both the vertical and horizontal directions at the same time with a single slit system. The beam in both sections can be collimated independently by means of two different collimators.

Figure 5.39 shows the graphical output of the G4beamline simulation of MUH3 used to optimize and characterize the design.

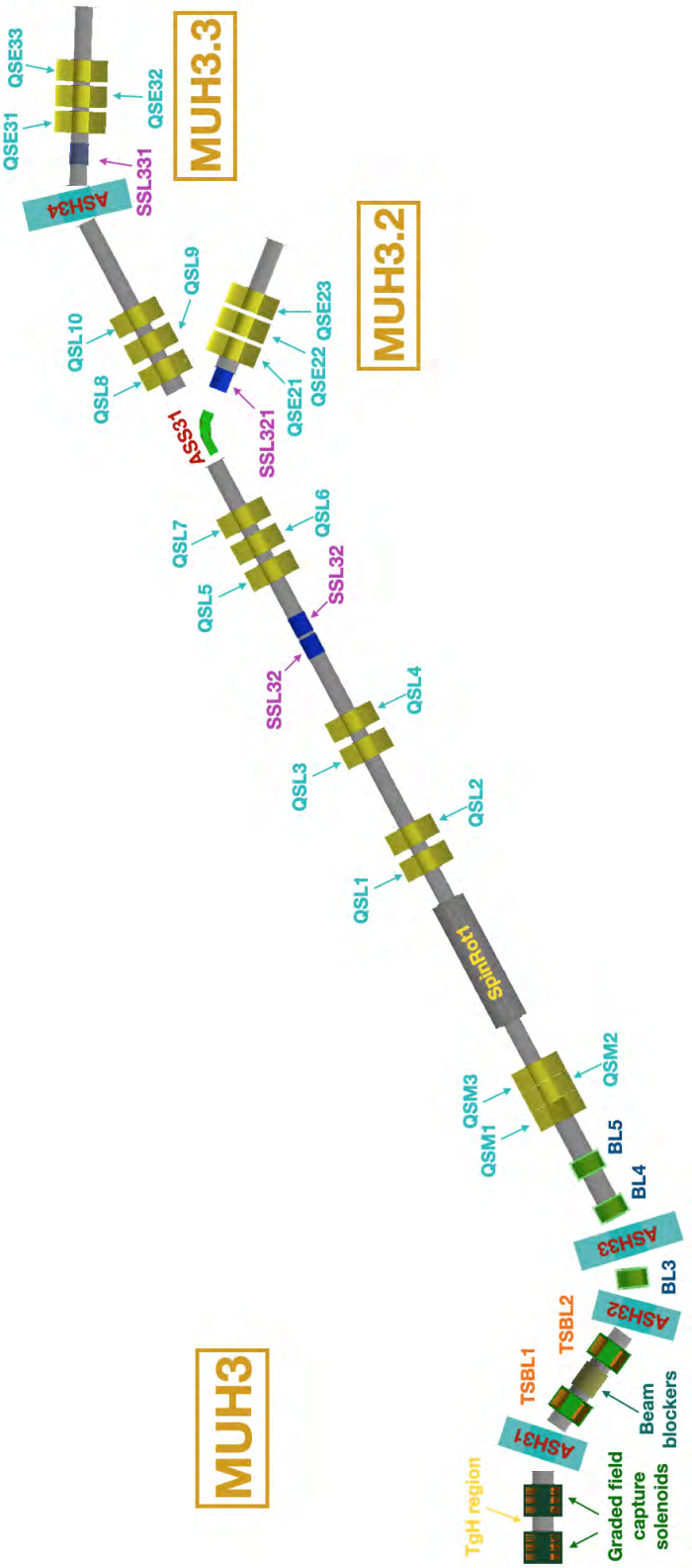

Figure 5.39: *MUH3 model in G4beamline. The layout is dated from October 2023. The MUH2 capture solenoid (on the left) is included and set to the surface muon tune. The labelling is to be considered provisional and useful only in the context of this thesis to address the parameter space: ASH31 is a radiation hard dipole; the TSBL elements are radiation hard transport solenoids; ASH32, ASH33 and ASH34 are non-radiation hard dipoles and a slit system is implemented in ASH33; the BL elements are non-radiation hard solenoids; ASS31 is the septum magnet steering the beam to either of the two experimental areas fed by this beamline, MUH3.2 and MUH3.3; the SSL dipoles are steering magnet to compensate for potential offsets when delivering the beam to the two areas; QSM, QSL and QSE are quadrupolar magnets. Mock version of the two beam blockers are included to show their occupancy.*

5.5.2 Optimization strategy

MUH2 suffers from the limited current that can drive the solenoids and it is not possible to scale the tune to higher momenta. For MUH3 this stays true up to BL4, but the following section is based on quadrupoles, which are not limited by the same constraint. The optimization here is therefore aimed at matching the first section up to the QSM triplet, to the following section which is only scaled according to the selected momentum.

The matching is performed by maximizing transmission through Spin Rotator 1, which due to its narrow acceptance, is selecting only a very specific region of the phase space at any momentum. Such tunes are shared for the three possible running modes of MUH3:

- MUH3.2 mode: the whole beam is deflected to the MUH3.2 area
- MUH3.3 mode: the whole beam is deflected to the MUH3.3 area
- shared mode: the beam is split in two with the septum magnet and delivered at the same time to both MUH3.2 and MUH3.3 areas

The tune for the elements downstream of SpinRot1 can then be found for surface muons and linearly scaled for the other momenta. In this work, a tune for the full antimuon spectrum is found up to SpinRot1 and the matching strategy is shown for a focus between QSL2 and QSL3. The so-found tune can then be further optimized in a tighter parameter space centered around it.

The tuning of the MUH3 beamline for surface muons, and therefore for the elements downstream to SpinRot1, is carried out by Eremey Valetov [87] using a staged Bayesian optimization: a Bayesian optimizer is used to maximize transmission through consecutive sections of the beamline. The optimized sections overlap to avoid local maxima and the process is reiterated. The latest step is the optimization of the beam spot by creating a dedicated figure of merit. Due to the large number of parameters and to the lower transmission than MUH2, such optimization is computationally expensive and still ongoing. Here only the optimization up to SpinRot1 is shown and a proof of principle of the matching is given.

5.5.3 Antimuons spectrum

The optimization up to SpinRot1 consists in maximizing transmission to its downstream side. The search space includes 14 parameters:

- captureCurrent_i: three currents, one for each coil pancake, to characterize transmission in the capture solenoid
- BFieldi: the peak field in each of the three dipoles in this section

- currentTSBLi: the current in each of the two radiation hard solenoids
- currentBLi: the current in each of the three non-radiation hard solenoids
- currentQSMi: the current in each of the three quadrupoles in the QSM triplet

The parameter space is defined by the following ranges:

- $[0\,\mathrm{T},\ 0.45\,\mathrm{T}]$ for currentCupture_1, currentCupture_3 and currentTSBLi
- $[-0.45\,\mathrm{T},\ 0.45\,\mathrm{T}]$ for currentCapture_2
- $[-0.55\,\mathrm{T},\ 0.55\,\mathrm{T}]$ for currentBLi
- $[0\,\mathrm{T},\ 0.2\,\mathrm{T}]$ for BFieldi
- $[0\,\mathrm{T},\ 0.3318\,\mathrm{T}]$ for currentQSM1 at pole tip
- $[-0.3318\,\mathrm{T},\ 0.3318\,\mathrm{T}]$ for currentQSM2 and currentQSM3 at pole tip

QSM1 is constrained to be horizontally focusing to narrow the search space and prepare injection in the SpinRot1. The ranges used here are less restrictive than the ones used in the optimization of MUH2 as this is the first study of this specific layout and no starting point was available.

The QSM triplet and SpinRot1, which is always kept off during the optimization, limit the acceptance of the beamline. To compensate for this issue, each trial is run by transmitting $5 \times 10^5\ \mu^+$, to be compared with the $10^5\ \mu^+$ in the case of MUH2. For each optimization, the transmitted muons are selected within $\pm 5\,\mathrm{MeV/c}$ from the nominal momentum.

NSGA-II is used to maximize the number of antimuons transmitted to the downstream side of SpinRot1 with a population of 100 individuals per generation. The optimization was run for 5 nominal momenta: $30\,\mathrm{MeV/c}$, $40\,\mathrm{MeV/c}$, $50\,\mathrm{MeV/c}$, $60\,\mathrm{MeV/c}$ and $70\,\mathrm{MeV/c}$. Each optimization was stopped after $4000\,\mathrm{core-hours}$ and the full set of optimizations was run in $\sim$3 days. Figure 5.40 shows the maximum rate obtained for each momentum at the downstream side of SpinRot1. For the sake of comparison with MUH2, transmission up to the exit of BL5 is included up to which the channel is purely solenoidal and the layouts are similar. The corresponding positron and pion rates with SpinRot1 off are shown. Additionally to the particles generated at TgH, muons from pion decay in flight are included as *deep (D.) muons*.

The maximum rate is achieved for surface muons, up to $6.88 \times 10^9\ \mu^+/\mathrm{s}$ at the exit of BL5 and up to $1.75 \times 10^9\ \mu^+/\mathrm{s}$ at the end of SpinRot1 for a proton current of 2.4 mA. Table 5.6 shows the rates and phase space parameters at the end of SpinRot1 for each tune. The phase space parameters are computed as the mean and standard deviation of the distribution of the

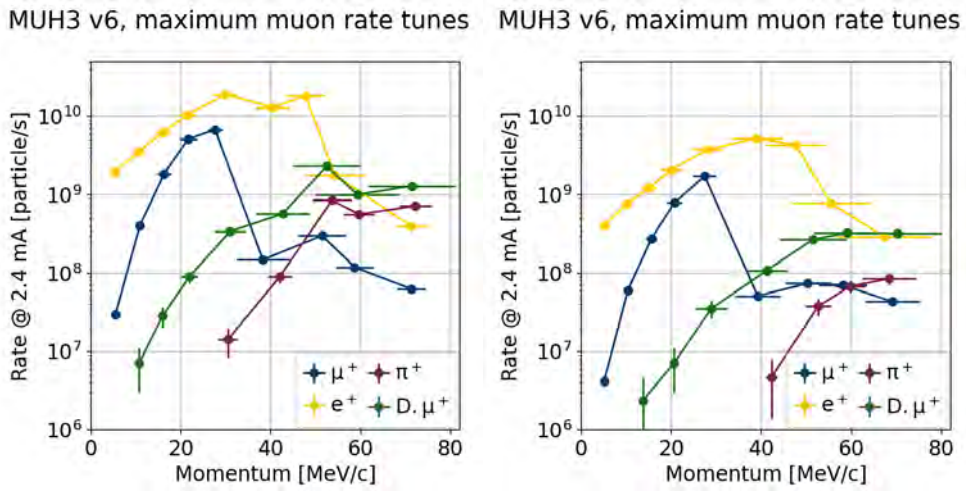

(a) BL5 exit **(b)** SpinRot1 exit

Figure 5.40: *Maximum deliverable rate to the end of BL5 (left) and at the end of SpinRot1 (right) in MUH3. The rate was maximized for antimuons and computed for positrons and pions with the same tunes. SpinRot1 is off. Deep (D.) muons are shown in green. The error bars in the vertical direction are the statistical uncertainty on the computed rates. The error bars in the horizontal direction correspond to ± 1 standard deviation of the transmitted momentum spectrum. Tunes lower than 30 MeV/c have been scaled down linearly from the surface muon tune.*

transmitted muons. As anticipated above, the narrow acceptance of SpinRot1 defines the transmitted phase space at all momenta. As an example, the envelope of the transmitted muons is shown in Figure 5.44.
For future reference, the tunes for maximum transmission are collected in Appendix K.

5.5.3.1 Muon polarization

For μSR applications the polarization of the implanted muons is relevant to probe the magnetic properties of the samples. The polarization of surface muons, as explained in Chapter 1, is due to the neutrinos being left-handed. In the rest frame, the muon is always left-handed to conserve the spin. In the laboratory frame instead, it depends on the direction of the boost of the decayed pion: while the momentum of the muon depends on the boost of the pion, the spin does not change direction under Lorentz transformations. Therefore, in the rest frame of the pion, the polarization of the muon is always negative, but if the boost of the pion in the laboratory frame is higher than the boost of the muon in the rest frame, depending on the direction of emission, the momentum of the muon can change direction under Lorentz transformation. This happens for pions with momentum higher than 39.35 MeV/c. This causes a change in the sign of the polarization of

the muon, leading to a positive component. In Table 5.6, the polarization of both prompt and deep components of the muon beams are shown. Two different trends can be observed:

- prompt muons: the polarization is negative for surface muons and null for other momenta.
- deep muons: the polarization is positive and decreases with higher momenta.

Prompt muons are collected close to the target, meaning that they can be generated by pions which can be either collinear or anti-collinear to the muon in the rest frame. Deep muons instead are selected in the forward direction only. Because the momentum distribution of pions generated at target drops to zero for low momenta, low energy muons are more likely generated anti-collinear to the decaying pion with the pion having a boost higher than that of surface muons, leading to a sign flip of the polarization. At higher momenta, the polarization decreases due to the presence of muons collinear to the pions.
The drop in the polarization of cloud muons at increasing momentum is steeper in case of a wide beamline acceptance: the selection of a wider pion momentum causes a higher degree of mixing between collinear and anti-collinear decays. Figure 5.42 shows the correlation between the polarization of the muon at the exit of SpinRot1 and the momentum of the decayed pion for the 50 MeV/c and 70 MeV/c tunes. Two populations are clearly distinguishable: for pions with a momentum close to that of the generated muon, the polarization is negative; for anti-collinear pions and muons the polarization is proportional to the momentum of the pion and peaks for positive polarizations.

Due to the poor degree of polarization, the tunes found with this study for cloud muon beams are not suited for μSR applications, but the quality could be possibly improved through polarization filters and dedicated R&D.

Nominal momentum	27 MeV/c	40 MeV/c	50 MeV/c	60 MeV/c	70 MeV/c
Prompt muon Rate [μ^+/s]	1.75×10^9	5.43×10^7	7.92×10^7	7.56×10^7	4.41×10^7
Deep muon Rate [μ^+/s]	4.01×10^7	1.32×10^8	3.00×10^8	4.15×10^8	3.68×10^8
$\hat{x}$ [mm]	-4.39	8.47	-0.33	-7.24	4.63
STD(x) [mm]	62.21	62.06	60.52	62.25	50.64
$\hat{x'}$ [mrad]	-0.49	3.74	4.12	-0.43	-0.52
STD(x') [mrad]	43.25	55.81	52.50	47.33	48.96
$\hat{y}$ [mm]	2.37	-19.27	-19.18	8.62	-31.92
STD(y) [mm]	125.24	122.72	120.29	128.71	117.47
$\hat{y'}$ [mrad]	1.87	-3.04	-7.69	-6.63	-11.31
STD(y') [mrad]	45.01	54.72	50.55	57.90	36.58
$\hat{P}z$ [MeV/c]	27.37	39.26	50.16	58.14	69.05
STD(Pz) [MeV/c]	2.61	5.23	5.09	5.48	6.17
$\varepsilon_x(90\,\%)[\pi\,\mathrm{rad\,mm}]$	5.61	8.32	7.69	7.36	5.75
$\varepsilon_y(90\,\%)[\pi\,\mathrm{rad\,mm}]$	9.83	11.14	12.35	12.65	9.57
Prompt muon polarization $\hat{P}$	-0.99	-0.09	-0.06	-0.09	-0.07
Prompt muon STD(P)	0.12	0.58	0.55	0.57	0.55
Deep muon $\hat{P}$	0.67	0.38	0.19	0.08	-0.01
Deep muon STD(P)	0.36	0.60	0.67	0.70	0.72

Table 5.6: Phase space parameters and polarization of prompt antimuons propagated with the tunes for maximum rate. The phase space parameters of deep muons are not shown as they are consistent with those of prompt muons. The rates are computed for a proton current of 2.4 mA.

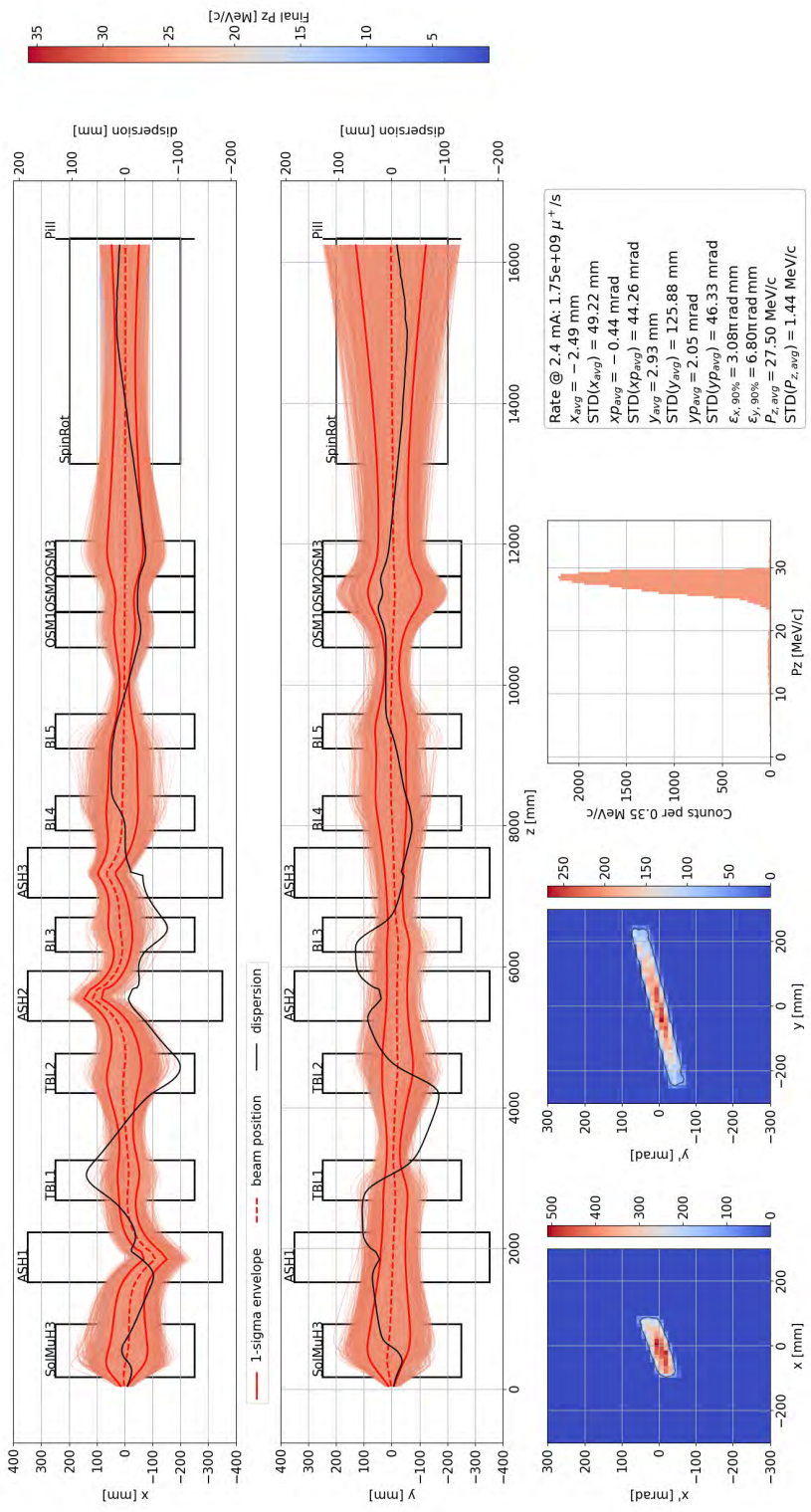

Figure 5.41: *Prompt surface muon beam envelopes and phase spaces for maximum transmission through SpinRot1. The dispersion curves shown here are computed based on the correlation between the position and the longitudinal momentum at each position. TgH is positioned at the origin of the coordinate system.*

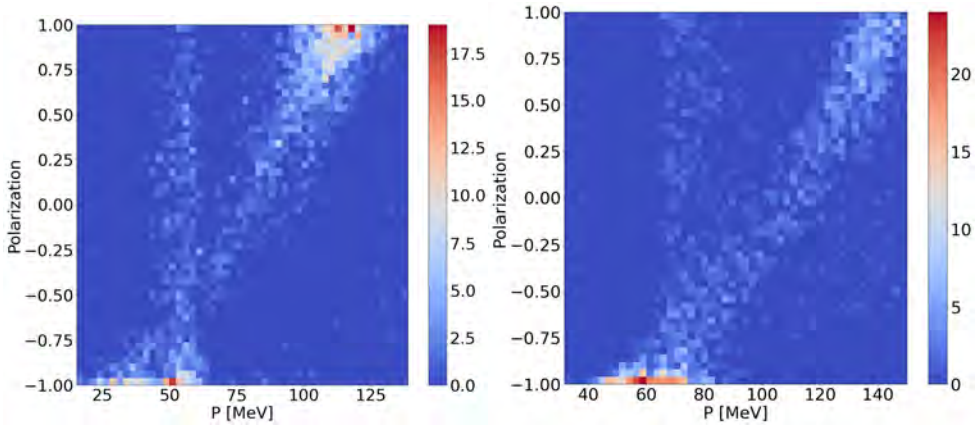

(a) 50 MeV/c tune **(b)** 70 MeV/c tune

Figure 5.42: *Correlation between muon polarization and decayed pion momentum for the* 50 MeV/c *(left) and for the* 70 MeV/c *(right) tunes. Muons generated in the same direction of the boost of the pion are negatively polarized. Muons generated in the opposite direction are positively polarized.*

5.5.3.2 MUH3 quadrupole matching

To show a possible matching between the quadruople and solenoid sections, a tune for a focus between QSL2 and QSL3 was found. The search space is analogous to that used to maximize transmission through SpinRot1 with the addition of QSL1 and QSL2. NSGA-II is used. The objective space is 6-dimensional and defined as follows:

- Transmission: number of transmitted muons. Maximized.
- STD(x) and STD(y): standard deviations in the horizontal and the vertical direction respectively. Minimized.
- $|\rho_x|$ and $|\rho_y|$: correlations between divergence and beam spot distribution in the horizontal and in the vertical direction respectively. Minimized.
- $\sqrt{(\hat{x})^2 + (\hat{y})^2}$: squared sum of the position of the beam spot in the two transverse directions. Minimized.

It is important to include a different figure of merit for each of the two transverse phase spaces due to the presence of quadrupolar elements, which can introduce asymmetries in the beam size along the two transverse directions. Due to the high dimensionality of both the search (14 dimensions) and objective (6 dimensions) spaces, the population size of each generation is increased to 200 individuals. For each trial, $5 \times 10^6\ \mu^+/s$ were transmitted. The optimization has been run for 20 000 core $-$ hours in $\sim$5 days.

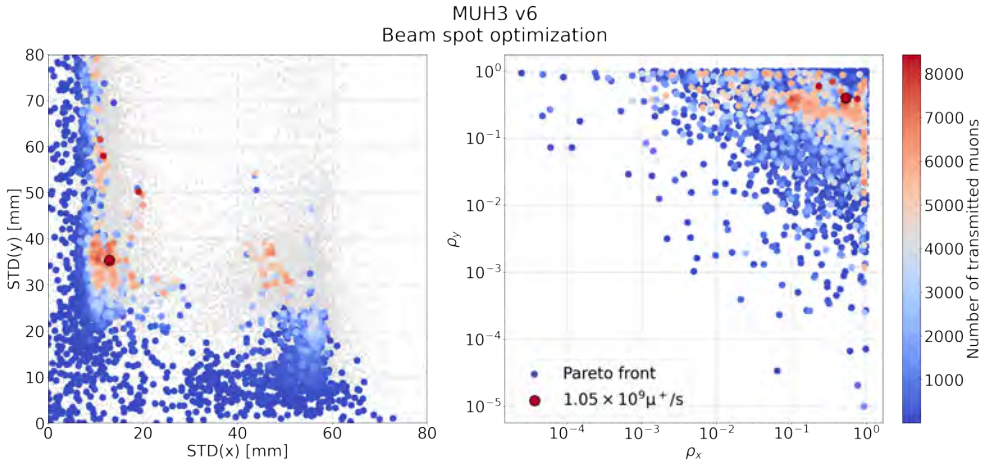

Figure 5.43: *Beam spot optimization for surface muons in MUH3. The colored markers represent the pareto front. The transmission is shown in color code. The other trials are shown in grey. The chosen tune is shown with a larger marker. The objective space is projected in the STD(x) vs STD(y) (left) and in the ρ_x vs ρ_y (right) planes.*

Figure 5.43 shows the projected pareto front in the STD(x) vs STD(y) and in the ρ_x vs ρ_y planes. The transmission is shown in color code. The chosen tune is shown with a larger marker. The chosen tune delivers 1.05×10^9 μ^+/s at a proton current of 2.4 mA. The beam is focused in both directions, with a high divergence in the horizontal direction and a wider beam spot along the vertical direction. Such configuration is preferred because of the acceptance of SpinRot1: in the horizontal plane the beam is *parallel* as it is constrained to propagate within the narrow 200 mm aperture between the electrodes; in the vertical plane the beam is divergent and transmission through the QSL doublet is maximal when QSL1 is focusing in the vertical plane and defocusing in the horizontal. Subsequently, QSL2 is focusing in the horizontal again. The matching is performed on both the surface muon beam and the 50 MeV/c tune: the tune in the section upstream to SpinRot1 is that for maximum transmission found in Section 5.5.3; the tune for the first QSL doublet, which is after SpinRot1, is obtained by linearly scaling to match the central momentum transmitted through SpinRot1. Table 5.7 shows the tunes for optimized focus and the two matched tunes.
Table 5.8 shows a comparison between the phase space parameters of the two matched beams and the optimized focusing tune. The envelopes and phase spaces of the matched beams are shown in Figure 5.44 and Figure 5.45.

As for the surface muon beam, the matched 50 MeV/c muon beam shows a higher divergence in the horizontal direction and a wider beam spot along the vertical direction, with similar phase space parameters. The main difference is found in the vertical divergence: along this direction the aceptance of SpinRot1 is wider than in the horizontal plane and inherent differences

		Peak/Pole fields [T]		
		Optimized beam spot	Matched	
Nominal momentum		27 MeV/c	27 MeV/c	50 MeV/c
US of SpinRot1	currentCapture_1	0.426	0.442	0.435
	currentCapture_2	0.0924	0.210	0.450
	currentCapture_3	0.254	0.0516	0.312
	BField1	0.0527	0.0562	0.100
	currentTSBL1	0.310	0.382	0.380
	currentTSBL2	0.303	0.354	0.449
	BField2	0.0637	0.0645	0.122
	currentBL3	-0.407	-0.372	0.480
	BField3	0.0359	0.0363	0.0578
	currentBL4	0.217	-0.281	-0.445
	currentBL5	0.242	-0.302	0.419
	currentQSM1	0.118	0.105	0.0768
	currentQSM2	-0.133	-0.142	-0.173
	currentQSM3	0.102	0.0805	0.113
DS	currentQSL1	-0.0582	-0.0582	-0.108
	currentQSL2	0.0861	0.0861	0.159

Table 5.7: Comparison between the optimized focus tune in the section of the beamline upstrem (US) of SpinRot1 and the matched tunes in the downstream (DS) section. For solenoids and dipoles, the value reached by the field at its peak is shown. For quadrupoles, the value of the field at their pole tip is shown. The optimization of the focus is performed for surface muons on the full search space including all the elements of the beamline up to QSL2. The matching is done by linearly scaling the field in QSL1 and QSL2 and by setting the section upstream to SpinRot1 to the tune found for maximum transmission at both 27 MeV/c and 50 MeV/c.

in transmission in the momentum spectrum appear. The matching of the surface muon beam shows that the optimization downstream to SpinRot1 is sufficient, thus reducing the parameter space. After matching, additional optimizations can be performed in a reduced search space to improve the centering. As an additional remark, the transmission of the matched prompt surface muon beam is $\sim$14 % higher than for the optimized beam spot tune. Due to the high dimensionality of the search space, the convergence to the pareto front is not granted if not in the asymptotic regime. Yet again, the improvement of the transmission with the matching shows that indeed the optimization of the section upstream to SpinRot1 can be decoupled from that of the downstream section.

	Optimized beam spot		Matched			
Nominal momentum	27 MeV/c		27 MeV/c		50 MeV/c	
Muon Rate [μ^+/s]	7.66×10^8	9.44×10^6	1.05×10^9	1.89×10^7	4.73×10^7	1.38×10^8
$\hat{x}$ [mm]	-0.25	8.48	0.24	-0.88	3.21	2.35
STD(x) [mm]	13.01	18.75	15.83	17.49	16.99	22.04
$\hat{x'}$ [mrad]	9.13	-6.53	7.63	19.83	1.27	-0.33
STD(x') [mrad]	90.98	90.61	91.50	93.62	89.36	100.76
$\hat{y}$ [mm]	2.77	5.76	2.84	5.81	22.01	-3.46
STD(y) [mm]	38.10	27.85	38.28	47.99	48.31	55.50
$\hat{y'}$ [mrad]	1.16	6.98	1.34	3.07	-11.67	-3.71
STD(y') [mrad]	33.36	24.47	33.05	22.47	40.17	48.65
$\hat{P}z$ [MeV/c]	27.44	28.77	27.50	28.67	50.74	50.90
STD(Pz) [MeV/c]	1.49	2.52	1.36	3.06	3.79	7.25
$\varepsilon_x(90\,\%)[\pi\,\mathrm{rad\,mm}]$	5.30	2.01	3.99	3.06	4.42	7.24
$\varepsilon_y(90\,\%)[\pi\,\mathrm{rad\,mm}]$	5.36	1.53	4.54	3.05	5.52	6.94
Muon polarization $\hat{P}$	-0.98	0.69	-0.98	0.80	-0.07	0.23
muon STD(P)	0.11	0.43	0.12	0.23	0.57	0.67

Table 5.8: Phase space parameters and polarization of prompt and deep antimuons. The beamline is optimized for a focus between QSL2 and QSL3 for surface muons. For 50 MeV/c muons the solenoidal section is tuned for maximum transmission through SpinRot1 and the quadrupolar section is linearly scaled from the tune found for surface muons. The rates are computed for 2.4 mA.

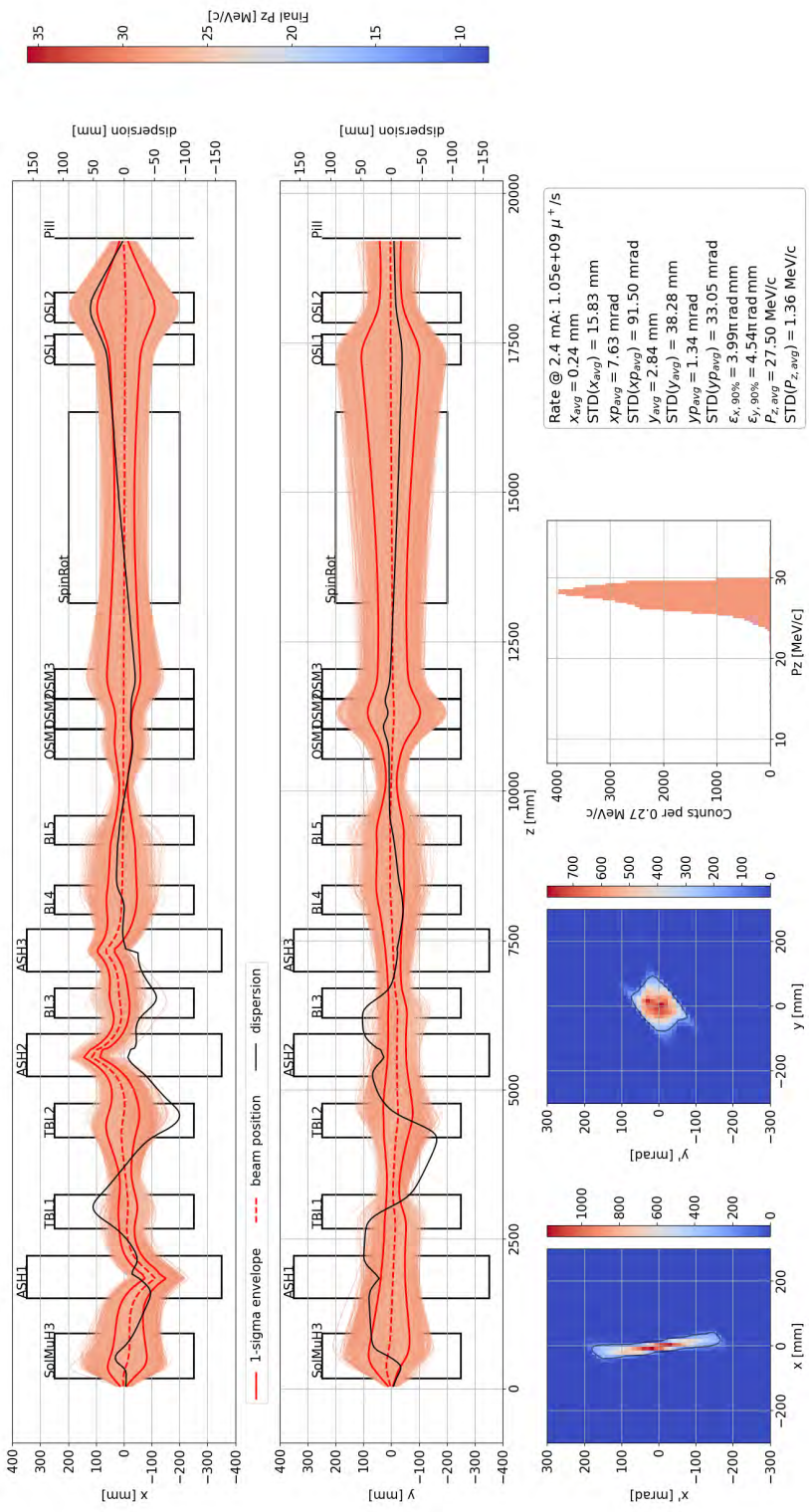

Figure 5.44: *Prompt surface muon beam envelopes and phase spaces. The dispersion curves shown here are computed based on the correlation between the position and the longitudinal momentum at each position. TgH is positioned at the origin of the coordinate system.*

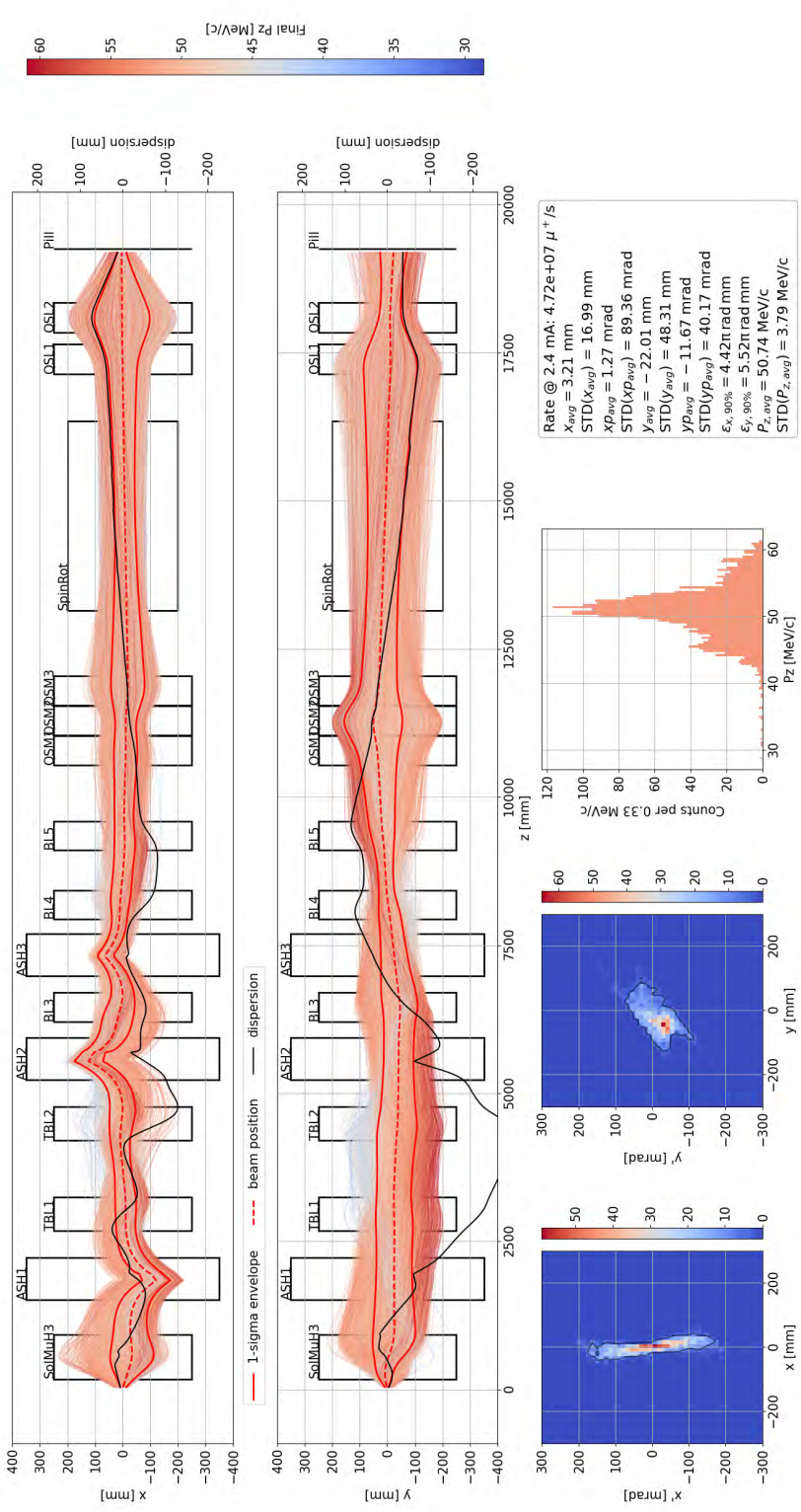

Figure 5.45: *Prompt muon beam envelopes and phase spaces at* 50 MeV/c*. The dispersion curves shown here are computed based on the correlation between the position and the longitudinal momentum at each position. TgH is positioned in the origin of the coordinate system. The solenoidal section is tuned for maximum transmission through SpinRot1. The currents in the quadrupolar section are linearly scaled from the surface muon momentum to the* 50 MeV/c *momentum.*

Conclusions

Within this thesis, the commissioning of the Compact Muon Beam Line (CMBL) has been completed (see Chapter 3) and the performances of the High Intensity Muon Beams (HIMB) beamlines have been addressed for transmission of muons, pions and electrons (see Chapter 5). Furthermore, the analysis framework of the MEG II experiment has been extended for the measurement of the beryllium anomaly [8, 9] (see Chapter 4). Here a general overview of the main results is given.

In the context of charged Lepton Flavor Violation (cLFV) the Mu3e experiment aims to measure the $\mu^+ \to e^+e^+e^-$ decay with a sensitivity of 10^{-15} on the branching ratio in its first phase of data taking. To reach this goal, the CMBL was designed to deliver $\mathcal{O}(10^8\,\mu^+/s)$ to the Mu3e target. The commissioning of the CMBL started in 2014, prior to the beginning of this work, and continued until 2018 without the Mu3e spectrometer magnet [5, 6], which was delivered to PSI only in 2020 [7]. Here, the beam commissioning campaigns between 2021 and 2023 were presented.
In 2021, the Mu3e magnet was moved into the πE5 area for the first time and the muon beam was successfully transmitted to its center. The main aim of the beam campaign was to tune the beamline to deliver the muon beam to a minimal version of the final detectors. At this stage, optimal transmission was not yet achieved and the rate at the center of the Mu3e spectrometer was limited compared to the expected performances [4], measuring $4.4 \times 10^7\,\mu^+/s$ at a proton current of 2.2 mA. This was probably caused by non optimal transmission through AST41 and ASC41, two dipoles of the πE5 beamline that are consecutive and therefore can transmit the beam with a variety of tunes. Due to this, the following commissioning campaign started from the tune found in 2019 for the MEG II experiment, which measures the $\mu^+ \to e^+\gamma$ decay in the same experimental area.
In 2022, the requirements on the beam intensity for the first phase of the Mu3e experiment were met and surpassed, delivering $6.89 \times 10^7\,\mu^+/s$ at a proton current of 2.2 mA, but because not all the sextupole magnets of the

beamline were operational, maximal transmission could not yet be found. Additionally, the characterization of the transverse phase space was improved with a pepper-pot measurement during the MEG II beam time.
The resulting phase space was implemented in the existing G4beamline simulation of the CMBL and used to optimize the position of the 600 µm Mylar® moderator required to degrade the energy of the muons in front of the Mu3e target. The found position was tested and confirmed in 2023.
With the full beamline operational and the moderator installed, the muon rate delivered to the center of the Mu3e spectrometer was 7.5×10^7 μ^+/s at a proton current of 2.2 mA.

In the context of rare physics processes, the MEG II detector allows to test additional channels aiding the search for Beyond Standard Model (BSM) physics. Thanks to the Cockroft-Walton accelerator available to the collaboration for calibration purposes, a proton beam of up to 1.08 MeV in energy can be used to induce the $^7\mathrm{Li}(p,\gamma)^8\mathrm{Be}$ reaction in the center of the detector. In 2016 the ATOMKI collaboration has claimed an excess in the distribution of the angular correlation between the internal conversion pairs [8, 9] in this process and since then, the anomaly, or correspondigly a potential X17 boson, has not yet been confirmed with a different detection scheme. With minimal adaptations to the set-up, the MEG II detector can be used to independently perform this measurement.
As part of this work, the X17 target region, consisting of a lightweight vacuum chamber and a new target, was assembled and tested and a data taking was carried out in 2023. The analysis framework of the MEG II experiment has been extended for the analysis of this channel. Initially, a likelihood based on parametrised probability distribution functions (PDF) has been defined and implemented in the framework both for a binned and an unbinned analysis. Preliminary PDFs of the expected backgrounds have been defined based on a limited Monte Carlo (MC) sample produced in July 2023. The expected backgrounds consist of the internal pair creation (IPC) pairs and of the external pair creation (EPC) pairs from the 18.15 MeV and the 15.12 MeV lines. The latter are not expected to be significant in the signal region, but a large MC production of these populations is not possible due to the limited resources available to the collaboration. The effect of the limited possible MC statistics on the systematic uncertainties has been studied and found to be large with the available PDFs. An alternative likelihood a la Beeston-Barlow [72] has been implemented for the backgrounds and tested to fit the data with templates, correctly accounting for their limited statistics. To perform an estimate of the eventual X17 mass, the signal is modelled with a parametrized PDF.
The Feldman-Cousins construction has been adapted for the new likelihood and thoroughly tested, showing that a reduced MC production of the EPCs does not affect the sensitivity of the analysis in the case of the null hypoth-

esis. More specifically, two MC production scenarios have been considered: the *ideal statistic* scenario, where each EPC population is modelled with a template of 10^5 MC events; the *current statistic* scenario, closer to the expected final statistics, where each EPC population is modelled with a template of 10^4 MC events. The sensitivities estimated in the two scenarios are compatible within the statistical uncertainties and are $275(4)$ and $272(4)$ respectively, to be compared with the expected $\sim$450 in the 2023 data taking if assuming the hypothesis of the ATOMKI collaboration. The effect of a lower EPC MC statistics is observed instead in the significance of the signal which is expected to be of 4.27σ in the ideal statistic scenario and of 3.36σ in the current statistic scenario, assuming the hypothesis of the ATOMKI collaboration.

The HIMB project aims at exceeding the current intensity limits of surface muon beams by two orders of magnitude, reaching $\mathcal{O}(10^{10}\,\mu^+/\mathrm{s})$. Such an increase would push the sensitivity of cLFV searches with muons, for instance allowing to reach the sensitivity goal of the second phase of Mu3e of 10^{-16}, and improve the current limitations of the μSR technique. To do so, the HIMB project focuses on improving the surface muon yield with a new target geometry [6, 86] and on increasing capture and transmission with a large aperture solenoid-based beamline. Two new beamlines are planned: the MUH2 beamline will be dedicated to particle physics delivering the highest muon intensities with a solenoid-only layout; the MUH3 beamline will serve μSR instruments and improve the delivered muon rate with a solenoid-only section coupling into a quadrupole-only section to shape the beam and deliver it to the experiments.
Within this project, the use of hyperparameter search algorithms to optimize high-intensity muon transfer lines has been explored. The Non-dominated Sorting Genetic Algorithm II (NSGA-II) [45] has shown to be a powerful tool to optimize the muon beamlines of the HIMB project, performing as fast or faster than Bayesian [102] optimization for parameter spaces of $\mathcal{O}(20)$ dimensions and higher, delivering equal or better results. NSGA-II has been proven to perform well in mono-objective optimizations, where only one figure of merit is optimized, i.e. the muon rate, and in multi-objective optimizations, where multiple figures of merit are optimized simultaneously.
With the mono-objective optimization it has been shown that both MUH2 and MUH3 can reach the goal of exceeding $10^{10}\,\mu^+/\mathrm{s}$. As part of this work, emphasis was put in the optimization of the beamlines in the full momentum spectrum allowed by the current design of the dipoles of up to 80 MeV/c. In the case of MUH2, the maximum delivarable rates of positrons and pions were found as well.
With the multi-objective optimization, a set of tunes has been found trading off the muon rate with the beam spot size in the full muon momentum spectrum delivered by MUH2. Three cases relevant for particle physics were

additionally considered for MUH2: the optimization of the positron contamination in the surface muon beam; the minimization of the momentum spread of a 50 MeV/c positron beam; the optimization of the beam spot of a negative pion beam. The latter two cases are relevant for the MEG II experiment as calibration sources. For MUH3, the multi-objective optimization has been proven to be effective in the many-objective regime with 6 objectives describing the muon beam transmission and phase space. A suitable tune has been found for surface muons. A matching procedure has been established between the first section of the beamline up to the spin rotator and the second section of the beamline up to the instruments, allowing to perform the multi-objective optimization separately in the second section only on surface muons and limit the needed computing resources.

Appendix A

CMBL campaign 2022: muon beam rate vs Mu3e magnetic field

Here, a collection of beam scans performed at the center of the Mu3e spectrometer during the commissioning of the CMBL in 2022 (Chapter 3) is shown. Here the beam is scanned on the vertical and horizontal axes only. Within the range of scan, the beam spot is interpolated with a cubic spline. The tails (orange) are obtained with a gaussian fit to the three points on the sides. The 2D heatmaps shown, represent the beam spot in the assumption of no correlation between the vertical and horizontal directions. The black square represents the scanning range. An increase in the delivered rate is observed with a higher magnetic field in the spectrometer.

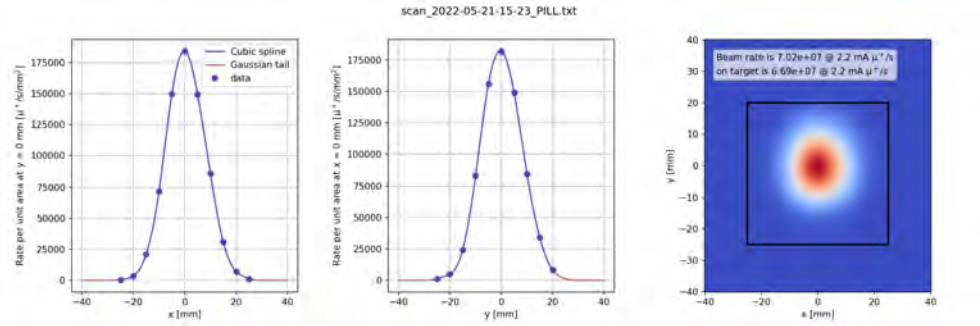

Figure A.1: *Cross-scan at Mu3e center. Beamline set to focus at Mu3e center. Left: horizontal scan. The blue dots are the measured points. The solid line in blue is the interpolation with a cubic spline. The solid lines in red are gaussian tails. Center: vertical scan. Right: 2D extrapolation for rate calculation. The two transverse directions are assumed to be non-correlated.*

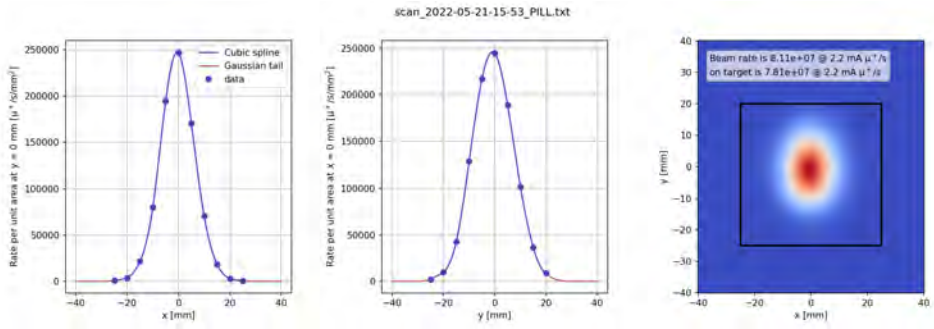

Figure A.2: *Cross-scan at Mu3e center. The field of the Mu3e solenoid is increased by* $5\,\%$*. Left: horizontal scan. The blue dots are the measured points. The solid line in blue is the interpolation with a cubic spline. The solid lines in red are gaussian tails. Center: vertical scan. Right: 2D extrapolation for rate calculation. The two transverse directions are assumed to be non-correlated.*

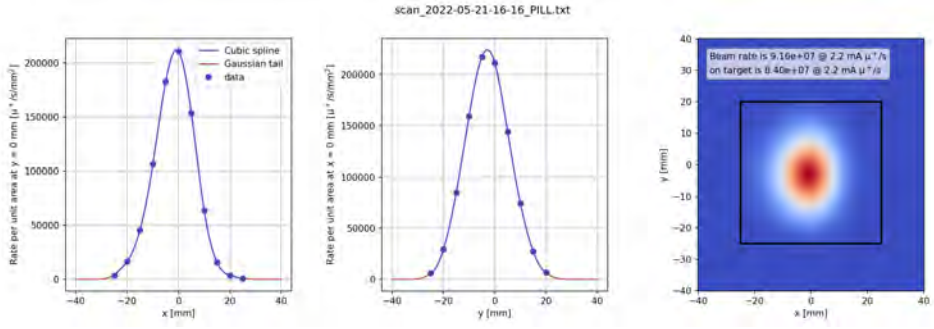

Figure A.3: *Cross-scan at Mu3e center. The field of the Mu3e solenoid is increased by* $10\,\%$*. Left: horizontal scan. The blue dots are the measured points. The solid line in blue is the interpolation with a cubic spline. The solid lines in red are gaussian tails. Center: vertical scan. Right: 2D extrapolation for rate calculation. The two transverse directions are assumed to be non-correlated.*

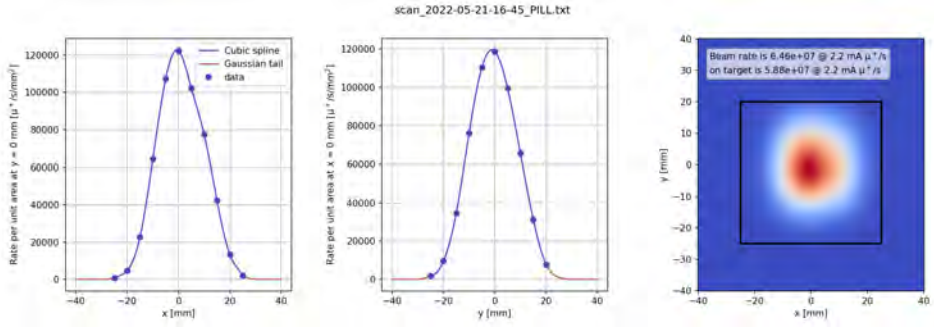

Figure A.4: *Cross-scan at Mu3e center. The field of the Mu3e solenoid is decreased by* $5\,\%$*. Left: horizontal scan. The blue dots are the measured points. The solid line in blue is the interpolation with a cubic spline. The solid lines in red are gaussian tails. Center: vertical scan. Right: 2D extrapolation for rate calculation. The two transverse directions are assumed to be non-correlated.*

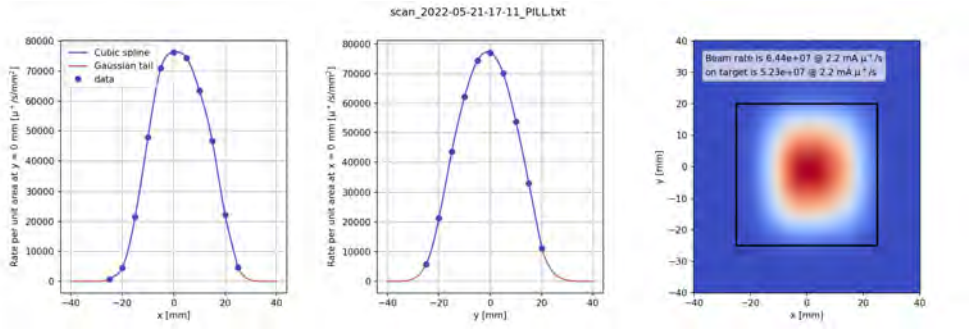

Figure A.5: *Cross-scan at Mu3e center. The field of the Mu3e solenoid is decreased by* $10\,\%$*. Left: horizontal scan. The blue dots are the measured points. The solid line in blue is the interpolation with a cubic spline. The solid lines in red are gaussian tails. Center: vertical scan. Right: 2D extrapolation for rate calculation. The two transverse directions are assumed to be non-correlated.*

Appendix B

CMBL campaign 2022: vertical phase space fit to pepper-pot beamlets

Here, the results of the fit to the measured vertical beamlets in the divergence phase space are shown. The details of the measurement and of the fitting procedure are reported in Section 3.3.1. Figure B.1 shows the fit to the measured beamlets after subtracting the positron background. Figure B.2 shows the comparison between the unfolded beamlets after removing the Multiple Coulomb Scattering (MCS) contribution and the measured data points.

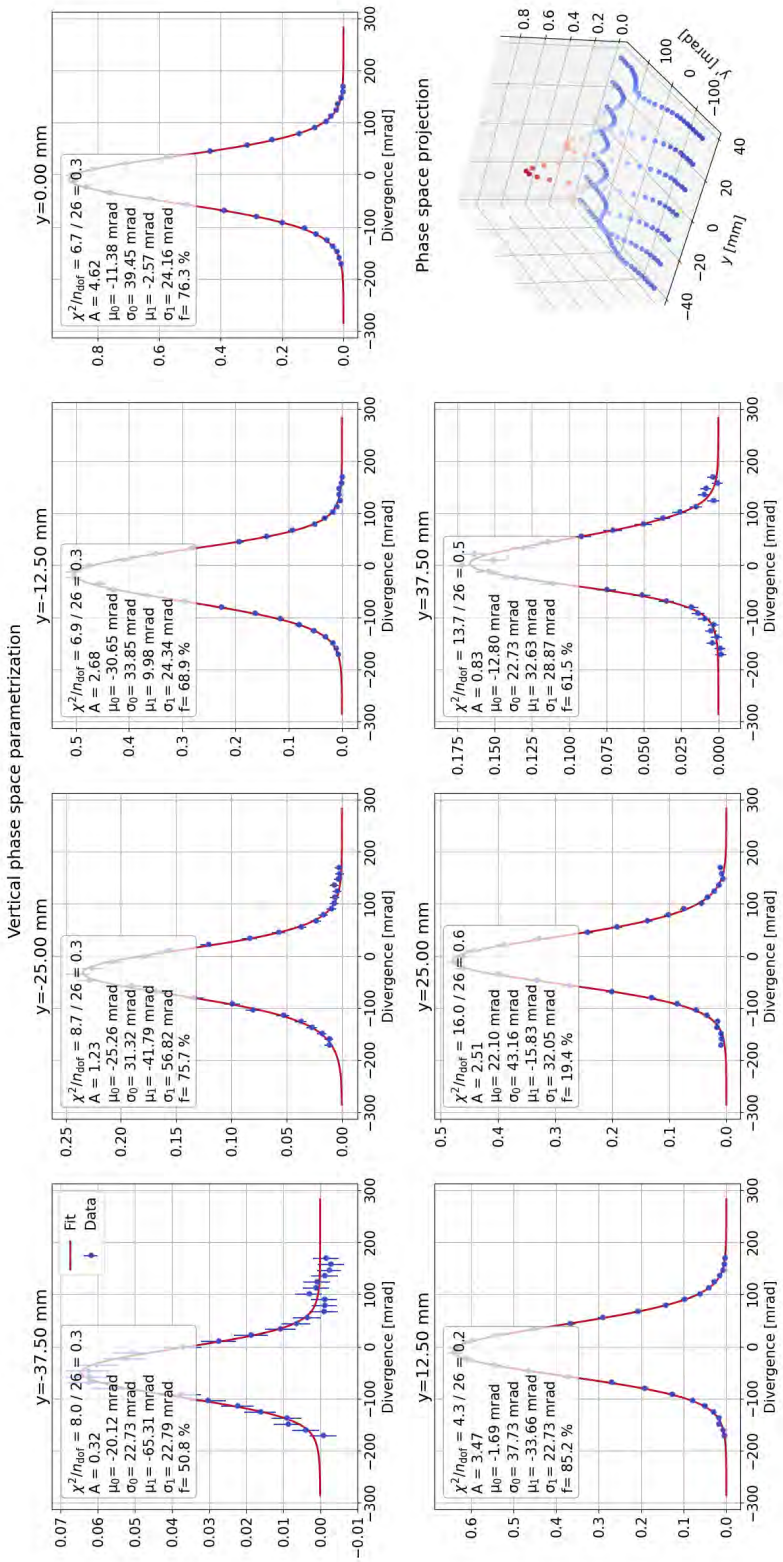

(a) Vertical phase space

Figure B.1: *Fit (red line) to the measured beamlets profiles (blue points) for the vertical scans. The profiles are transformed to divergences through the distance between the pepper-pot plate and the Pill monitor. The error bars are the statistical error. Each beamlet is parametrized with Equation 3.11 fixing the MCS contribution to the parameters in Table 3.4. The 3d plot in the bottom-right corners show the combined beamlets in the transverse phase space.*

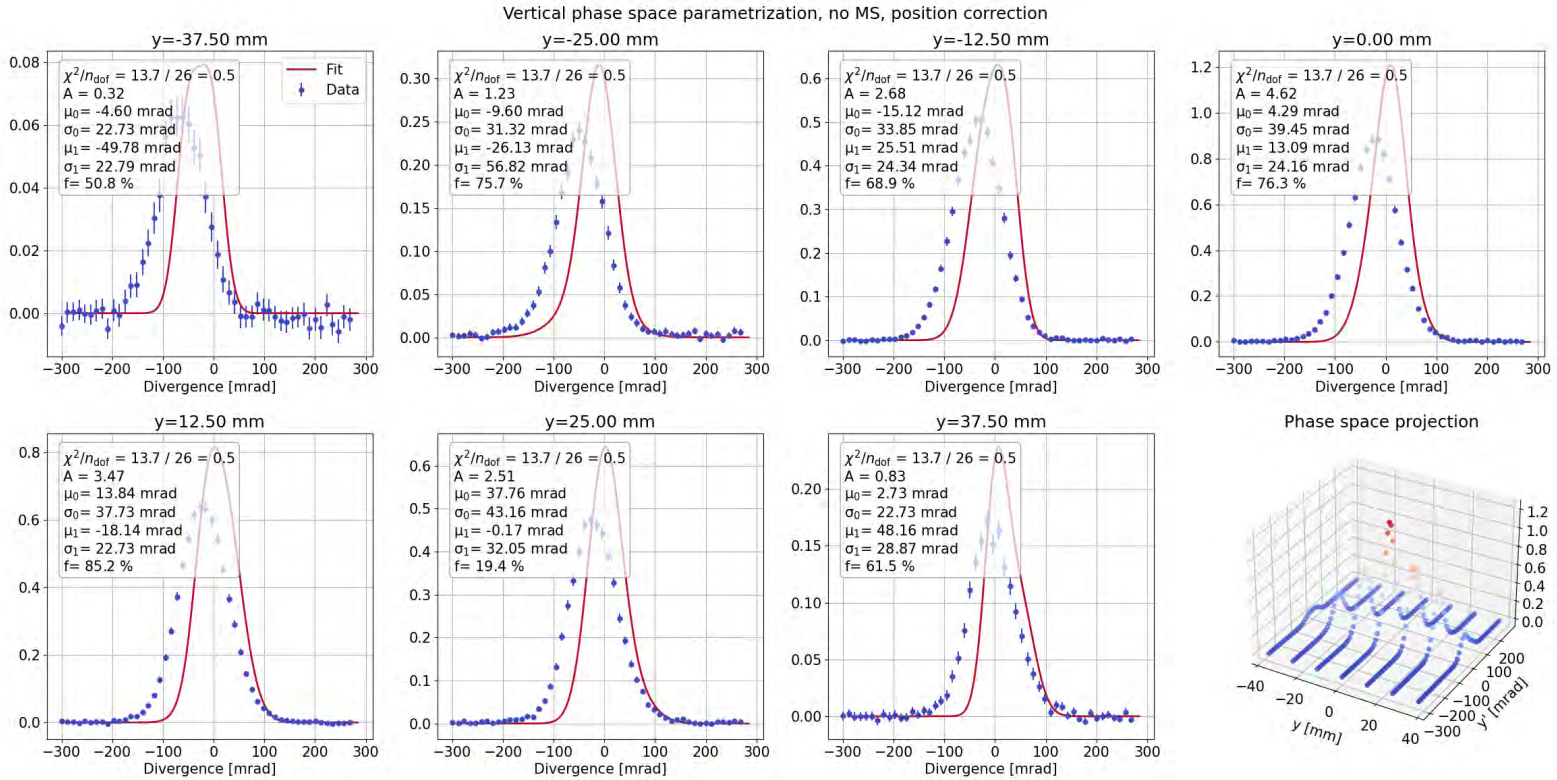

Figure B.2: *Comparison between the measured beamlets (blue points) and the unfolded beamlets (red lines), after removing the MCS contribution for the vertical scans.*

Appendix C

CMBL campaign 2022: transmission plots for optimized moderator and collimator position

Here, a collection of the simulated transmission to the center of Mu3e with G4beamline. The strength of the beamline elements and the position of the moderator are optimized to maximize transmission. The measurement of the transmitted phase space is shown in Section 3.3.

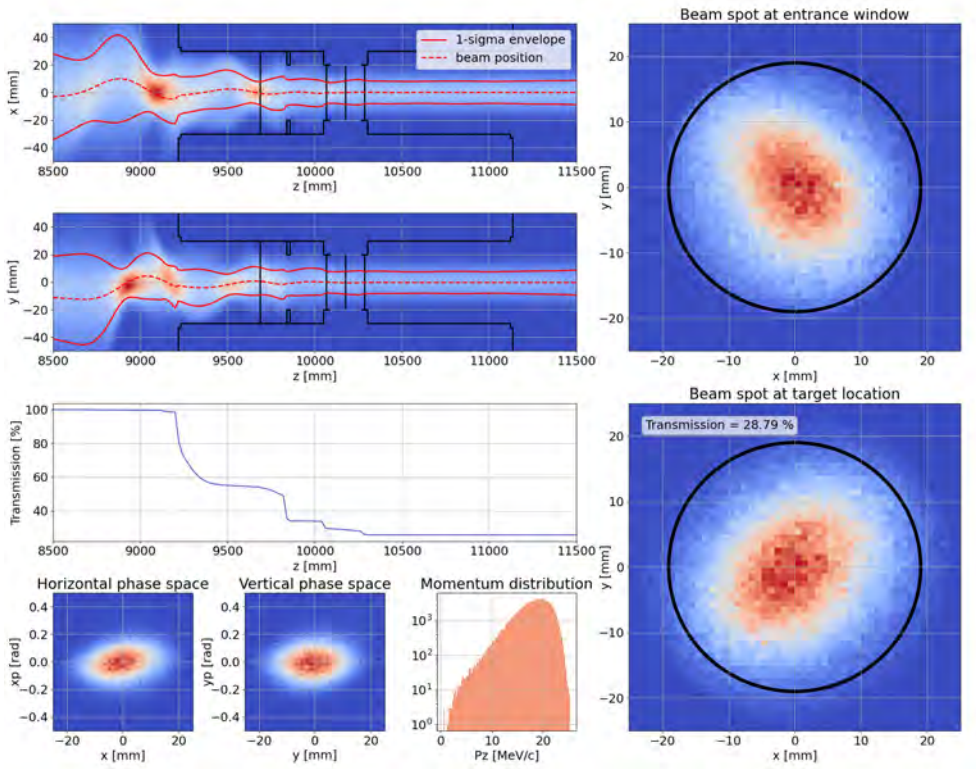

Figure C.1: *Transmission to the center of the Mu3e spectrometer. The tune and the position of the moderator are optimized for the nominal Mu3e spectrometer field value. The collimator position is optimized to minimize the muon rate on the inner layer of the Mu3e pixel tracker. On the left from the top: the envelopes in the horizontal and vertical plane, the black lines show the size of the beam pipe; the transmission from the entrance of the magnet; the phase space at the center of the Mu3e magnet. On the right from the top: the beam spot at the vacuum window and the beam spot at target location. The black circles show the size of the target cross section.*

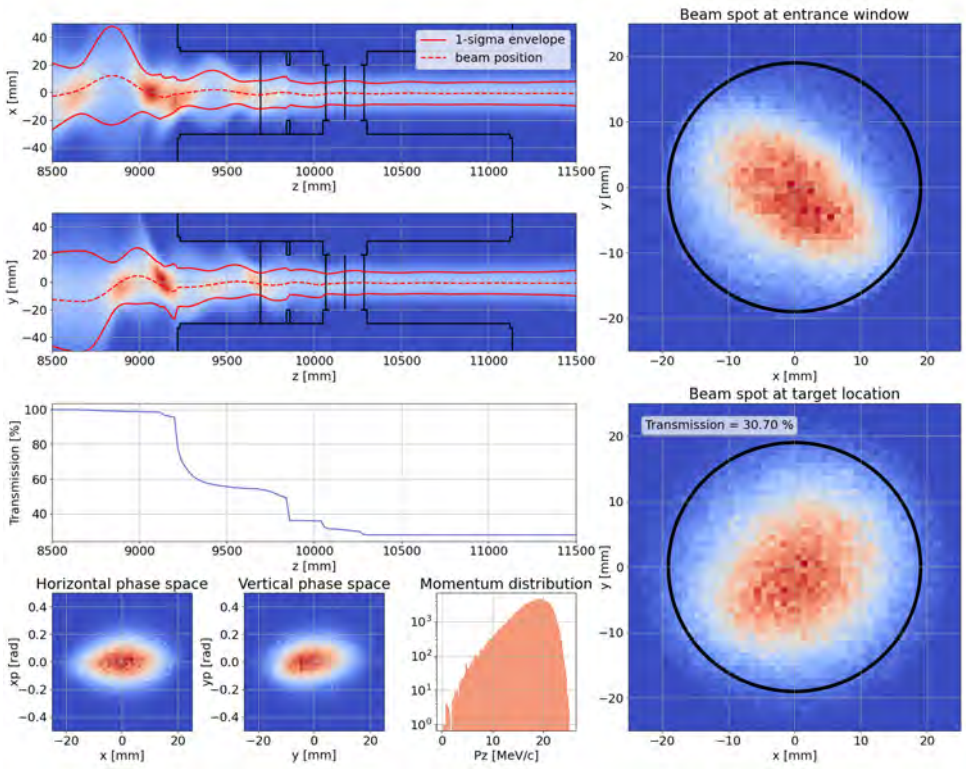

Figure C.2: *Transmission to the center of the Mu3e spectrometer. The tune and the position of the moderator are optimized for* 110 % *the nominal Mu3e spectrometer field value. The collimator position is optimized to minimize the muon rate on the inner layer of the Mu3e pixel tracker. On the left from the top: the envelopes in the horizontal and vertical plane, the black lines show the size of the beam pipe; the transmission from the entrance of the magnet; the phase space at the center of the Mu3e magnet. On the right from the top: the beam spot at the vacuum window and the beam spot at target location. The black circles show the size of the target cross section.*

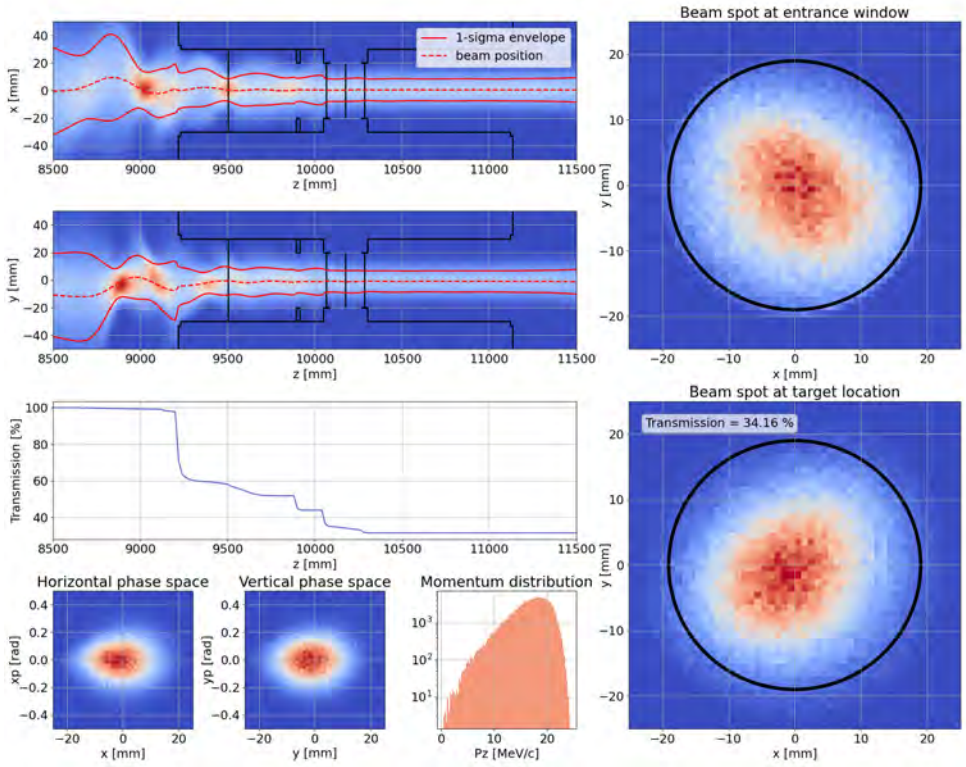

Figure C.3: *Transmission to the center of the Mu3e spectrometer. The tune and the position of the moderator are optimized for* 120 % *the nominal Mu3e spectrometer field value. The collimator position is optimized to minimize the muon rate on the inner layer of the Mu3e pixel tracker. On the left from the top: the envelopes in the horizontal and vertical plane, the black lines show the size of the beam pipe; the transmission from the entrance of the magnet; the phase space at the center of the Mu3e magnet. On the right from the top: the beam spot at the vacuum window and the beam spot at target location. The black circles show the size of the target cross section.*

Appendix D

Test probability density functions for the likelihood analysis of the beryllium anomaly measurement with the MEG II apparatus

Here, the parametrization of the probability density functions (PDFs) used in Chapter 4 to test the analysis framework of the X17 analysis are shown. The variables used in the test are the energy sum E_{sum} of the electron-positron pair and the relative angle θ_{rel} between the two particles.
The PDFs were defined by Francesco Renga, who is also working on this analysis, fitting the available Monte Carlo (MC) sample of the 4 background populations shown in Figure 4.7:

- internal and external pair conversion from the 18.15 MeV line (IPC18 and EPC18)
- internal and external pair conversion from the 15.12 MeV line (IPC15 and EPC15)

The parametrizations shown here are normalized to unity in the likelihood analysis depending on the data range set.
A different PDF is used for IPC and EPC backgrounds. For IPC:

- The energy sum is parametrized with the sum of two gaussian functions

$$\begin{aligned} p(E_{\text{sum}}|\mu,\sigma_1,\sigma_2,f) &= f\frac{1}{\sqrt{2\pi}\sigma_1}\exp\left(-\frac{1}{2}\frac{(E_{\text{sum}}-\mu)^2}{\sigma_1^2}\right)+ \\ &+ (1-f)\frac{1}{\sqrt{2\pi}\sigma_2}\exp\left(-\frac{1}{2}\frac{(E_{\text{sum}}-\mu)^2}{\sigma_2^2}\right). \end{aligned}$$

- The relative angle is parametrized with a 4th order polynomial function:

$$p(\theta_{\text{rel}}|p_0, p_1, p_2, p_3) \quad = \quad \sum_{i=0}^{4} p_i \theta_{\text{rel}}^i.$$

Figure D.1 shows a comparison between the MC sample and the PDFs for IPC18 and IPC15. Table D.1 shows the fitted parameters and errors.

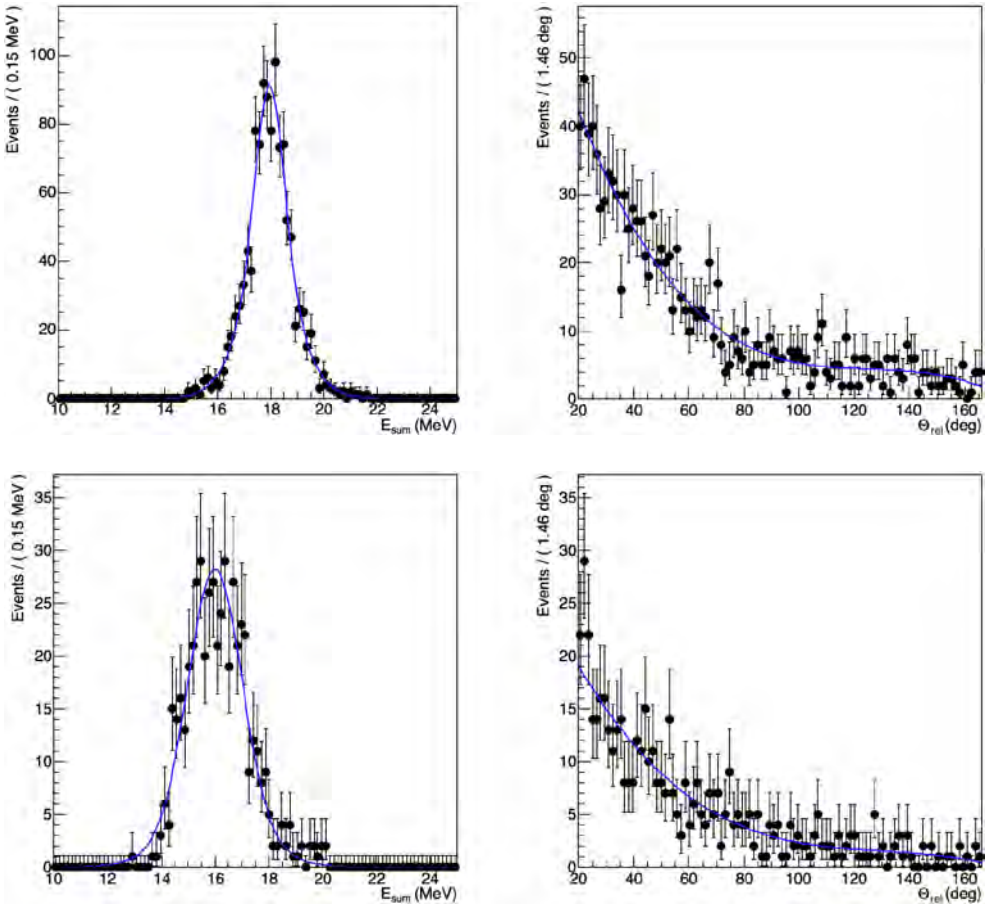

Figure D.1: *Comparison between the Monte Carlo (MC) sample (black points) and the probability density functions (PDFs) (blue lines) for the internal pair conversion backgrounds in the* 15.12 MeV *(bottom) and* 18.15 MeV *(top) lines of the* $^7\text{Li}(\text{p}, \text{e}^+\text{e}^-)^8\text{Be}$ *reaction in* E_{sum} *(left) and* θ_{rel} *(right). The PDFs are fitted to the MC sample in Figure 4.7. Gentle courtesy of Francesco Renga.*

		IPC energy sum PDF parameters and errors			
		μ [MeV]	σ_1 [MeV]	σ_2 [MeV]	f
IPC18	par.	17.95	0.54	1.13	0.48
	err.	0.03	0.08	0.08	0.12
IPC15	par.	16.000	0.99	1.9	0.83
	err.	0.012	0.06	0.3	0.10
		IPC relative angle PDF parameters and errors			
		p_0 [°]	p_1	p_2 [$^{\circ -1}$]	p_3 [$^{\circ -2}$]
IPC18	par.	1	-2.187×10^{-2}	1.723×10^{-4}	-4.57×10^{-7}
	err.	0	0.014×10^{-2}	0.015×10^{-4}	0.07×10^{-7}
IPC15	par.	1	-2.08×10^{-2}	1.55×10^{-4}	$-3.971\,44 \times 10^{-7}$
	err.	0	0.05×10^{-2}	0.07×10^{-4}	$0.274\,48 \times 10^{-7}$

Table D.1: Parameters of the probability density functions (PDFs) of the internal pair conversion backgrounds in the 15.12 MeV and 18.15 MeV lines of the $^7\mathrm{Li}(\mathrm{p}, \mathrm{e}^+\mathrm{e}^-)^8\mathrm{Be}$ reaction. The PDFs are fitted to the Monte Carlo (MC) sample in Figure 4.7. The parameters with zero errors are fixed and not fitted. A comparison between the MC sample and the PDFs is shown in Figure D.1.

For EPC:

- The energy sum is parametrized with an asymmetric gaussian function

$$\begin{aligned} p(E_{\mathrm{sum}}|\mu, \sigma_L, \sigma_R) &= (E_{\mathrm{sum}} < \mu) \exp\left(-\frac{1}{2}\frac{(E_{\mathrm{sum}} - \mu)^2}{\sigma_L^2}\right) + \\ &+ (E_{\mathrm{sum}} > \mu) \exp\left(-\frac{1}{2}\frac{(E_{\mathrm{sum}} - \mu)^2}{\sigma_R^2}\right). \end{aligned}$$

- The relative angle is parametrized with a gaussian function with asymmetric asymptotes

$$\begin{aligned} p(\theta_{\mathrm{rel}}|\mu, \sigma, \alpha_L, \alpha_R) &= (\theta_{\mathrm{rel}} < \mu) \exp\left(-\frac{1}{2}\frac{(\theta_{\mathrm{rel}} - \mu)^2}{\sigma^2 + \alpha_L^2(\theta_{\mathrm{rel}} - \mu)^2}\right) + \\ &+ (\theta_{\mathrm{rel}} > \mu) \exp\left(-\frac{1}{2}\frac{(\theta_{\mathrm{rel}} - \mu)^2}{\sigma^2 + \alpha_R^2(\theta_{\mathrm{rel}} - \mu)^2}\right). \end{aligned}$$

Figure D.2 shows a comparison between the MC sample and the PDFs for EPC18 and EPC15. Table D.2 shows the fitted parameters. The error on the parameters from the fit are reported with the subscript fit. Due to the limited statistics which is expected to be available for the EPC MC, an estimate of the error on the parameters was obtained by sampling 10^4 events from each EPC PDF and then fitting the sampled events with the same PDF. The errors obtained this way are reported with the subscript *est*.

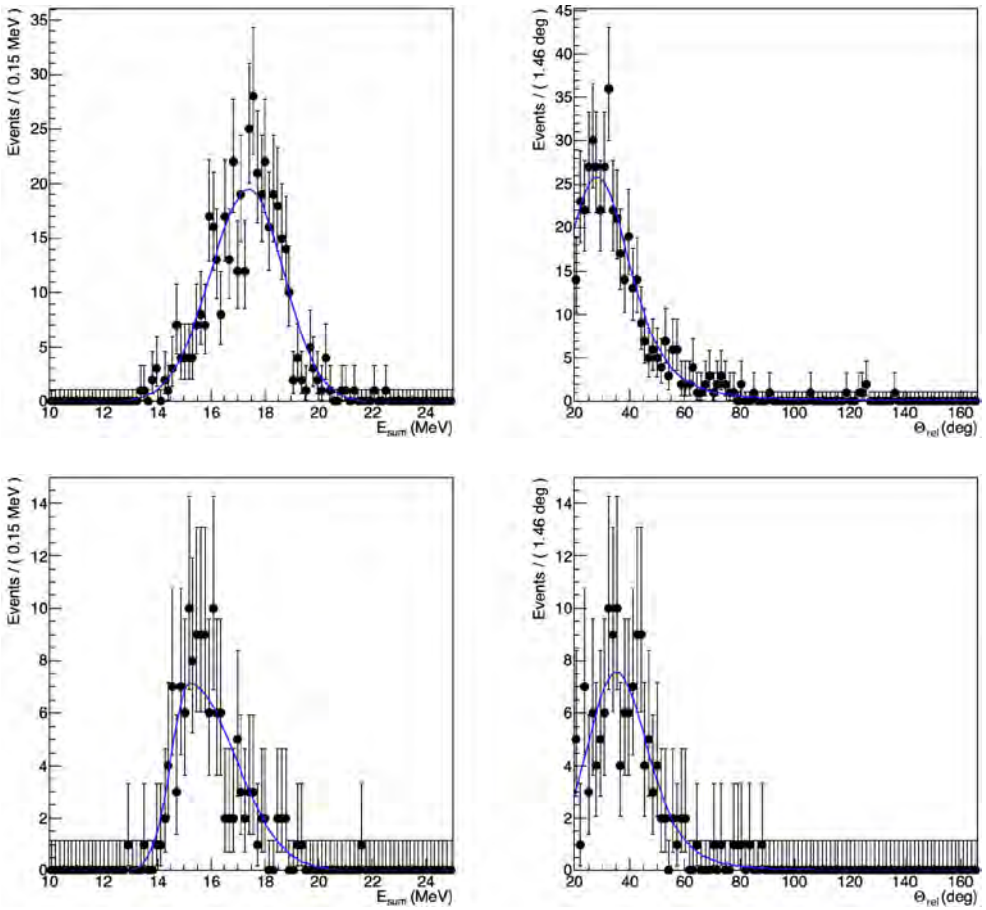

Figure D.2: *Comparison between the Monte Carlo (MC) sample (black points) and the probability density functions (PDFs) (blue lines) for the external pair conversion backgrounds in the* 15.12 MeV *(bottom) and* 18.15 MeV *(top) lines of the* $^{7}\mathrm{Li}(\mathrm{p},\mathrm{e}^{+}\mathrm{e}^{-})^{8}\mathrm{Be}$ *reaction in* E_{sum} *(left) and* θ_{rel} *(right). The PDFs are fitted to the MC sample in Figure 4.7. Gentle courtesy of Francesco Renga.*

		EPC energy sum PDF parameters and errors			
		μ [MeV]	σ_L [MeV]	σ_R [MeV]	-
EPC18	par.	17.41	1.43	1.30	
	err._{fit}	0.14	0.10	0.09	
	err._{est}	0.03	0.02	0.02	
EPC15	par.	15.21	0.684	1.70	
	err._{fit}	0.17	0.108	0.14	
	err._{est}	0.03	0.016	0.02	
		EPC relative angle PDF parameters and errors			
		μ [°]	σ [°]	α_L	α_R
EPC18	par.	28.2	11.34	0.01	0.174
	err._{fit}	1.5	1.20	0	0.016
	err._{est}	0	0.16	0	0.003
EPC15	par.	35.3	10.94	0.01	0.142
	err._{fit}	1.4	1.45	0	0.030
	err._{est}	0	0.15	0	0.003

Table D.2: Parameters of the probability density functions (PDFs) of the external pair conversion backgrounds in the 15.12 MeV and 18.15 MeV lines of the $^{7}\text{Li}(\text{p},\text{e}^{+}\text{e}^{-})^{8}\text{Be}$ reaction. The PDFs are fitted to the Monte Carlo (MC) sample in Figure 4.7. The parameters with zero errors are fixed and not fitted. A comparison between the MC sample and the PDFs is shown in Figure D.2.

Appendix E

Maximum transmission tunes for MUH2

Here, the tunes for maximum transmission found in Section 5.4.3 of μ^+, e^+ and π^+ are collected respectively in Table E.1, Table E.2 and Table E.3. The tunes for particles below 30 MeV/c are obtained by scaling down linearly from the surface muon tune for antimuons and from the 30 MeV/c tune for positrons and pions. The resulting rates are collected in Figure 5.28.

Parameters	Design central momentum of the μ^+ beam in MUH2					
	27 MeV/c	30 MeV/c	40 MeV/c	50 MeV/c	60 MeV/c	70 MeV/c
currentCapture_1 [T]	0.433	0.382	0.450	0.449	0.447	0.450
currentCapture_2 [T]	0.0448	0.145	0.323	0.385	0.443	0.450
currentCapture_3 [T]	0.218	0.172	0.218	0.268	0.392	0.449
BField1 [T]	0.0534	0.058	0.0777	0.0971	0.116	0.136
currentTSBL1 [T]	0.270	0.341	0.419	0.285	0.265	0.293
currentTSBL2 [T]	0.232	0.342	0.344	0.390	0.439	0.330
currentTSBL21 [T]	0.231	0.334	0.351	0.396	0.439	0.449
BField2scale	0.969	0.928	1.008	0.992	0.979	1.017
currentBL3 [T]	0.207	0.235	0.319	0.411	0.517	0.443
currentBL32 [T]	0.236	0.217	0.370	0.428	0.523	0.509
currentBL4 [T]	0.259	0.277	0.407	0.507	0.550	0.548
currentBL41 [T]	0.315	0.344	0.499	0.540	0.547	0.541
currentBL5 [T]	0.429	0.473	0.544	0.548	0.550	0.547
WienB [T]	-0.0146	-0.013	-0.0115	-0.00922	-0.00907	-0.00485
MUH2sign	-1	-1	1	1	1	1
MUH3sign	-1	-1	1	1	1	1
FirstSSectionSign	-1	-1	-1	-1	-1	1
SecondSSectionSign	-1	-1	1	1	1	1

Table E.1: MUH2 tunes for maximum tranmission of μ^+ for different design central momenta. The resulting delivered rates are collected in Figure 5.28.

Parameters	Design central momentum of the e^+ beam in MUH2				
	30 MeV/c	40 MeV/c	50 MeV/c	60 MeV/c	70 MeV/c
currentCapture_1 [T]	0.446	0.450	0.449	0.449	0.449
currentCapture_2 [T]	0.122	0.343	0.393	0.449	0.450
currentCapture_3 [T]	0.220	0.185	0.221	0.382	0.449
BField1 [T]	0.0582	0.0777	0.0971	0.116	0.136
currentTSBL1 [T]	0.369	0.387	0.361	0.282	0.297
currentTSBL2 [T]	0.317	0.313	0.436	0.448	0.427
currentTSBL21 [T]	0.260	0.333	0.443	0.450	0.440
BField2scale	1.028	0.980	0.976	1.010	1.026
currentBL3 [T]	0.247	0.284	0.385	0.527	0.473
currentBL32 [T]	0.267	0.364	0.441	0.511	0.446
currentBL4 [T]	0.296	0.399	0.497	0.549	0.549
currentBL41 [T]	0.356	0.482	0.534	0.542	0.541
currentBL5 [T]	0.469	0.550	0.548	0.529	0.542
WienB [T]	-0.00305	-0.00322	-0.00334	-0.00446	-0.00187
MUH2sign	1	1	1	1	1
MUH3sign	1	1	1	1	1
FirstSSectionSign	1	-1	1	1	1
SecondSSectionSign	1	-1	1	-1	1

Table E.2: MUH2 tunes for maximum tranmission of e^+ for different design central momenta. The resulting delivered rates are collected in Figure 5.28.

Parameters	Design central momentum of the π^+ beam in MUH2				
	30 MeV/c	40 MeV/c	50 MeV/c	60 MeV/c	70 MeV/c
currentCapture_1 [T]	0.444	0.449	0.449	0.449	0.449
currentCapture_2 [T]	0.201	0.313	0.410	0.448	0.448
currentCapture_3 [T]	0.129	0.238	0.246	0.400	0.449
BField1 [T]	0.058	0.0777	0.0971	0.116	0.136
currentTSBL1 [T]	0.305	0.437	0.279	0.303	0.291
currentTSBL2 [T]	0.265	0.364	0.395	0.449	0.373
currentTSBL21 [T]	0.265	0.349	0.407	0.435	0.450
BField2scale	1.022	1.021	1.003	0.993	1.021
currentBL3 [T]	0.223	0.295	0.417	0.510	0.480
currentBL32 [T]	0.293	0.371	0.435	0.534	0.486
currentBL4 [T]	0.315	0.412	0.509	0.548	0.549
currentBL41 [T]	0.394	0.480	0.537	0.547	0.547
currentBL5 [T]	0.490	0.548	0.548	0.538	0.537
WienB [T]	-0.0169	-0.0123	-0.0111	-0.0101	-0.00626
MUH2sign	1	1	1	1	1
MUH3sign	1	1	1	1	1
FirstSSectionSign	-1	1	-1	-1	1
SecondSSectionSign	-1	1	1	1	1

Table E.3: MUH2 tunes for maximum tranmission of π^+ for different design central momenta. The resulting delivered rates are collected in Figure 5.28.

Appendix F

Optimized beam spot tunes for MUH2

Here, the tunes for optimized beam spot found in Section 5.4.3.1 of μ^+, Mott positrons and CEX pions are collected in Table F.1. The tune of μ^+ including the contamination cut is shown in Table 5.3.

Parameters	Design central momentum							
	μ^+						e^+	π^+
	27 MeV/c	30 MeV/c	40 MeV/c	50 MeV/c	60 MeV/c	70 MeV/c	50 MeV/c	70 MeV/c
BField1 [T]	0.0521	0.0554	0.0793	0.0950	0.111	0.132	0.0939	0.548
BField2scale	0.952	0.952	0.977	0.963	0.958	1.022	0.983	0.248
currentBL3 [T]	0.207	0.363	0.287	0.265	0.018	0.537	0.422	0.284
currentBL32 [T]	0.236	0.348	0.370	0.433	0.508	0.109	0.432	0.544
currentBL4 [T]	0.263	0.286	0.418	0.307	0.309	0.306	0.294	0.547
currentBL41 [T]	0.225	0.249	0.354	0.396	0.512	0.550	0.347	0.137
currentBL5 [T]	0.364	0.389	0.549	0.549	0.548	0.542	0.548	0.986
WienB [T]	-0.0158	-0.0157	-0.00906	-0.00939	-0.00806	-0.00791	-0.00415	-0.00976

Table F.1: MUH2 tunes of μ^+, Mott positrons and CEX pions for optimized beam spot.

Appendix G

Dispersion calculation in MUH2 and MUH3 envelope plots

Dispersion (see Chapter 2.2.2) in particle beam dynamics is used to account for the effects of a finite momentum spread on the trajectory of the single particles. If we consider a particle that would be transmitted to the horizontal position x_0 in absence of dispersion, we can calculate the position x of the particle with a finite momentum difference Δp as:

$$x = x_0 + D\frac{\Delta p}{p_0} = x_0 + D\delta \tag{G.1}$$

where D is the dispersion function and δ is the momentum spread relative to the central momentum p_0. A first order approximation of the dispersion function can be computed in the assumption that the correlation between x_0 and δ is zero, which is analogous to say that any correlation is induced by the dispersion itself. In this case, the dispersion can be computed by calculating the correlation between x and δ:

$$\begin{aligned} \langle x\delta \rangle &= \langle (x_0 + D\delta)\delta \rangle && \text{(G.2)} \\ &= \langle x_0\delta \rangle + D\langle \delta^2 \rangle && \text{(G.3)} \\ &= D\langle \delta^2 \rangle && \text{(G.4)} \\ \Rightarrow D &= \frac{\langle x\delta \rangle}{\langle \delta^2 \rangle} && \text{(G.5)} \end{aligned}$$

This formula is used to evealuate the dispersion in the envelopes shown in Chapter 5 and in Appendix I and J.

Appendix H

Time-of-flight spectra modeling of MUH2 with G4beamline

In Section 3.2.2, the measurement of the time-of-flight (TOF) of the particles delivered in the πE5 area at PSI is shown. The measurement is performed by triggering on the particle detected at the PILL and then measuring the time difference with the next RF pulse, perfoming a modulo operation. Figure H.1 shows the measured TOF with SEP41 in three different configurations:

- SEP41 off: in yellow, both muons and positrons are measured. The peak is due to positrons generated at TgE* (see Section 1.5.2). The uniform component is the sum of muons, Michel positrons from TgE* and Michel positrons from muon decays in the PILL.
- SEP41 set to muons: in blue.
- SEP41 set to positrons: in green.

The uniform component of the spectrum is fitted between -39.5 ns and -37 ns and between -30 ns and -25 ns with a constant. The fitted costant is subtracted from the spectrum to isolate the peak structures, which are integrated separately. The integral of the full spectrum is computed as well and used for the fractions in Figure H.1. The fraction of Michel positrons for SEP41 set for positron transmission is used to benchmark the modeling of pion production cross-section in G4beamline used for HIMB simulations [6, 86]. The TOF modeling is done by impinging 10^{10} protons on TgE* in G4beamline. The implementation of the πE5 beamline is based on [5] and SEP41 is kept off. The protons are generated with gaussian time distribution assuming a bunch length of 58 mm and a kinetic Energy of 585 MeV. The period of the proton RF is set to 19.75 ns.
Figure H.2 shows the simulated spectra. The absolute rate do not match the actual measurement, but the relative yield of the population is fairly consis-

tent with the data: the simulated fraction of Michel positrons produced at TgE* is 56.2 % to be compared with the measured 62 %.

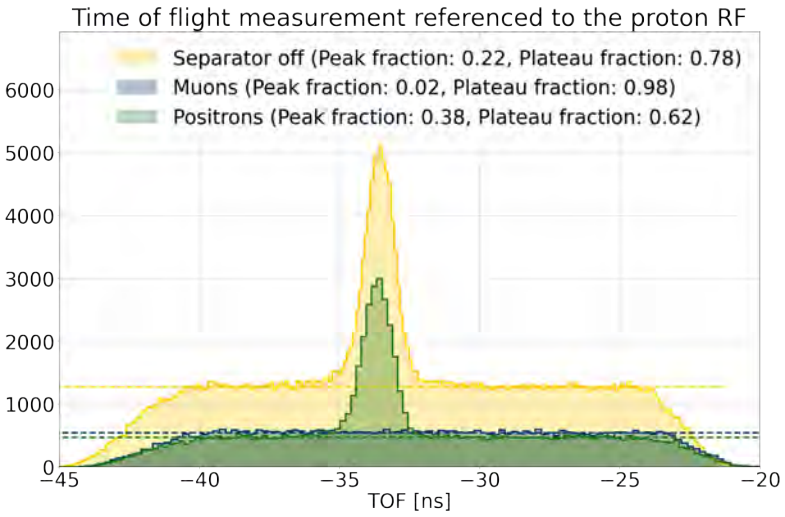

Figure H.1: *Time-of-flight spectrum measured at collimator for different SEP41 settings: off (yellow), muons (blue) and positrons (green). The TOF is defined as the difference between the discriminated Pill signals and the RF-signal. The scale does not represent the delivered rates. The tails of the distributions are due to the finite resolution of the apparatus and to the time walk of the DRS4 evaluation board, which measures the time the signals exceed the threshold and not the time they reach a fraction of their maximum.*

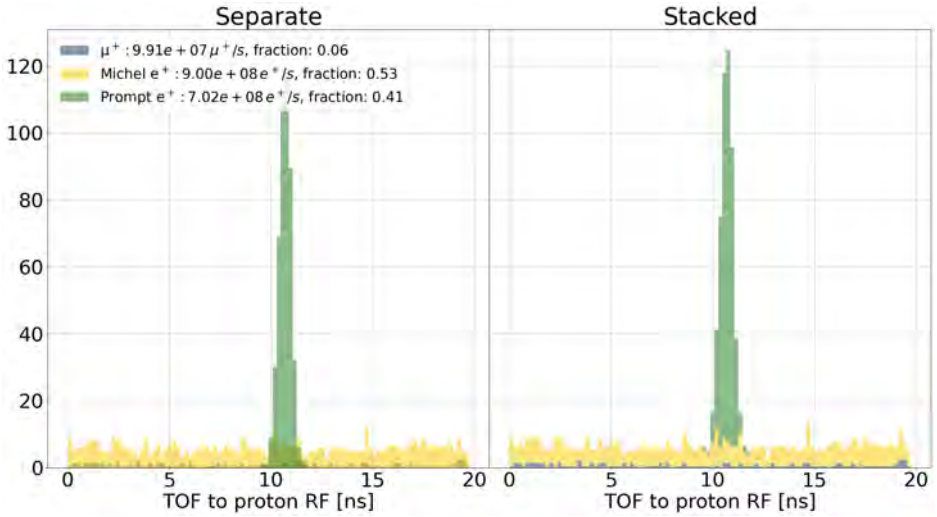

Figure H.2: *Simulated TOF spectrum for* 27 MeV *tune in πE5. SEP41 is off. The particles are generated by impinging* 10^{10} protons *on TgE*. Left: the histograms are shown separately, without stacking them. Right: the histograms are stacked. The shown fractions are different than that quoted in the text as here it is referred with respect to the total transmission including muons, and in the text with respect positrons only.*

Appendix I

MUH2 Mott positron beam envelope

Envelope and phase space of the Mott positron beam delivered by MUH2. The tune is obtained in Section 5.4.3.1 by optimizing the transmission, the beam spot size and the beam centering with NSGA-II.

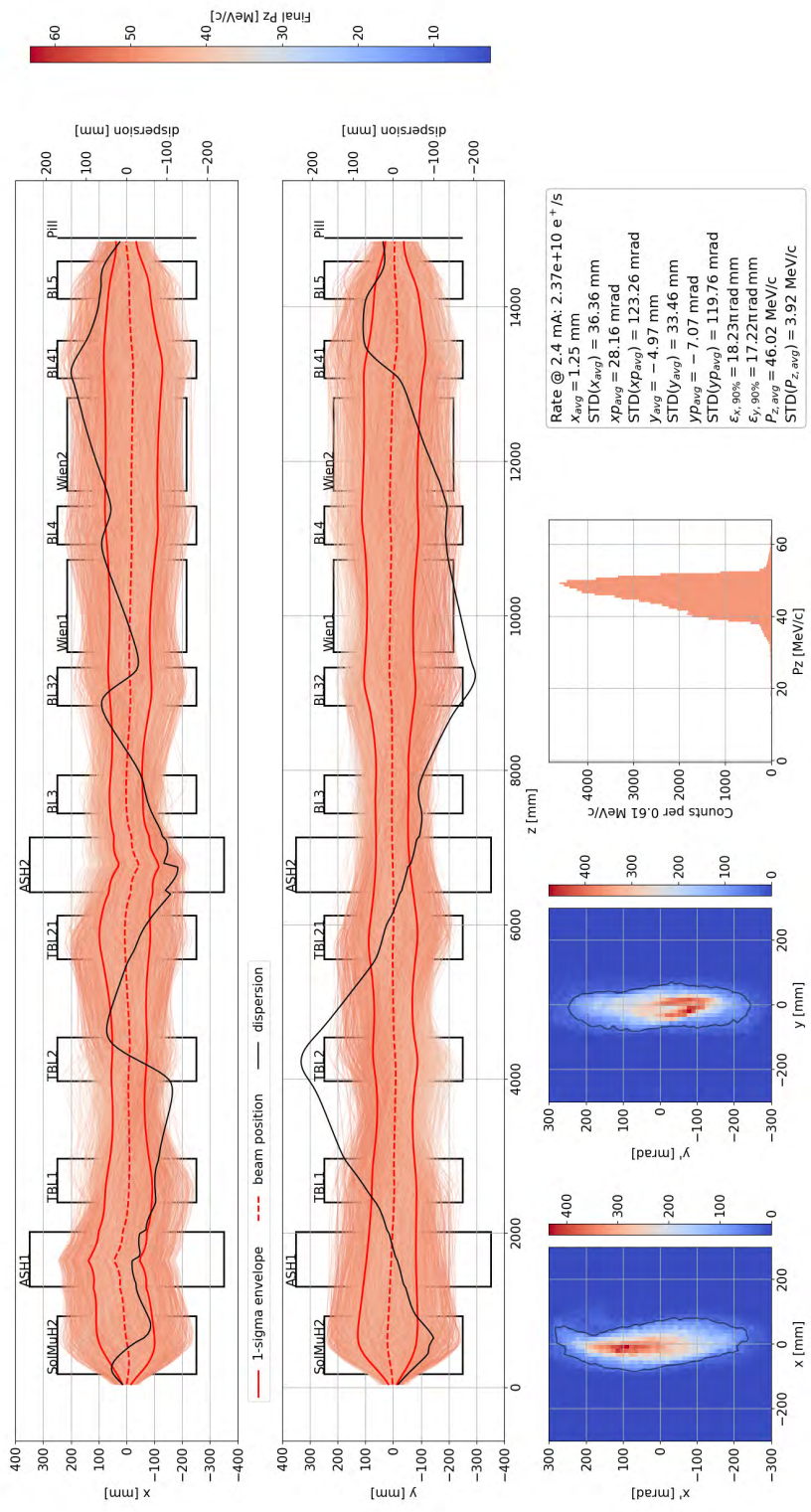

Figure I.1: *Mott positron beam envelopes and phase spaces. The dispersion curves shown here are computed based on the correlation between the position and the longitudinal momentum at each position. TgH is positioned at the origin of the coordinate system.*

Appendix J

MUH2 CEX pion beam envelope

Envelope and phase space of the CEX negative pion beam delivered by MUH2. The tune is obtained in Section 5.4.3.1 by optimizing the transmission, the beam spot size and the beam centering with NSGA-II.

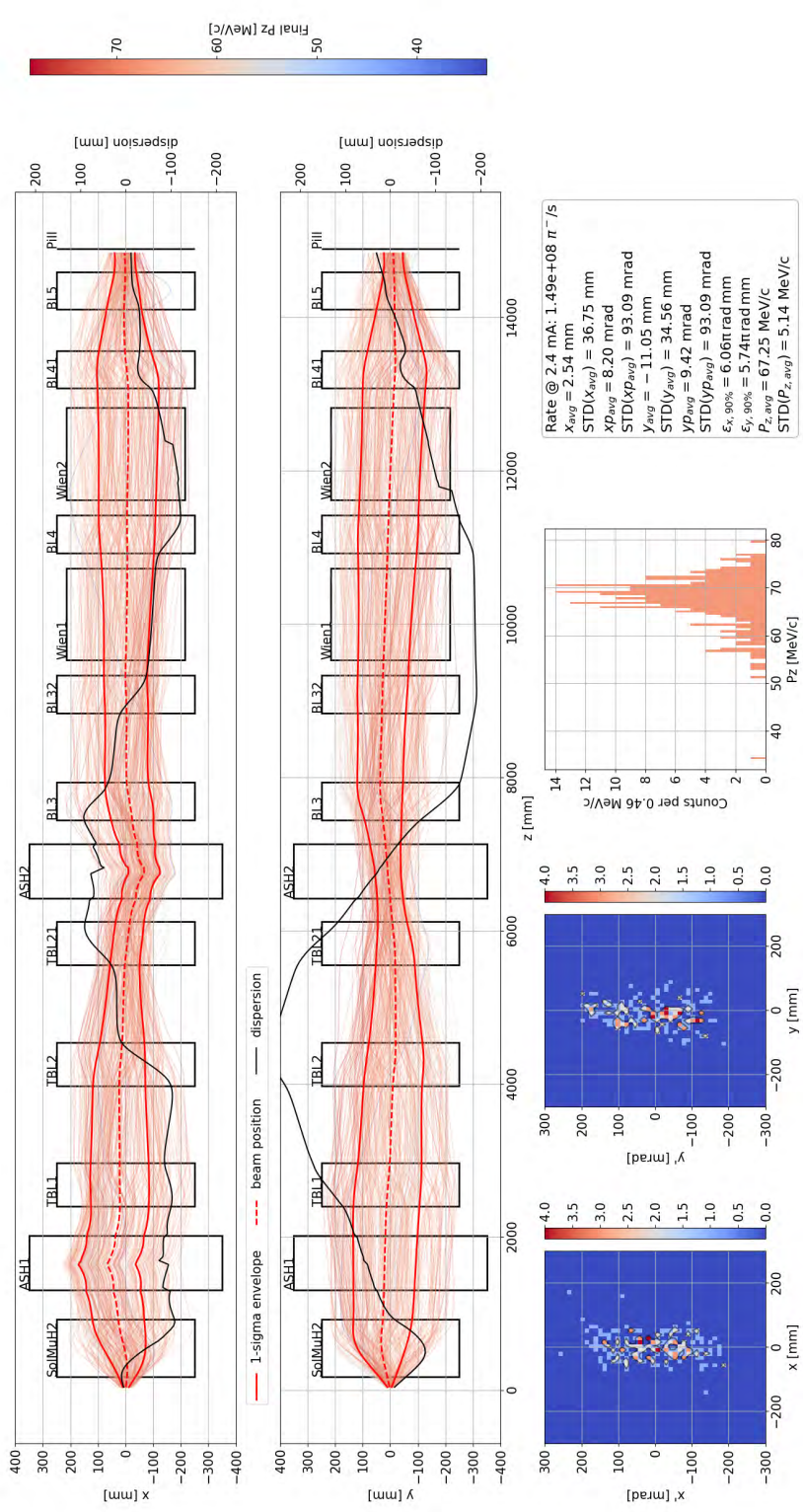

Figure J.1: *CEX pion beam envelopes and phase spaces. The dispersion curves shown here are computed based on the correlation between the position and the longitudinal momentum at each position. TgH is positioned at the origin of the coordinate system.*

Appendix K

Maximum transmission tunes for MUH3

Here, the tunes for the maximum transmission found in Section 5.5.3 of μ^+ are collected in Table K.1. The tunes for particles below 30 MeV/c are obtained by scaling down linearly from the surface muon tune.

	Peak/Pole fields [T] Design central momentum of the μ^+ beam in MUH3				
Nominal momentum	27 MeV/c	40 MeV/c	50 MeV/c	60 MeV/c	70 MeV/c
currentCapture_1	0.442	0.447	0.435	0.450	0.449
currentCapture_2	0.210	0.432	0.450	0.447	0.431
currentCapture_3	0.0516	0.0980	0.312	0.414	0.427
BField1	0.0562	0.0772	0.100	0.121	0.155
currentTSBL1	0.382	0.288	0.380	0.122	0.00150
currentTSBL2	0.354	0.374	0.449	0.440	0.207
BField2	0.0645	0.101	0.122	0.137	0.182
currentBL3	-0.372	-0.548	0.480	0.473	-0.392
BField3	0.0363	0.0532	0.0578	0.068	0.0741
currentBL4	-0.281	0.338	-0.445	0.164	-0.425
currentBL5	-0.303	0.225	0.419	-0.397	0.502
currentQSM1	0.105	0.0232	0.0768	0.0570	0.103
currentQSM2	-0.142	-0.0793	-0.173	-0.108	-0.192
currentQSM3	0.0805	0.0732	0.113	0.0376	0.115

Table K.1: MUH3 tunes for maximum tranmission of μ^+ for different design central momenta. For solenoids and dipoles, the value reached by the field at its peak is shown. For quadrupoles, the value of the field at their pole tip is shown. The resulting μ^+ delivered rates are collected in Figure 5.40.

Acknowledgements

I would like to express my sincere gratitude to my advisor **Klaus Kirch** for the constant support and the insightful feedbacks. Seeing you involved in every laboratory activity and still deeply committed to teaching at ETH is always of inspiration.

I would like to thank also **Wataru Ootani** and **Johannes Bernhard** for having agreed on reviewing this work.

I would like to express my deepest gratitude to **Angela Papa** and **Andreas Knecht** for having guided me through this experience. Thank you Angela for the chance of joining the πE5 activities already during my master and thank you for your constant dedication. From you I started learning to do research and I will be always grateful for that. Thank you Andreas for your patience and for your calm approach to physics and life. It was important for me to always find a peaceful environment in stressed and booked periods. Thank you both for your invaluable trust.

I would also like to thank **Peter-Raymond Kettle** from whom I learned so much during my first beam time in MEG II and later on when working on HIMB and the CMBL.

Next, I would like to thank **Aldo Antognini** for the constant positive exchanges and suggestions. It was a pleasure to work with you and Klaus, first as a TA and then for exam preparation. I only regret the absence of a photon gas in our last exam.

Furthermore, I would like to thank **Stefan Ritt** for all the help and support. I am grateful for the invaluable support you gave me during beam time, always on very short notice.

I would also like to thank **Anita van Loon** for taking care of all my administrative needs.

I would like to thank **Malte Hildebrandt** and the detector group for the construction of the pepper-pot plates and in general for the great support during the beam time.

I would like to thank the MEG II and Mu3e collaborations. I am grateful for the constant work and discussion. Particular thanks go to **Bastiano Vitali** and **Hicham Benmansour** for the working and leisure hours spent together and to **Kensuke Yamamoto** for the nice time spent in and outside the office and the many discussions.

Special thanks go to all my PhD and PostDoc colleagues, former and current, who made my life in Switzerland so easy. Thanks to **Jonas Nuber** and **Giuseppe Lospalluto** for having tried so hard, and yet failed, to get me into bouldering. Thanks to **Stergiani Vogiatzi**, **Katharina von Schoeler**, **Thomas Rudzki**, **Thomas Senger**, **Luigi Vigani**, **Lukas Affolter**, **Ahmed Ouf**, **Siddarth Rajamohanan**, **Patrick Mullan**, **Joanna Peszka**, **Anastasia Doinaki** for the nice time spent in office 131 and for the lunch breaks, very much needed and appreciated to get through the day. Thanks to **Chavdar Dutsov**, **Ljiljana Morvaj**, **Timothy Hume**, **Ritwika Chakraborty**, **Diego Alejandro Sanz Becerra**, **David Höhl** and **Philipp Schmidt-Wellenburg** for the nice discussions, chats and early lunches. Then, thanks to the old school students, **Manuel Zeyen**, **Oguzhan Kara**, **Ryoto Iwai**, and **Mikio Sakurai**. Special thanks go to the many of you who coped with my bad jokes inside and outside of the office and with my karaoke performances.
I need to thank also my dear nerd colleagues who have shared with me their passion for anime movies and board games, **Patrick Schwendimann**, **Lukas Gerritzen**, **Nathalie Ziel**, **Mirsoław Marszałek**.
There is no way I can thank you all enough. I feel blessed for having been part of such a nice and diverse group, with infinite opportunities to learn from you all.

I would like to thank the many housemates I have had in Windisch especially **Bart**, **Debbie** and **Dominic**.

Finally, I would not be here without the constant support of my family and friends. I am deeply grateful to my parents, my brother, nonna and all the many Dal Masos, Meuccis and affiliates who have been a constant presence throughout my whole life.

Bibliography

[1] Y. Kuno and Y. Okada. "Muon decay and physics beyond the standard model". In: *Rev. Mod. Phys.* 73 (1 2001), pp. 151–202. DOI: 10.1103/RevModPhys.73.151. URL: https://link.aps.org/doi/10.1103/RevModPhys.73.151.

[2] MEG II Collaboration et al. *Operation and performance of MEG II detector*. 2023. arXiv: 2310.11902 [physics.ins-det].

[3] A.M. Baldini et al. "The design of the MEG II experiment". In: *Eur. Phys. Journal C* 78.380 (2016). URL: https://doi.org/10.1140/epjc/s10052-018-5845-6.

[4] K. Arndt et al. "Technical design of the phase I Mu3e experiment". In: *Nuclear Instruments and Methods in Physics Research Section A: Accelerators, Spectrometers, Detectors and Associated Equipment* 1014 (Oct. 2021), p. 165679. ISSN: 0168-9002. DOI: 10.1016/j.nima.2021.165679. URL: http://dx.doi.org/10.1016/j.nima.2021.165679.

[5] F. A. Berg. "CMBL - A High-Intensity Muon Beam Line & Scintillation Target with Monitoring System for Next-Generation Charged Lepton Flavour Violation Experiments". Doctoral Thesis. Zurich: ETH Zurich, 2017. DOI: 10.3929/ethz-b-000213470.

[6] Z. Hodge. "Production, Characterization, and Monitoring of Surface Muon Beams for Charged Lepton Flavor Violation Experiments". Doctoral Thesis. Zurich: ETH Zurich, 2018. DOI: 10.3929/ethz-b-000288571.

[7] I. Paraskevas. "Preparations for the Mu3e experiment: Magnet commissioning, beamline studies and a study of fake tracks". Doctoral Thesis. London: UCL (University College London), 2021. URL: https://discovery.ucl.ac.uk/id/eprint/10142359.

[8] A. J. Krasznahorkay et al. "Observation of Anomalous Internal Pair Creation in ^{8}Be: A Possible Indication of a Light, Neutral Boson". In: *Phys. Rev. Lett.* 116 (4 2016), p. 042501. DOI: 10.1103/PhysRevLett.116.042501. URL: https://link.aps.org/doi/10.1103/PhysRevLett.116.042501.

[9] J. Gulyás et al. "A pair spectrometer for measuring multipolarities of energetic nuclear transitions". In: *Nuclear Instruments and Methods in Physics Research Section A: Accelerators, Spectrometers, Detectors and Associated Equipment* 808 (2016), pp. 21–28. ISSN: 0168-9002. DOI: https://doi.org/10.1016/j.nima.2015.11.009. URL: https://www.sciencedirect.com/science/article/pii/S0168900215013716.

[10] G. Dal Maso. "Beam diagnostic and calibration tools for the MEGII experiment". In: (Sept. 2020). URL: https://etd.adm.unipi.it/t/etd-08262020-123015/.

[11] D. J. Griffiths. *Introduction to elementary particles; 2nd rev. version*. Physics textbook. New York, NY: Wiley, 2008. URL: https://cds.cern.ch/record/111880.

[12] M. Lubej. *The Standard Model of particle physics*. 2015. URL: https://www.physik.uzh.ch/groups/serra/StandardModel.html.

[13] P. W. Higgs. "Broken Symmetries and the Masses of Gauge Bosons". In: *Phys. Rev. Lett.* 13 (16 1964), pp. 508–509. DOI: 10.1103/PhysRevLett.13.508. URL: https://link.aps.org/doi/10.1103/PhysRevLett.13.508.

[14] Particle Data Group et al. "Review of Particle Physics". In: *Progress of Theoretical and Experimental Physics* 2022.8 (Aug. 2022), p. 083C01. ISSN: 2050-3911. DOI: 10.1093/ptep/ptac097. eprint: https://academic.oup.com/ptep/article-pdf/2022/8/083C01/49175539/ptac097.pdf. URL: https://doi.org/10.1093/ptep/ptac097.

[15] L. Calibbi and G. Signorelli. "Charged Lepton Flavour Violation: An Experimental and Theoretical Introduction". In: *Riv. Nuovo Cim.* 41.2 (2018), pp. 71–174. DOI: 10.1393/ncr/i2018-10144-0. arXiv: 1709.00294 [hep-ph].

[16] B. Pontecorvo. "Mesonium and anti-mesonium". In: *Sov. Phys. JETP* 6 (1957), p. 429.

[17] Z. Maki, M. Nakagawa, and S. Sakata. "Remarks on the unified model of elementary particles". In: *Prog. Theor. Phys.* 28 (1962), pp. 870–880. DOI: 10.1143/PTP.28.870.

[18] R.H. Bernstein and P. S. Cooper. "Charged lepton flavor violation: An experimenter's guide". In: *Physics Reports* 532.2 (2013). Charged Lepton Flavor Violation: An Experimenter's Guide, pp. 27–64. ISSN: 0370-1573. DOI: https://doi.org/10.1016/j.physrep.2013.07.002. URL: https://www.sciencedirect.com/science/article/pii/S0370157313002688.

[19] A. Crivellin et al. "Renormalisation-group improved analysis of $\mu \to$ e processes in a systematic effective-field-theory approach". In: *Journal of High Energy Physics* 2017.5 (2017). ISSN: 1029-8479. DOI: https://doi.org/10.1007/JHEP05(2017)117. URL: https://link.springer.com/article/10.1007/JHEP05(2017)117#citeas.

[20] D. Kaneko. "Upgrade of the Liquid Xenon γ-ray detector in the MEG experiment". In: *Nuclear Instruments and Methods in Physics Research Section A: Accelerators, Spectrometers, Detectors and Associated Equipment* 732 (2013). Vienna Conference on Instrumentation 2013, pp. 457 –462. ISSN: 0168-9002. DOI: https://doi.org/10.1016/j.nima.2013.06.008. URL: http://www.sciencedirect.com/science/article/pii/S0168900213008280.

[21] A. J. Krasznahorkay et al. "Observation of Anomalous Internal Pair Creation in ^{8}Be: A Possible Indication of a Light, Neutral Boson". In: *Phys. Rev. Lett.* 116 (4 2016), p. 042501. DOI: 10.1103/PhysRevLett.116.042501. URL: https://link.aps.org/doi/10.1103/PhysRevLett.116.042501.

[22] A.M. Baldini et al. "A new cylindrical drift chamber for the MEG II experiment". In: *Nuclear Instruments and Methods in Physics Research Section A: Accelerators, Spectrometers, Detectors and Associated Equipment* 824 (2016). Frontier Detectors for Frontier Physics: Proceedings of the 13th Pisa Meeting on Advanced Detectors, pp. 589 –591. ISSN: 0168-9002. DOI: https://doi.org/10.1016/j.nima.2015.10.103. URL: http://www.sciencedirect.com/science/article/pii/S016890021501342X.

[23] M. De Gerone et al. "Design and test of an extremely high resolution Timing Counter for the MEG II experiment: Preliminary results". In: *Journal of Instrumentation* 9 (Dec. 2013). DOI: 10.1088/1748-0221/9/02/C02035.

[24] *LYSO Scintillation Material. Lu1.8Y.2SiO5:Ce*. Saint Gobain Crystals. URL: https://www.crystals.saint-gobain.com/sites/imdf.crystals.com/files/documents/lyso-material-data-sheet_1.pdf.

[25] S. Ritt. "The DRS chip: cheap waveform digitizing in the GHz range". In: *Nuclear Instruments and Methods in Physics Research Section A: Accelerators, Spectrometers, Detectors and Associated Equipment* 518.1 (2004). Frontier Detectors for Frontier Physics: Proceedings, pp. 470 –471. ISSN: 0168-9002. DOI: https://doi.org/10.1016/j.nima.2003.11.059. URL: http://www.sciencedirect.com/science/article/pii/S016890020302922X.

[26] The MEG Collaboration. *Search for the Lepton Flavour Violating Decay $\mu^+ \to e^+\gamma$ with the Full Dataset of the MEG Experiment*. 2016. arXiv: 1605.05081 [hep-ex].

[27] O. Chubar, P. Elleaume, and J. Chavanne. "A three-dimensional magnetostatics computer code for insertion devices". In: *Journal of Synchrotron Radiation* 5.3 (1998), pp. 481–484. URL: https://doi.org/10.1107/S0909049597013502.

[28] H. Wiedemann. *Particle Accelerator Physics*. Springer Nature, 2015. DOI: 10.1007/978-3-319-18317-6. URL: https://link.springer.com/book/10.1007/978-3-319-18317-6.

[29] *πE5 Beamline*. URL: https://www.psi.ch/en/sbl/pie5-beamline.

[30] U. Rohrer. *PSI Graphic TRANSPORT Framework by U. Rohrer based on a CERN-SLAC-FERMILAB version by K.L. Brown et al.* 2007. URL: http://aea.web.psi.ch/Urs_Rohrer/MyWeb/trans.htm.

[31] J. Adam et al. "The MEG detector for μ+→e+γ decay search". In: *The European Physical Journal C* 73.4 (2013), p. 2365. ISSN: 1434-6052. DOI: 10.1140/epjc/s10052-013-2365-2. URL: https://doi.org/10.1140/epjc/s10052-013-2365-2.

[32] R. Bitter, T. Mohiuddin, and M. Nawrocki. *LabVIEW: Advanced programming techniques*. Crc Press, 2006.

[33] S. Ritt and P.A. Amaudruz. "The MIDAS data acquisition system". In: 1997, pp. 309–312. URL: https://scholar.google.ch/citations?view_op=view_citation&hl=en&user=7UOrlDYAAAAJ&citation_for_view=7UOrlDYAAAAJ:zYLM7Y9cAGgC.

[34] *MIDAS wiki*. URL: https://daq00.triumf.ca/MidasWiki/index.php/Introduction.

[35] S. Ritt and P.A. Amaudruz. "New components of the MIDAS data acquisition system". In: 1999, 116 – 118. DOI: 10.1109/RTCON.1999.842578. URL: https://www.scopus.com/inward/record.uri?eid=2-s2.0-80455156668&doi=10.1109%2fRTCON.1999.842578&partnerID=40&md5=7cf9e7aed21d659fcbb0e355908547ae.

[36] S. Ritt, R. Dinapoli, and U. Hartmann. "Application of the DRS chip for fast waveform digitizing". In: *Nuclear Instruments and Methods in Physics Research Section A: Accelerators, Spectrometers, Detectors and Associated Equipment* 623.1 (2010). 1st International Conference on Technology and Instrumentation in Particle Physics, pp. 486–488. ISSN: 0168-9002. DOI: https://doi.org/10.1016/j.nima.2010.03.045. URL: https://www.sciencedirect.com/science/article/pii/S0168900210006091.

[37] Muons Inc. *G4beamline (version 3.06)*. 2019. URL: http://www.muonsinternal.com/muons3/G4beamline.

[38] P. Virtanen et al. "SciPy 1.0: Fundamental Algorithms for Scientific Computing in Python". In: *Nature Methods* 17 (2020), pp. 261–272. DOI: 10.1038/s41592-019-0686-2.

[39] (Geant4 collaboration) S. Agostinelli et al. "Geant4 – a simulation tool-kit". In: *Nucl. Instrum. Methods A* 506 (2003), pp. 250–303. URL: https://doi.org/10.1016/S0168-9002(03)01368-8.

[40] J. Allison et al. "Geant4 developments and applications". In: *IEEE Trans. Nucl. Sci.* 53 (2006), pp. 270–278. URL: https://doi.org/10.1109/TNS.2006.869826.

[41] J. Allison et al. "Recent develpments in Geant4". In: *Nucl. Instrum. Methods A* 835 (2016), pp. 186–225. URL: https://doi.org/10.1016/j.nima.2016.06.125.

[42] M. Zhang. "Emittance formula for slits and pepper-pot measurement". In: (Oct. 1996). DOI: 10.2172/395453. URL: https://www.osti.gov/biblio/395453.

[43] G. Dal Maso. *PepperPotCheck*. https://github.com/gdalmaso96/PepperPotCheck. 2023.

[44] F. James and M. Roos. "Minuit - a system for function minimization and analysis of the parameter errors and correlations". In: *Computer Physics Communications* 10.6 (1975), pp. 343–367. ISSN: 0010-4655. DOI: https://doi.org/10.1016/0010-4655(75)90039-9. URL: https://www.sciencedirect.com/science/article/pii/0010465575900399.

[45] K. Deb et al. "A fast and elitist multiobjective genetic algorithm: NSGA-II". In: *IEEE Transactions on Evolutionary Computation* 6.2 (2002), pp. 182–197. DOI: 10.1109/4235.996017.

[46] T. Akiba et al. "Optuna: A Next-generation Hyperparameter Optimization Framework". In: *Proceedings of the 25th ACM SIGKDD International Conference on Knowledge Discovery and Data Mining*. 2019.

[47] A. S. Hofler. "Genetic algorithms and their applications in accelerator physics". In: (Dec. 2013). URL: https://www.osti.gov/biblio/1113658.

[48] J. L. Feng et al. "Protophobic Fifth-Force Interpretation of the Observed Anomaly in ^{8}Be Nuclear Transitions". In: *Phys. Rev. Lett.* 117 (7 2016), p. 071803. DOI: 10.1103/PhysRevLett.117.071803. URL: https://link.aps.org/doi/10.1103/PhysRevLett.117.071803.

[49] J. L. Feng et al. "Particle physics models for the 17 MeV anomaly in beryllium nuclear decays". In: *Phys. Rev. D* 95 (3 2017), p. 035017. DOI: 10.1103/PhysRevD.95.035017. URL: https://link.aps.org/doi/10.1103/PhysRevD.95.035017.

[50] J. L. Feng, T. M. P. Tait, and C. B. Verhaaren. "Dynamical evidence for a fifth force explanation of the ATOMKI nuclear anomalies". In: *Phys. Rev. D* 102 (3 2020), p. 036016. DOI: 10.1103/PhysRevD.102.036016. URL: https://link.aps.org/doi/10.1103/PhysRevD.102.036016.

[51] T. A. Tran. "Confirmation of the 8Be anomaly with a different spectrometer". 52nd international Symposium on Multiparticle Dynamics - ISMD 2023. 2023. URL: https://indico.cern.ch/event/1258038/contributions/5538280/.

[52] J. L. Feng et al. "Particle physics models for the 17 MeV anomaly in beryllium nuclear decays". In: *Phys. Rev. D* 95 (3 2017), p. 035017. DOI: 10.1103/PhysRevD.95.035017. URL: https://link.aps.org/doi/10.1103/PhysRevD.95.035017.

[53] M. Meucci. "Search for the X(17) particle in the 7Li(p, e+e-)8Be reaction with the MEG II detector". Doctoral Thesis. Rome: La Sapienza University of Rome, 2022. URL: https://hdl.handle.net/11573/1638985.

[54] F. Tanedo. *The Delirium over Beryllium*. 2016. URL: https://www.quantumdiaries.org/2016/08/25/the-delirium-over-beryllium/.

[55] Firak, D. S. et al. "Confirmation of the existence of the X17 particle". In: *EPJ Web Conf.* 232 (2020), p. 04005. URL: https://doi.org/10.1051/epjconf/202023204005.

[56] A. J. Krasznahorkay et al. "New anomaly observed in ^{4}He supports the existence of the hypothetical X17 particle". In: *Phys. Rev. C* 104 (4 2021), p. 044003. DOI: 10.1103/PhysRevC.104.044003. URL: https://link.aps.org/doi/10.1103/PhysRevC.104.044003.

[57] A. J. Krasznahorkay et al. "New anomaly observed in ^{12}C supports the existence and the vector character of the hypothetical X17 boson". In: *Phys. Rev. C* 106 (6 2022), p. L061601. DOI: 10.1103/PhysRevC.106.L061601. URL: https://link.aps.org/doi/10.1103/PhysRevC.106.L061601.

[58] A. Aleksejevs et al. *A Standard Model Explanation for the "ATOMKI Anomaly"*. 2021. arXiv: 2102.01127 [hep-ph].

[59] Daniele S. M. Alves et al. "Shedding light on X17: community report". In: *The European Physical Journal C* 83.3 (2023), p. 230. ISSN: 1434-6052. DOI: 10.1140/epjc/s10052-023-11271-x. URL: https://doi.org/10.1140/epjc/s10052-023-11271-x.

[60] A.F.V. Cortez et al. "A spectrometer for the measurement of anomalies in the angular correlation of electron and positron internally produced in excited 8Be and 4He". In: *Nuclear Instruments and Methods in Physics Research Section A: Accelerators, Spectrometers, Detectors and Associated Equipment* 1047 (2023), p. 167858. ISSN: 0168-9002. DOI: https://doi.org/10.1016/j.nima.2022.167858. URL: https://www.sciencedirect.com/science/article/pii/S0168900222011500.

[61] Gervino, Gianpiero et al. "X17 search project with EAR2 neutron beam". In: *EPJ Web Conf.* 279 (2023), p. 13007. DOI: 10.1051/epjconf/202327913007. URL: https://doi.org/10.1051/epjconf/202327913007.

[62] G. Azuelos et al. "Status of the X17 search in Montreal". In: *Journal of Physics: Conference Series* 2391.1 (2022), p. 012008. DOI: 10.1088/1742-6596/2391/1/012008. URL: https://dx.doi.org/10.1088/1742-6596/2391/1/012008.

[63] D. Banerjee et al. "Improved limits on a hypothetical $X(16.7)$ boson and a dark photon decaying into e^+e^- pairs". In: *Phys. Rev. D* 101 (7 2020), p. 071101. DOI: 10.1103/PhysRevD.101.071101. URL: https://link.aps.org/doi/10.1103/PhysRevD.101.071101.

[64] Paola Gianotti and on behalf of the PADME collaboration. "The study of the X17 anomaly with the PADME experiment". In: *Journal of Physics: Conference Series* 2586.1 (2023), p. 012140. DOI: 10.1088/1742-6596/2586/1/012140. URL: https://dx.doi.org/10.1088/1742-6596/2586/1/012140.

[65] P. Schwendimann. "Charged Lepton Flavour Violation Search and Exotic Physics with the MEG II Apparatus – Positron Beam Calibration Methods, MEG II Spectrometer Characterisation and Towards a Prototype for Future High Precision Calorimetry". Doctoral Thesis. Zurich: ETH Zurich, 2021. DOI: 10.3929/ethz-b-000512152.

[66] M.V. Pham et al. "Differential cross section measurements of the 6.13 MeV gamma ray from proton-induced reaction of fluorine". In: *Nuclear Instruments and Methods in Physics Research Section B: Beam Interactions with Materials and Atoms* 499 (2021), pp. 118–123. ISSN: 0168-583X. DOI: https://doi.org/10.1016/j.nimb.2021.03.011. URL: https://www.sciencedirect.com/science/article/pii/S0168583X21001026.

[67] R. Brun and F. Rademakers. "ROOT — An Object Oriented Data Analysis Framework". In: 389 (1997). See also https://root.cern.ch/, Release v6.28.00., pp. 81–86. DOI: 10.1016/S0168-9002(97)00048-X.

[68] J. R. Klein and A. Roodman. "BLIND ANALYSIS IN NUCLEAR AND PARTICLE PHYSICS". In: *Annual Review of Nuclear and Particle Science* 55.1 (2005), pp. 141–163. DOI: 10.1146/annurev.nucl.55.090704.151521. eprint: https://doi.org/10.1146/annurev.nucl.55.090704.151521. URL: https://doi.org/10.1146/annurev.nucl.55.090704.151521.

[69] W. Waltenberger, W. Mitaroff, and F. Moser. "RAVE—a Detector-inde-pendent vertex reconstruction toolkit". In: *Nuclear Instruments and Me-thods in Physics Research Section A: Accelerators, Spectrometers, Detectors and Associated Equipment* 581.1 (2007). VCI 2007, pp. 549–552. ISSN: 0168-9002. DOI: https://doi.org/10.1016/j.nima.2007.08.048. URL: https://www.sciencedirect.com/science/article/pii/S0168900207017196.

[70] J. Rauch and T. Schlüter. "GENFIT — a Generic Track-Fitting Toolkit". In: *Journal of Physics: Conference Series* 608.1 (2015), p. 012042. DOI: 10.1088/1742-6596/608/1/012042. URL: https://dx.doi.org/10.1088/1742-6596/608/1/012042.

[71] G. J. Feldman and R. D. Cousins. "Unified approach to the classical statistical analysis of small signals". In: *Phys. Rev. D* 57 (7 1998), pp. 3873–3889. DOI: 10.1103/PhysRevD.57.3873. URL: https://link.aps.org/doi/10.1103/PhysRevD.57.3873.

[72] R.Barlow and C. Beeston. "Fitting using finite Monte Carlo samples". In: *Computer Physics Communications* 77.2 (1993), pp. 219–228. ISSN: 0010-4655. DOI: https://doi.org/10.1016/0010-4655(93)90005-W. URL: https://www.sciencedirect.com/science/article/pii/001046559390005W.

[73] J. Conrad et al. "Including systematic uncertainties in confidence interval construction for Poisson statistics". In: *Phys. Rev. D* 67 (1 2003), p. 012002. DOI: 10.1103/PhysRevD.67.012002. URL: https://link.aps.org/doi/10.1103/PhysRevD.67.012002.

[74] M. A. Acero et al. *The Profiled Feldman-Cousins technique for confidence interval construction in the presence of nuisance parameters*. 2022. arXiv: 2207.14353 [hep-ex].

[75] Samuel S Wilks. "The large-sample distribution of the likelihood ratio for testing composite hypotheses". In: *The annals of mathematical statistics* 9.1 (1938), pp. 60–62.

[76] E. Gross and O. Vitells. "Trial factors for the look elsewhere effect in high energy physics". In: *The European Physical Journal C* 70.1 (2010), pp. 525–530. ISSN: 1434-6052. DOI: 10.1140/epjc/s10052-010-1470-8. URL: https://doi.org/10.1140/epjc/s10052-010-1470-8.

[77] F. James and M. Roos. "Minuit: A System for Function Minimization and Analysis of the Parameter Errors and Correlations". In: *Comput. Phys. Commun.* 10 (1975), pp. 343–367. DOI: 10.1016/0010-4655(75)90039-9.

[78] R. P. Brent. *Algorithms for Minimization without Derivatives*. 1st. Englewood Cliffs, New Jersey: Prentice-Hall, 1973.

[79] A. Signer, K. Kirch, and C. Hoffman. *Particle Physics at PSI*. In: *SciPost Phys. Proc.* vol. 5 (2021), p. 001. DOI: 10.21468/SciPostPhysProc.5.001.

[80] A. Amato. *Heavy-fermion systems studied by μSR technique*. 1997. DOI: 10.1103/RevModPhys.69.1119. URL: https://link.aps.org/doi/10.1103/RevModPhys.69.1119.

[81] E. Morenzoni et al. "Low-Energy Muons at PSI: Examples of Investigations of Superconducting Properties in Near-Surface Regions and Heterostuctures". In: *Proceedings of the International Symposium on Science Explored by Ultra Slow Muon (USM2013)*. 2013. DOI: 10.7566/JPSCP.2.010201. URL: https://journals.jps.jp/doi/abs/10.7566/JPSCP.2.010201.

[82] A. Amato et al. *Probing the ground state properties of iron-based superconducting pnictides and related systems by muon-spin spectroscopy*. Superconductivity in Iron-Pnictides. 2009. DOI: https://doi.org/10.1016/j.physc.2009.03.017. URL: https://www.sciencedirect.com/science/article/pii/S0921453409000999.

[83] R. Khasanov et al. *High pressure research using muons at the Paul Scherrer Institute*. 2016. DOI: 10.1080/08957959.2016.1173690. URL: https://doi.org/10.1080/08957959.2016.1173690.

[84] Z. Guguchia. *Unconventional Magnetism in Layered Transition Metal Dichalcogenides*. 2020. DOI: 10.3390/condmat5020042. URL: https://www.mdpi.com/2410-3896/5/2/42.

[85] T. Shang and T. Shiroka. *Time-Reversal Symmetry Breaking in Re-Based Superconductors: Recent Developments*. 2021. DOI: 10.3389/fphy.2021.651163. URL: https://www.frontiersin.org/articles/10.3389/fphy.2021.651163.

[86] F. Berg et al. "Target studies for surface muon production". In: *Phys. Rev. Accel. Beams* 19 (2 2016), p. 024701. DOI: 10.1103/PhysRevAccelBeams.19.024701. URL: https://link.aps.org/doi/10.1103/PhysRevAccelBeams.19.024701.

[87] R. Eichler and et al. *IMPACT conceptual design report*. 2022. URL: https://www.dora.lib4ri.ch/psi/islandora/object/psi%3A41209.

[88] D. Taqqu. "Compression and Extraction of Stopped Muons". In: *Phys. Rev. Lett.* 97 (19 2006), p. 194801. DOI: 10.1103/PhysRevLett.97.194801. URL: https://link.aps.org/doi/10.1103/PhysRevLett.97.194801.

[89] Y. Bao et al. "Muon Cooling: Longitudinal Compression". In: *Phys. Rev. Lett.* 112 (22 2014), p. 224801. DOI: 10.1103/PhysRevLett.112.224801. URL: https://link.aps.org/doi/10.1103/PhysRevLett.112.224801.

[90] I. Belosevic et al. "muCool: a novel low-energy muon beam for future precision experiments". In: *Hyperfine Interactions* 240.1 (2019), p. 41. ISSN: 1572-9540. DOI: 10.1007/s10751-019-1589-4. URL: https://doi.org/10.1007/s10751-019-1589-4.

[91] M. Aiba et al. *Science Case for the new High-Intensity Muon Beams HIMB at PSI*. Nov. 2021. arXiv: 2111.05788 [hep-ex].

[92] A. Antognini et al. "Studying Antimatter Gravity with Muonium". In: *Atoms* 6.2 (2018). ISSN: 2218-2004. DOI: 10.3390/atoms6020017. URL: https://www.mdpi.com/2218-2004/6/2/17.

[93] T. Prokscha et al. "The new μE4 beam at PSI: A hybrid-type large acceptance channel for the generation of a high intensity surface-muon beam". In: *Nuclear Instruments and Methods in Physics Research Section A: Accelerators, Spectrometers, Detectors and Associated Equipment* 595.2 (2008), pp. 317–331. ISSN: 0168-9002. DOI: https://doi.org/10.1016/j.nima.2008.07.081. URL: https://www.sciencedirect.com/science/article/pii/S016890020801067X.

[94] P. Bakule and E. Morenzoni. "Generation and applications of slow polarized muons". In: *Contemporary Physics* 45.3 (2004), pp. 203–225. DOI: 10.1080/00107510410001676803. eprint: https://doi.org/10.1080/00107510410001676803. URL: https://doi.org/10.1080/00107510410001676803.

[95] Dal Maso, Giovanni et al. "Future facilities at PSI, the High-Intensity Muon Beams (HIMB) project". In: *EPJ Web Conf.* 282 (2023), p. 01012. DOI: 10.1051/epjconf/202328201012. URL: https://doi.org/10.1051/epjconf/202328201012.

[96] P. Royer. *Solenoidal Optics*. Tech. rep. Geneva: CERN, 1999. URL: https://cds.cern.ch/record/479729.

[97] P. C. Kohnke. "ANSYS". In: *Finite Element Systems: A Handbook*. Ed. by C. A. Brebbia. Berlin, Heidelberg: Springer Berlin Heidelberg, 1982, pp. 19–25. ISBN: 978-3-662-07229-5. DOI: 10.1007/978-3-662-07229-5_2. URL: https://doi.org/10.1007/978-3-662-07229-5_2.

[98] COMSOL Multiphysics. "Introduction to COMSOL multiphysics®". In: *COMSOL Multiphysics, Burlington, MA, accessed Feb* 9 (1998), p. 2018.

[99] R. Frosch. Tech. rep. Villigen: Paul Scherrer Institut, 1980.

[100] R. Frosch. Tech. rep. Villigen: Paul Scherrer Institut, 1995.

[101] D. Ioanoviciu. "Ion Optics". In: *Aspects of Charged Particle Optics*. Ed. by Peter W. Hawkes. Vol. 73. Advances in Electronics and Electron Physics. Academic Press, 1989, pp. 1–92. DOI: https://doi.org/10.1016/S0065-2539(08)60567-3. URL: https://www.sciencedirect.com/science/article/pii/S0065253908605673.

[102] J. B. Mockus and L. J. Mockus. "Bayesian approach to global optimization and application to multiobjective and constrained problems". In: *Journal of Optimization Theory and Applications* 70.1 (1991), pp. 157–172. ISSN: 1573-2878. DOI: 10.1007/BF00940509. URL: https://doi.org/10.1007/BF00940509.

[103] P. I. Frazier. *A Tutorial on Bayesian Optimization*. 2018. arXiv: 1807.02811 [stat.ML].

[104] James Bergstra et al. "Algorithms for Hyper-Parameter Optimization". In: *Advances in Neural Information Processing Systems*. Ed. by J. Shawe-Taylor et al. Vol. 24. Curran Associates, Inc., 2011. URL: https://proceedings.neurips.cc/paper_files/paper/2011/file/86e8f7ab32cfd12577bc2619bc635690-Paper.pdf.

[105] J. Bergstra, D. Yamins, and D. Cox. "Making a Science of Model Search: Hyperparameter Optimization in Hundreds of Dimensions for Vision Architectures". In: *Proceedings of the 30th International Conference on Machine Learning*. Ed. by Sanjoy Dasgupta and David McAllester. Vol. 28. Proceedings of Machine Learning Research 1. Atlanta, Georgia, USA: PMLR, 2013, pp. 115–123. URL: https://proceedings.mlr.press/v28/bergstra13.html.

[106] W. Lyu et al. "Multi-objective bayesian optimization for analog/RF circuit synthesis". In: June 2018, pp. 1–6. DOI: 10.1145/3195970.3196078.

[107] R. Saravanan, S. Ramabalan, and C. Balamurugan. "Evolutionary optimal trajectory planning for industrial robot with payload constraints". In: *The International Journal of Advanced Manufacturing Technology* 38 (Oct. 2008), pp. 1213–1226. DOI: 10.1007/s00170-007-1169-7.